This is to certify that the

dissertation entitled

HREM EXAMINATION OF CORE STRUCTURES OF DISLOCATIONS IN B2 INTERMETALLIC COMPOUND Co-Al

presented by

Yu Zhang

has been accepted towards fulfillment of the requirements for

Ph.D. degree in Materials Science

Major professor

Date 10/26/95

HREM EXAMINATION OF CORE STRUCTURES OF DISLOCATIONS IN B2 INTERMETALLIC COMPOUND Co-Al

By

Yu Zhang

A DISSERTATION

Submitted to
Michigan State University
in partial fulfillment of the requirements
for the degree of

Doctor of Philosophy

Department of Materials Science and Mechanics

1995

ABSTRACT

HREM EXAMINATION OF CORE STRUCTURES OF DISLOCATIONS IN B2 INTERMETALLIC COMPOUND Co-Al

By

Yu Zhang

Mechanical properties of single crystal B2 Co-Al intermetallic compounds were measured at both room and elevated temperatures. Off-stoichiometric Co-48Al and Co-52Al are stronger at high temperatures and more brittle at room temperatures than stoichiometric Co-50Al. Dislocations in deformed Co-Al were investigated via diffraction TEM analysis ($\mathbf{g}\cdot\mathbf{b}=0$ criteria). Slip system activation was found to be temperature and orientation dependent. <010> type edge dislocations were found to always dominate the deformation under the various conditions. <111> and <110> dislocations were observed following deformation at 1300 K and are regarded as the reaction products of <010> dislocations. Stoichiometry deviations were found to have no effect on the selection of slip systems. Core structures of the predominant <010> dislocations generated by 1300 K deformation were examined via high resolution transmission electron microscopy (HREM). No significant core dissociation is observed in Co-50Al, while significant dissociation is seen in Co-48Al and Co-52Al. Simulations of HREM images, based on theoretical structures were compared with the experimental observations. The simulations match well only with the experimental results in Co-50Al. The dislocation core structures in Co-Al were compared with those observed in Ni-Al and Fe-Al. The <010> dislocations in off-stoichiometric Co-Al have significantly more complicated core structures than in off-

off-stoichiometric Co-Al have significantly more complicated core structures than in off-stoichiometric Ni-Al or Fe-Al. The core structures of <010> edge dislocations in B2 alloys are responsible for the high strength and low ductility and are highly sensitive to deviations from stoichiometry.

To my wife and daughter

ACKNOWLEDGEMENTS

I would like to express my sincere appreciation to Dr. M.A. Crimp, my major advisor, for his guidence and support throughout my doctoral studies and for his many helpful suggestions and paintaking reviews during the preparation of the dissertation.

I would like to thank the Office of Naval Research and Dr. G. Yoder (scientific officer). This research would not have been fulfilled without the ONR's support and funding (contract number: N00014-90-J-1910).

I would like to acknowledge the committee members for their precious time on reviewing my disseratation and attending the comprehensive and oral examinations.

A special thank you is to be extended to Mr. P. Madill, vice president and general manager of Stevens International Corp./Bernal Division for his understanding and support.

I also wish to thank the following groups of people: Dr. D. Farks of Virginia Polytechnic Institute and State University for providing EAM calculation results; Naval Air Research Development Center and Dr. D. Pope of the University of Pennsylvania for providing single crystal Co-Al; Electron Microanalysis Laboratory and Dr. J. Mansfield of the University of Michigan for the use of the JOEL-4000EX; Mr. Z. Cai, the Ph.D candidate of Dr. D. Grummon's Thin Film Laboratory for providing assistance in mechanical testing; Mr. B. Holmes of the Case Center for his thoughtful assistance in computer program-

ming and EMS software package; Mr. S.C. Tonn and Mr. D. Scharrott, my research partners and friends, for their invaluable assistance; Mr. A. Gibson and his wife Mrs. B. Gibson for their proof reading my first manuscript.

In addition, I owe gratitude to my Chinese friends and colleagues at the department, including Mr. Y. Wu, Mr. Z. Yeh, Mr. L. Wang and Dr. P. Sheng, for their assistance and friendship.

Last but not least, a special thank you is to be extended to my wife, Yuqing and daughter, Chloe for their patience, understanding and continual encoragement during the many months of this research.

TABLE OF CONTENTS

LIST OF TABLES

LIST OF FIGURES

1. Introduction/Background

1.1 Barriers to industrial application of B2 intermetallic compounds

Conventional superalloys are becoming less capable of meeting the growing demands for lighter weight, higher temperature, high performance engine materials. Recently, considerable research has been focused on suitable alternatives, such as intermetallic compounds (IC), metal matrix composites (MMC), intermetallic matrix composites (IMC) and ceramic matrix composites (CMC). Among these, several intermetallic compounds such as titanium aluminides, nickel aluminides and iron aluminides, promise to be near-term replacement materials with distinguished properties (see excellent reviews [1-4]). Compared to nickel based superalloys, having the B2 structure (fig. 1) CoAl, NiAl and FeAl offer the advantages of lower density, higher strength at elevated temperature, larger coefficients of thermal conductivity, higher Young's modulus, higher diffusional stability and better resistance to oxidation and corrosion. This makes B2 alumnides potentially competitive and attractive materials for high temperature service necessary to increase engine thrust-to-weight ratios.

Unfortunately, like most high temperature and high strength intermetallic compounds, CoAl and NiAl are extremely brittle at ambient temperature. This lack of ductility and low toughness limit the fabrication and application of these aluminides. Therefore, most studies of B2 intermetallics have been focused on understanding and improving their poor ductility [1].

The low ductility of B2 intermetallic compounds may be attributed to intrinsic and/or extrinsic brittleness. Intrinsic brittleness may be related to lack of sufficient slip systems, low density of mobile dislocations, presence of high energy boundaries, impurity

scale, stoichiometry and texture. Poor grain boundary cohesion may result from high ordering energies, large differencs in electronegativity, valence electron configurations between transition elements (Co, Ni and Fe) and aluminium [1]. This lack of grain boundary strength can sometimes be reduced by adding small amounts of boron [5], refining the grain size [6], or eliminated by using single crystals. Microstructural control and microalloying with iron, gallium and molybdenum significantly improves the ductilities of most B2 alloys [7,8,9]. Reducing the interstitial content or scavenging the interstitials through certain alloying additions may help to avoid dislocation-point defect interaction and thus increases the plasticity [1].

Extrinsic brittleness is mainly associated with environmental effects and pressurization. The ductility of NiAl or FeAl is very poor when tested in air and increases dramatically in vacuum or oxygen envionments [10,11]. Hydrostatic pressure increases the ductility in NiAl [12]. The high temperature strength of these aluminides can be raised by adding ceramic particles, the precipitation of second phases and/or solid-solution hardening by substitutional elements. However, these enhancements typically must be balanced with decreases in ductility.

The mechanical properties of intermetallic compounds depend to a large extent on dislocation mobility, especially at low to intermediate temperatures at which diffusion rates are negligble. Dislocation mobility in turn is determined by the mobile dislocation density, dislocation interaction and multiplication, and lattice friction. Therefore, understanding dislocation substructures and their corresponding mechanical behavior may be one of keys to overcoming the barriers to industrial applications of B2 intermetallic compounds.

1.2 Mechanical properties of B2 structure CoAl, NiAl and FeAl

Even though they have the same ordered bcc structures, the strengths and ductilities of the B2 aluminides differ considerably. As cobalt, nickel and iron are neighbors in the periodic table, and the electron structures of these elements have only one electron difference in their d-shells, their aluminides have the same crystal structure, almost identical lattice parameters and similar material densities and melting temperatures (table 1). It might be expected that these similarities would make the mechanical properties of these materials similar, but large differences exist in the following areas:

1.2.1. Hardness

In one of the earliest examinations of the mechanical behaviors of B2 aluminides, Westbook [13] studied the temperature dependence of the hardnesse of polycrystalline CoAl, NiAl and FeAl. The order of hardness at room temperature is: FeAl>CoAl>NiAl; at 773 K, the order is: CoAl>FeAl>NiAl and at 1073 K, the order becomes: CoAl>NiAl>FeAl. The results indicate that CoAl has the best capability to maintain its strength at elevated temperatures. The effect of composition changes on hardness at 1073 K is shown in Figure 2. Stoichiometric CoAl and NiAl have the lowest hardness for their respective systems. Small deviations from stoichiometry in CoAl increases the hardness more significantly than for NiAl, whereas in FeAl, the hardness decreases continously with increasing iron content.

1.2.2. Critical resolved shear stress

Slip begins when the shearing stress on the slip plane in the slip direction reaches a threshold value called the critial resolved shear stress (CRSS). Selected CRSS values

determined at room temperature for various B2 aluminides are given in table 2. The CRSS for <111>{110} slip in Fe-49Al [14] is smaller than that [15] of Co-50Al. This suggests that <111>{110} slip systems are more easily activated in FeAl and consequently this material is less brittle than CoAl. However, even though the CRSS values for <111>{110} in FeAl are larger than those for <100> slip in NiAl [16] at room temperatue, it does not follow that NiAl is more ductile than FeAl. This is because there are only three independent <100>{110} slip systems while <111>{110} slip results in more than five independent slip systems. Consistent with the hardness behavior noted by Westbrook [13], the CRSS varies with stoichiometry in FeAl. The CRSS for <111> slip in Fe-39Al is much lower than that in Fe-49Al tested under the same conditions [14]. Information on the CRSS-composition relationship is not available for CoAl and NiAl.

1.2.3. Ductility

CoAl is extremely brittle at room temperature. Chisel toughness is a simple measurement of room-temperature toughness [17]. A steel chisel and either a light or a heavy harmmer are used to define a four-level toughness scale as follows: level 0, broken on cooling after casting or broken with a light tap of a light hammer; level 1, required repeated sharp blows for fracture with a light hammer (160 g); level 2, required a sharp blows with a heavy hammer (729 g); and level three, not fractured even with a heavy hammer. The Chisel toughness of CoAl is zero [17]. This material displays no tensile elongation and exhibits less than 1% compressive plastic strain at ambient temperature [15]. As the temperature is raised, CoAl displays limited but increasing compressive ductility. Like CoAl, NiAl is also very brittle. Stoichiometric NiAl displays 1-2% tensile elongation

at 297 K, while hypo-and hyper-stoichiometric changes in composition results in a loss of this ductility [18]. In contrast, stoichiometric Fe-50Al displays zero ambient temperature ductility, while Fe-rich deviations result in ductility enhancement.

1.2.4. Yield strength

The yield strength of these materials is affected by both temperature and composition. With increasing temperature, the 0.2% proof stress ($\sigma_{0.2}$) continously decreases in NiAl. Off-stoichiometric compositions have higher $\sigma_{0.2}$ values than the stoichiometric composition in NiAl [19]. This is reflected in compression tests [20], where stoichiometric compostions have lower values of flow stress at the temperatures below 1273 K. In contrast, above 1273 K, Ni-50Al is stronger than Ni-46Al and Ni-56Al.

1.2.5. Brittle-ductile transition temperature (BDTT)

Stoichiometric polycrystalline Co-Al has the lowest compressive BDTT value (about 527 K) of Co-Al alloys. However, this value increases to over 827 K in both the Co-rich and Al-rich sides of stoichiometry (fig.3) [21]. Thus the BDTT is very sensitive to stoichiometry in CoAl. In contrast, the tensile BDTT of polycrystalline Ni-50Al is 550 K [22]. A lower value (300 K) is obtained if the Ni-50Al specimens are compressed (fig. 4) [23]. But in Ball and Smallman's experiments [24], the BDTT of Ni-50Al was found to be 827 K, whereas the BDTT of Ni-51Al was found to be 727 K and the BDTT of Ni-48Al was found to be 627 K. The difference between Pascoe's [23] and Ball's [24] BDTT observations may result from the effect of grain size and strain rate. However, it is interesting that stoichiometry deviations increase the BDTT in CoAl but decrease it in NiAl.

In single crystal NiAl, the BDTT also depends on crystal orientation. Darolia [2] found that the BDTT is 623-670 K in the <100> orientation and around 473 K in the <111> orientation.

1.2.6. Creep strength

Hocking et al. [25] first observed that single crystal CoAl has a greater resistance to creep than single crystal NiAl at 1323 K (fig.5). Creep strain rates were found to be at least 1.5 orders of magnitude greater for NiAl than CoAl tested at the same stress. Yaney and Nix [26] examined polycrystalline materials using the strain rate change technique. They concluded that NiAl, exhibiting pure-metal type behavior (dislocation slip deformation), is weaker than CoAl which undergoes a transition from pure-metal to alloy-type deformation (dislocation climb deformation). Wittenberger [27, 28] examined the compressive behaviors of these two alloys at slow plastic strain rates and results were consistant with the results of Hocking el at. and Yaney and Nix (fig. 6). Deviation in stoichiometry greatly affects the creep strengths of both CoAl and NiAl. Contrary to hardness and BDTT experiments, where Co-50Al is considered a "weak" composition, the highest creep strength is obtained at this composition. Another feature of figure 6 is that the creep strength of CoAl is much more sensitive to stoichiometry than that of NiAl. A 1% change in stoichiometry results in a 16-37% change in the creep strength of CoAl but only a 4.4% change in the creep strength of NiAl.

The reason for the differences in the mechanical behavior of CoAl, NiAl and FeAl are still unclear. It is well known that the creep behavior of materials is mainly controlled by dislocation and/or diffusion factors. At high homologous temperatures, the activation

energy for deformation in many materials is approximately equal to the activation energy for lattice self-diffusion [26]. As the self-diffusion activation energy can be regarded approximately as a linear function of the crystal melting point T_m [24] ($Q = 34 (\pm 20) T_m$), the Q_{CoAl} may be nearly equal to Q_{NiAl} because of their similar melting temperatures. The diffusivities of Co^{60} in the two compounds are plotted as a function of temperature in fig. 7 [29]. While the diffusivity of Co^{60} in NiAl is markedly greater than in CoAl at temperatures lower than 1300 K, the difference is quite small at 1300 K, the creep testing temperature. This result was reinforced by a more accurate experiment measuring the diffusivity of Ni^{63} in NiAl [30]. These results suggest that the superior creep strength of CoAl at 1300 K may not be related to the differences in diffusivities between CoAl and NiAl.

Yaney and Nix [26] pointed out that any drop in elastic stiffness as temperature increases will result directly in lower strengths at elevated temperatures. If the stiffness of NiAl were considerably less than that of CoAl at 1300 K, the difference in strength between these two compounds could be easily understood. But this is not the case. The Young's modulus of CoAl and NiAl have been determined as a function of temperature (eq.1 and eq.2) and are given by the experimental relations:

$$E(CoAl)=327.88 - 0.167T \quad \text{.....(1) [31]}$$

$$E(NiAl) =199.80 - 0.040T \quad \text{..... (2) [32]}$$

At 1300 K, E(CoAl)=110.78 GPa and E(NiAl)=147.8 GPa. This data does not support the above stiffness assumption. Therefore, neither diffusivity nor stiffness can be used to explain the difference in creep strength at 1300 K between CoAl and NiAl.

Another difficult aspect to understand is the disparity in room temperature ductility between these alloys. Ductility is highly affected by structure, precipitation, grain boundaries, hydrogen concentration, impurity levels and texture. This difficulty can be more simply addressed by examining single crystals. Fracture analysis [33, 34] has shown that CoAl and NiAl single crystals tend to fracture by cleavage on {011} planes in <111> and <110> orientations and on {112} planes in the <100> orientation. These cleavage planes are the same as the slip planes of these aluminides (as will be discussed in the following sections). Thus, it may be reasonable to relate the ductility and fracture differences to dislocation slip in these materials. Assuming a dislocation mechanism, the lack of understanding of the DBTT and sensitivity to stoichiometry might be explained by the onset of dislocation climb, thermally activated slip, unlocking of dislocations from vacancies, and additional slip systems. All of these mechanisms are related to the mobility of dislocations. Therefore it is reasonable to believe that the behavior of mobile dislocations control the deformation processes in these B2 aluminides.

1.3 Dislocations and slip modes

The slip direction in bcc structures is almost always 1/2<111>, which corresponds to the smallest perfect dislocation Burgers vector. The corresponding slip planes are {110} {112} and/or {123}. In B2 ordered bcc structures, 1/2<111> dislocation movement produces an anti-phase boundary(APB) and increases the energy. This results in <100> often becoming a more favorable slip vector. Selection of the operative slip system can also depend on crystal orientation, temperature and composition. A single crystal specimen oriented to a <100> compression axis shows a macroscopic yield strength many

times higher than if it is oriented to a non-<100> direction. This is due to the fact that the resolved shear stress for the "easy" <100> slip direction is zero in the <100> crystal. Therefore, <100> oriented crystals are denoted as "hard" crystals and non-<100> oriented crystals are referred to as "soft" crystals. Considerable research on the temperature and composition effects on the slip systems and deformation mechanisms has been reported for NiAl and FeAl, while information is very limited for CoAl.

1.3.1. Slip in CoAl

In 1971, Hocking et al. [25] first reported their observations of dislocations introduced in single crystal CoAl by creep testing at 1300 K. Because the arrangement and appearance of dislocations in CoAl were very similar to those in NiAl (discussed in 1.3.2), the dislocations in CoAl were assumed to be <100> dislocations. In 1986, Nix et al. [35] observed <100> and <111> edge dislocations in polycrystalline Co-49.3 at%Al extruded at 1505K. The corresponding slip planes for <100> dislocations were {001} and {110}, while <111> dislocations were observed on {110} planes. <110> dislocations were not observed in their studies. Drelles [15] examined the dislocations in single crystal CoAl deformed at room temperature. <111> screw dislocations were found for all orientations remote from the <111> corner of the unit triangle. For orientations near the <111> corner, the primary dislocations had Burgers vectors of [001] and were of a screw character. The corresponding slip planes were {110}, {211} and {321} for the <111> dislocations and {110} for the <001> dislocations. Dissociation of the dislocations was not observed by the weak-beam technique [15]. The presence of <111> slip at room temperature is contrary to Yamaguchi and Umakoshi's predication of <100> slip [36]. Research work on

dislocation structures in off-stoichiometric CoAl has not been reported.

1.3.2. Slip in NiAl

A large number of studies have examined the dislocation substructures involved in the deformation of NiAl alloys. The observed slip systems in "soft" stoichiometric single crystals NiAl are predominantly <100>{110} and <100>{001} at both ambient and elevated temperatures [37-39]. However, <011> dislocations and <111> dislocations are occasionally observed, presumely as a result of interection of two or three glide <100> dislocations [40,41]. In "hard" stoichiometric NiAl, <111>{112}, <111>{110} and <110>{110} slip systems are observed at elevated temperatures. <111> dislocations are usually preferred at lower temperatures (77°K-600°K) and <110> dislocations at higher temperatures (above 600°K) [2,42,43]. <110> slip is not activated at room temperature. There are also a few reports that <100> crystals deformed in compression may deform by an extremely localized glide of <100> dislocations (termed "kinking") [44,45].

Deviation from stoichiometry affects the activiation of slip systems. {110} slip planes disappear in favor of {001} slip planes in [011] oriented Ni-48Al and Ni-51Al deformed at 600°K [46]. <111> dislocations are observed in nickel-rich Ni-42Al extruded at 1023°K [47].

1.3.3. Slip in FeAl

At high temperatures (T >0.45Tm), <100>{110} slip systems are observed in both "soft" and "hard" orientations [51]. This suggests that <100> slip has a much lower CRSS than <111> slip at elevated temperatures. The observed slip systems are generally not affected by alloy stoichiometry with some slip systems being observed in both aluminum-rich and iron-rich compositions. At room temperature, <111> slip is dominant [14,49].

However, Munroe and Baker observed <100> dislocations created through the interaction of the <111> dislocations in iron-rich FeAl [53]. There is still controversy as to how the aluminium content affects the activation of slip systems [48,52,53].

In summary [table 3], at high temperature and in soft orientation, the predominant dislocations in all three B2 aluminides have <100> Burgers vectors. At high temperature and in hard orientation, <110> or <111> dislocations are operative in NiAl while <100> dislocations are active in FeAl. At room temperature and in any orientation, <111> dislocations are favored in CoAl and FeAl, while <100> dislocations are activated in NiAl.

Analyzing the experimental results mentioned above, the following questions may be raised:

Why is CoAl more brittle than NiAl (with <100> slip) and why is FeAl more ductile than NiAl at room temperature despite the fact that <111> slip is exhibited in both CoAl and FeAl at ambient temperatures ?

Why does CoAl have the highest creep strength at elevated temperatures where <100> slip dominates in all three materials ?

The answer might be a dislocation controlled deformation mechanism. In simple binary single crystals, dislocation controlled deformation mainly depends on slip, cross slip, climb, twinning, dislocation-point defect interactions, dislocation-dislocation interaction and dislocation-planar defect interaction. Furthermore, the motion of dislocations is mainly affected by lattice friction, crystal geometry, temperature and stress. In B2 single crystals, for given testing conditions, lattice friction may play a very important role in manipulating dislocation behavior. According to the Peierls-Nabarro model, lattice friction is caused by reluctant motion of dislocation cores. For this reason, it is necessary to explore the core structures of dominant dislocations in B2 crystals in order to elucidate the dissimilarity in mechanical properties.

1.4 Dislocation Cores

Many properties of dislocations are governed by the long range stress and strain field of dislocations, such as dislocation-dislocation intersection and dislocation-grain boundary interaction. However, some physical and mechanical phenomenon occur as a result of interactions very close to the center of dislocations. For example, lattice resistance and point defect-dislocation interactions depend on the atomic structure of dislocations. Thus, in order to fully understand the dislocation slip and dislocation behavior of the B2 aluminides, it is necessary to examine the dislocation core structure.

1.4.1 Brief history of core theory development

For a long time, metallic materials were treated as elastic continua. The effect of dislocation cores on deformation has not been emphasized in studies of deformation mechanisms. However, basic theory of the selection of slip systems cannot explain the violation of Schmid's law in bcc metals (slip is not confined to well-defined low index planes [54]) and β-brass (both non-crystallographic and {110} crystallographic slip are observed [55]). Nor can basic theories explain the temperature/orientation dependence of the flow stress in most bcc and B2 structures.

Theoretical research on core structures began much earlier than experimental observations. The first models were presented by Frenkel and Kontorara[57], Peierls[58] and Nabarro [59]. In their so-called semi-continuum models, only the atomic planes adjacent to the slip plane were treated discretely while the rest of the crystal was regarded as a continuum. These models are suitable for planar and compact dislocation cores and therefore are only suitable for pure fcc metals.

Later, a large number of studies were conducted in bcc structures. It has been theorized that the cores of 1/2<111> screw dislocations in the bcc structures are not confined to their slip planes but instead extend into several planes of the <111> zone (fig.8) [56]. This renders the dislocation sessile and provides a plausible explanation for the large Peierls stress and the strong temperature dependence of the flow stress observed in bcc metals, along with accounting for the slip asymmetry and complex orientation dependence.

Theoretical studies on dislocation cores have been accelerated since 1970's. So far, various models for bcc [56,60,61], fcc [57,58,59], hcp [61,63], B2 [62,67,68], DO_3 [66], $L1_2$ [62,64] and DO_{22} [65] have been established.

1.4.2 Construction methods of core models

Although there are a large varity of methods for modelling dislocation cores, all of these models use the same general approach. The theoretical models are based on an empirical interatomic potential by which a perfect lattice is determined. This perfect lattice is then divided into an inner region with a surrounding border region as shown in fig.9. In the inner region, a dislocation is introduced by imposing the elastic displacements upon all the atoms corresponding to a dislocation in the center of the block. The core configuration is then set by minimizing the total energy using a relaxation method (static or dynamic method). During the relaxation, the positions of the atoms in the border region are either kept fixed or modified in response to the changes which occur in the inner region, i.e. fixed or flexible boundary conditions. Figure 10 is a calculation diagram for static relaxation method with the fixed boundary condition.

1.4.3 Differential displacement tensor

Since a displacement field in a core is highly localized, a quantity which is large in the core and vanishes far from the core is used to map this field. Vitek [61] first introduced the differential displacement, a stress tensor, inside the core. The differential displacement is drawn as normalized arrows along the dislocation line and described using the following equation.

$$\alpha_i^{\alpha\beta} = \frac{1}{2\Omega_i}\sum_j \frac{d\phi|\underline{r}_{ij}|}{d|\underline{r}_{ij}|} \bullet \frac{r_{ij}^{\alpha} r_{ij}^{\beta}}{|\underline{r}_{ij}|} \qquad \text{.....(3)}$$

Where;

$\alpha_i^{\alpha\beta}$ is differential displacement tensor at the atom i

$|\underline{r}_{ij}|$ is the position vector of atom i relative to atom j

α, β are the coordinates in x, y axis

Ω_i is the local atomic volume

ϕ is the interatomic potential

1.4.4 Types of cores

In general, there are three types of cores: planar cores, non-planar cores and split cores. In planar cores, core spreading is confined to certain crystallographic planes containing the dislocation line. In non-planar cores, the core spreads into several non-parallel planes of the zone of a dislocation line. Non-planar cores can be further divided into cross slip cores and climb cores. A dislocation has a cross slip core if the Burgers vectors of fractional dislocations or continuously distributed dislocations all lie in the planes of core spreading. A climb core has the Burgers vectors of the dislocations possessing components perpendicular to the planes of spreading. Split cores are termed as non-compact

cores. They are further divided into dissociated cores and decomposed cores. In dissociated cores, the superdislocations are dissociated into several superpartials with an APB (anti-phase boundary), CSF (complex stacking fault) or other stacking fault in between, for example, $[01\bar{1}]=1/2[01\bar{1}]+\gamma+1/2[01\bar{1}]$. The stacking fault planes are often not the slip planes of the original superpdislocations and thus the superpartials can be sessile. In decomposed cores, one type of superdislocation can decompose into another type of superdislocation without the formation of stacking faults, for example, [011]= [010] +[001]. The slip planes of the so-formed dislocations may or may not be the slip planes of "ordinary" dislocations. For example, both <100>{001} dislocations and <110>{001} dislocations have the same slip planes, while <100>{001} dislocations have the different slip planes from <110>{110} dislocations. Among these types of cores, the non-planar cores and split cores will strongly affect the dislocation motion.

1.4.4.1 Core structures in the bcc crystal structure

1.4.4.1.1 $\frac{1}{2}<111>$ screw dislocation in bcc structure

Extensive experimental evidence indicates that many distinguishing features of the low temperature plastic behavior of bcc metals are controlled by a special core structure of 1/2<111> screw dislocations. As the stacking fault energy is high in bcc structures, simulations have found no dislocation dissociations. Instead, Vitek [61,69,70] found core structures are clearly non-planar and are spread principally into three intersecting {110} planes (fig. 11 a and b). This non-planar 1/2[111] core can be regarded as the sum of three 1/6[111] fractional dislocations with generalized unstable stacking faults on {110} planes. The cores of these 1/6[111] dislocations can be further spread asymmetrically onto {112}

planes resulting in a larger shear strain in the twinning than in the anti-twinning sense. This asymmetry of 1/2[111] dislocation cores can be used to explain the twinning-anti-twinning asymmetry of slip in bcc metals.

1.4.4.1.2 Effect of stress on core structures of 1/2 <111> dislocations in bcc metals

Dislocation core configurations may change under the inflence of external stresses. The transition behavior of a core depends on the interatomic potentials of the material and the sense of the applied stress [93]. In the case of 1/2[111] screw dislocations in bcc, there are three core transformation modes resulting from stress [61, 93].

1. The transformation from one degenerate configuration to the other. For example, the core structure in fig.11(a) can convert into the structure shown in figure 11(b).

2. The formation of extended multilayer faults on {112} planes [61]. As the stress is gradually increased, the trailing fractional dislocation on the (110) plane disappears, while the leading fraction dislocation on $(\bar{1}01)$ extends into the $(01\bar{1})$ plane. Since the core is not confined exactly to either the $(\bar{1}01)$ or $(01\bar{1})$ plane, the dislocation establishes a multilayer fault on the (112) planes.

3. The formation of an extended single layer fault on a {110} plane [61]

As the shear stress increases, the leading fractional dislocation extends itself on the $(\bar{1}01)$ plane, leaving a single layer fault on this plane, while the trailing fractional dislocation on $(\bar{1}10)$ is constricted towards the core center and the fractional on $(0\bar{1}1)$ is also con-

stricted slightly (fig.12 a). With further stress increases, fractional dislocations on $(0\bar{1}1)$ begins to spread on $(\bar{1}10)$ plane in the opposite direction (fig. 12b). As the stress increases further, the leading fractional spreads steadily on the $(\bar{1}01)$ plane, while two $(\bar{1}10)$ fractionals become increasly constriced (fig. 12c). Finally, the whole dislocation moves freely on the $(\bar{1}01)$ plane.

The application of an external stress significantly changes the core structure of a dislocation before it moves. The unstressed dislocation core with non-planar spreading can therefore be regarded as sessile.

1.4.4.1.3 [111](110) edge dislocation core in bcc

The structure of non-screw 1/2<111> dislocations in bcc metals is significantly different from the 1/2<111> screw cores. Chang and Graham [72] studied [111](110) edge dislocations with a line direction $[11\bar{2}]$ in bcc iron. The core atoms were moved one Burgers vector according to the anharmonic potential and Johnson potential [72]. A maximum potential barrier (the Pererls barrier) of about 0.029 eV was obtained at the distance 1/4**b** from the equilibrium position. The dislocation energy data in the region beyond a distance of about 0.5 nm from the core center agreed well with those predicted from continuum anisotripic elasticity theory. The calculated Peierls stress of a <111> edge core is 1.3-4.0 x $10^{-3}\mu$, significantly lower than that of a <111> screw dislocation (27-29 x 10^{-3} μ) according to reference [61].

1.4.4.2 Core Structures in B2

1.4.4.2.1 <111> screw dislocations in B2

The B2 structure is one of the ordered bcc lattices (DO_3 as well) and in many ways, the dislocation structures in bcc and B2 are related. In B2 structures, only one type of APB can exist on {110} and {112} planes, which is created by a $\frac{1}{2}\langle 111\rangle$ displacement. No other stable stacking faults have been found [68]. Therefore, <111> dislocations in B2 crystals may have a 2 fold dissociation:

$$a_o\langle 111\rangle = \frac{a_0}{2}\langle 111\rangle + APB + \frac{a_0}{2} < 111 > \qquad \text{.....(4)}$$

Elastic calculations have found the APB either on {110} or {112} planes [62] with the corresponding fault widths of 2 nm and 1.7 nm respectively. The 1/2<111> cores with an anti-phase boundary on {110} planes have a lower energy than cores with the APB on {112} planes.

1.4.4.2.2 <100> core in NiAl

<100> dislocations are frequently found in B2 alloys after high temperature deformation. The edge <100>{001} dislocations have two configurations as illustrated in figure 13 [45,68]. The local stoichiometry of these two configuration are different. NiAl, for example, can have one configuration with Ni atom at the termination of the extra half planes (fig. 13a), while configuration "B" terminates with a Al atom . Configuration A has a lower energy than configuration B in NiAl. The distortion of the core is spread in compact planes of the type {110}. In NiAl, the minimum stress to initiate motion for this edge core is high, 0.018-0.022 μ (about 2580 MPa) due to non-planarity [68]. In contrast to <001>{001} edge dislocations, <001>{011} cores are spread predominantly on {110}

glide planes, although some non-planarity is present on {111} planes. The stress required to initiate motion of this core is nearly 90% lower, 0.002-0.003 μ (about 320 MPa). In Parthasarathy's calculation [68], the <010>{001} slip systems are the most difficult to initiate (mobility comparison in table 4). This is not in agreement with previous experimental results which show that the critical stress to move the <100> edge dislocation on the {100} plane is comparable with that for motion on the {110} plane. Therefore, there must exist some factors not considered in the core models, such as out of slip plane displacements, or the tendency of the core to spread on the {110} planes.

1.4.5 Core structures and potentials

Details of the core configuration of a dislocation depend sensitively on the interatomic potentials used. For the same crystal, different core structures are produced when different potential functions are employed. In early studies of the core structures of the 1/2<111> screw dislocation in bcc crystal, Vitek [61] used the Johnson potential [75,76] to calculate the core structures and found that 1/2<111> dislocation cores have non-planar degenerate structures, while Takeuchi [73] argued that a non-degenerate configuration of the screw dislocaton may exist according to his calculation using a different potential. Therefore, the accuracy of the interatomic potentials used to determine the interaction between atoms is key to a successful computer simulation.

1.4.5.1 Summaries of potentials

There are two types of potentials currently used to simulate core structures: pair-potentials and embedded atom (EAM) N-body potentials. The pair potentials can be also

divided into five catagories: empirical potentials, semi-empirical potentials, pseudopotentials, tight-binding approximation and ab-initio pair potentials. These pair-potentials [74] are briefly described below:

1.4.5.1.1 Empirical potentials

The functional form of the empirical potentials are arbitary and may be any reasonable function which will fit a large number of physical parameters. The function coefficients are usually determined by matching crystal structure, elastic properties, phonon spectra, vacancy formation energy, stacking fault and APB energies, and alloying and ordering energies. The typical type of empirical potentials are Johnson-I potentials [75] that were developed for bcc in order to model α-Fe. The short range elastic constants c_{ij} for a bcc lattice can be related to the first and the second derivatives of the spherically symmetric potential at the first and the second neighbor equilibrium sites.

$$(c_{11}-c_{12})_{SR} = \frac{2}{3r_2}\left(\frac{6}{r_1}\phi'_1 + 3\phi''_2 + \frac{3}{r_2}\phi'_2\right) \qquad \text{.....(5)}$$

$$(c_{44})_{SR} = \frac{2}{3r_2}\left(\phi''_1 + \frac{2}{r_1}\phi'_1 + \frac{3}{r_2}\phi'_2\right) \qquad \text{.....(6)}$$

$$(B)_{SR} = \frac{2}{3r_2}\left(\phi''_1 - \frac{2}{r_1}\phi'_1 + \phi''_2 - \frac{2}{r_1}\phi'_2\right) \qquad \text{.....(7)}$$

Where;

$\phi(r)$ is the spherically symmetric potential

c_{11}, c_{12} and c_{44} are short range (SR) elastic constants

B represents the bulk modulus and r is the distance from origin.

The solution of the above differential equations gives the potentials for bcc metals by two polynomial functions:

$$\phi = a_4 r^4 + a_3 r^3 + a_2 r^2 + a_1 r + a_0 \qquad r_n \le r \ge r_m \qquad \text{.....(8)}$$

$$\phi = b_4 r^4 + b_3 r^3 + b_2 r^2 + b_1 r + b_0 \qquad r_m \le r \ge r_c \qquad \text{.....(9)}$$

where;

r_m is chosen midway between the first and the second neighbor distances

r_c is chosen between the second and third neighbor distances

r_n is chosen so that a potential $\phi(r)$ results which contains a minimum reflection point. a and b are constants.

These bcc potentials are fitted to the vacancy and interstitial formation energies and give reasonable agreement with other properties, but were not fitted to the cohesive energy. In addition to Johnson-I, the Johnson-II [76] potential was originally derived for γ-Fe. The Johnson-II does not hold the iron lattice at its equilibrium spacing. The physical values predicated by Johnson-II are good. In 1980's, a new potential for transition metals was created by March and co-workers [77,78]. They introduced the d-band electron theory into the potential function. The d-shells lead to considerably harder repulsive core interactions than in simpler sp metals. De Hosson et al. [79] investigated the use of March's d-band potentials in the simulation of the core structure of a 1/2<110> screw dislocation in pure nickel and concluded that the potential based on the d-band force model was quite reasonable for depicting core structures.

1.4.5.1.2. Semi-empirical potential

For semi-empirical potentials, the functional form of a potential is developed based on theory and the few appropriate coefficients are determined by matching a small number of physical results. One of the semi-empirical potentials is the Morse function

$$\phi(r_{ij}) = \phi_0\left[exp\{-2\alpha(r_{ij}-r_0)\} - 2exp\{-\alpha(r_{ij}-r_0)\}\right] \quad .....(10)$$

where;

α is constant with dimensions of reciprocal lattice

ϕ_0 is equal to the dislocation dissociation energy

The energy of an individual atom is the sum of the interaction energies with N neighbor atoms in sphere of influence, i.e.

$$E_i = \sum_{j=1}^{N} \phi(r_{ij}) \quad .....(11)$$

The Morse potential was used to calculate the atomic configurations for fcc metals. The disadvantage of semi-empirical potentials is that they are long-range and a lattice sum consists of a large number of terms that requires long computation times.

1.4.5.1.3. Pseudo-potentials

In pseudo potentials [81], the strong potential inside an ion core is replaced by a weaker potential in which the core electrons are only weakly disturbed by the ions. The theory of the pseudo potentials has been frequently applied to the alkali metals. However, in transition metals, because of their large incomplete d-shells, the d-band structures are quiet different from free electron states. Therefore pseudo potentials are not suitable for transition metal modeling.

1.4.5.1.4. Tight binding approximation and moments approach

The tight binding approximation was developed for defect calculations in transition metals. This model was used to explain the difference between the orientation depedence of the Peierls stress for Ta, W and Mo. Masuda et. al. [82,83] calculated the Peierls stress and the core energy of 1/2<111> screw dislocations in bcc metals using this

stress and the core energy of 1/2<111> screw dislocations in bcc metals using this approach. It was found that the general behavior of screw dislocation motion in transition metals strongly depends on the filling of the d-bands. Small differences in filling can result in significant differences in dislocation core structures and Peierls stresses.

1.4.5.1.5. Ab-initio pair potential

The ab-initio pair potential model was developed by Willians, Kubler and Gelatt [84] for metallic compounds. In this model, the roles of s, p and localized d-electrons in the binding process are considered. The total energy is obtained from the independently compressed atom calculation and the cohesive energy can be written as a sum of pair interaction energies:

$$E_T(r_1) = \frac{1}{2}\Sigma_i n_i \phi(s_i r_1) \qquad \text{.....(12)}$$

where;

$\phi(r)$ is the pair potential

n_i is the number of atoms in the i-th shell at a distance $R_i=s_i r_1$, from the atom of the origin.

r_i is the nearest neighbor distance

s_i is the atom coodinate

Given the value of E_T as function of r_1, the pair potential can be found by inversion.

1.4.5.1.6 Embeded Atom Method (EAM)

Though pair potentials have been used to calculate various types of dislocation

core structures, boundaries, phase transformations and cohensive energies, these models have their own serious limitations.

The problem comes from their framework:

$$E = \frac{1}{2} \sum_{i \neq j = 1}^{N} \phi_{ij}(r_{ij}) + U(\rho) \qquad \text{.....(13)}$$

where:

ϕ_{ij} is the pair potential

$U(\rho)$ is the density dependent part of the energy,

ρ is the average density of the material.

The models were constructed on the assumption of constant volume and may describe the energy changes associated with the variation of atomic configuration at constant volume. But in intermetallic compounds, the difference between the atom sizes of constitutional species can be large (for example in the B2 alumnides r_{Co}=0.126 nm, r_{Ni}=0.124 nm and r_{Al}=0.143 nm). Thus the local volume change caused by core stoichiometry change may introduce a large calculation error. To overcome this problem, the embedded atoms method (EAM) [85] and N-body potentials (F-S) method [86] have been developed. In this approach, the energy of the metal is viewed as the energy to embed an atom into the local electron density provided by the remaining atoms of the system. In the EAM approximation, the energy of the lattice is written as:

$$E = \frac{1}{2} \sum_{i \neq j = 1}^{N} \phi_{ij}(r_{ij}) + \sum_{i = 1}^{N} F_i(\rho_i) \qquad \text{.....(14)}$$

where;

F_i is the many-body interaction and/or embedding part of the energy which replaces $U(\rho)$

$\phi_{ij}(r_{ij})$ is the pair part of the interaction

ρ_i is the local electron density which is calculated as a linear superposition of atomic electron densities $\rho_i = \sum_{j \neq i} \Phi(r_{ij})$.

The EAM and N-body potentials (F-S) remove some inadequacies of the pair potentials and provide a better physical basis to compute atomistic structures of materials. However, the local distortion near the core center is far from equilibrium conditions. As the N-body potential must fit the materials parameters such as structure type, cohensive energy and vacancy energy in the equilibrium condition, it might be questionable whether its use can be extended to the non-equilibrium reality.

A severe problem of all the methods is that all the potentials were created for specific metals, mostly for pure elements. However these potentials have been widely used to calculate the atomic configurations of crystal defects in other materials. The accuracy of description of real situations in the other structures is therefore not guaranteed. For those reasons, the theoretical models need to be verified and modified by experimental evidence.

1.4.6 High resolution electron microscopy

High resolution electron microscopy makes it possible to directly image some of the details of the atomic structure of a dislocation core. So far, the experimental observations of dislocation cores have been sparsely reported in $L1_2$ [86, 94, 95], B2 [87, 88] and $L1_0$ TiAl [96]. Technical difficulties are the main reasons for the limited studies. Crimp [86] examined $[\bar{1}01]$ screw dislocations in $L1_2$ structured Ni_3Al. The screw dislocations were dissociated into 2-fold $\frac{1}{2}[\bar{1}01]$ superpartial dislocations separated by an APB on the (010) plane. The superpartials were further dissociated into Shockley $1/6[11\bar{2}]$ partials with complex stacking faults (CSF) on the (111) primary plane or (111) cross-slip plane.

core dissociation remained unchanged. In $L1_0$ structural TiAl, Hemker, Vigwer and Mills [87] found that the core of "ordinary" $\frac{1}{2}\langle 01\bar{1}\rangle$ dislocations are compact and that the motion of these dislocations is inhibited by lattice friction and not by core dissociation. In contrast, the core of a screw $\frac{1}{2}\langle 110\rangle$ superdislocation was dissociated in a non-planar configuration. In B2 NiAl [88,89], <010> edge dislocations were found to be compact, while <011> edge dislocations are highly split. Some of these dislocations were climb dissociated, while others were decomposed into perfect <010> edge dislocations (shown in the following relations).

$$\text{Dissociation} \quad \langle 01\bar{1}\rangle = \frac{a}{2}[11\bar{1}] + APB + \frac{a}{2}[\bar{1}1\bar{1}] \qquad \text{.....(15)}$$

$$\text{Decomposition} \quad \langle 01\bar{1}\rangle = \langle 010\rangle + \langle 00\bar{1}\rangle \qquad \text{.....(16)}$$

These experimental results are in agreement with conventional TEM observations: <010> type dislocations dominate the high temperature in the soft orientations, while <011> slip corresponds to a high critical resolved shear stress in the hard orientations.

It is important to note that a HREM picture is significantly affected by defect geometry, sample conditions and operating factors such as surface relaxation of dislocation, kinks of dislocation lines, specimen thickness, surface contamination, magnetic nature, defect interaction effects, residual stresses, beam damage, defocus values, astigmism and beam misalignment. Therefore, interpretation of HREM images is not straightforward and needs the support of computer simulations. For example, the contrast changes of several atoms in core regions were observed in HREM studies of Ni_3Al and TiAl [86,87]. These features were successfully explained after computer simulations produced the same phenomenon: stacking faults modulate the the local image contrast corresponding to APB or ISF or ESF planes.

sponding to APB or ISF or ESF planes.

HREM computer simulations are performed using electron optics software. The data files used in simulations are atom coordinates in a dislocation core. These can either be atomic coordinates from core simulations or best-guess structures. These image simulations allow direct comparison of experimental images with model structures. For a number of resons, these comparisons may not result in a satisfactory match. One reason may be that the potentials used in the simulations may not represent the the true atomic bonding. Additionally, core calculations are usually performed at 0 K, whereas the experimental images may reflect the core structure at either the deformation or observation temperatures. Also, atomistic models are unable to account for climb dissociation which may occur in real materials. Thus, mismatches between simulations and experimental observations are not necessarily unexpected.

1.5 General characteristics of CoAl

The cobalt-aluminum phase diagram, along with those for the Ni-Al and Fe-Al systems, is shown in fig. 14 [90]. It is very similar to the nickel-aluminum system, but somewhat different from Fe-Al system. Co50Al melts congruently at 2191 K, approximately 575 K higher than Ni-based superalloys. The single β' phase has the ordered body-centered cubic crystal structure of cesium chloride or B2 type. It consists of two interpenetrating primitive cubic cells, where cobalt occupies the corner sites and aluminium occupies the body central sites (fig. 1). The B2 structure of β' phase is stable for large deviations from stoichiometry. This wide field allows alloying for improvements of mechanical properties without entering a two phase field.

1.6 Motivation of this research

It is difficult to elucidate some of the unusual mechanical behavior of B2 aluminides using general deformation and dislocation theories. The problems may be related to core structures of those dislocations that play the major role in the deformation process of the materials.

The effect of core structures on mechanical behavior has not been emphasized until very recently. Traditionally, the resistance to dislocation slip has been dealt with as the Peierles-Nabarro stress according to the form:

$$\tau_{p-n} \propto Ge^{-2\pi\frac{W}{b}} \qquad \text{.....(17)}$$

where;

G is the modulus of elasticity in shear

τ_{p-n} is the Peierls stress

W is the width of a dislocation core,

$$W = \frac{a}{1-\upsilon} \quad \text{for edge dislocation}$$

$$a \quad \text{for screw dislocation}$$

a is the interplanar spacing

b is the Burgers vector

This equation indicates that the Peierls stress for a given slip system decreases with increasing interplanar spacing. But dislocation width is not simply a function of interplanar spacings of slip planes. As shown in fig. 15, the spacing of slip planes (a) and spacing of atoms (b) can be almost same while the dislocation widths (w) are distinctly different. The dislocation width must be dependent on the atomic structure and the nature of the atomic bonding forces. For example, when the bonding force is spherical in distribution and acts along the line of atom centers, the dislocation width is large and conse-

quently the Peierls stress is small. By contrast, when the bonding forces are highly directional (such as bcc), the dislocation width is narrow and the Peierls stress is correspondingly large [91]. The equation of Peierls stress is too simple to consider the exact shape of the displacement field around a core and core spreading geometry.

The equation (17) is too simple to explain the nature of the Peierls stress. Core splitting, core dissociation, atomic row bending, core stoichiometry and the corresponding displacement field are all related to lattice resistance. In addition to above intrinsic factors, core configurations may be changed by environmental factors, such as:

1. Temperature: this may lead not only to thermally activated core motion but may also change the core configuration as well.

2. Stress: Vitek [61] predicted that core structure may change before slip occurs when applying stress to the model crystal.

3. Heat Treatment and interstitial atoms: fast cooling after annealing of single crystal NiAl increases its fracture toughness K_Q dramatically from 2.8 to 15.6 ($MPaM^{1/2}$) [92]. This phenomena may be related to the interaction of interstial solute atoms with dislocation core structures.

4. Deviations from stoichiometry: a small deviation from a stoichiometric composition may not change the core chemistry but may change local atom profiles.

From the above analysis, it is clear that the investigation of core-related behavior is critical. Although previous work has already recorded some <100> and <110> cores in NiAl, the effect of stoichiometry is still not understood. Furthermore, the core structures of CoAl have not been examined yet. In order to thoroughly understand the deformation mechanisms in B2 aluminides, it is necessary to investigate dislocation cores in other

alloys such as CoAl.

1.7 Expected impact of the project

The HREM examination of dislocation cores in B2 intermetallic compounds CoAl, NiAl and FeAl will have an impact in both the basic understanding and practical development of these alloys. First, it may provide some clarification for the differences in both high temperature strength and room temperature ductility of these materials. After this, an improved effort will be directed to obtain a better balance of strength to ductility for these materials. Second, it will help to develop dislocation theory. Core structure is a very weak link in the chain of dislocation theory. Experimental images of cores may supply some valuable new ideas and help to establish better theoretical models. Third, in the near-term, the comparison of HREM observations with computer simulations will test the accuracy of current theoretical models and the associated interatomic potentials. These potentials are widely used in other research areas, such as the studies of grain boundary structures. Finally, since the understanding of CoAl is not as complete as that of NiAl and FeAl, the dislocation analysis and HREM core examination of CoAl will contribute to the understanding of deformation mechanisms of this material.

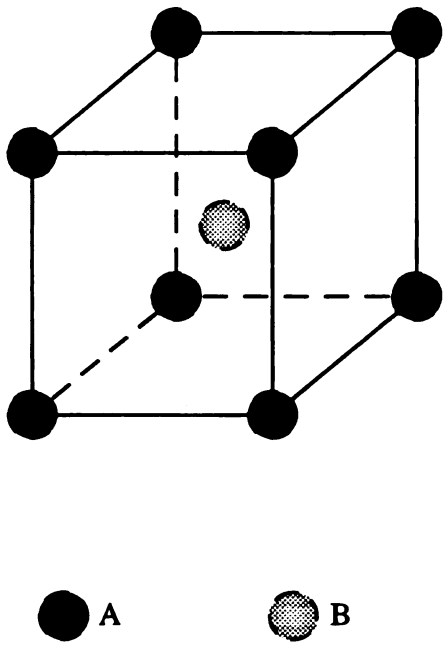

Figure 1 B2 structure is the ordered bcc lattice. Two kinds of atoms (A and B) occupy the corner positions or body center postion respectively.

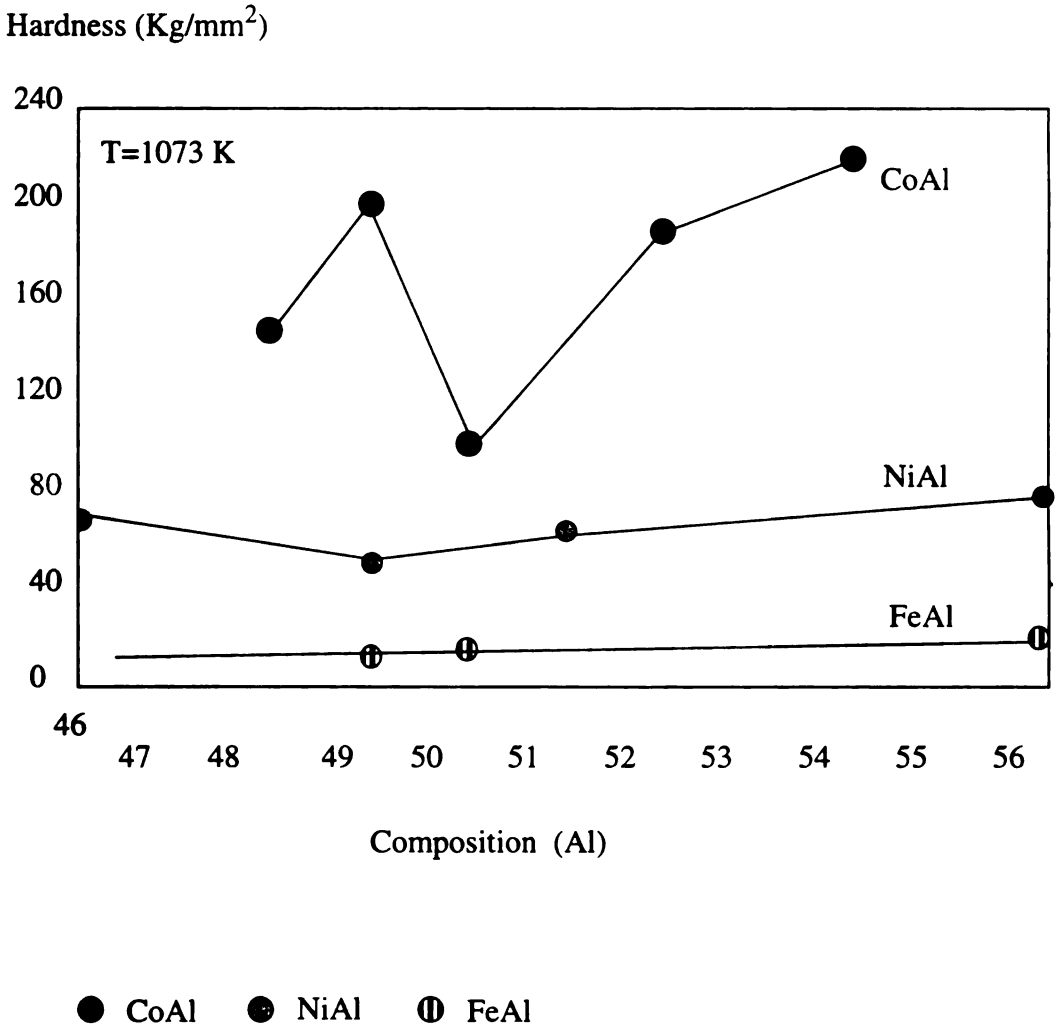

Figure 2 Hardness-composition isotherms in B2 intermetallic compounds. This figure shows the high-temperature hardness and sensitivity to composition deviation of these compounds.

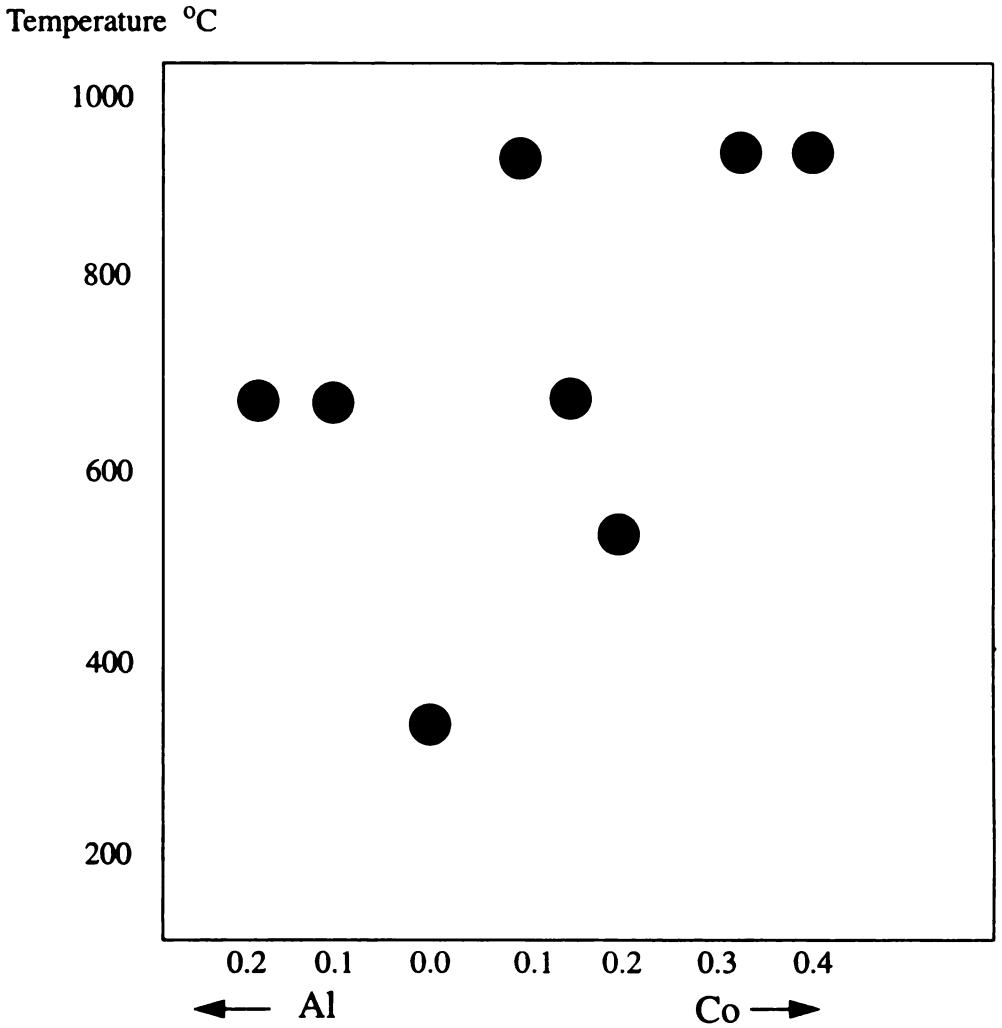

Figue 3 Ductile-to-brittle transition temperature for binary Co-Al alloy [21]. The transition temperature is the lowest at stoichiometric Co-50Al. Deviation from stoichiometry results in increase of the transition temperatures.

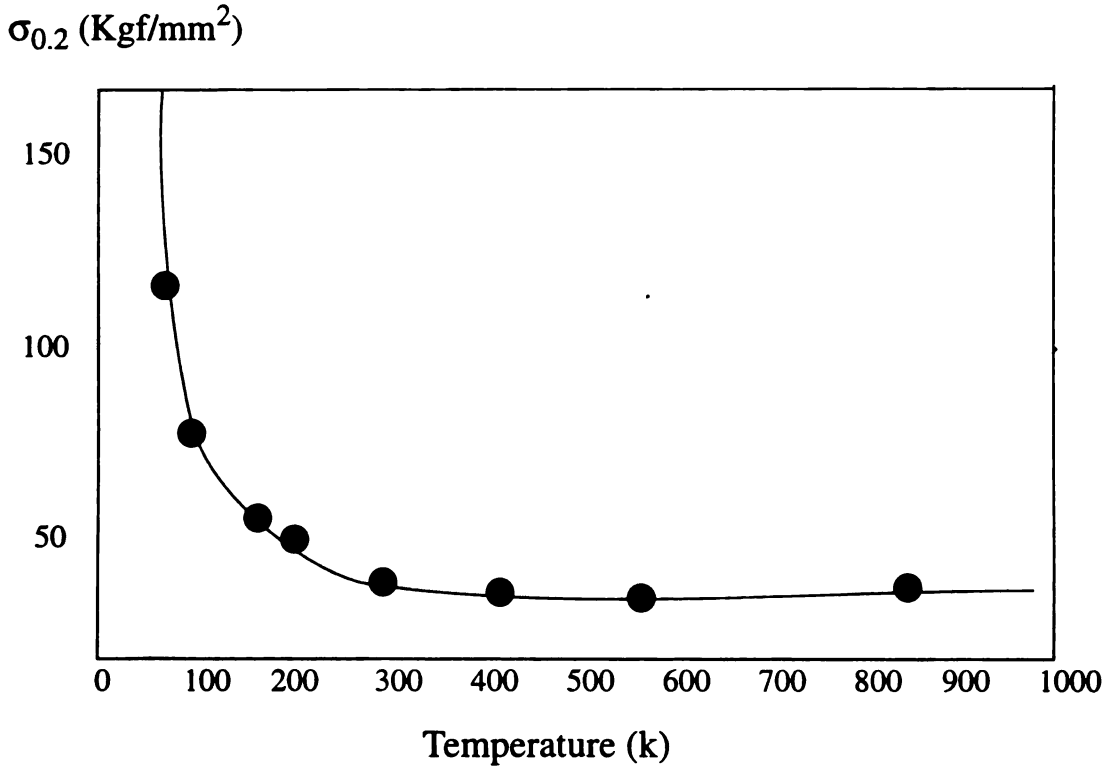

Figure 4 Temperature-dependent of the yield stress of stoichiometric NiAl single crystal of soft orientation [23]. Brittle-to-ductile transition temperature is around 150 K.

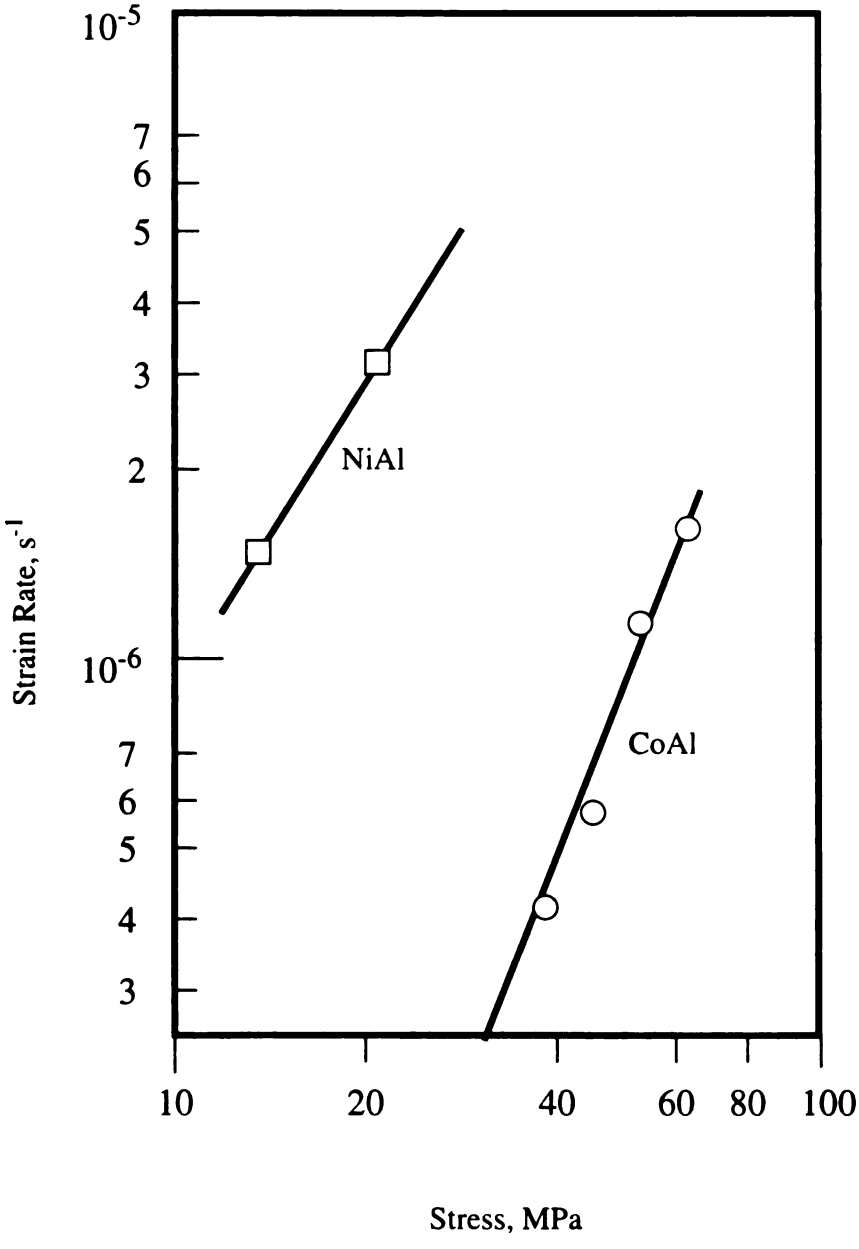

Figure 5 Creep resistance of CoAl and NiAl at temperature 1300 K [25]. CoAl has significantly slower strain rates than NiAl.

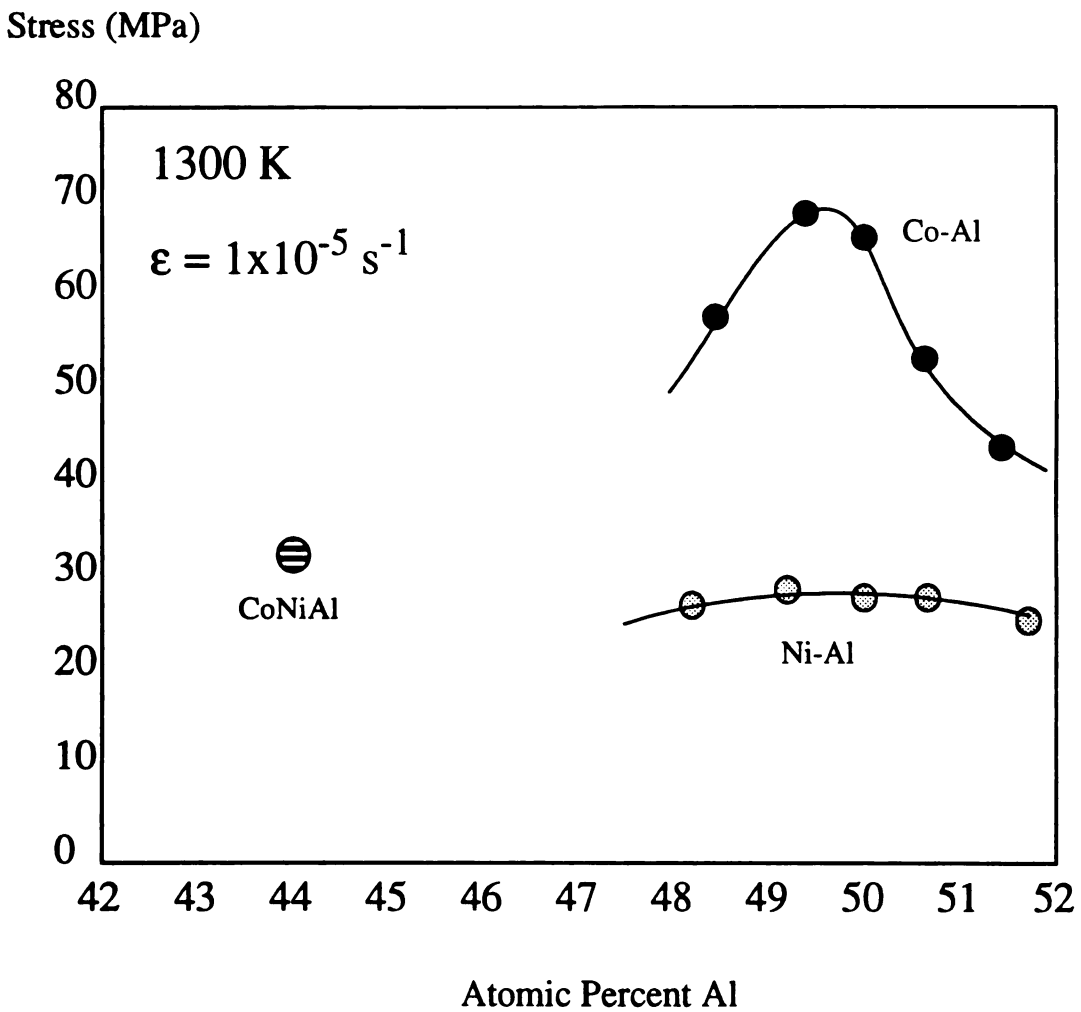

Figure 6 Creep stress of polycrystalline Co-Al and Ni-Al [27]. CoAl has higher creep strength than NiAl. On the other hand, the creep strength is more sensitive to composition deviation in CoAl than in NiAl.

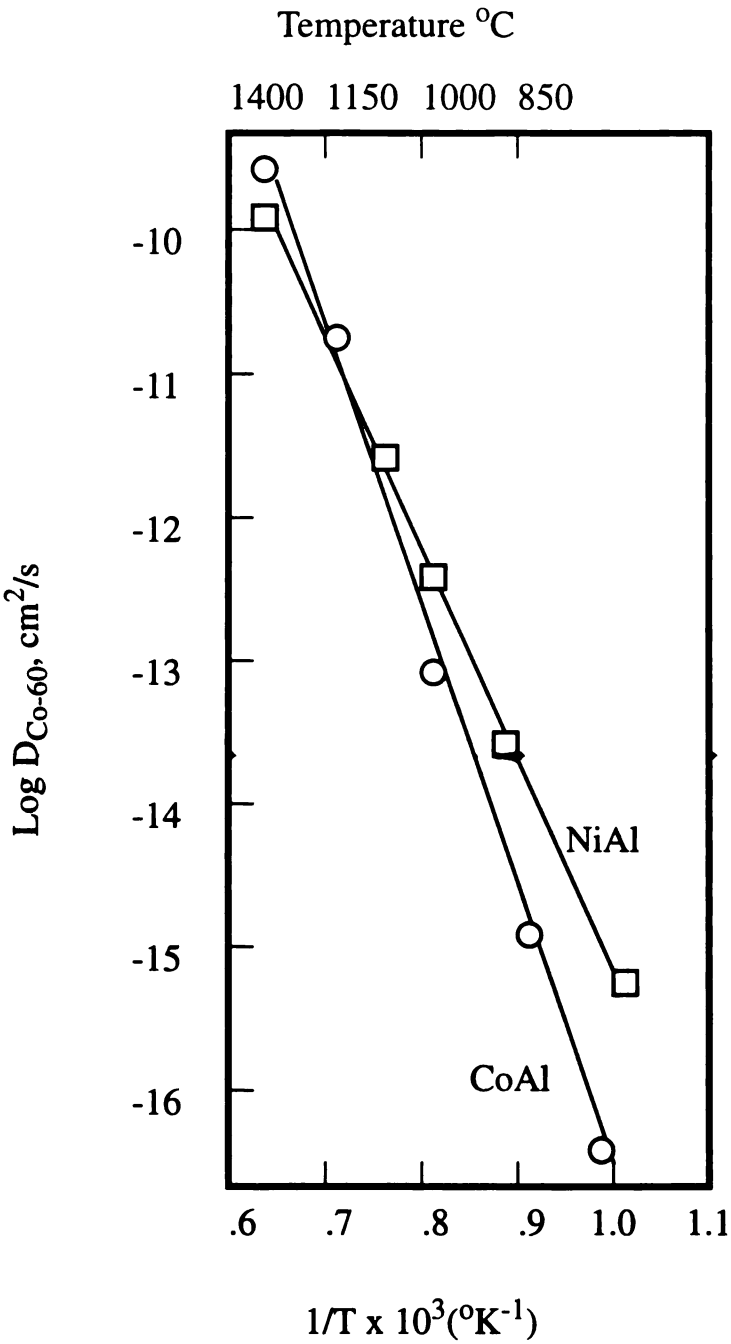

Figure 7 Diffusivities of Co^{60} in CoAl and in NiAl [29]. Around 1000 K -1400 K, CoAl has comparable diffusion coefficients to NiAl.

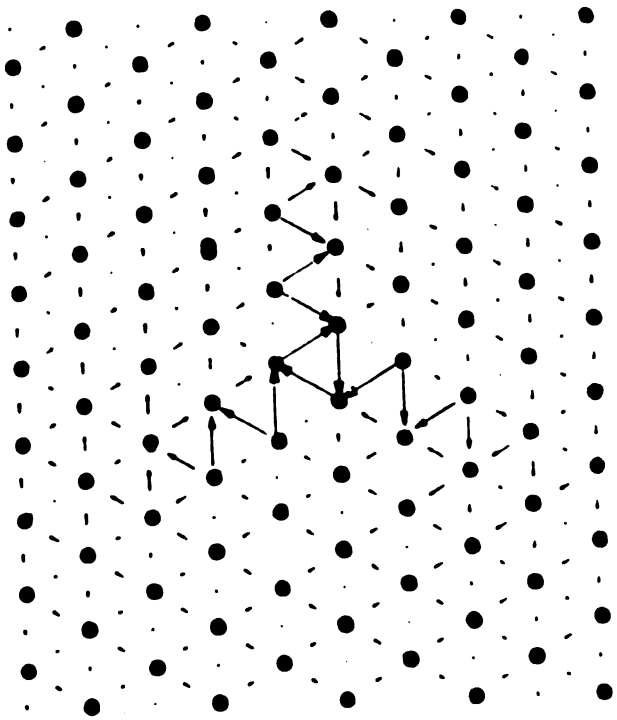

Figure 8 Core strucuture of 1/2<111> screw dislocation in bcc structure [56].

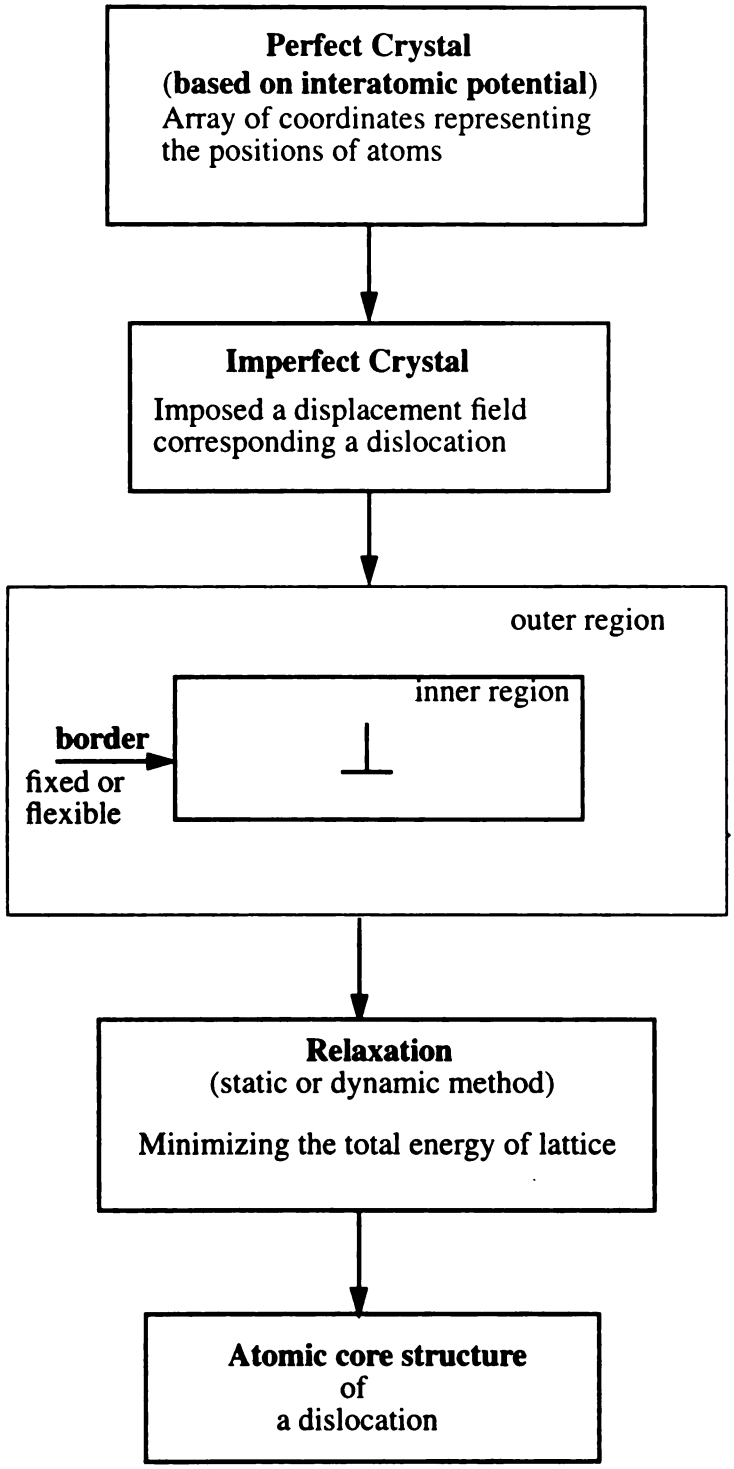

Figure 9 Diagram of computer modelling. Introduction of displacement field and application of boundary conditions and relaxation method are key steps in core modelling.

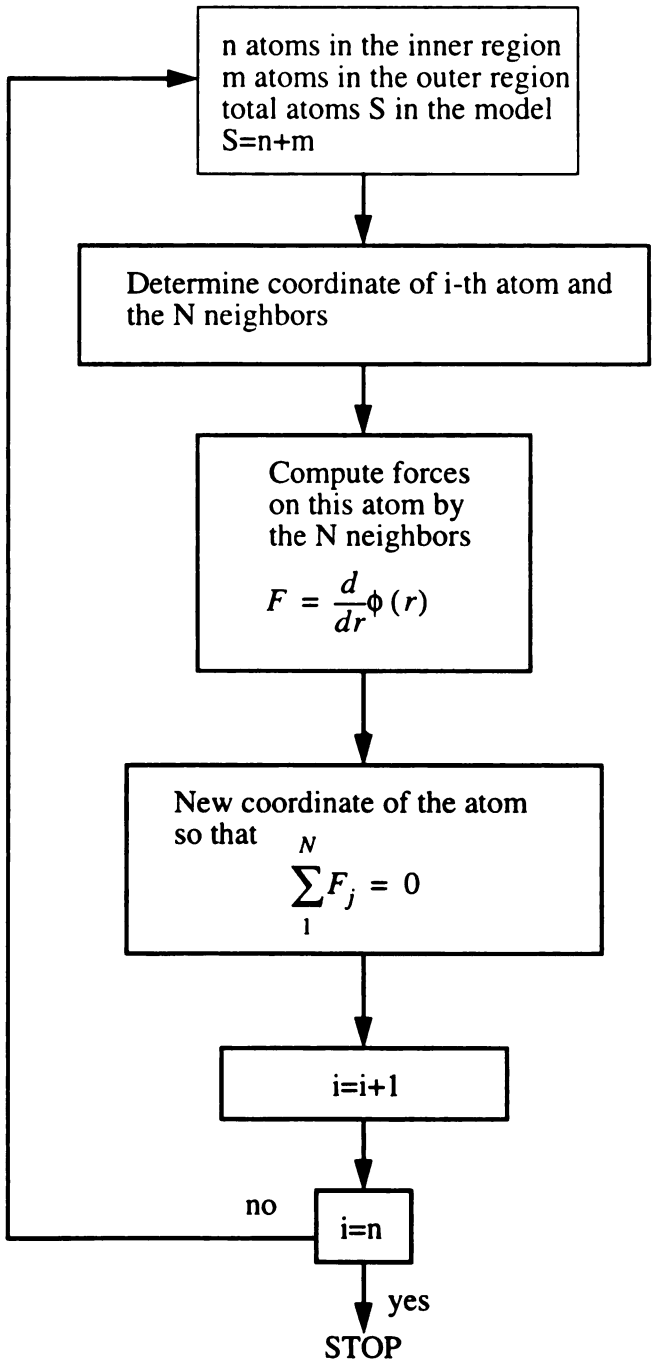

Figure 10 Diagram of relaxation calculation. When the displaced lattice reaches its equalibrium condition, the force upon an atom should be balanced.

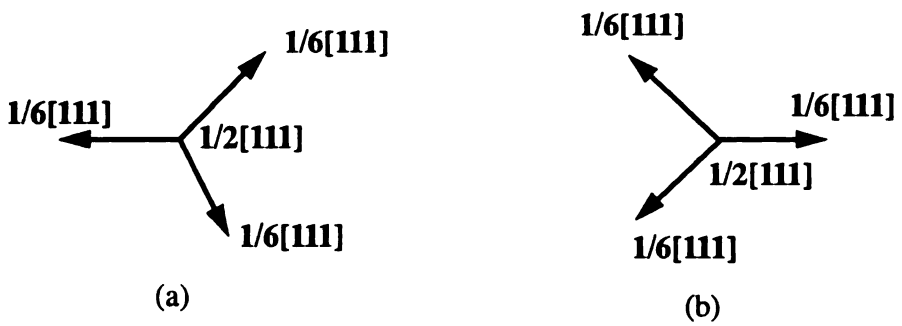

Figure 11 Two configurations of dissociated screw dislocation 1/2[111]. The arrow directions indicate that the 1/2[111] screw dislocation spreads on three intersected planes.

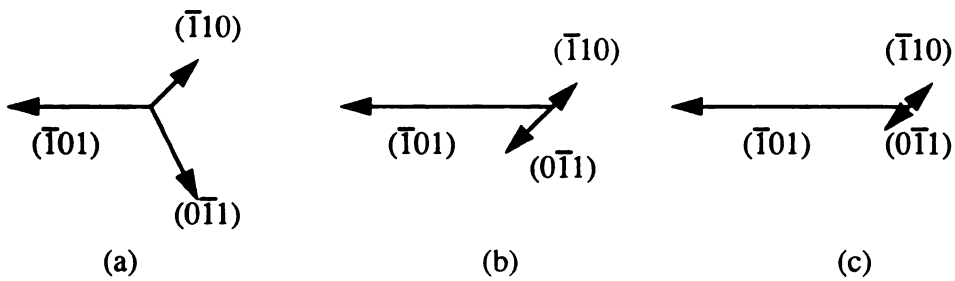

Figure 12 Changes in core structure under influence of stress. The non-planar spreading of 1/2<111> dislocation on (110) and (011) are contracted under the applied stress. The process is shown from (a) to (c).

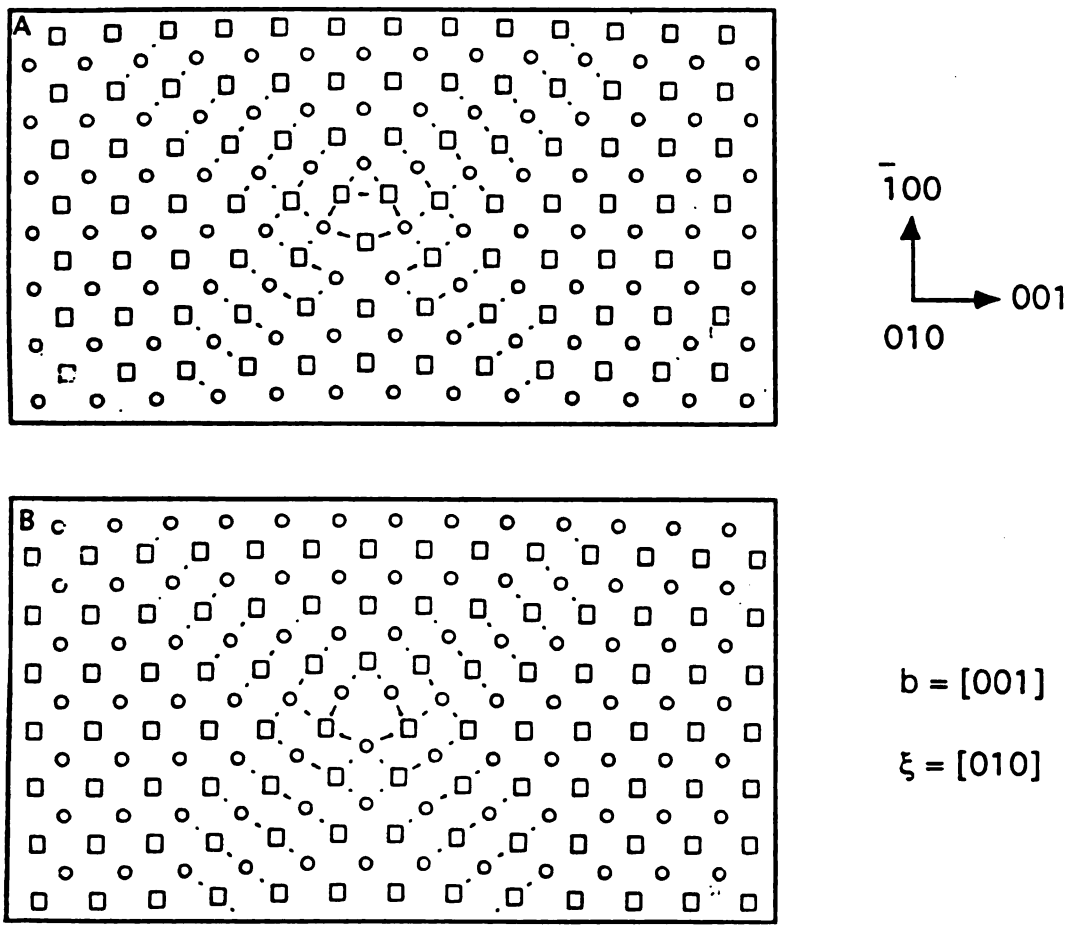

Figure 13 Two configurations of simulated core structure of <100> edge dislocation in B2 structure.

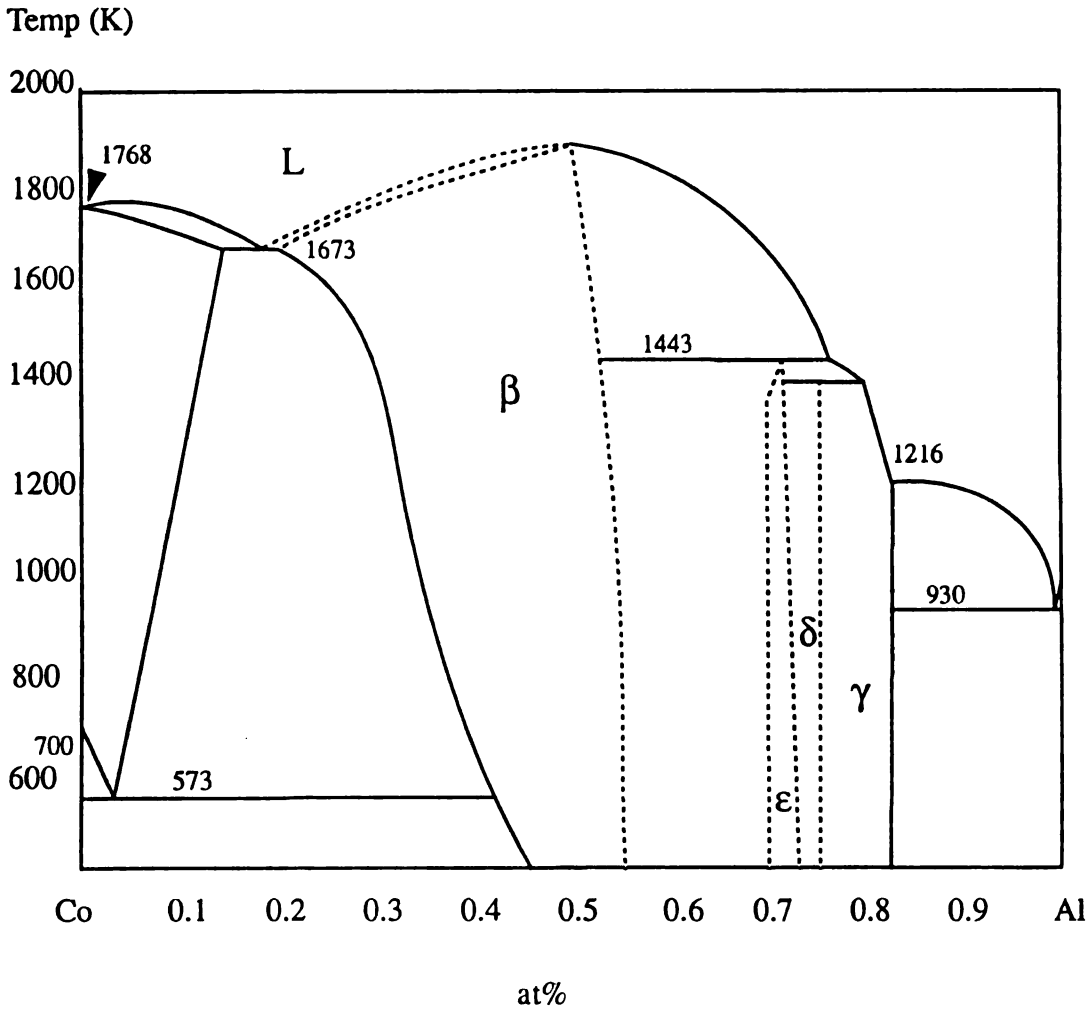

(a)

Figure 14 Phase diagram for binary B2 system. (a) Co-Al diagram [90] (B2 structure (β) can be found in the range of composition 0.45-0.55 Al at% at room temperatures), (b) Ni-Al diagram and [130], (c) Fe-Al diagram [131].

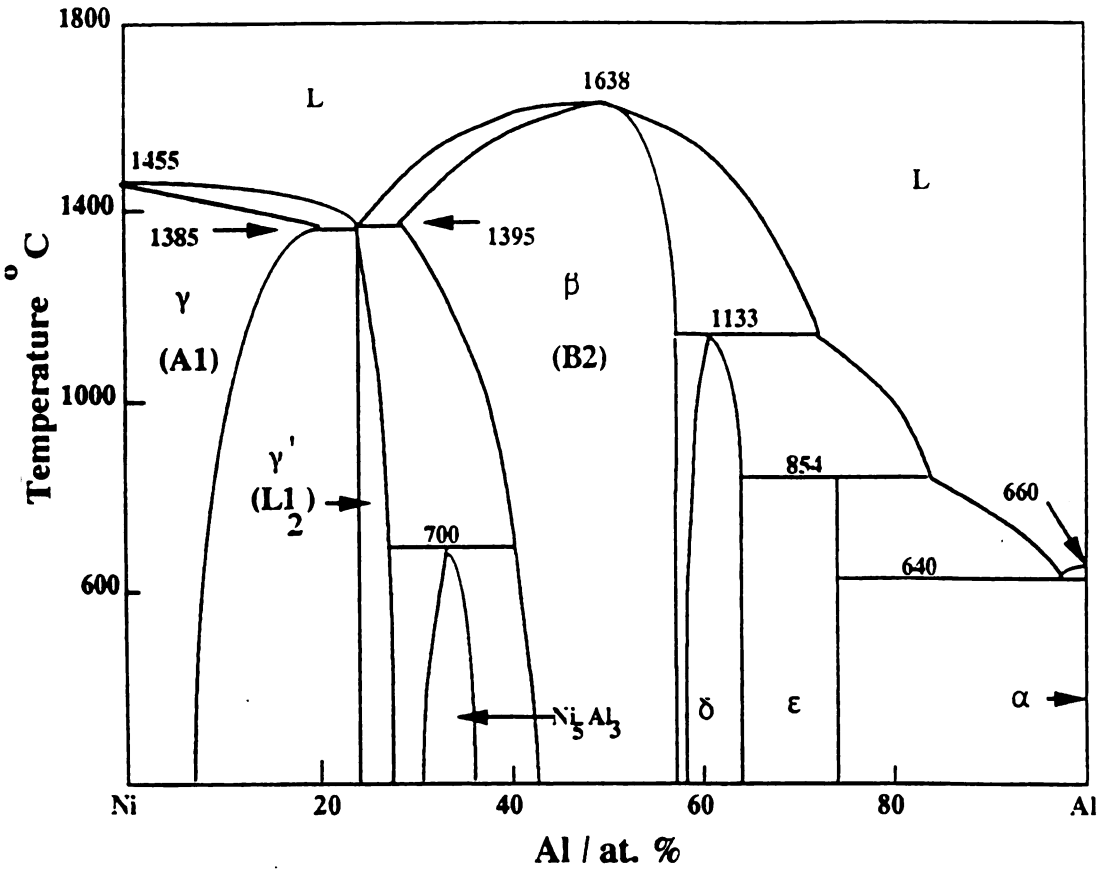
1800
1400
1000
600
Temperature °C
L
1638
1455
1385
1395
L
γ
(A1)
β
(B2)
1133
γ'
(L1 2)
854
660
700
640
Ni5Al3
δ
ε
α
Ni
20
40
60
80
Al
Al / at. %

(b)

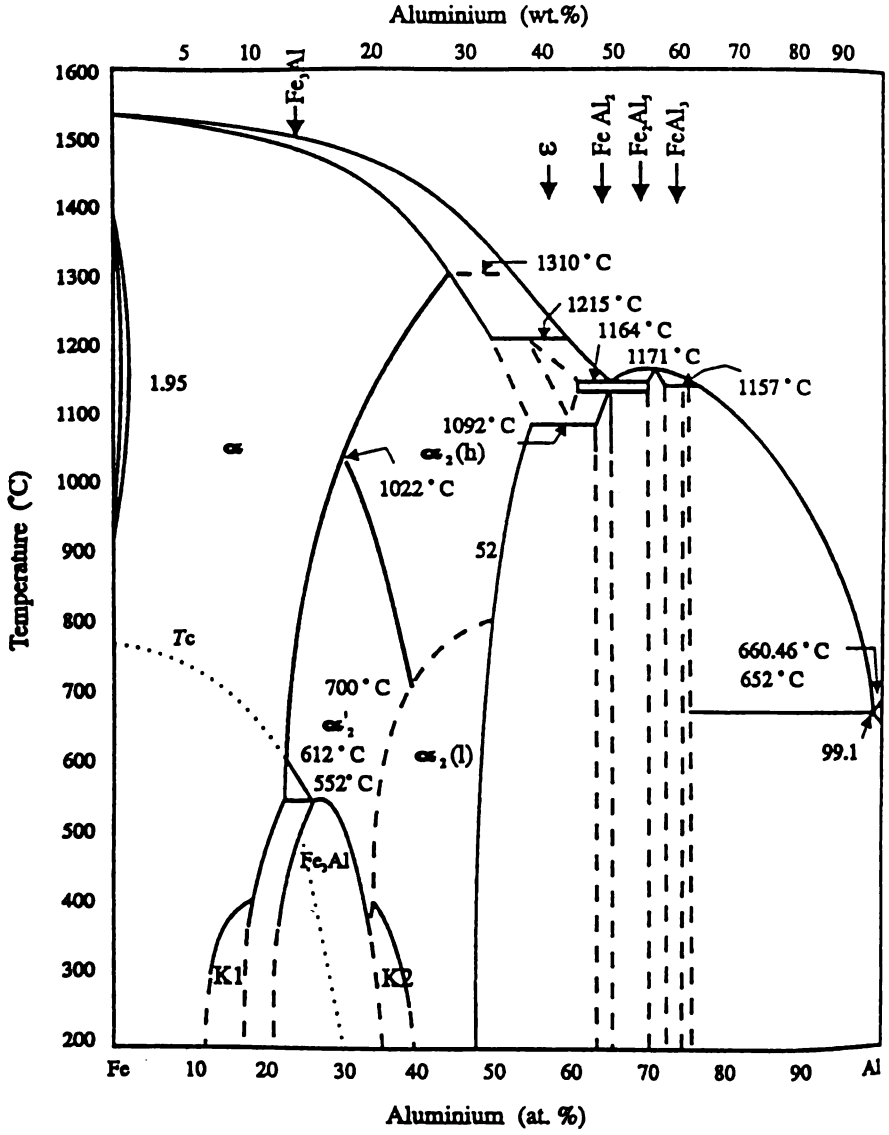
Aluminium (wt.%)
5 10 20 30 40 50 60 70 80 90
Fe3Al
ε
Fe Al2
Fe2Al5
FeAl3
1310 °C
1215 °C
1164 °C
1171 °C
1157 °C
1.95
α
1092 °C
α2(h)
1022 °C
52
Tc
700 °C
α'2
612 °C
552 °C
α2(l)
660.46 °C
652 °C
99.1
Fe2Al
K1
K2
Temperature (°C)
1600 1500 1400 1300 1200 1100 1000 900 800 700 600 500 400 300 200
Fe 10 20 30 40 50 60 70 80 90 Al
Aluminium (at. %)

(c)

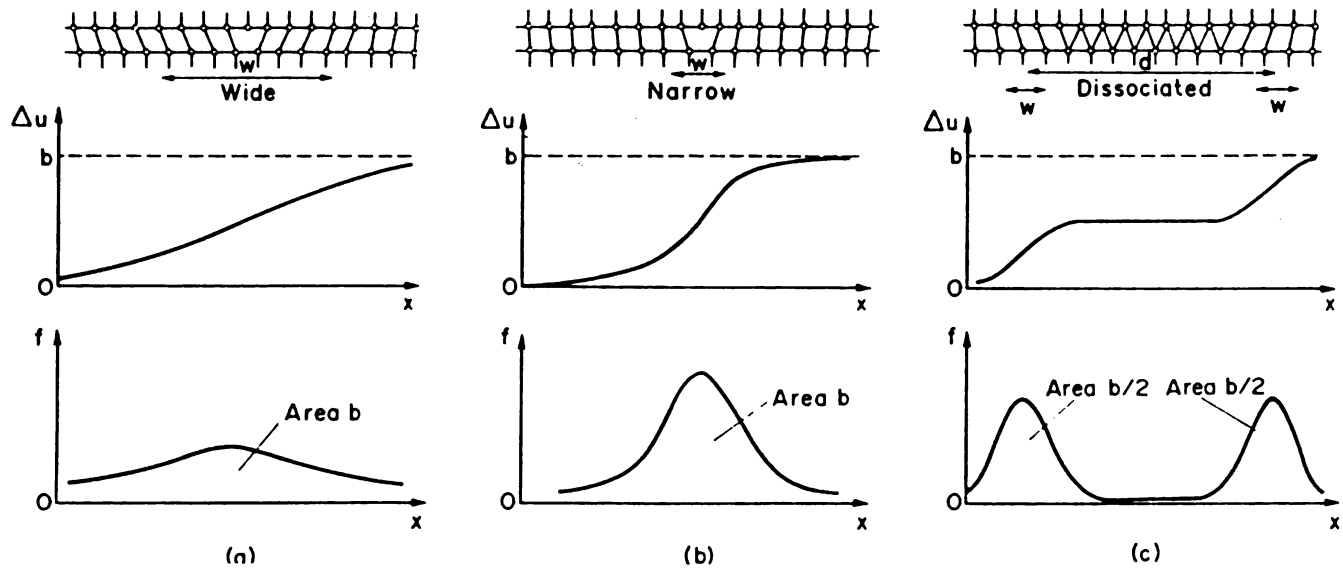

Figure 15 Schematic of an edge dislocation width (adapted from [63]).

Table 1 Physical parameters of stoichiometric CoAl and NiAl

Material	Structure	Lattice Parameter (Å) at room temp.	Melting temperatue (K)	Young's Modulus (GPa)	Density (g/cc)
CoAl	B2	2.86	1921	278	6.07
NiAl	B2	2.88	1913	238	5.85

Table 2 CRSS of some B2 aluminides

Material	Slip System	CRSS (MPa)	Reference
Co50Al	<100>{110}	258	[15]
Co50Al	<111>{110}	272	[15]
Co50Al	<111>{112}	343	[15]
Co50Al	<111>{123}	324	[15]
Ni50Al	<100>{110}	68.6	[16]
Fe50Al	<111>{110}	202	[14]
Fe40Al	<111>{110}	97.0	[14]

Table 3 Slip Systems in CoAl, NiAl and FeAl

Temp	Orientation	CoAl[1]	CoAl[2]	NiAl[1]	NiAl[2]	FeAl[1]	FeAL[2]
H	Soft	<100>{001}	N/A	<100>{001}	<100>{001}	<100>{110}	<100>
H	Soft	<100>{110}	N/A	<100>{110}	N/A	N/A	<111>*
H	Soft	<111>{110}	N/A		N/A	N/A	N/A
H	Hard	N/A	N/A	<110>	N/A	<100>{110}	N/A
H	Hard	N/A	N/A	<111>	N/A	N/A	N/A
R	Soft	<111>{110}	N/A	<100>{001}	<100>	N/A	<111>
R	Soft	<111>{112}	N/A	<100>{110}	N/A	N/A	N/A
R	Soft	<111>{123}	N/A	<100>{012}	N/A	N/A	N/A
R	Hard	<111>{110}	N/A	<111>{110}	<111>{110}	N/A	<111>
R	Hard	<111>{112}	N/A	<111>{112}	<111>{112}	N/A	N/A
R	Hard	<111>{123}	N/A	<111>{123}	<111>{123}	N/A	N/A

Temp: Temperature; H=High Temperature; R=Room Temperature
[1]: Stoichiometric Composition; [2]: Off-stoichiometric Composition
* Only apply for Fe-35Al

Table 4 Summary of the simulation results for the various slip systems in the order of decreasing mobility [68]

Slipsystem	Dislocation type	Critical stress $10^2\mu$
<001>{110}	Screw Edge	0.16-0.18 0.20-0.30
<111>{110}	Screw Edge	0.60-0.80 0.53-0.67
<111>{112}	Screw Edge	1.00-1.30 0.40-0.53
<110>{110}	Screw Edge	>6.0 >8.0
<010>{100}	Screw Edge	>0.21 1.80-2.20

2. Experimental Method

2.1 Materials

The study was concentrated on single crystal Co-Al aluminides. Some joint research on Ni-Al and Fe-Al aluminides with S. Tonn and D. Sharrott was also conducted. CoAl crystals were obtained from the Naval Air Research Development Center (Waimister, PA) and Dr. D. Pope at the University of Pennsylvania. NiAl crystals were donated by Dr. R. Darolia, GE Aircraft Engines, Cincinatti, OH. Single crystals FeAl were available from a previous study [14]. The nominal composition of the specimens were Co-50at%Al (hereafter Co-50Al), Co-48Al and Co-52Al. The materials used for comparison in the joint reserach were Ni-50Al, Ni-48Al, Ni-52Al, Ni-51Al, Fe-40Al and Fe-50Al.

2.2 Specimen preparation

Single crystal slabs were oriented to a specified direction using the back-reflection Laue technique. A Cu x-ray tube was used at a voltage of 24 kV resulting in a tube current of 35 mA. The exposure time was 4 minutes for Polaroid type 57 film.

Specimens for compression testing were electric-discharge machined (EDM) from the oriented single crystals to a nominal size of 3x3x9 mm. In order to minimize end effects and buckling, the height/width ratio was set at approximately 3. The EDM made use of a wire saw and was set to produce a voltage of 180 V. The specimens were notched in a upper-right corner to indicate orientation (fig. 16), and mechanically ground down to a final size of 3x3x9 mm. These specimens were then electro-polished in order to remove any surface scratches and mechanical polishing marks. Brittle materials, such as CoAl, are very sensitive to surface defects. A smooth surface can avoid early fracture and more

clearly show slip lines. The polishing was performed by using a 10% perchloric methenol solution with a current of 250 mA at -20°C.

2.3 Mechanical testing

The polished specimens were deformed in compression at a nominal strain rate of $2x10^{-4}$ /sec. The mechanical testing was performed under vacuum at the desired temperatures using an MTS 810 servohydraulic load frame with a Centor vacuum furnace. The strain was limited to 5% in order to introduce enough dislocations for TEM/HREM observation, but to avoid unwanted dislocation interactions. Al_2O_3 compression pads were used to separate the specimen from the compression head and to reduce the friction. The stress-strain data were recorded by an IBM-PC and plotted using the *Excel* software package.

2.4 Slip trace analysis

Slip lines on the surface of the deformed specimens were observed using optical microscopy. Two-surface slip trace analyses was used to determine the slip planes involved in deformation. Figure 17 represents a specimen where slip lines **ab** and **ac** constitute the slip plane. After recording the slip lines on two orthogonal surfaces ABCD and ABEF, the angles between the slip lines and the reference axis AB were measured. The trace of plane abcd was then drawn α degrees from point B (south pole) and β degrees from point B (east pole). The intersection of two traces is the normal of slip plane.

The intersection angle of slip lines depends on the surface orientation of a single crystal specimen. If the surfaces are (100) and $(01\bar{1})$, the intersection angle is 90° on the

(100) plane and 0^o on the $(01\bar{1})$ plane. If the surfaces are not the (100) and $(01\bar{1})$ planes, the slip trace and intersection angle can be determined in a simple formula shown below.

Figure 18 is the coordinate system for [011] orientation. θ is the rotation angle between $[100][01\bar{1}][011]$ system and [u1 v1 w1][u2 v2 w2][011] system. [x y z] is the direction of slip traces in $[100][01\bar{1}][011]$ system, while [x' y' z'] is the direction of slip lines in [u1 v1 w1][u2 v2 w2][011] system.

$$[xyz] = \begin{bmatrix} \cos\theta & -\sin\theta & 0 \\ \sin\theta & \cos\theta & 0 \\ 0 & 0 & 1 \end{bmatrix} \begin{bmatrix} x' \\ y' \\ z' \end{bmatrix} \quad \text{.....(18)}$$

$$[x'y'z'] = \begin{bmatrix} \cos\theta & \sin\theta & 0 \\ -\sin\theta & \cos\theta & 0 \\ 0 & 0 & 1 \end{bmatrix} \begin{bmatrix} x \\ y \\ z \end{bmatrix} \quad \text{.....(19)}$$

If there are two sets of slip traces [x1' y1' z1'] and [x2' y2' z2'], the angle between slip trace can be determined by the following formula:

$$\cos\theta = \frac{[x1'x2' + y1'y2' + z1'z2']}{\sqrt{x1'^2 + y1'^2 + z1'^2} \bullet \sqrt{x2'^2 + y2'^2 + z2'^2}} \quad \text{.....(20)}$$

The above method can be used to sort the slip traces associated with multi-slip system and to confirm the results of trace analysis.

2.5 Transmission electron microscopy

After the slip plane was determined, TEM foils were sectioned parallel to the slip plane by electrical discharge machining (EDM). Sections were sliced to an approximate thickness of 500 μm. The thickness of the sections was reduced to approximately 250 μm

by grinding with 400 grit metallographic paper, then 3 mm diameter discs were produced by spark machining. These discs were further thinned to 150 μm by grinding with 600 grit paper. Jet polishing was carried out using a Struers Tenupol Twin Jet polisher operated at -30°C using an 8% perchloric acid in methanol solution with a flow rate setting of 4 and an applied voltage of 10 V.

2.6 Dislocation analysis

2.6.1 g•b=0 analysis

Standard diffraction contrast analysis (**g•b**=0 method) was used to determine Burgers vectors for dislocations observed under various deformation conditions. Screw dislocations in elastically isotropic materials become invisible when **b** lies in the reflection plane. After forming a series of images with two-beam conditions (g-vectors) and $0 < w < 1.0$ (w is dimentionless deviation parameter from the Bragg reflection) for individual reflections in different zones, two reflection vectors in which the screw dislocations are out of contrast may be obtained. Therefore **b** must be the zone axis of these two planes, i.e. $\mathbf{b}=\mathbf{g}_1 \times \mathbf{g}_2$. Often edge dislocations are invisible only if the reflection plane is perpendicular to the dislocation line **u**, that is **gxu**=0, or equivalently, **g•b**=0 and **g•bxu**=0. With anisotropic crystals, the dislocation may not be completely invisible even though **g•b**=0 and **g•bxu**=0 are satisfied. However the g•b=0 typically leads to reduced visibility and can be used for a guide for simulation.

2.6.2. Computer simulation

Due to the fairly high anisotropic nature of CoAl, NiAl and FeAl (table 5), it is some-

times difficult to unambiguously determine the Burgers vectors via the **g•b**=0 method. For this reason, an image matching technique was sometimes used to confirm the Burgers vectors. This technique is based upon computer simulation of a series of dislocation images obtained with different operative reflections for the exact reflecting conditions.

The simulation program was adopted from Head et al [97]. In order to apply this program, the reflecting vector **g**, beam direction **B**, deviation parameter **s**, dislocation direction **u**, the thin foil normal **FN** and the foil thickness **t** are required. The Burgers vector **b** is varied until an experimental/simulation image match is obtained. All the input data was measured from TEM micrographs and the corresponding diffraction patterns. The details are given in Appendix 1.

2.7 High resolution electron microscopy

To directly resolve details of individual atomic arrangements in the core region of dislocations, high resolution electron microscopy (HREM) was employed. HREM thin foils were sectioned perpendicular to the line direction of the dislocations of interest in specimens deformed under the identical conditions as for **g•b**=0 dislocations analysis (fig. 19). The thinning and jet polishing conditions were the same as for TEM specimens. However, HREM foils need to be thinner and flatter than the regular TEM foils. Consequently, fewer suitable foils were produced. These foils were then examined using a JEOL-4000 EX operated at 350 kv at the University of Michigan Electron Microbeam Analysis laboratory.

In HREM, dislocations must be imaged down the line direction. Generally speaking, HREM requires (1) a low index zone, (2) the defect to be parallel to beam direction,

(3) displacements perpendicular to the beam direction. Therefore, only displacements perpendicular to the optic axis are displayed, while the displacements parallel to the beam direction cannot be resolved. For these reasons, edge dislocation cores are easily imaged, while the screw dislocation cores are difficult to image. In mixed dislocations, the displacements revealed in the core region only represent the edge components of the strain field.

Although the JEOL 4000-EX has better than a 0.17 nm point-to-point resolution and the lattice parameter of CoAl is 0.286 nm (NiAl: 0.287 nm, FeAl: 0.291 nm), not all the dislocations can be imaged at the atomic level. This is because the lattice images provided by HREM are only two-dimensional projected pictures along the beam direction. When the minimum projected atom column to atom column spacing is less than or close to the instrument resolution, core examination becomes impossible. In the case of edge dislocations in B2 intermetallic compounds, the possible slip systems are <010>{001}, <001>{110}, <100>{012}, {111}{11$\bar{2}$}, <111>{12$\bar{3}$}, <111>{1$\bar{1}$0}, <011>{0$\bar{1}$1}, <1$\bar{1}$0>{001}, <1$\bar{1}$0>{111} and <1$\bar{1}$0>{11$\bar{2}$}. Table 6 lists the line directions of the edge dislocations of these systems.

The projected lattice images and minimum atom to atom spacings of these dislocations are shown in figure 20. Only in the line directions <100> and <111>, can the individual atom spacings be resolved. Therefore, only <010>{001}, <011>{0$\bar{1}$1) and <1$\bar{1}$0>{11$\bar{2}$} edge dislocations are reasonable candidates for HREM examinations in B2 alloys. In the case of screw dislocations, examination of the atomic structure is only possible for the <100> and <111> dislocations. However, since the Burgers vector is parallel to the beam direction, the displacement field of a screw dislocation core cannot be

resolved. However, the shear strain field existing in the core region may change the contrast of the individual atoms. With the help of computer simulations, the screw dislocation core structures may be solved. In contrast, core investigation in the <111> edge dislocations and <110> screw dislocations is impossible. Based on the above reasons, the selection of dislocations for core examination is limited by the resolution of HREM.

In the present study, <010>{001} edge dislocations were expected to be activated in samples oriented to [011]. <011>{011} dislocations are expected when compression specimens are either oriented to <100> hard orientations and deformed at room temperature or oriented to soft orientations and deformed at high temperature. <111> screw dislocations are expected when specimens are deformed at room temperature or oriented to a hard orientation and deformed at high temperature.

HREM employs phase contrast imaging in which the contrast depends on the phase shift $\Phi(u)$ between Bragg-scattered beams and the transmitted beams and is given by:

$$\Phi(u) = \frac{2\pi}{\lambda}\left(C_s\frac{\lambda^4 u^4}{4} + \Delta f\frac{\lambda^2 u}{2} \right) \qquad \text{.....(21)}$$

Here **u** is the position vector in reciprocal space and Δf is the defocus value

If $\Phi(u)$ is an even integer multiple of π, atoms will appear bright and when $\Phi(u)$ is an odd integer multiple of π, atoms will appear dark. Therefore the image contrast can be controlled by defocusing. It is very important to locate the optimum defocus of the objective lens to prevent improper interpretation of the images. A small negative defocusing is necessary to give adequate and accurate HREM images.

The number of beams in the image is also important; too few will give rise to serious truncation effects in the image; too many may generate spurious contrast effects, due

to the inclusion of strong subcell reflections.

Thick specimens may cause multiple scattering and absorption of the electron beam, preventing phase contrast imaging. A regular lattice image may become a superlattice image with increasing thickness. Correspondingly, a <010> dislocation may be misinterpreted as a 1/2<011> dislocation (fig. 21). Therefore, the thickness in an analytical area should not exceed 10 nm. In order to avoid being misled, the construction of a Burgers circuit should refer to the diffraction pattern.

2.8 HREM image simulation

Because HREM images are highly sensitive to the instrument, operation and sample conditions, images can get hopelessly confused and are prone to be mis-interpreted. Therefore it is necessary to employ computer-simulation techniques to interpret phase contrast images. Matching of simulated images and experimental images over a range of parameters (e.g. specimen thickness, specimen orientation, microscope focus) is at present the most accurate method of image interpretation.

Stadelmann's EMS software package [98] was used to generate the HREM simulations using a Sun workstation based Unix system. Images of dislocation cores were simulated using atom positions of cmputed cores as input data. These atom positions which were the result of AEM calculations of dislocations in B2 aluminides, were provided by D. Farkas at Virginia Polytechnic and State University.

The EMS program uses the multislice method to calculate the wavefunction of an electron in the crystal. As shown in figure 22, the electron wavefield exiting the bottom of the specimen ψ_t is calculated by considering the successive interaction of the incident

wavefield Ψ_o with the crystal potential Φ_p of each slice.

$$\Psi_1 = [\Psi_0 \otimes P_1] \bullet Q_1 \qquad \text{.....(22)}$$

$$\Psi_n = [\Psi_{n-1} \otimes P_n] \bullet Q_n \qquad \text{.....(23)}$$

Here P_n is free space propagator between the $[n-1]^{th}$ and n^{th} slices and the symbol $\otimes$ represents a convolution. Q_n is the transition function of the n^{th} slice and is a function of crystal potential Φp:

$$Q_n = exp\left[i \sigma \Phi_p\right] \qquad \text{.....(24)}$$

Where;

σ is the relativistic electron interaction constant,

Φp is the crystal potential per unit length projected along the beam direction;

δz is the thickness of each slice

If the crystal is perfect, Φ_p will repeat periodically along the beam direction so that Q_n is constant as a function of thickness. If crystal contains a dislocation (or other defect), Φ_p is no longer periodic in the beam direction, and the variation of Φ_p is discretized into slabs of constant thickness.

The simulation path is shown in figure 23. The data files containing atom positions from Prof. Farkas were converted into supercell files by a conversion program (given in appendix 2). In the supercell, the x and y axes are perpendicular to beam direction, while the z axis is parallel to beam direction (dislocation line direction) (fig. 24) and a>>t, b>>t as shown in figure 25. The dislocation line is always at the center of the supercell.

The *SC* subroutine is then used to generate the phase object function (POF) (xxxxxx.pof) and the Fresnel propagator function (FRE) (xxxxxx.fre). The POF is calcu-

lated directly in Fourier space by calculating the structure factors at the (h,k,0) sampling points. The .pof and .fre files are used by the multislice interation.

The major problem of the multislice method is the selection of the right slice thickness and sampling of the projected potential. When the slice thickness is too large, the phase object approximation fails and when the sampling is too coarse, the projected potential could possibly become complex or negatively valued. In order to check the validity of the calculation of the projected potential, a unitary test program (*UT*) is used to test the number of sampling points and the slice thickness of the .pof file. If the supercell height is too large, it is necessary to slice the unit cell in the beam direction into several thinner subslices. Figure 26 is the map for "*slice*" program.

The *SC* subroutine is applied to each of the subslice files to generate a .pof file. When the .pof file passes the unitary test, the multislice interation is performed in the manner shown in figure 26. The first subslice is iterated with the second subslice and so on. After each individual iteration, a new wavefunction is produced. This new wavefunction continues to interact with the POF in next subslice to give another new wavefunction. The procedure is controlled by a so-called "*autorun*" script program in a C-shell (given in appendix 3). The *MS* program was kept "on" until a desired foil thickness was reached.

The IM subroutine is used to calculate the HREM images. These images are displayed through the subroutine "*PR*".

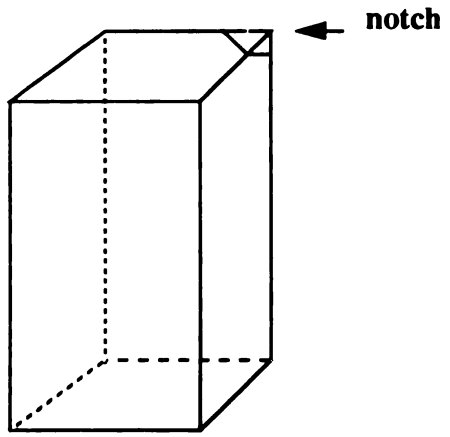

Figure 16 The size of compression specimen is 3x3x9 and a notch was made at upper right corner.

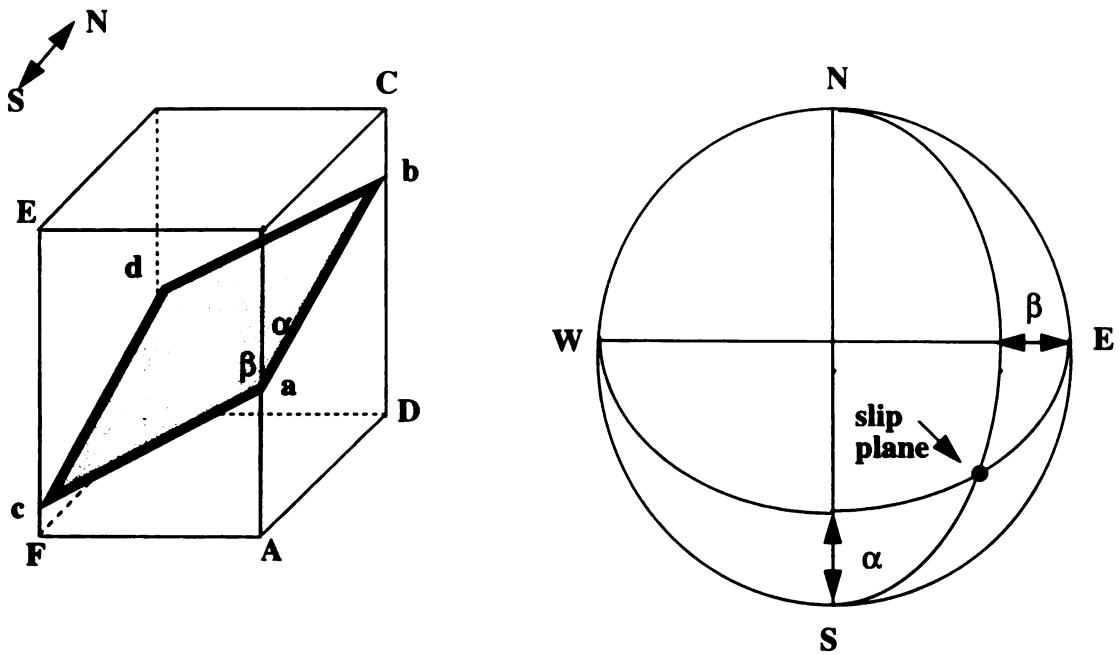

Figure 17 Slip trace analysis. The angles α and β were measured on the surface and the normal of slip plane was determined using a Wulff net.

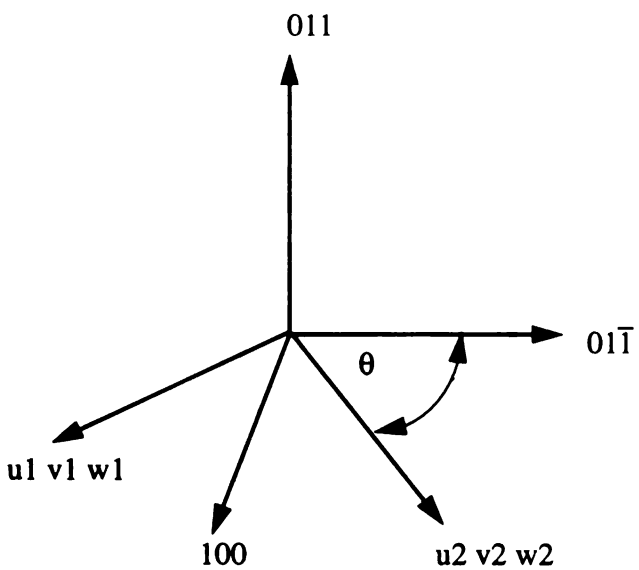

Figure 18 Coordinate system for [011] oriented single crystal Co-Al. The angles between slip traces depend on the coordinate system. Slip traces in [100][011][011] system can be easily identified. Slip traces in the other system can be determined using eqs. 18 and 19.

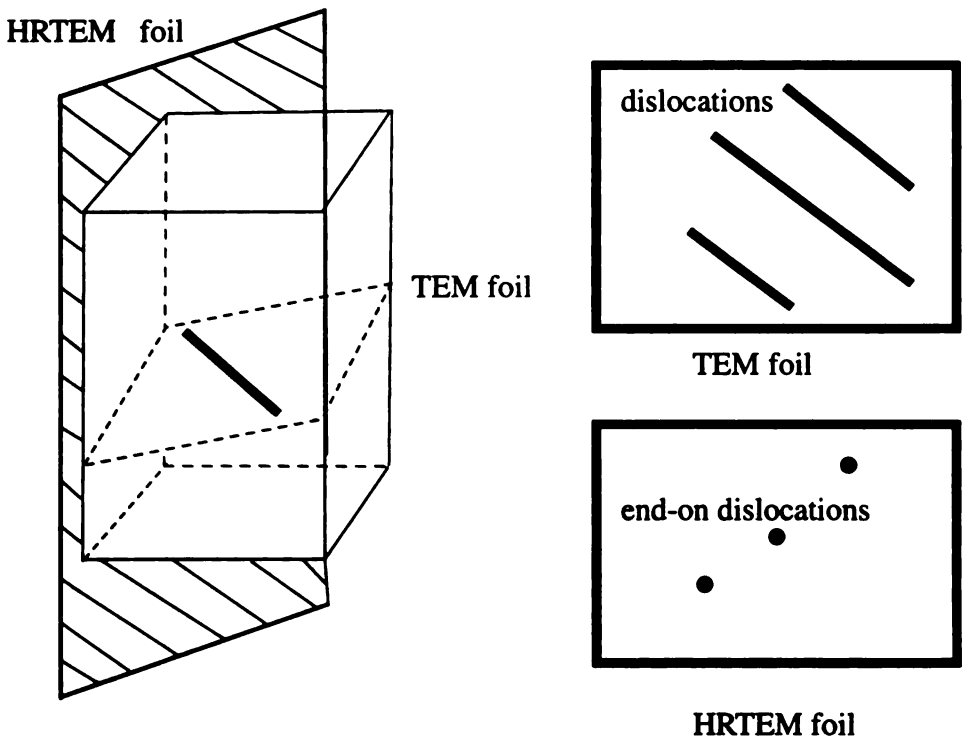

Figure 19 HRTEM foil section, and end-on dislocations. The TEM foils were sectioned in the direction parallel to the slip plane while the HREM foils were sectioned in the direction perpendicular to the dislocation line.

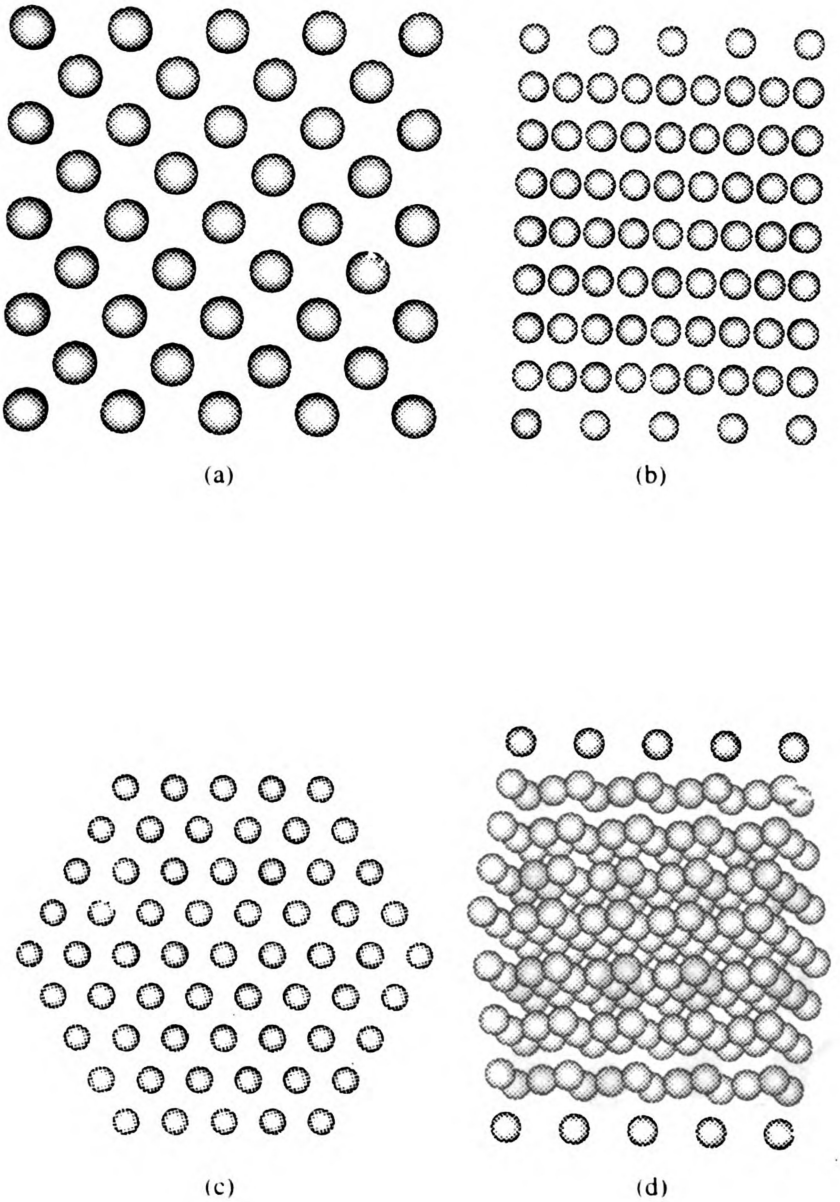

Figure 20 Projected lattice for dislocation lines corresponding to various zones. For some zones (<110> and <112>), projected atom spacings of the lattices are below the resolution of the high resolution transmission eletron microscope. (a) <100> (b) <110> (c) <111> (d) <112>.

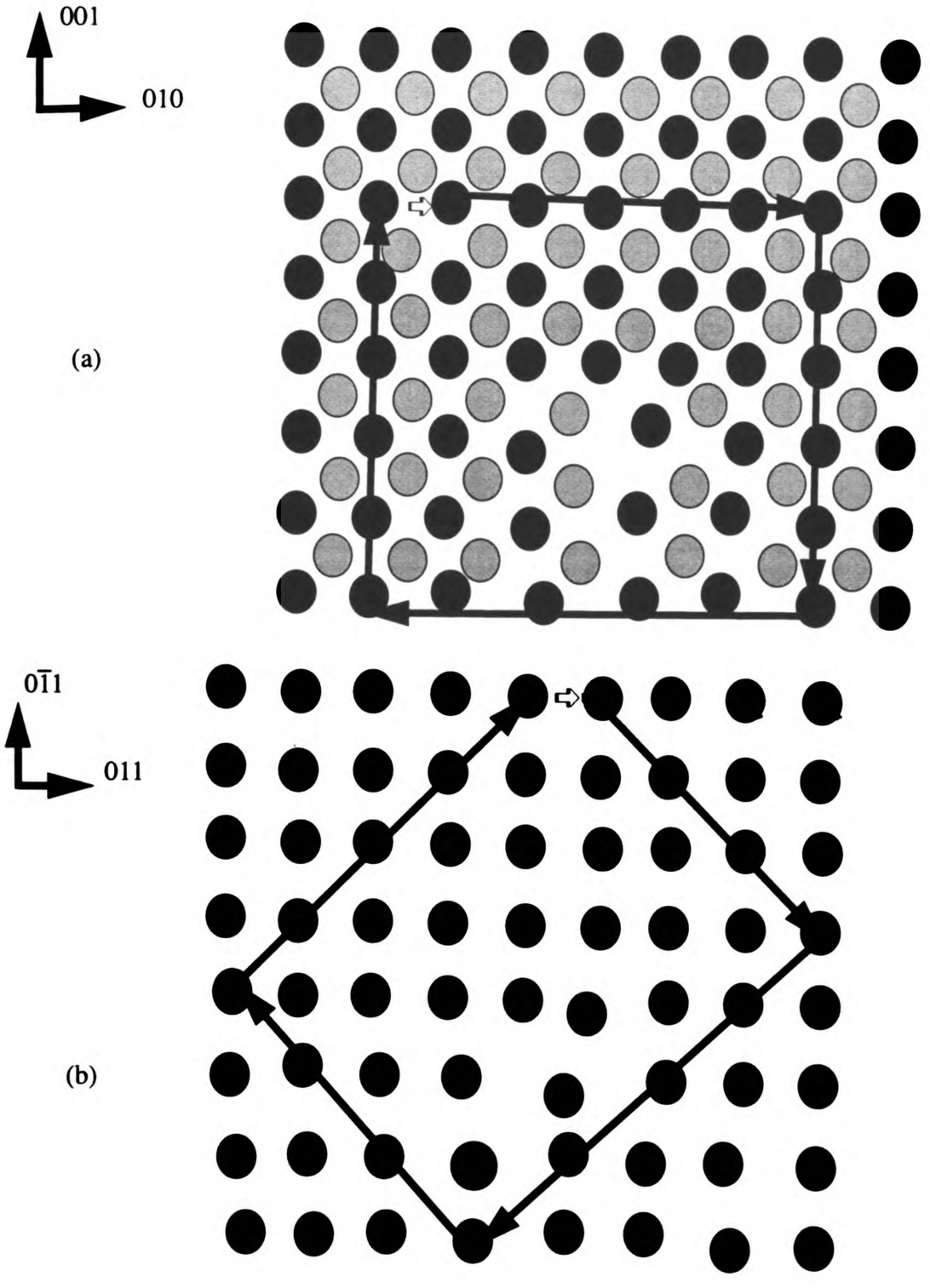

Figure 21 (a) Regular lattice: schematic core structure of [010] dislocation.
(b) Superlattice: schematic core structure of [010] dislocation.

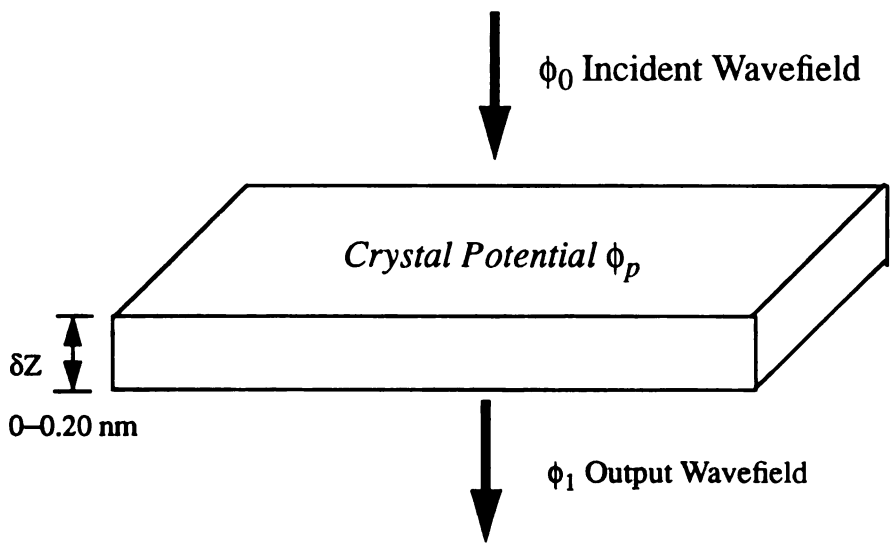

Figure 22 Schematic representation of the multislice principal. The incident wavefield interacts with the crystal potentials, resulting in a modified output wavefield.

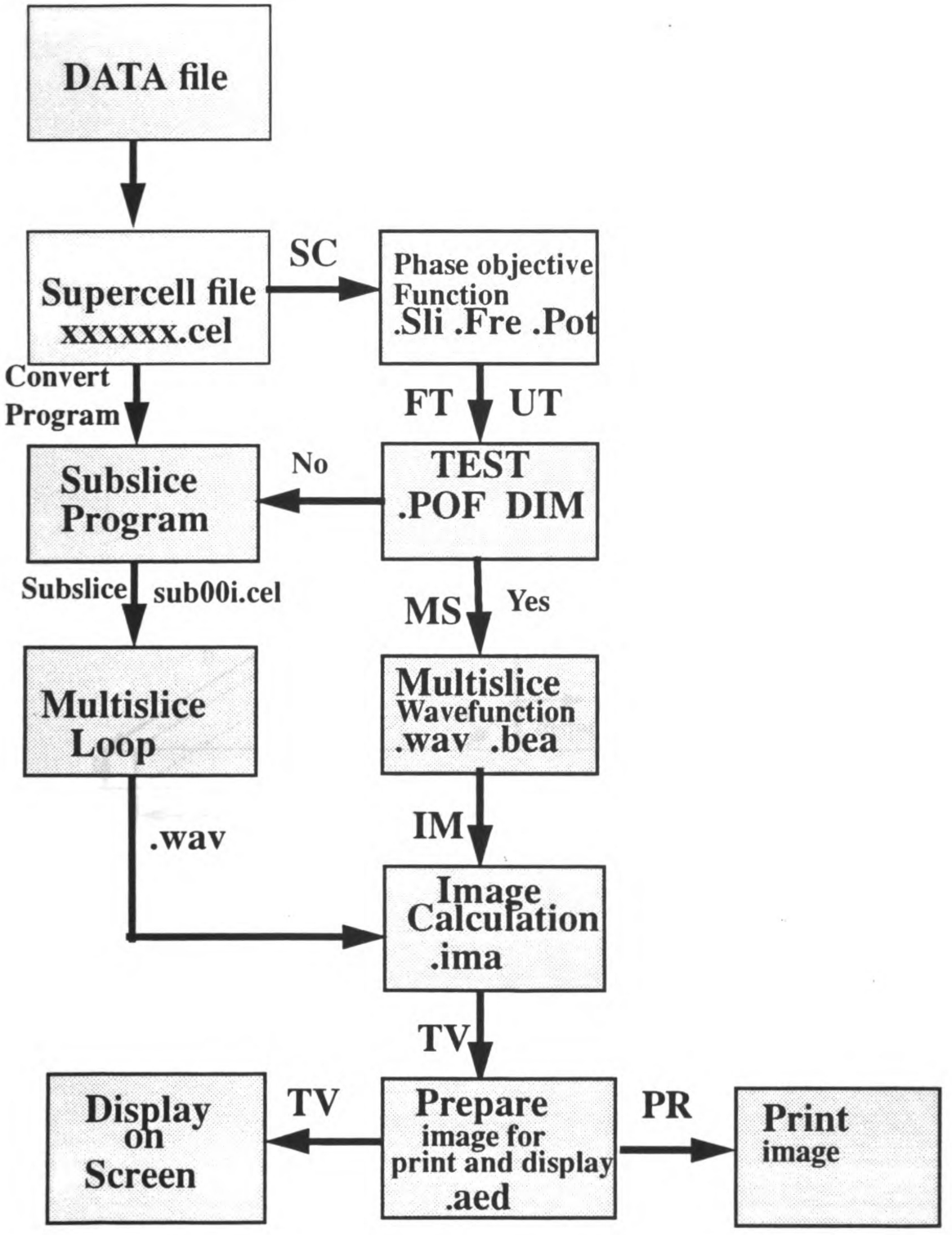

Figure 23 Simulation path for multislice calculations. Phase objective function, wave function and image calculation are key steps in HREM simulation.

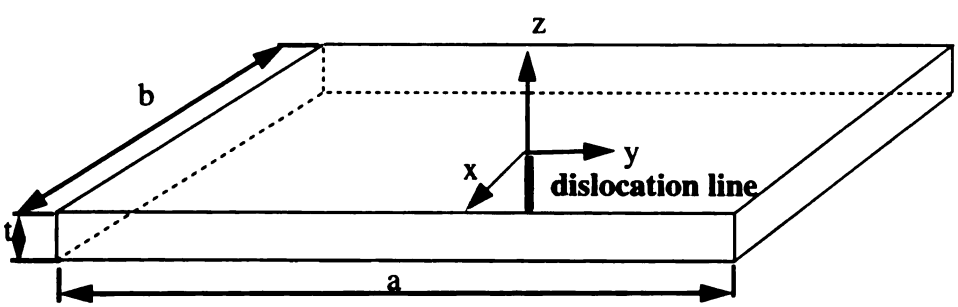

Figure 24 Representation of a supersell used for image simulation. The supercell was made with a and b borders much longer than its thickness.
Note: the z direction corrsponds to the beam direction.

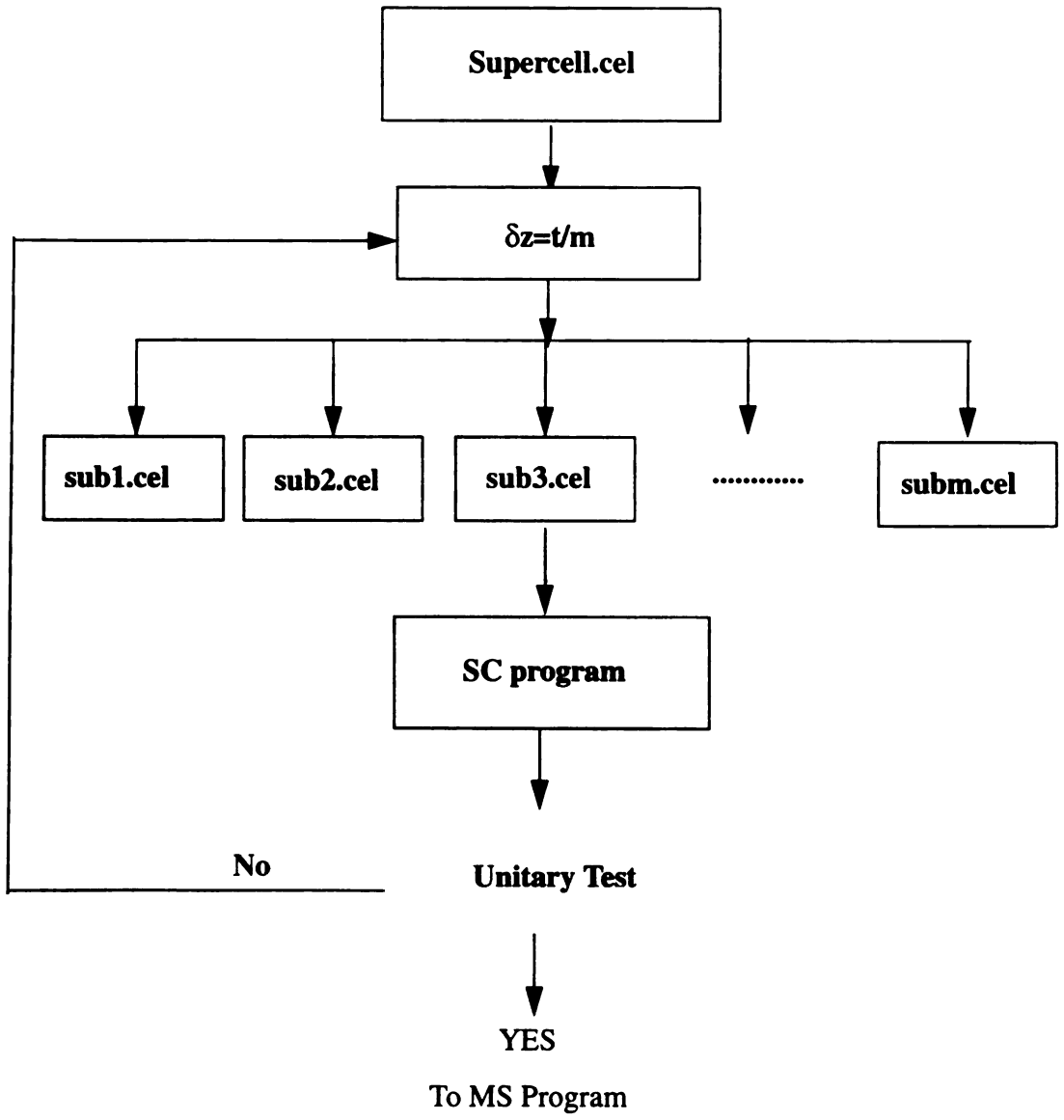

Figure 25 Slice program map. The number of slices should be large enough in order to pass the unitary test.

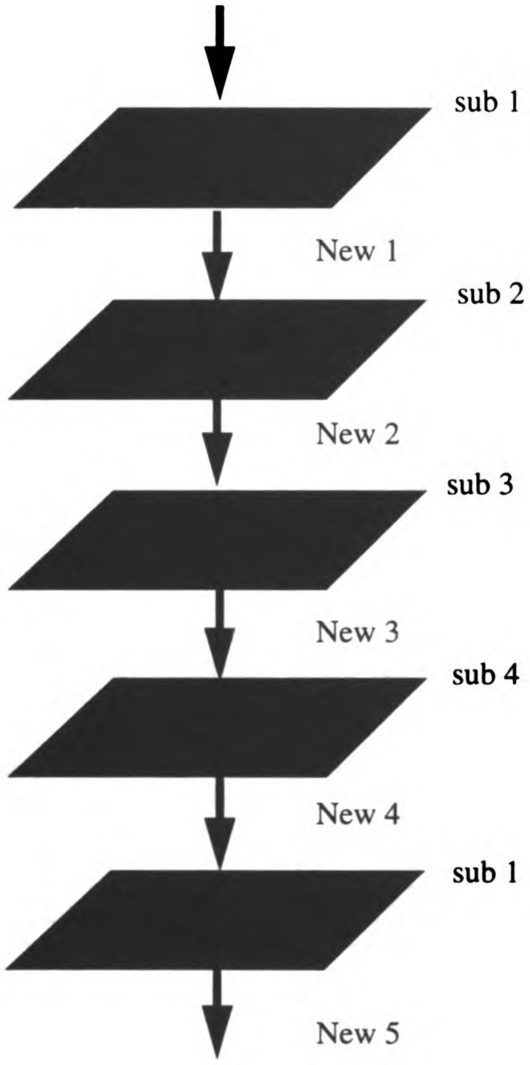

Figure 26 Iteration diagram illustrating iteration procedure. The exit wavefunction of the previous subslice was regarded as the incident wavefunction of the current subslice.

Table 5 Elastic constants of Co-Al, Ni-Al and Fe-Al

	C11	C12	C44
Co-50Al [122]	270	107	140
Ni-50Al [128]	203	134	116
Fe-50Al [129]	181	114	127

Table 6 Edge dislocations and the corresponding line direction in B2 structure

Burgers Vector	Slip Plane	Line Direction
010	001	100
001	110	$1\bar{1}0$
100	012	$0\bar{2}1$
111	$1\bar{1}0$	$11\bar{2}$
111	$11\bar{2}$	$1\bar{1}0$
111	$12\bar{3}$	$\bar{5}41$
011	$0\bar{1}1$	100
$1\bar{1}0$	001	110
$1\bar{1}0$	111	$11\bar{2}$
$1\bar{1}0$	$11\bar{2}$	111

Chapter 3 Results and Discussion

In the following sections, results of the experimental studies will be presented. These results will be analysed and compared with the previous studies in B2 alloys section by section. A comprehensive discussion that intergrates deformation behaviors, slip systems, dislocation activation and core structures is not included in this chapter. It will be presented in Chapter 4.

3.1 Mechanical behavior of Co-Al alloys

3.1.1 Deformation of Co-Al under high temperature compression

Representative true stress-strain curves for three [011] oriented Co-Al alloys with different compositions compressed at a stain rate of $2x10^{-3}$ s^{-1} at 1300 K are presented in figure 27. The curves (a), (b) and (c) show the results for Co-50Al, Co-48Al and Co-52Al respectively. The deformation features are summarized in the following paragraphs.

Off-stoichiometric Co-52Al and Co-48Al both exhibit significantly higher stress levels for corresponding strains than stoichiometric Co-50Al, with the aluminium rich Co-52Al displaying higher strength than the cobalt rich Co-48Al. This is consistent with the hardness-composition data for Co-Al of Westbrook [13] and Whittenberger's slow strain rate creep compression experiments for polycrystalline Co-Al [27]. Similar yield strength vs. composition trends have also been observed in the Ni-Al system (Ni-51Al, Ni-50Al and Ni-49Al) deformed at a strain rate of $1.41x10^{-3}$ s^{-1} at temperatures below 673 K [99]. However, this trend disappeared at 1273 K [99,100]. This comparison indicates

that Co-Al is more sensitive to stoichiometry deviations than Ni-Al with respect to deformation behavior at high temperatures around 1300 K.

The observed compressive stress-strain curves (fig. 27) of Co-Al are indicative of B2 alloy deformation behavior [26,99,100], in which the stress-strain curve increases rapidly during the first 0.8-1.0% deformation and then remains more or less constant with respect to stress. Co-52Al and Co-48Al exhibit different strain-hardening behavior than Co-50Al. As shown in figure 27, the work hardening exponent is very low for Co-50Al. In off-stoichiometric Co-Al, this work hardening exponent (0.174) is significantly higher than that of Co-50Al. Because the observed dislocation densities in off-stoichiometric Co-Al are lower than in stoichiometric Co-50Al (discussed in 3.2), dislocation interaction is not likely in this work hardening. Therefore, the difference in yield strength strain-hardening behavior may be related to differences in the mobility of dislocations in these materials.

Comparison with Wittenburger's previous compression results [26] for polycrystalline Co-Al shows that the true stress levels in single crystal Co-Al are lower than those in corresponding polycrystalline Co-Al. This may be explained by the fact that the compression axis is a soft orientation for slip in single crystals, while the compression axis varies between soft and hard orientations in polycrystals. Secondly, deformation in polycrystal requires grain boundary compatibility.

A true stress-strain curve for the [001] oriented Co-50Al, compressed at a strain rate of $2x10^{-3}$ sec^{-1} is presented in figure 28, and compared with a curve for [011] oriented Co-50Al. An interesting deformation phenomenon was noticed in [001] oriented Co-

50Al: the strength drops after yielding and continues until a minimum stress is reached, beyond which the strength slowly increases. Macroscopic examination of the deformed specimens reveals that they were deformed via kinking and/or bending. This phenomenon is known as strain-softening. Whether or not strain-softening is followed by strain-hardening depends on the nature of the material. Strain-softening also exists in NiAl [42,100,101] and has been explained by kinking mechanisms [101]. Strain-softening can occur irrespective of the prior uniform deformation and is dependent on testing conditions. Corresponding to the kinking phenomenon, much higher deformation resistance occurs when the compression axis is parallel to the [001] crystal orientation as compared to the [011] orientation. This high strength in [001] oriented Co50Al may be related to the critical resolved shear stress (CRSS) values for initiation of predominant slip systems and will be discussed in detail later. In NiAl [99], the difference in yield stress caused by orientation is significant at temperatures below 700 K, but not obvious at temperatures above 800 K. Since the operative slip systems are <011>{011}/<011>{111} at higher temperatures and <111>{011}/<111>{11$\bar{2}$} at lower temperatures in [001] oriented NiAl, it seems that the CRSS of <011> dislocations may drop more rapidly as the temperature increases.

3.1.2 Mechanical behavior of Co-Al and Ni-Al at room temperature

[011] oriented single crystal Co-50Al, Co-52Al and Ni-50Al were compressed at room temperature with the resulting stress-strain curves being given in figure 29. Co-50Al and Co-52Al crystals displayed completely elastic behavior and fractured at an early stage of deformation. Co-52Al crystals were more difficult to deform elastically than Co-50Al, possibly reflecting the effects of stoichiometry shifts on the atomic bonding strength. Examination by electron microscopy did not reveal any deformation-introduced

strength. Examination by electron microscopy did not reveal any deformation-introduced dislocations, indicating a high CRSS values for the dislocations. In contrast, Ni-50Al crystals have significant compressive plasticity at room temperature and do not fracture during deformation.

Compression tests were also performed at 673 K and 1000 K. Due to an interface problem, the computer could not receive the data from MTS. Therefore the mechanical behaviors under those conditions were not successfully recorded.

3.1.3 Slip trace analysis

Figure 30 illustrates slip lines on the surfaces of a [011] oriented Co-50Al specimen deformed at 873 K. Two sets of slip lines intersect each other on the surfaces. The intersection angle of slip lines depends on surface orientation of single crystal specimen. If the specimen surfaces are (100) and $(01\bar{1})$ and the slip planes are (001) and (010), the two sets of slip lines intersect at 90 degrees on the (100) face and 0 degrees on the $(01\bar{1})$ face. If the surfaces are not the (100) and $(01\bar{1})$ planes, the slip traces and intersection angles can be determined in a simple formula shown in section 2.4

The slip planes corresponding to the slip traces shown in figure 30 were determined to be (010) and (001) by using a stereographic projection, indicating the existance of "cube" slip. Figure 31 and figure 32 displays the slip lines on [011] Co-48Al and [011] Co-52Al deformed at 873 K respectively. Obviously, the slip lines observed on Co-52Al specimen are less dense than those on Co-50Al, indicating deformation is more difficult in Co-52Al. This also explains the premature fracture of the specimen during the 1300K compression. However, the observed slip planes in both Co-48Al and Co-52Al are also

(010)/(001), indicating cube slip. This fact suggests that internal friction of the slip system plays an important role in Co-Al plastic deformation.

Recording slip traces at 1300 K was not as successful as at 873 K. Due to high temperature oxidation, the surface slip lines are too faint to be clearly indentified. One exception is shown in figure 33. The slip traces on [011] Co-50Al specimen after 1300 K compression are faint but still discernible. These slip lines indicate "cube" slip is operative. This suggests that raising testing temperature does not change the selection of slip planes.

3.2 Dislocation analysis

Dislocations were introduced during the compression tests under various conditions of temperature, orientation and composition. The Burgers vectors of these dislocations were determined using the $\mathbf{g \cdot b}=0$ analysis method, while the line directions of the dislocations were determined using trace analysis. In selected cases, these diffraction contrast studies were supplemented with dislocation image simulation and matching. The experimental results are outlined in following sub-sections.

3.2.1 As-grown single crystal Co-50Al

The dislocation densities in the as-grown Co-50Al thin foils are generally very low. Most of the areas in the foils are dislocation-free and the majority of the dislocations are observed in a few locations. This indicates that the dislocation distribution is not uniform. A typical area containing dislocations is shown in figure 34. The dislocations are divided into two groups according to line orientations and are marked "a" and "b" respec-

tively. The projected line directions of dislocations and the corresponding configurations vary with the electron beam directions. For example, dislocations "a" are straight under the beam direction near $[\bar{1}1\bar{1}]$ (figure 34a), but they appear curved when the beam direction is near $[10\bar{1}]$ (figure 34b). Therefore the average direction of dislocation lines will be considered. Since the projected line direction of the dislocations "a" is [020] under the beam direction [001], [011] under the beam direction $[0\bar{1}1]$, and [121] under the beam direction $[1\bar{1}1]$, the true average line direction of these dislocations is roughly [010] (see the sterographic projection diagram in figure 35). However, dislocation "b" is highly curved and its line direction is not well defined. With the **g**=(011) (fig. 34c) and **g**=(020) (fig. 34d), dislocations "a" are either out of contrast or show weak contrast. Thus the Burgers vector of these dislocations is **b**=[100], according to the **g•b**=0 invisibility criterion. The dislocation labeled "b" is in contrast at **g**=$[10\bar{1}]$ (fig. 34a), **g**=[101] (fig. 34b) and **g**=(011) (fig. 34c), and out of contrast at **g**=(020) (fig. 34d), **g**=(200) (fig. 34e) and **g**=$(\bar{1}\bar{1}0)$ (fig. 34f). Thus the Burgers vector of the dislocation labeled "b" is **b**=[001]. Because the line direction of dislocations "a" is perpendicular to the corresponding Burgers vector, these dislocations are of edge characters and have slip plane of (001).

3.2.2 [123] oriented Co-50Al deformed at high temperatures

3.2.2.1 [123] Co-50Al deformed at 1300 K

The deformation substructure resulting from deformation at 1300 K was found to contain a relatively low dislocation density. An example of the structure is shown in figure 36. Many different types of dislocations were observed, but no dislocation dissociation or anti-phase boundaries were seen. Generally, the dislocations exist individually

and are straight or slightly curved in nature. However, some dislocations appear as junctions among groups of dislocations and some dislocation loops were observed as well. Three types of dislocations [011], [111] and [100], marked "a","b" and "c" respectively in fig. 36(a) have been analyzed by diffraction contrast and computer simulation experiments. The details of these studies are outlined below.

Figure 36(b and c) show the results of a diffraction contrast analysis of dislocation type "a". These dislocations are visible in the $(1\bar{2}\bar{1})$ reflection (fig. 37a), but are weak or invisible with the (200) (fig. 37b) and $(\bar{2}11)$ reflections (fig. 37c). Thus the dislocations have the Burgers vector $\mathbf{b}=[01\bar{1}]$. These "a" type of dislocations are observed both as isolated dislocations and in networks. The average dislocation line direction, determined using trace analysis, is [100]. Thus, these $[01\bar{1}]$ dislocations are of edge character. Figure 37 shows an analysis of a dislocation reaction observed in a different foil sectioned from the same deformed specimen. Two sets of dislocations with different type <100> Burgers vectors intersect one another, forming a junction dislocation $\mathbf{b}=[01\bar{1}]$ resulting in a decrease in elastic energy. Similarly, many studies [3,6,25] of dislocations in NiAl have found the short segments of <011> dislocations arising from the interaction of two gliding <001> type dislocations in the manner:

$$[00\bar{1}] + [010] = [01\bar{1}] \qquad \text{.. .....(25)}$$

These dislocations are usually considered to be sessile [3,6,25]. But Miracle [13] and Dollar [14] have recently reported the occurrence of active <011> slip in NiAl. The observations in the present study cannot rule out the possibility of either active <011> or inactive <011> slip in CoAl. However, based on the overall low number of <011> dislocations in this material, it is reasonable to conclude that these dislocations contribute to

plastic strain on a relatively small scale.

Dislocations of type "b" lie roughly in the direction [$\bar{4}$,23,3] (close to [010]) in fig. 36a. It was not possible to completely characterize the dislocations labeled "b" using conventional invisibility criteria. For a fairly anisotropic material such as CoAl, dislocations may display strong residual contrast even though the **g•b**=0 and **g•bxu**=0 conditions are satisfied. For example, dislocations "b" appear somewhat weak and display dotted contrast using the (1$\bar{1}$0) reflection in fig. 36c. Assuming this condition is near invisibility, the **g•b**=0 criteria suggests [111], [11$\bar{1}$], [110] and [001] as possible slip vectors. Figure 38 contains computed images for these possible Burgers vectors for the diffracting conditions **g**=(1$\bar{1}$0), **g**=(0$\bar{1}$1) and **g**=(1$\bar{2}$1). The appearance of the dislocation simulations is described in table 7. The experimental image of the dislocation with g=(1$\bar{1}$0) in figure 38 is characterized with many segments whose orientations deviate from the line direction of the dislocation. Both **b**=[11$\bar{1}$] and **b**=[111] simulations match this feature. However, an alternative contrast fluctuation along the dislocation line can be observed at the reflection vector (0$\bar{1}$1) in fig. 38. The simulation under this condition shows that only the b=[111] simulation matches the experimental image. When this dislocation was imaged at **g**=(1$\bar{2}$1), it appers as a long straight line. Again, the simulation for the Burgers vector [111] is close to the experimental image (fig. 38). Therefore only **b**=[111] consistently matches the experimental images for different conditions. Because this Burgers vector is neither parallel nor perpendicular to the line direction, the [111] dislocation is of mixed character. No evidence of any dislocation networks involving [111] dislocations was observed. In contrast, dislocation reactions between <111> and <100> dislocations are readily observed in FeAl [10,102,103].

Most of the dislocations produced in CoAl deformed in non-<100> orientations are expected to be <001> dislocations based on the theory of self-energy and relative mobility [16] as well as the anisotropic elasticity theory [26]. Due to elastic anisotropy, the dislocations labeled "c" in fig. 36a are only completely out of contrast for one reflection, $\mathbf{g}=(01\bar{1})$ in fig. 36e. Therefore images of [100], [011] and $[\bar{1}11]$ and [111] dislocations were simulated at the diffraction conditions $\mathbf{g}=(0\bar{1}1)$, $\mathbf{g}=(1\bar{1}0)$ and $\mathbf{g}=(1\bar{2}1)$. Comparison of these simulations and corresponding experimental images are presented in fig. 39 and table 8. For example, using the condition $\mathbf{g}=(0\bar{1}1)$ (fig. 40), the computed image for the Burgers vector [011] has double image feature, contrary with the experimental image. For the $[\bar{1}11]$ Burgers vector, the simulation shows that ends of the four segments are visually indented while the experimental image does not. At the condition $\mathbf{g}=(1\bar{1}0)$, the simulations for $\mathbf{b}=[\bar{1}11]$ and $\mathbf{b}=[111]$ are significantly different from the experimental image, while both $\mathbf{b}=[100]$ and $\mathbf{b}=[011]$ simulations are close to the experimental condition. However, under the two beam condition $\mathbf{g}=[1\bar{2}1]$, the simulation for $\mathbf{b}=[011]$ (as well as $\mathbf{b}=[\bar{1}11]$ and $\mathbf{b}=[111]$) fails to match the experimental image. Hence, it is reasonable to conclude that the type "c" dislocations have the Burgers vector $\mathbf{b}=[100]$. The line direction of these dislocations, measured using the stereographic analysis, is [010]. Thus these [100] dislocations are edge in character and the slip plane can be determined to be (001) from the cross product of the line direction and Burgers vector.

Considering the Schmid factor of 0.21 and 0.25 for [100](001) and [100](011) respectively under the [123] compression axis, the resolved shear stress for those two slip systems is very close. With respect to dislocation slip in NiAl [26], both <100>{011} and <100>{001} systems have been observed at low and high temperatures ($<0.45T_m$ and

$>0.45T_m$ respectively), indicating the critical resolved shear stress (CRSS) is similar for both systems. Thus it may be deduced that the CRSS of [100](011) is higher than that of [100](001) in CoAl deformed at 1300 K. On the other hand, Yaney et al. [35] tried to theoretically determine the directional instability of a dislocation in extruded polycrystal CoAl using an inverse Wulff plot. In the resulting plot, the inverse of the line energy of a dislocation, is plotted in polar coordinates as a function of the angle between the Burgers vector and the dislocation line. If dislocations are in a high energy orientation, a zig-zagged shape should be expected. Yaney's calculation shows that <100> dislocations on {011} planes are unstable about both pure edge and screw orientations, whereas <100> dislocations on {001} planes are unstable only about the screw orientation. This result, along with present experimental observation that the [100] dislocations do not exhibit the sharp bends (fig. 36-39), may help to explain why <100>{001} slip dominates the deformation at 1300 K.

Ball and Smallman [37] have predicted the operative slip directions in B2 compounds, based on the dislocation self-energy (E) and mobility parameters (S) using anisotropic elasticity theory. Their calculations for compounds NiAl, CuZn and CsBr are in good agreement with the slip directions observed in these materials. Drelles [15] extended the analysis of Ball and Smallman to include CoAl (table 9), showing that <001> type dislocations have the lowest value for a combination of E and S. The experimental results of the present study support this approach: [100] slip, which is much easier than [111] slip and [011] slip, dominates the plastic deformation.

If the data in table 9 are considered, it is expected that <011> slip would be the second most likely slip mode to contribute to the plastic deformation. However, in NiAl,

where the same would be expected, <111> slip has been reported at low temperatures in [001] oriented crystal [35] while <011> has only been reported to occur at high temperatures [44,104,105,106,107]. Potter [104] suggested that the atomic ordering places restrictions on certain slip systems. The operation of <011> slip causes like atoms to become nearest neighbors at the half slipped position, which increases the total energy of the lattice. Thus, even in [001] NiAl, [011] slip is less likely to operate. Therefore, in the present study, it appears that <011> slip is more difficult than <100> slip and <111> slip.

3.2.2.2 [123] Co-50Al deformed at 1000 K

In order to examine the effect of temperature on the selection of slip systems in single crystal CoAl, additional compression tests were carried out at 1000 K. Trace analysis shows the operation of (001) and (010) cube slip planes. Figure 40a illustrates the dislocation arrangement in foils sectioned parallel to the (001) slip plane. There exist five types of dislocations labelled "a" ,"b" ,"c" "d" and "e". Burgers vectors and line directions of these dislocations were determined in the same manner as described in 3.2.1, from which a three-dimensional distribution of active dislocations was determined (fig. 40b). Dislocations "a" are [010](001) edge dislocations; dislocations "b" are [100](001) edge dislocations; dislocations "c" are [001](010) edge dislocations and dislocations "d" are [100](001) edge dislocations. Dislocation loops lableled "e" were not identified in this study. This distribution is in good agreement with the slip trace analysis and dislocation projections onto the micrograph (fig. 40b). At this temperature, only <100>{001} slip was observed. <111> slip and <011> slip, which was observed in 1300 K, was not found. This result suggets that the CRSS of <111> slip and <011> slip increase relative to the

CRSS for <100>{001} slip as the temperature decreases. As it has been reported [15] that only <111> slip is observed in deformed single crystal CoAl at room temperature, it is likely that the operative slip systems in CoAl are temperature dependent and a transition temperature is expected.

3.2.3 [011] Co-Al deformed at elevated temperatures

In this section, dislocations and the corresponding slip systems analyzed in [011] oriented Co-48, 50 and 52Al deformed at 873 K and 1300 K will be summarized. The effect of stoichiometry and temperature on selection of slip systems are discussed.

3.2.3.1 [011] Co-Al deformed at 873 K

3.2.3.1.1 Co-50Al

Slip lines are clearly observed on the Co-50Al specimen surfaces after deformation at 873 K. The operative slip plane determined by the two surface trace analysis corresponds exactly to {100} type slip (fig. 30). Foil sections cut parallel to the {100} slip planes exhibited a large number of dislocations (fig. 41a). Three dislocation types exist in terms of their configurations. Dislocations marked "a" and "b" appear to be lying near plane of the foil. Dislocations "c" appear as "dots" with line direction is perpendicular to the foil. Dislocations ("a" and "b") lie in the same direction and are located in the slip bands. There are only a few dislocations between slip bands. Both $\mathbf{g}=(110)$ and $\mathbf{g}=(200)$ satisfy the $\mathbf{g}\cdot\mathbf{b}=0$ invisibility criterion for dislocations "a" (fig. 41b c) and hence $\mathbf{b}=[001]$ is the Burgers vector. Unlike dislocations "a", dislocations "b" do not lose contrast at $\mathbf{g}=(110)$ (fig. 43b). Instead they only have weak contrast (near invisibility) at $\mathbf{g}=(10\bar{1})$ (fig.

41d) and disappear at **g**=(200) (fig. 41a). Therefore the Burgers vector of dislocations "b" is [010]. Line direction analysis reveals that both dislocations "a" and "b" to be [100]. Because the Burgers vectors of these dislocations are perpendicular to their line direction, both dislocations "a" and "b" are edge dislocations. This helps to explain the limited invisibility. Both disloctions "a" and "b" display minimum visibility when **g**=**u** satisfying the **g**•**b**=0 and **g**•**bxu**=0 criterion for edge dislocations. The end-on dislocations "c" are analyzed in the same manner as mentioned above. These end-on dislocations are weak with **g**=(110) and **g**=(200) (fig. 41b,c). Therefore, the corresponding Burgers vector of the end-on dislocations is [001]. The line direction of these end-on dislocations is [010], indicating edge character. Figure 42 is a schematic showing the three-dimensional distribution of the dislocations in the thin foils (end-on dislocations and dislocation loops are not included in this drawing).

Dislocation reaction and interaction were not observed under this deformation temperature.

3.2.3.1.2 Co-52Al

Figure 33 shows the surface slip traces on Co-52Al deformed at 873 K. These slip lines are less dense than observed for Co-50Al, indicative of the difficulties in plastic deformation of Co-52Al. However, as in Co-50Al, the active slip planes in Co-52Al are {001} type.

The dislocation distribution in Co-52Al is similar to that in Co-50Al. Figure 43(a) shows two types of dislocations labeled "a" and "b". The Burgers vector analysis was performed as follows. When $(\bar{2}00)$ is the operative reflecting vector (fig. 42b), both disloca-

tion types are in poor contrast, while dislocations "a" are out of contrast at $\mathbf{g}=(\bar{1}0\bar{1})$ (fig. 43c) and dislocations "b" disappear at $\mathbf{g}=(\bar{1}10)$ (fig. 43d). Therefore, the Burger's vectors of the dislocations are $\mathbf{b}=[010]$ and $\mathbf{b}=[001]$ for dislocations "a" and "b" respectively. Trace analysis indicates both of these dislocations have the average line direction of $\mathbf{u}=[100]$, thus both dislocations "a" and "b" are of edge character. In addition to the dislocations inclined in the thin foil, a limited number of dislocation loops and the end-on dislocations are also observed. For the reflection planes $(\bar{2}00)$ and $(\bar{1}10)$, some of the loops and end-on dislocations lose their contrast, defining the Burgers vector to be $\mathbf{b}=[001]$, indicative of edge nature of end-on dislocations with respect to their line direction of [010]. Dislocation reactions or interactions were not found in this foil.

3.2.3.2 [011] Co-Al alloys deformed at 1300 K

In order to examine the core structures of the dislocations generated by deformation at 1300 K, it is necessary to first perform a TEM substructure analysis. Unfortunately, due to the higher temperature, surface oxidation of the deformed specimens made it extremely difficult to identify the activated slip planes. Hence, no "slip plane" parallel sections could be made. However, sections perpendicular to the deformation axis were taken so that $\mathbf{g}\cdot\mathbf{b}=0$ analysis could be performed. These sections were not as convenient but still produced foils that allowed a substructure analysis to be performed.

3.2.3.2.1 [011] oriented Co-50Al

On the oxidized surfaces of the Co-50Al deformed in the [011] orientation, slip lines were faint but still discernible and featured cube slip of (010)/(001) (fig. 34). Figure

44 shows a typical dislocation structure observed from this material. The structure was generally characterized by <100> dislocations. However, the other dislocations were also observed. In the example shown in figure 44, four types have been analyzed. Figure 44(a)-(d) show detailed examples. The dislocations labeled "a" are invisible with **g**=($\bar{2}$00) and **g**=(1$\bar{1}$0) (fig. 44a,b) and therefore have a Burgers vector of [001]. The average line direction of dislocations "a" is [100]; hence these dislocations are edge in character. Dislocations "b" are out of contrast at **g**=($\bar{2}$00) and **g**=(101) (fig. 44a, c), and therefore have a Burgers vector of [010]. Dislocations "c" are out of constrast only at **g**=(0$\bar{1}$1). The corresponding Burgers vector has the possibilities of [100], [111] and [011]. Regarding to the slip plane (001) and dislocation line direction [010] of these dislocations, the "c" type of dislocations most likely have [100] Burgers with edge character. The dislocation loops labeled "d" have prismatic shape. The parallel borders of these loops are invisible or in weak contrast at **g**=(200) and **g**=(0$\bar{1}$1) respectively, resulting in [011] Burgers vectors and edge character (fig. 44). The reason why no operative **g** vectors can make the loops completely disapper can be given by the **g•bxu**=0 criteria. These loops have line directions of [100] and [0$\bar{1}$1] (fig. 44). Only those **g**-vectors whose direction is perpendicular to Burgers vector and is parallel to the line direction, can make dislocation completely out of contrast. The [011] edge loops may be generated by vacancy disc collapse.

Dislocation reactions were also observed at this foil. At the positions labeled R and Q, the short junctions of dislocations were determined to be [$\bar{1}\bar{1}$1] Burgers vector because these dislocations disappears at both **g**=(1$\bar{1}$0) (fig. 44b) and **g**=[101] (fig. 44c). This dislocation reaction have three possibilities.

$[\bar{1}\bar{1}1] = [\bar{1}00] + [0\bar{1}0] + [001]$ decomposition .....(26)

$[\bar{1}00] + [0\bar{1}0] + [001] = [\bar{1}\bar{1}1]$ interaction .....(27)

$[\bar{1}00] + [0\bar{1}1] = [\bar{1}\bar{1}1]$ interaction .....(28)

<111> dislocation discomposition is less likely because it would cause the elastic energy of the dislocations to increase at least according to isotropic linear elasticity. The other reason is that at the temperature of 873 K, only <100> type of dislocations were observed. It is reasonable to believe that higher temperature increases the interaction opportunities for thermally activated <100> dislocations. On the other hand, dislocation interaction between <100> dislocations and/or between <100> dislocations and <011> dislocations are both energetically favorable. This result is in agreement with the observation of <111> dislocations in [123] Co-50Al deformed at 1300 K (section 3.2.2.1). However, the [123] orientation resulted in free <111> dislocations, while [011] orientation resulted in sessile <111> node dislocations.

3.2.3.2.2 [011] oriented Co-48Al

The dislocation density in [011] Co-48Al deformed at 1300 K is visually lower than that in Co-50Al deformed under the same conditions. An example of this is shown in figure 45. Dislocations labeled "a" are lying roughly in the [200] direction; dislocations "b" are aligned in the [020] direction. Here dislocations "a" have a [010] Burgers vector due to the invisibility with $\mathbf{g}=(10\bar{1})$ and $\mathbf{g}=(\bar{2}00)$ (fig. 45 a,b). Dislocations "b" are invisible at $\mathbf{g}=(01\bar{1})$ and $\mathbf{g}=(020)$ (fig. 45 c,d), and therefore their Burgers vector is defined as [100]. Therefore dislocations "a" and "b"are all edge in character.

In addition to the <100> dislocations, there are many dislocation reactions in Co-

48Al than Co-50Al. The dislocation reactions in Co-48Al featured by forked dislocations. A dislocation fork with the branch labeled u,v and w is analysed in figure 45. Branch **u** is almost out of contrast at **g**=($\bar{2}$00) (fig. 45b) and in weak contrast at **g**=(020) (fig. 45d), indicating **b**=[001]. Branch v is invisible at **g**=(10$\bar{1}$) (fig. 48a), indicating **b**=[010]. Branch w is in weak contrast at **g**=($\bar{2}$00) (fig. 45b) and **g**=(01$\bar{1}$) (fig. 45c), indicating **b**=[011]. Therefore the dislocation reaction is formulated.

$$[010] + [001] = [011] \quad \text{.....(29)}$$

This <100> dislocation interaction is also energetically favorable according to linear elasticity. However, [011] dislocation is less mobile than <100> dislocations. They may inhibit the glide motion of <100> dislocations. Thus the deformation structure may be indicative of a balance bwtween glide and lowering the dislocation energy.

3.2.3.2.3 [011] oriented Co-52Al

The observed dislocation density in [011] oriented Co-52Al (deformed at 1300 K) visually is the lowest of three compositions investigated in this study. Deformation of Co-52Al generated two types of dislocations, as shown in figure 46a. The first type, labeled "a" in figure 46 may be the [001] dislocations which are invisible at **g**= (200) (fig. 46a) and in contrast at **g**=(00$\bar{2}$) and **g**=(10$\bar{1}$)(fig. 46 b and d). Figure 46b and 46c shows that dislocations "b" are out of contrast at **g**=(00$\bar{2}$) and **g**=(0$\bar{1}$1), therefore having a Burgers vector of [100]. Because dislocations "a" have the approximately projected line direction [200] under the beam direction [010], and [200] under the beam direction [011], indicating the line directioin **u**=[100]. Dislocations "b" have the projected line direction of [00$\bar{2}$] under the beam direction [010], and [0$\bar{1}$1] under the beam direction [011], indicating

[010] line direction. Hence, both dislocations "a" and dislocations "b" are of edge character. In figure 46, some dislocations have the same line direction as dislocations "a", but have different contrast. They may have different Burgers vectors. Unfortunately, the Burgers vector can not be determined using the existing g-vectors.

In figure 46a-d, there appears to be a dislocation reaction at the position labeled R. However, when the foil was tilted, two complete dislocations were observed (fig. 46e and f). Therefore the "interaction" in position R, is only the image of of two dislocations contacting each other. Because the nobs of these dislocations do not move when the foil was tilted, the dislocations may intersect and lock each other. The gap pointed in fig. 46f is due to the local contrast change which results from the strain field compensation between two dislocation perpendicular to each other. Lack of dislocation interaction in Co-52Al may be due to the low density of <100> dislocations.

3.2.4 [001] Co-Al deformed at high temperatures

3.2.4.1 Dislocation structures in [001] oriented Co-50Al

As shown in section 2.1, [001] Co-50Al has a much higher compressive strength than the [011] Co-50Al (figure 28) and the former also displays a kinking phenomena. In general, kinking is a process which happens when normal plastic deformation is difficult due to . Due to the high temperature oxidation, slip lines could not be readily observed on these samples. Dislocations observed in [001] oriented Co50Al foils are distributed uniformly and are in good contrast at $\mathbf{g}=(\bar{1}0\bar{1})$ (fig. 47a). However, the observed dislocations "a" in the area of view are in extremely poor contrast at $\mathbf{g}=(020)$ and $\mathbf{g}=(0\bar{1}\bar{1})$ (figure 47b, c); the others marked "b" disappear at $\mathbf{g}=(200)$ (figure 47d) and are in weak contrast at

g=(020) (fig. 47b); dislocations "c" are out of contrast at **g**=($\bar{1}0\bar{1}$) (fig. 47a) and **g**=(200) (fig. 47d). Hence the dislocations "a" have a [100] Burgers vector; dislocations "b" have a [001] Burgers vector; and dislocations "c" [010] Burgers vector.

Because the dislocations have the projected line direction of [020] for dislocations "a", [200] for dislocations "b" and [$\bar{1}\bar{1}$0] for dislocations "c" under the [001] beam direction; [020] for dislocations "a", [101] for dislocations "b" and [1$\bar{2}$1] for dislocations "c" under [$\bar{1}$01] beam direction; [011] for dislocations "a", [200] for dislocations "b" and [211] for dislocations "c" under [0$\bar{1}$1] beam direction, the average line directions of the dislocations are [010] for dislocations "a", [100] for dislocation "b" and [101] for dislocations "c". Therefore, dislocations "a", "b" and "c" are all of edge character.

A question might be raised after the Burgers vector analysis: why are <001> dislocations activated under zero resolved shear stress (the Schmid factor is zero for <100>{001} system under <010> stress orientation)? To investigate further, more foils were examined. Figure 48 is a typical example.

The majority of the deformation structure is composed of three sets of dislocations lying roughly perpendicular to each other (fig. 48a). Dislocations labeled "a" have the projected line direction of [110] under the [001] beam direction, [211] under the [111] beam direction and [$\bar{1}\bar{1}$1] under the [011] beam direction. Therefore, the dislocation line direction is [11$\bar{1}$]. Dislocations "b" have the projected line direction of [0$\bar{1}$1] under the [001] beam direction, [1$\bar{1}$2] under the [$\bar{1}$11] beam direction and [1$\bar{1}$1] under [011] beam direction, indicating that [1$\bar{1}$1] is the true direction of these dislocation lines. Dislocations "c" have roughly the same line direction as the dislocations "a". Dislocations "a" are out of contrast at reflection vector **g**=(01$\bar{1}$) (fig. 48b) and are in weak contrast at **g**=(200) (fig.

48b), defining their Burgers vector as [011], while the dislocations labeled "b" disappear at both **g**=(101) and **g**=(020) (fig.48d and e), and therefore have a $[\bar{1}01]$ Burgers vector. Dislocations "c" disappear at **g**=(101) and are in weak contrast at **g**=$(01\bar{1})$ and **g**=$(\bar{1}\bar{1}0)$. Their corresponding Burgers vector is **b**=$[\bar{1}11]$. Since the burgers vectors of both "a" and "b" dislocations are perpendicular to the corresponding line directions, these dislocations are of edge character and glide on $(21\bar{1})$ and (121) plane respectively.

Substantial evidence of dislocation reactions were found in this foil. The dislocations labeled "c" are involved in typical examples. One of the interacted dislocations which is labeled "f" is determined as $[\bar{1}00]$ dislocation because it is invisible at **g**=$(01\bar{1})$ (fig. 48b) and **g**=(020) (fig. 48e). Unfortunately, rest of the interacted dislocations can not be indentified using the existing **g**-vectors. Therefore, the reaction shown in figure 48 is a <111> -related dislocation interaction. Three possible reactions are listed below:

$$[\bar{1}11] = [\bar{1}00] + [011] \quad \text{.....(30)}$$

$$[\bar{1}11] = [\bar{1}00] + [010] + [001] \quad \text{.....(31)}$$

$$[\bar{1}00] + [011] = [\bar{1}11] \quad \text{.....(32)}$$

The first two reactions are dissociations of <111> dislocations. Although these seem unfavorable in term of dislocation elastic energy, the dissociation may occur under certain conditions. One of conditions is the anisotropic nature of B2 materials, such as CoAl and NiAl. It was reported that <111> dislocations decomposed into three <100> in NiAl extruded at 1505 K [40]. The other condition is that lack of plasticity in [001] CoAl increases strain energy in the material. Decomposition of <111> dislocations will release the strain energy because <100> dislocations are more mobile than <111> dislocations. When the decrease in strain energy is larger than the increase in dislocation elastic energy,

the <111> decomposition occurs simultaneously.

Interaction between <110> dislocations and <001> dislocations are also possible because this interaction is energetically favorable.

The above mentioned analysis shows that in the [001] orientation, single crystal Co-50Al is deformed under compression stress via <011>{211} slip. Since the activation of this slip system is much more difficult than that of the <100>{001} system, the compressive stress is very high (fig. 28). As the deformation continues, the slip planes are rotated toward the [001] orientation. This reduces the resolved shear stress on the active slip system <011>{211} and further deformation becomes harder and harder until the kinking of the specimen occurs. Kinking changes the orientation of the single crystal locally and the <100>{001} slip systems are then favored. Therefore after kinking, the <100>{001} slip as well as <010>{101} slip dominates the deformation process.

Summary

In Co-Al system, <100>, <110> and <111> type dislocations are all generated, depending on temperature and orientation. Alloy stoichiometry does not have much influence on the selection of slip systems. Above 873 K, no matter what orientation is chosen, <100> slip dominates the deformation. However, a large number of non-<100> dislocations were also observed. <111> and <110> dislocations were observed in Co-50Al and Co-48Al deformed at 1300 K as the reaction products of <100> type dislocations. In [001] oriented Co-50Al, <110> dislocations dominate the deformation before kinking, while <100> dislocations dominate the deformation after kining. Therefore <100> dislocations play the most important role in the high temperature deformation of Co-Al single

crystals. Understanding core structures of dislocations is the key step to understand the dislocation behavior in Co-Al aluminides. The HREM results are presented in subsequent sections.

3.3 Core structures of <010> edge dislocations

For the most part, Burgers vector analysis was performed on the thin foils sectioned parallel to the observed slip planes and revealed the active slip systems in high temperature deformation. In order to elucidate the strength and ductility of B2 Co-Al alloys at a deeper level, it is necessary to examine core structures of dislocations. To do this, one has to view a dislocation along its line direction. To this end, foils for HREM were sectioned perpendicular to the dislocation line directions and the resulting "end-on" dislocations were investigated. Since the plastic deformation was limited to about 5% in this study to avoid possible dislocation intersection, the dislocation density in thin foils is relatively low. Additionally, in order to achieve usable lattice images, it is necessary to work at magnification in excess of 600,000 x. At these enlargements, the relative spacing of lattice positions becomes discernable. Often poor contrast under the many-beam image-forming condition can result in extreme difficulty in locating and identifing the end-on dislocations.

3.3.1 Co-50Al

Figure 49a is a HREM image of a [010](001) edge dislocation core in Co-50Al projected in the [100] direction. It is a white atom image, meaning the white spots represent lattice locations. The B2 ordering characteristics (ordered bcc) are clearly seen in fig-

ure 49a. It is impossible to differentiate Co from Al lattice positions in this picture. However, the corner atoms in the "apparent" fcc square lattice (projected images of B2 structures in the [100] direction) is arbitrarily assigned reliably as cobalt and the central one as aluminium. Though the overall resolution is very good, there exists a darker area very near the core center. This may be caused by a weaker exposure dose that is related to diffraction changes associated with the local strain field. A Burgers circuit around the dislocation core is illustrated and the closure failure of the circuit gives the Burgers vector [010]. This matches the results of the dislocation analysis on deformed Co-50Al in the previous section. The lattice distortion in a dislocation core is more clearly seen by observing the image from different orientations. This inspection is usually performed in the [001] direction (front view), [010] direction (side view), [011] and [$0\bar{1}1$] directions (45^{o} view) using either perspective or compressive viewing methods. In the perspective method, the scanned image is tilted 70-80 degrees, while in the compressive methods, the scanned image is squeezed to 1/3 of its original size so that small displacements are magnified. In order to observe the extra half planes more clearly, the HREM image was scanned into a TIFF file format and tilted 75^{o} using the "TILTER" program to produce a perspective view. The core is characterized by two extra half planes (one is the Co atom plane and the other is the Al atom plane) in figure 49b. The two extra half planes that are indicated by arrows in fig. 49b, terminate on (001) planes, and the atoms rows on these planes are continuous in the core center (fig. 49c). A single extra half plane terminates at the point on A, while second plane, 90^{o} away, terminates on B (fig. 49d and e). Because the points A and B are adjacent each other, this core has a compact nature. Correspondingly, the (001) plane is the slip plane of this [010] edge dislocation.

Figure 50a is another example of a core in Co-50Al. In the front view (fig. 50b), the two extra half planes terminate at positions aduacent to one another, a feature consistant with a compact core. However, when the core is examined in the $[0\bar{1}1]$ direction (fig. 50c), a single extra half plane is found at the position "A"; when the core is examined in the [011] direction (fig. 50d), a single extra half plane is found at the position "B". Obviously the position "A" does not coincide with the position "B". This indicates the existence of a finite dissociation in the dislocation core. After exposure under high energy electron beams for additional four minutes, the core structure was recorded and is displayed in figure 51. The core structure looks unchanged in the front view (figure 51b). However, the distance between the two termination locations of the extra half planes in the 45^{o} views is almost coincident now (fig. 51c and d), showing that the dissociation width is decreased after energy input. Comparison of two subsequent images of the same dislocation core indicates that core dissociation is a metastable state and it is transferred to a complete edge dislocation under the assistance of external energy.

Based on the above two examples, one can conclude that in Co-50Al, atoms in the core region are rearranged under the beams and the rearrangment results in a complete compact core.

3.3.2 Co-48Al

A dislocation core structure in deformed Co-48Al is shown in Figure 52. The closure failure of the Burgers circuit (fig. 52a) confirms the [010] edge character of this dislocation. This dislocation was considered an active dislocation by dislocation analysis in the 1300 K compression deformation experiment discussed in a previous section 3.2.3.2.2.

Unlike <100> cores in Co-50Al which always have compact appearance in the front view, the atomic arrangement in this core structure is more complicated (fig. 52b). Although the atom rows parallel to the (010) planes are well aligned and continuous in the side view (fig. 52c), the atom columns have slightly more distortion in Co-48Al than in Co-50Al. However, instead of being a compact core, the extra half Co plane is separated from the extra Al plane by a finite distance in the front view (fig. 52a). However, it is difficult to locate these extra half planes in the [100] view direction. The single extra half planes are more easily observed in the 45^0 directions. In this case, one single extra half plane terminates at point "A" in the $[0\bar{1}1]$ perspective (fig. 52c) and the other extra half plane terminates at point "B" in the [011] perspective (fig. 52d). The distance between "A" and "B" is a three atom spacings, i.e, 3x0.286=0.858 nm. This dissociation width is less than the resolution of weak beam TEM and therefore this dissociation cannot be determined via diffraction contrast transmission electron microscopy. Two separate Burgers circuits are built around the two extra half planes, indicating the possible partial dislocations 1/2[011] and $1/2[01\bar{1}]$, or $1/2[\bar{1}11]$ and $1/2[11\bar{1}]$ respectively (fig. 52 f). Because the 1/2<110> is not an atom to atom translation, the 1/2<111> is regarded as the superpartial dislocations. Because the 1/2<111> superpartial dislocations may have screw components which cannot be obsvered via HREM, the dislocation nature (edge, screw or mix) cannot be determined by the displacement observed on HREM micrograph. Therefore it is more likely that a [010] edge dislocation core is dissociated into two 1/2<111> partial dislocation cores.

$$\langle 010\rangle \rightarrow \frac{1}{2}\langle \bar{1}11\rangle + APB + \frac{1}{2}\langle 111\rangle \qquad \text{.....(33)}$$

Since the dissociation direction is [010], perpendicular to the slip plane, this type

of dissociation is also termed climb dissociation. After dissociation, the [010] edge core can not glide on the (001) plane because the slip planes of partial dislocations are not (001) planes. Therefore, atom reorganization may be required before the core moves under the applied stress.

3.3.3 **Co-52Al**

Co-52Al specimens have the highest compression strength and the lowest observed dislocation density among the Co-Al alloys studied. Core structures of this material are given special attention.

Figure 53a is an example of a dislocation core observed in a Co-52Al thin foil. Generally, the atom arrangement recorded had good resolution except for the left side of the core, here the point resolution is reduced to line resolution because of beam damage, twisting or strain.

A Burgers circuit was constructed around the core center and the resulting [010] displacement vector matches the Burgers vector analysis results in section 3.2.3.2.3. Viewing along the [010] direction (fig. 53b), the atom rows are found to be distorted more significantly than those in either Co-50Al or Co-48Al (fig. 49-52). The atom columns are well aligned in area away from the core center, while they are highly distorted near the core center. The extra half planes are difficult to identify in the front view because of image contrast fluctuation. Therefore it is necessary to use 45^{o} views to completely characterize the core. In the [011] directions, one single half plane is found at position "A"(fig. 53c) and the other single extra half plane is terminated at position "B" (fig. 53d). Position "A" and "B" represent the locations of two partial dislocations of this core in the

front view, and the distance between "A" and "B" is the width of the dissociation band and is equal to 4-5 atom spacings (1.144-1.430 nm). Similar to the climb dissociation observed in Co-48Al, the dissociation in Co-52Al occurs on the plane which is perpendicular to the slip plane. This means that the core is climb dissociated. Figure 54 is a HREM image of the same core structure taken after two minutes of beam exposure. With the help of 45° views, the Co atom extra half plane is found to terminate at point "A" (fig. 54b) and the Al atom extra half plane is found to terminate at point "B" (fig. 54c). Obviously the distance of "A" and "B" (14 atom spacing or 4.004 nm) is larger than that in figure 53a (1.144 nm). This means that energy input (high voltage electron beams) can assist in the development of climb dissociation and illustrates the need to be aware of anti-defacts. Since the dissociation plane is not on the original slip plane (001), the climb dissociation is non-planar. Figure 54d schematically represents two separated Burgers circuits around "A" and "B" (fig. 54d), giving the Burgers vector of the partial dislocations $1/2[11\bar{1}]$ and $1/2[\bar{1}11]$ (eq. 34).

$$[010] = \frac{1}{2}[111] + APB + \frac{1}{2}[111] \qquad \text{.....(34)}$$

Climb dissociation is a vacancy-related thermal activated process. In off-stoichiometric Co-Al alloys, there exists high concentrations of vacancies and anti-lattice defects [118,119]. This high concentration of point defects may promote the core transformation and dissociation via diffusion.

Figure 55 is another example of a dislocation core structure in Co-52Al. This core also has a Burgers vector of [010] (fig. 55a). Viewing along <011> direction, single extra half planes are found to terminate at the positions "A" and "B" (fig. 55d and e) respec-

tively. When "A" and "B" are marked in the experimental photo (fig. 55a), the core is found to be climb dissociated at a distance of four atom spacings (1.14 nm). Its (001) planes are more highly bent near the core center than in any other cores displayed thus far (figure 55c). Thus when core motion is needed, atoms on the (001) planes will have to follow a wavy path which combines glide and climb. This mode requires more energy than the pure glide mode in both Co-50Al and Co-48Al.

The core width is usually defined by the displacement range $-\frac{b}{4} < w < \frac{b}{4}$ on its corresponding slip plane [129]. Currently, precise measurement of core width is difficult because individual atom coordinates can not be precisely determined via digitization. The main problems are non-uniform illumination and irregular atom images. The core width of the dislocation shown in figure 55a is visually smaller than any of the other cores displayed in this chapter; the (010) planes are severely distorted in the narrow region ($-2a_o$~$+2a_o$) (see fig. 55b). Abrupt changes of orientation of (010) planes result in high stress concentrations in local areas and strongly scatters incoming electrons, resulting in darker contrast.

In addition to climb dissociated cores, a different type of core configuration is also observed in Co-52Al. The core structure shown in figure 56a is neither simply climb dissociated nor glide dissociated. Separation between the extra half plane of Cobalt atoms and Aluminum atoms is three atom spacings in the [010] direction and two atom spacings in the [001] direction. This combination of glide dissociation and climb dislocation is referred to as mixed dissociation. Movement of a dislocation with a mixed core structure needs a larger driving force than that required for either pure glide dissociation or pure

climb dissociation. Observing the core in the side view (fig. 56b), the slip planes are found to be discontinuous. Corresponding to points "E" and "F", extra half planes are observed in the [010] direction. Since the two extra half planes have opposite sign, no net displacement is produced. Figure 57 is the schematic drawing of the dislocation dissociation. This kind of core is unusual and its relationship to deformation remains unclear. This core may be immobile.

Summary:

The previous sections compared and discussed the core structures of <010> edge dislocations investigated in the various compositions of CoAl. Generally speaking, dislocations in stoichiometric Co-50Al have the simplest core structure, while non-stoichiometric compositions Co-48Al and Co-52Al introduce more complicated core configurations. Climb dissociation of dislocation cores is found in both Co-48Al and Co-52Al. Mixed dissociation of [010] cores is observed in Co-52Al. The non planar nature of these cores retards activation and/or movement of <100> dislocations. Since <100> edge dislocations dominate the high temperature deformation in Co-Al alloys, these core structure play the key role in controlling the mechanical behavior of these materials.

As seen in the HREM micrographs, the appearance of the dislocation core images is affected by various electron optic and specimen conditions, such as defocus value, foil thickness, specimen tilt, astigmatism, spherical aberration and beam damage. Additionally, the core images presented are [100] projections of real crystal defects. In other words, different dislocations, such as <110>, could appear as those observed. Hence, computer simulation of these cores must be perfomed to accurately qualify the HREM observations.

3.4 HREM Image Simulation Of Core Structures

A critical issue in HREM is how to interpret the experimental images. It is well established that images can be misleading, i.e. they may not be readily interpretable in a simple fashion. Thus it is necessary to compare experimental images with calculated images in order to interpret the results. All of the simulated images in the following sections are based on EAM models from Farkas and calculated by the multislice method using the full non-linear image calculation of Stalemann's EMS software.

3.4.1 Simulation of core structures for Co-Al system

3.4.1.1 <010>{001} edge dislocation

For the binary system Co-Al, only <100> edge dislocations have been modeled. Figure 57(a) shows a typical image simulation of a <100>{001} edge dislocation core. This core has a compact structure: it is neither dissociated nor decomposed. Two extra half planes (one Co and the other Al) terminate at the core center. Using the "*co*" subroutine of EMS, the atom positions (Al small dots and Co large dots) of the supercell have been superimposed onto the HREM image simulation (fig. 57b). The extra aluminium half plane extends lower than the extra nickel half plane by an amount of $\frac{\sqrt{3}}{2}$ of the lattice parameter. It should also be possible to construct a core in which the Co half plane extends lower. The lattice distortion parallel to the slip plane is more significant than perpendicular to Burgers vector. Viewing in the <011> directions, single extra half planes and corresponding lattice distortion are observed. The two single half planes in the two <011> directions terminate at the point which coincides with the bottom of the two extra

half planes in the front view ([100] direction). This feature illustrates the compact nature of this core. Figure 57 visually match well with the experimental observations and characterize the main features of the core structure of the [010](001) edge dislocations (fig. 49).

Because the HREM image characteristics can be affected by factors such as foil thickness, defocus and other microscope and sample parameters, it is necessary to examine the effect of these variables on the simulations. These effects are illustrated in the following paragraphs.

Figure 58 shows a through focal series of image simulations for the <100>{001} edge dislocation in a Co-50Al crystal 3.3 nm in thickness. The defocus ranges from -40 nm to -95 nm with steps of 5 nm. The details of the image change significantly as the defocus changes. The image contrast is too weak and difficult to see at df=-40 nm. From df=-50 nm to df=-55 nm, both atom types display essentually the same brightness, while from -65 nm to -80 nm, one atom type is weaker than the other. The approximate atom positions are represented by white or bright contrast (white atom images) for defocus values imaging from -60 nm to -80 nm. Conversely, for defocus values less than -85 nm and greater than -60 nm, the atoms are dark, and the tunnels between the atom columns appear as bright apots (white tunnel images). That is, there are contrast reversals at -60 nm and -85 nm for this thickness. These reversals will occur at different defocus values for different specimen thickness.

Figure 59 shows the effect of thickness on image details. The crystal thickness increases from 1.1 nm by 1.1 nm steps with a constant defocus value of -70 nm. In very thin areas, both Co atoms and Al atoms are clearly observed (white atom image), with Al

atoms displaying lower intensity than Co atoms. As the thickness increases, the intensity of the Al atom columns become weaker. This is to say, a regular lattice image becomes a superlattice image as the thickness increases. In the present case, a bcc or bcc-based B2 structure image degenerates into a simple cubic lattice structure image. Thus, the image analysis can be misleading if thickness effects are ignored. To further complicate the analysis, some Al atoms in the central core region become visible again as the thickness nears 10.2 nm (this figure is not included in figure 59). Therefore, both experiment and simulation should avoid thick crystals. In addition, the thickness effect varies with defocus value. Under the condition df=-60 nm (figure 60), two Co atoms at the dislocation center display lower intensities than the surrounding Co atoms in the thin crystal, and these atoms are completely out of contrast for thicknesses greater than 3.3 nm, forming a dark hole.

Temperature also affects HREM and must be considered when simulating images. The Debye-Waller factor is a measurement of the thermal vibration of an atom and is a function of temperature. A large Debye-Waller factor means that atoms strongly scatter the incoming electrons and thus affects the images. Reference [111] provides the Debye-Waller factors for all the elements at three specific temperatures. The D-W factors of Co, Ni, Fe and Al are listed in table 10.

Based on table 10, aluminium atoms have the largest Debye-Waller factor (nearly 2 times as large as the other elements). This may explain why the Al atoms look dim to some degree in simulations and in experimental observations. The Debye-Waller factors increase with temperature increases. Temperature effect was studied through simulation using different D-W factors and the results are presented in fig. 61.

The image intensity of Al atoms is too weak to be seen in fig.61(c), which corresponds to the temperature at which the microscopy was performed. This is contrary to the experimental images which clearly resolve the Al atom columns in the microscope. It seems that the temperature effect on experimental images is not as large as predicted by simulation. That is, the experimental images reveals clearly resolved Al and Co columns at room temperature.

3.4.1.2 <010>{01$\bar{1}$} edge dislocation

The [100](01$\bar{1}$) edge dislocation simulated in the present work is coordinated in a [100]-[01$\bar{1}$]-[011] system (fig. 62). The line direction of this dislocation is [011] and the slip plane is (01$\bar{1}$). Since the so-defined lattice has a repeat length of 0.4054 nm in the multi-slice direction (Z direction), there is a potential that a large slice thickness may introduce errors in FFT calculations. Stalemann recommends [112] a slice thickness of 0.2 nm for light atoms, while a slice of thickness of 0.05 nm is preferable for heavy atoms (i.e. periodic table mass). The supercell with the [100](01$\bar{1}$) dislocation was cut into two sub-slices (fig. 63). The wave functions were then calculated using the multislice program plus a script program that alternatively serves individual subslice data files one at a time to the multislice program. A typical simulation of an [100](01$\bar{1}$) core is presented in figure 64. The core only shows its superlattice structure because the projected distance between Co and Al atoms in the <011> direction is smaller than the microscope resolution. Therefore, experimental studies of [100](01$\bar{1}$) cores are limited by current microscope technology.

3.4.2 Simulation of core structures in the Ni-Al system

3.4.2.1 <010>{001} edge dislocations

Figure 65a shows a simulated core structure of an [010](001) edge dislocation in Ni-50Al. This simulation matches the main features of the experimental observation of Crimp, Tonn and Zhang [116] for the [010](001) core structure. However, the significant lattice distortion in the direction of Burgers vector on the experimental image [116] is not reflected in the simulation. This indicates that many factors that may affect the core structure, such as surface effects, may not be accounted for in the simulations. On the other hand, the core simulation is visually identical to the simulation of the Co-50Al core with the same Burgers vector. Superposition of the CoAl supercell (dots) onto the NiAl simulation shows a perfect match (fig. 65b). Since the mechanical properties are significantly different between CoAl and NiAl and the observed experimental core structures are also dissimilar to each other, it appears that the potentials or modelling techniques used do not satisfactorily reflect the differences in atomic bonding beween either Co-Al atoms or Ni-Al atoms.

Off-stoichiometric compositions can be formed by either anti-site defects (for example nickel atoms replace aluminum atoms, or visa versa) or vacancies. The anti-site situations can be further divided: local chemical composition change (one atom type replace the other at the core center) or random anti-sites (atom type replacement on random sites) . The following simulations test these conditions individually.

A model core structure with a local chemical change Ni-anti site defect is shown in figure 66a. To reveal the atom arrangement at different layers in one unit cell, a viewing direction of [1 1 20] has been chosen. This is a slight deviation from [001] direction. An

aluminum atom is replaced in the lower level by a nickel atom and therefore the local chemical composition is Ni-rich. In a multislice image simulation, the Ni-anti-site defect will be repeated in each slice, resulting in Ni enrichment along the entire dislocation line. A simulated HREM image corresponding to this model is displayed in figure 66b. The core structure has the same features as the core in figure 66a though the aluminum column with nickel substitutions appears brighter than the other columns. Therefore except slight intensity changes, the local atom replacement does not affect the core configuration to any noticeable degree. Neither do Al-rich anti-site defects (fig. 67a). The possibility of an Al atom exchanging position with a Ni atom at the core is illustrated in figure 68. Although the local chemical composition does not change, the bonding condition is changed locally. However, the element exchange does not affect the core configuration to any noticeable degree.

It is well known that vacancies can significantly affect dislocation behavior in crystals. The situation considered in figure 69(a) is that two nickel atoms are missing leaving two vacancies instead. This results in an Al-rich structure. The corresponding image simulation is shown in figure 69(b). Right in the core center, the image contrast at the two nickel atom positions is less than that at the regular nickel atom positions. This is because there is only one nickel layer at these positions and electrons are strongly scattered by the non-periodical potential field around the two vacancies. Except for the local contrast change, the right-in-core vacancies do not change the core structure and lattice distortion.

In non-stoichiometric alloys, it may be a more energetically favorable situation if the atoms being substituted for are not limited to the core center but occur randomly.

Ni48Al can be regarded as 2% Al randomly replaced by Ni (fig. 70). To describe the replacement in three-dimensional space, a large supercell file was constructed. In the z-direction, there are five layers and the atom arrangement on each layer is displayed in figures 70(a) through figure 70(e). Each layer defines one supercell and the stacking of supercells were processed by the multislice program. The simulation result (fig. 70f) indicates no significant changes in core structure occur. Figure 71 shows the result from another random distribution of excess Ni atoms. Figure 72 shows simulations for Ni-52Al with two differenct distributions of excess aluminum atoms. Again, no significant changes in core structure are revealed. Similarly, atom exchange of Ni and Al atoms at random positions does not affect the core structure of a dislocation (fig. 73). None of the calculations for off-stoichiometric compositions are able to explain the fact that significant changes in core structure with composition changes are observed experimently. Crimp, Tonn and Zhang [116] found significant distotions both parallel and perpendicular to Burgers vector in Ni-48Al. Additionally, the results presented in the present study show significant core changes with stoichiometry in Co-Al alloys. It may be that not only the point defect location changes, but also interatomic potential changes due to vacancy or anti-site defects need to be considered in model construction of core structures.

3.4.2.2 Simulalted core structures of <111> screw dislocations

<111> screw dislocations exist in B2 CoAl and NiAl under the certain conditions [113, 114]. Core structures of these <111> screw dislocations may affect the deformation behavior of these alloys. However, experimental observation of core structures of the screw dislocations is very difficult. Because the Burgers vector of a screw dislocation is

through the local image contrast changes. Therefore, computer simulation is necessary to interprete the HREM images of screw dislocation cores. For these core simulations, various theoretical models are used to generate the core images via the EMS software until a good agreement between the simulated and experimental images are reached.

Figure 74 is a HREM micrograph of a <111> dislocation in Ni-50Al provided by Sun [121]. The dislocation was imaged along its <111> line direction, resulting in a projected hexagonal lattice image pattern. Careful examination reveals that one particular bright spot is significantly brighter than the surrounding atoms and shifted slightly from the periodic position. This is where the dislocation core is suspected to be.

A screw dislocation core was simulated using a data file provided by Farkas et al.[122]. These atomic positions were calculated from a core model of a straight <111> screw dislocation. Even though the atom positions in the data file (fig. 75a) match well with those in the experimental image (fig. 74), the brightness contrast between the central spot and surrounding atoms, along with the spot shift, in the observed core structure are not seen in the simulation (fig. 75b). This indicates that the model of straight <111> screw dislocation is not able to describle the true configuration of the screw dislocation core.

Ideally for HREM imaging, dislocations will be straight, normal to the thin foil, and oriented along a low index zone axes. However, in practice dislocations may not remain normal to the foil because non-screw dislocations can often lower their energies by taking up a more screw like orientation. This is balanced by the minimization in dislocation line length (and energy) offered by remaining normal to the foil. A pure screw dislocation in a thin foil does not tend to move from the screw orientation. However, beause of

tion line length (and energy) offered by remaining normal to the foil. A pure screw dislocation in a thin foil does not tend to move from the screw orientation. However, beause of the unbalanced shear stress on surface, there exists a torque about the dislocation line. A screw dislocation is therefore twisted in a thin foil (fig. 76). This twist displacement was calculated by Eshelby [123] and verified by Tunstall et al. [124]. Because the dislocation configuration in bulk material may become more complicated when it is located in a thin foil, it may be useful to consider the so-called Eshelby twist effect when the core structure of a screw dislocation is simulated.

To simulate the twist imposed on the <111> screw dislocation core structure in NiAl, the dislocation was sliced into nine slabs of constant thickness. In each slab, the dislocation twist was simplified to a straight line and the data file of Farkas et al. was rotated. These data files which were based on the straight dislocation were then used to produce supercells. The twist displacement was also added into the displacement field of the dislocation through a modified "*convert*" program. The transmission function was calculated continuouly via combination of "*MS* (option c)" and "*autorun*" programs.

The Eshelby twist effect on the atom arrangement in the core region is illustrated in figure 77(a) for a left hand screw dislocation. The central atom is not displaced, while the rest of atoms are shifted in the circumferential direction. Figure 77(b) is a corresponding HREM simulation of the left hand screw dislocation with an Eshelby twist. Figure 78 and 79 show the focal series and thickness series. Simulations at 2.32 nm thickness display the effect of defocus value on images (fig. 78). The white atom images are observed only when are defocus values 70 nm and 80 nm, with 70 nm defocus resulting in the best defined core structure. The thickness is also important. If the foil is too thin (such as 0.58

nm), the Eshelby twist feature is not obvious, whereas it is easily recognized when the thickness is greater than 2.03 nm (fig. 79). The most apparent feature of these images are a higher intensity spot that is located in the center. This spot should represent the central atom in fig. 74.

Simulations of the <111> screw dislocation with Eshelby twist gives better interpretation of the experimental HREM image of this dislocation. However, Eshelby twist can not explain the slight displacement of two atom columns away from their lattice positions in the core center. This indicates that in addition to Eshelby twist, there may exist other factors influencing core configurations of <111> screw dislocations, such as local strain field distribution and relaxation at the free surfaces.

3.4.3 Simulation of core structures in Fe-Al system

FeAl exhibits the highest ductility and lowest room temperature strength of the B2 aluminides considered in this study (CoAl, NiAl and FeAl). In many regards, the mechanical properties of FeAl are more similar to NiAl than CoAl, while the dislocations activated in deformation are more similar between FeAl and CoAl, i.e., <111> dislocations are activated in low temperature deformation while <100> [125] dislocations are activated in high temperature deformation. <100> dislocations are more easily activated in FeAl than the other two alloys, even when the deformation axis is near <100>. This means that the CRSS of <100> dislocations is very low in Fe-Al. This characteristic of Fe-Al may be expected to be reflected in the core structures of <100> dislocations.

3.4.3.1 <010>{001} edge dislocations

Simulated [010](001) cores in FeAl visually have the same appearance as those in CoAl or NiAl. A typical example is shown in figure 80. For FeAl, two extra half planes in the [001] viewing direction and a Burger's circuit on (001) plane results in a [010] Burgers vector for the dislocation with a line direction of [100]. The glide plane is therefore the (001) plane. However, in the [022] or [02$\bar{2}$] directions, single extra half planes can be observed. The single extra half plane AB terminates at atom B (aluminum) and plane CD at atom D (iron) (see figure 80b). These two end atoms are also the bottom atoms of two extra half planes in the [100] viewing direction. This coincidence reflects the compact nature of this core. These simulations match the experimental images of [010](001) core structures in FeAl [117]. Unfortunately, core structure calculations for off-stoichiometric compositions are not available. In Fe-40Al, an apparent dissociation is observed experimentally [117] and more work on core models is needed to understand these differences.

3.4.3.2 <010>{101} edge dislocations

Since the minimum projected atom spacing in the [$\bar{1}$01] direction (distance between corner atoms and central atoms in the B2 unit cell) is smaller than the resolution limit of the instrument used in this study, no experimental images are available. The projected profile from the data file provided by Farkas et al. [122] was used for analysis instead. As shown in figure 81, the [010](01$\bar{1}$) core is dissociated along the (01$\bar{1}$) slip plane. The superpartial dislocations are located at position A and B respectively with an APB in between. An extra Fe half plane is separated from an extra Al half plane by distance of approximately 4 atom spacings. The Fe planes in the upper part of the core

(above the slip plane) align with the Al atom columns in the lower part of the core. Burgers circuits constructed around two extra half planes reveal the dislocation is dissociated into two 1/2[100] dislocations. It should be recalled however that only edge components of dislocations are revealed using HREM. Likewise, figure 81, being a two dimensional representation, only illustrates the edge components and does not reflect screw components along the line direction (into the image) of the dislocation. In fact, the EAM simulations of Farkas et al reveal that the atoms along the APB are in fact displaced 1/2[011] relative to each other. That is, each superpartial dislocation has a 1/2[011] screw component. The resulting dissociation scheme is

$$\frac{1}{2}[010] = \frac{1}{2}[\bar{1}11] + APB + \frac{1}{2}[11\bar{1}] \qquad \text{.....(36)}$$

Such a scheme is reasonable as 1/2[010] is not an atom-to-atom traslation, and consequently is expected to be a high energy position, while 1/2<111> is in fact an atom to atom translation and results in a stable APB. However, according to linear elasticity and Frank's rule, such a dissociation would not be energetically favorable. Thus, non-linear and/or anisotropic elasticity effects may be responsible for the dissociation. It should also be noted that HREM evidence for a similar dissociation mechanism has been observed for climb dissociated <010>{110} dislocations in NiAl [88] and FeAl [117].

In CoAl, simulations indicate that the core was compact with no evidence of glide or climb dissociation. The reason there is no dissociation of this <100>{011} dislocation in CoAl may be the higher APB in CoAl relative to FeAl. Evidence for a higher APB energy in CoAl comes from the fact that weak beam microscopy cannot image the superpartials of <111> superdislocations, while in FeAl, the 1/2<111> superpartials can be imaged [86] at least in Fe-rich alloys.

In summary, simulations of core structures of the <010>{001} edge dislocations in B2 aluminides have successfully interpreted the HREM images of dislocations for stoichiometric compositions. However, dissociation of a <010>{001} cores in off-stoichiometric alloys can not be simulated by modelling. The effect of point defects on potentials and modelling procedures may be a key to solving this problem.

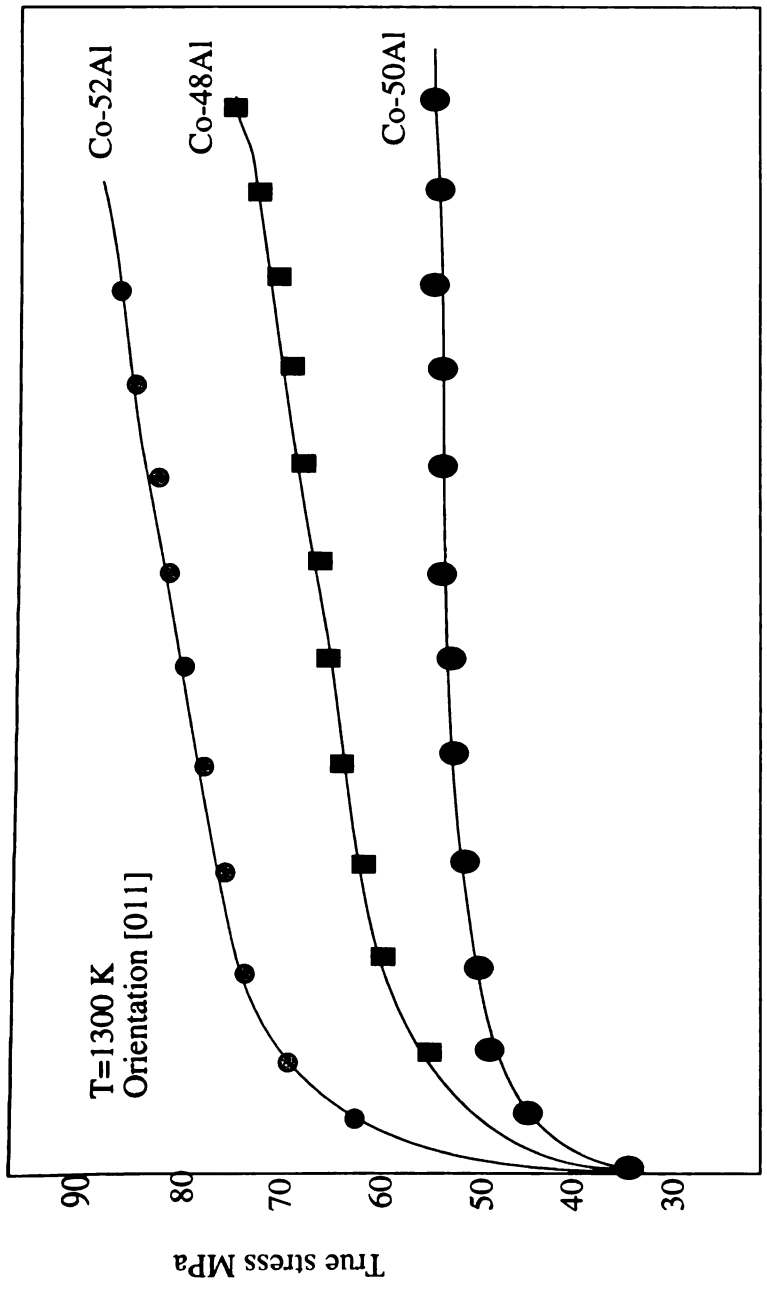

Figure 27 Mechanical behavior of [011] oriented Co-Al deformed at 1300 K. Co-52Al has the highest resistance to deformation and Co-50Al has the lowest resistance to deformation at this temperature.

Figu

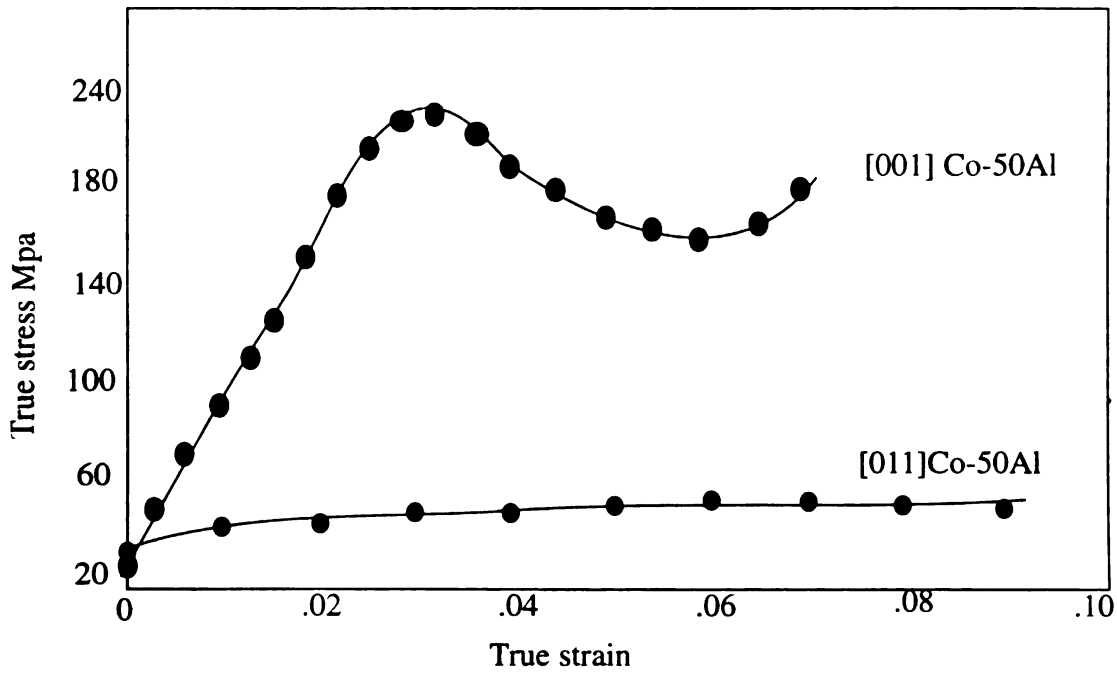

Figure 28 Effect of orientation on mechanical behavior of Co-50Al at T=1300 K. [001] oriented Co-50Al displayed kinking during deformation.

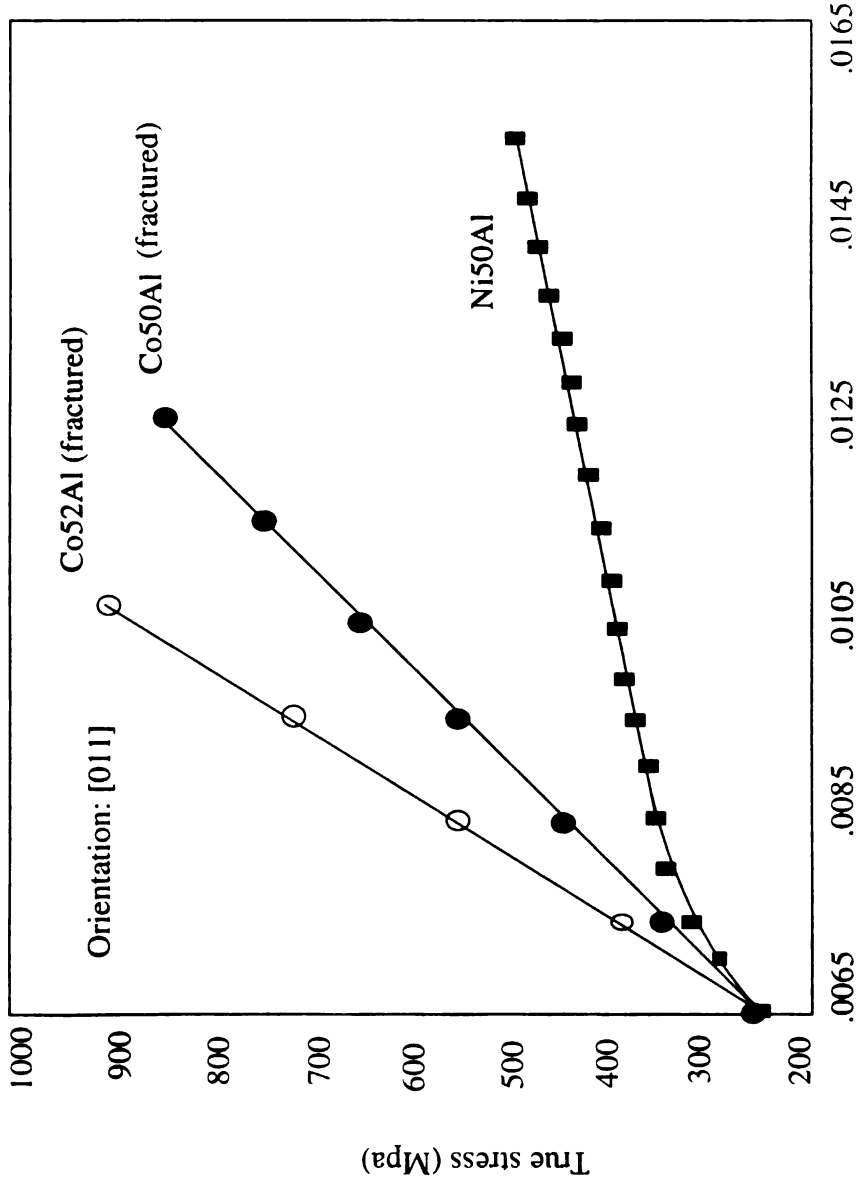

Figure 29 Mechanical behavior of Co-Al and Ni50Al in compression at room temperature. Co-Al appears to be more brittle than Ni-50Al.

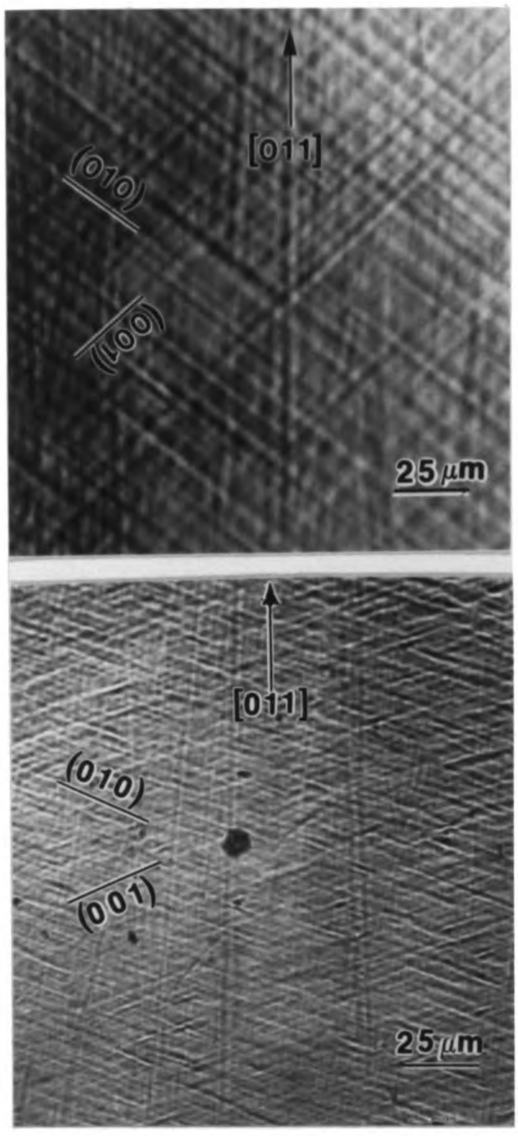

Figure 30 Slip traces on two perpendicular surfaces of Co-50Al. The specimen was oriented in the [011] direction and deformed at 873 K.

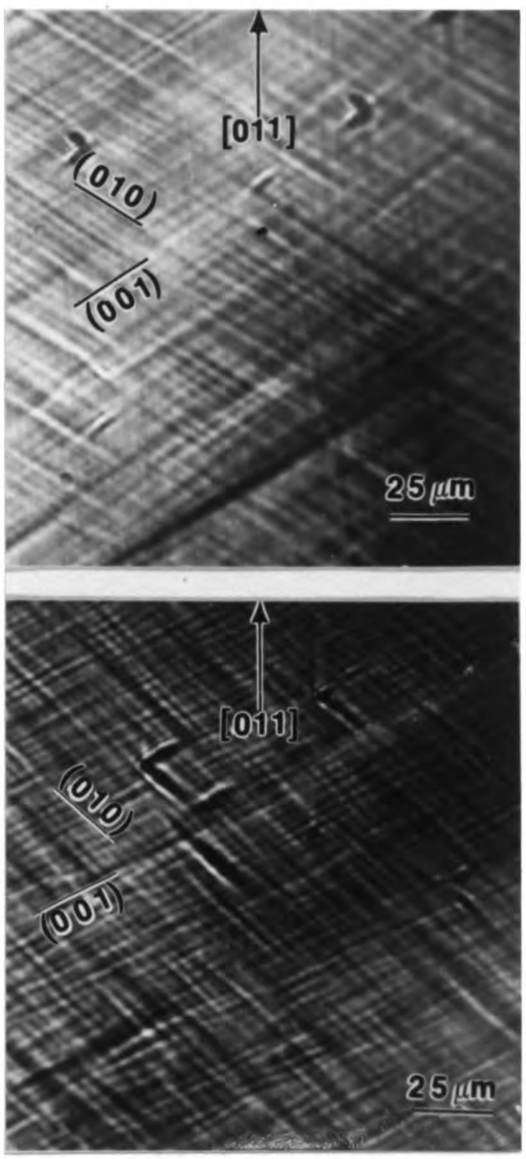

Figure 31 Slip traces on two perpendicular surfaces of Co-48Al. The specimen was oriented in the [011] direction and deformed at 873 K.

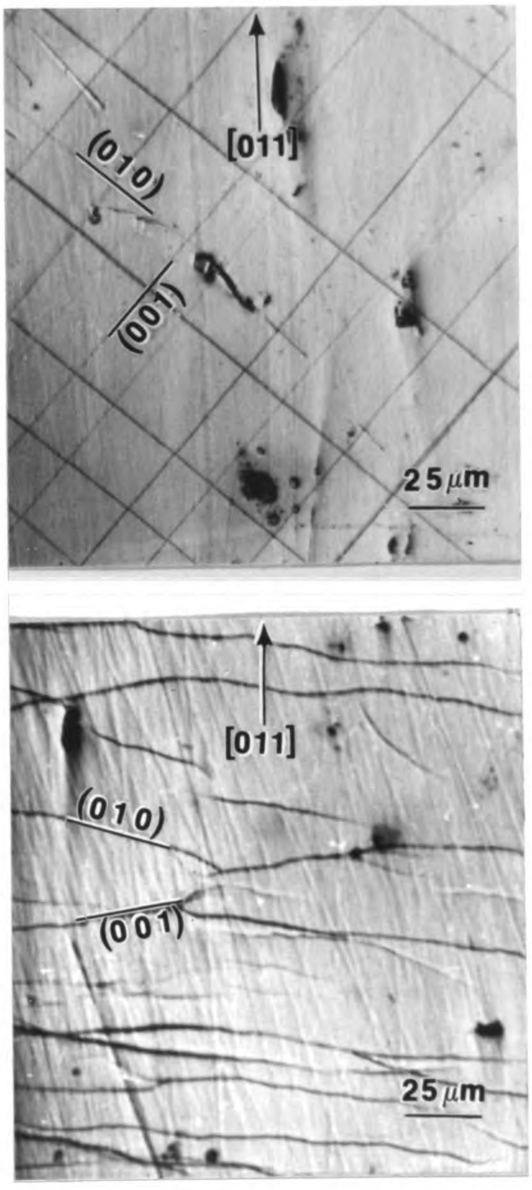

Figure 32 Slip traces on two perpendicular surfaces of Co-52Al. The specimen was oriented in the [011] direction and deformed at 873 K.

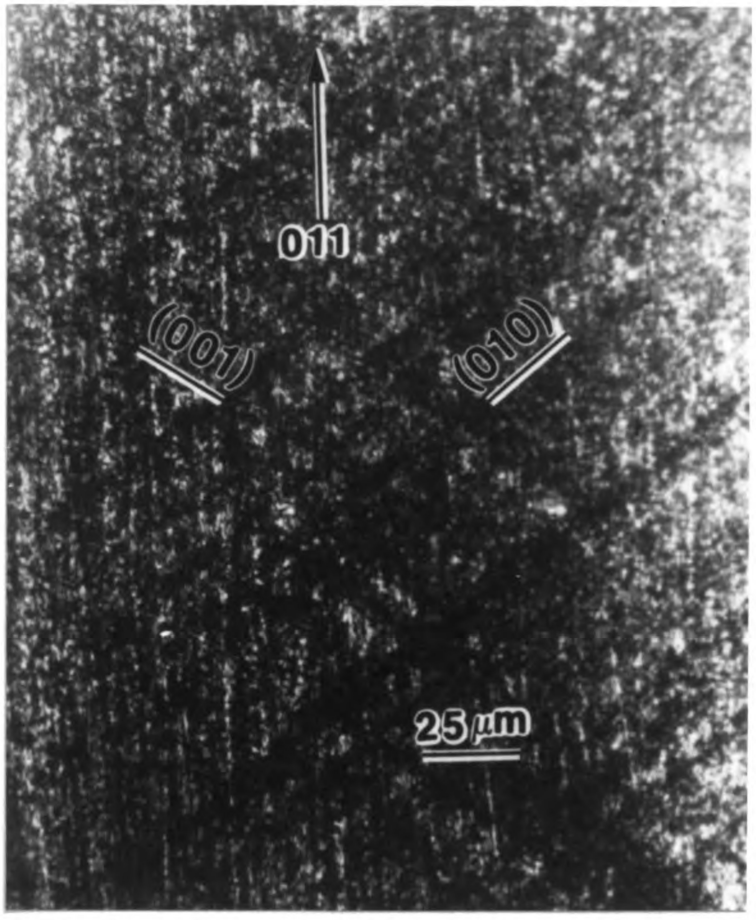

Figure 33 Slip traces on two perpendicular surfaces of Co-50Al. The specimen was oriented in the [001] direction and deformed at 1300 K.

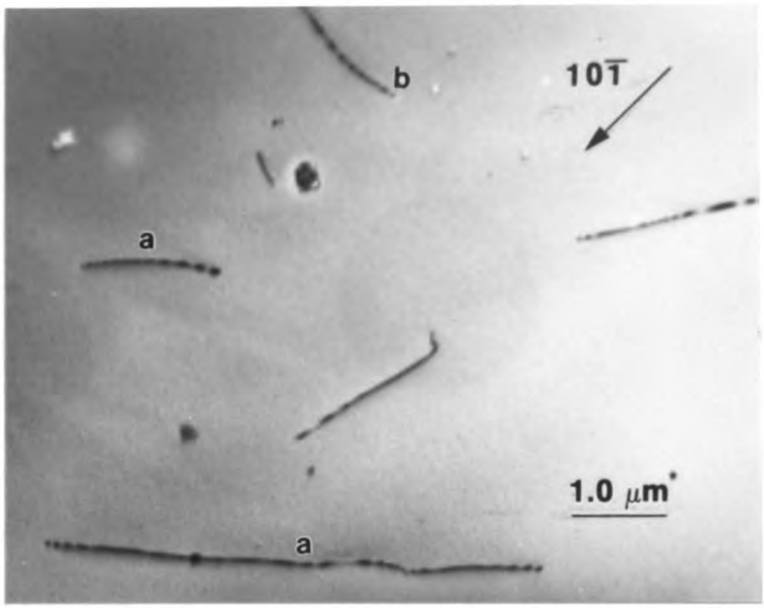

(a)

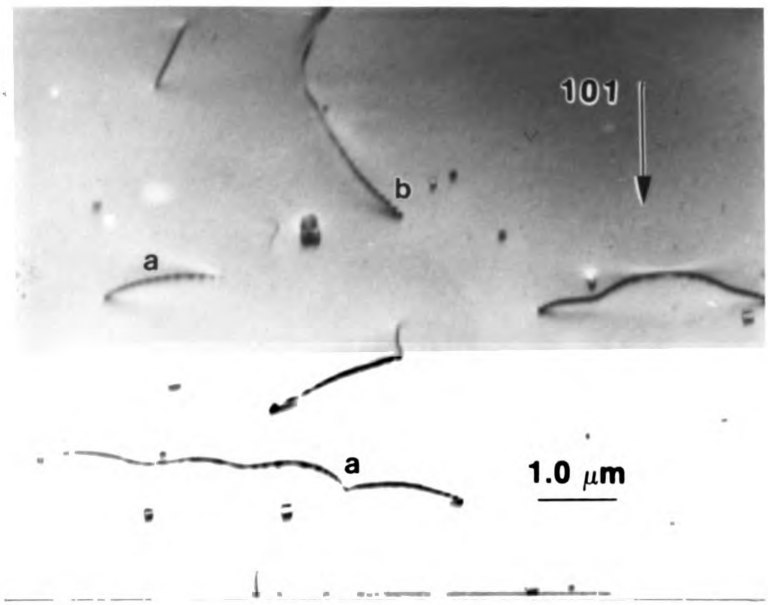

(b)

Figure 34 Analyis of dislocations in as-grown single crystal Co-50Al. There exist two types of dislocations labeled a and b. (a) ($1\bar{1}\bar{1}$) zone, (b) ($\bar{1}0\bar{1}$) zone, (c) ($1\bar{1}1$) zone, (d) (001) zone, (e) (011) zone, (f) (001) zone.

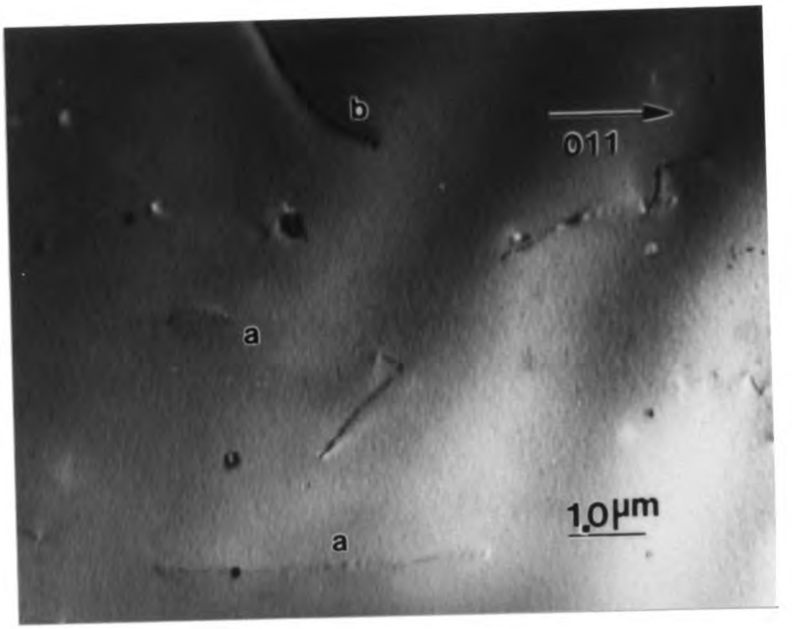

(c)

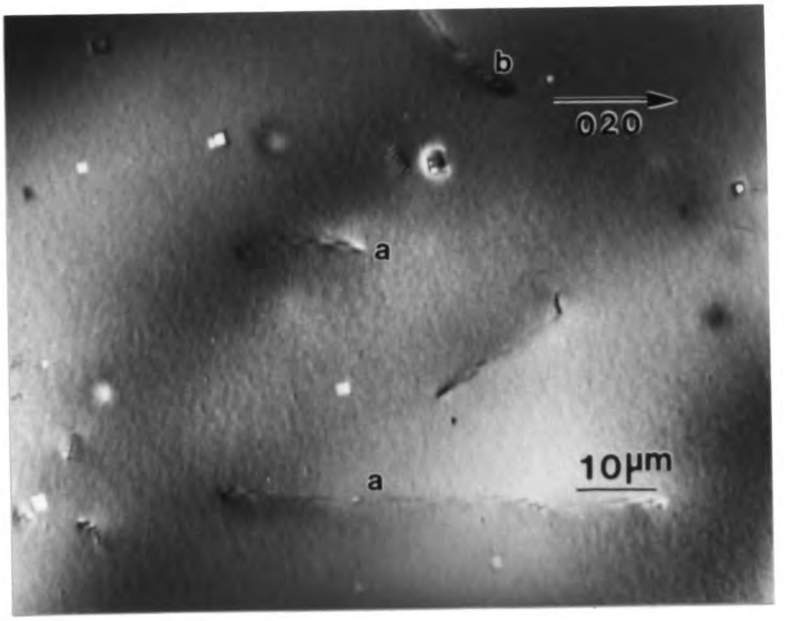

(d)

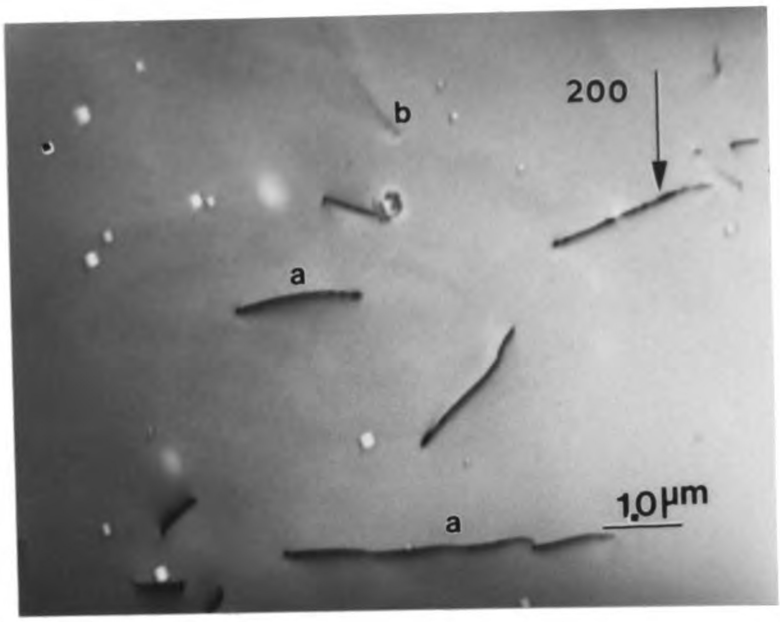

(e)

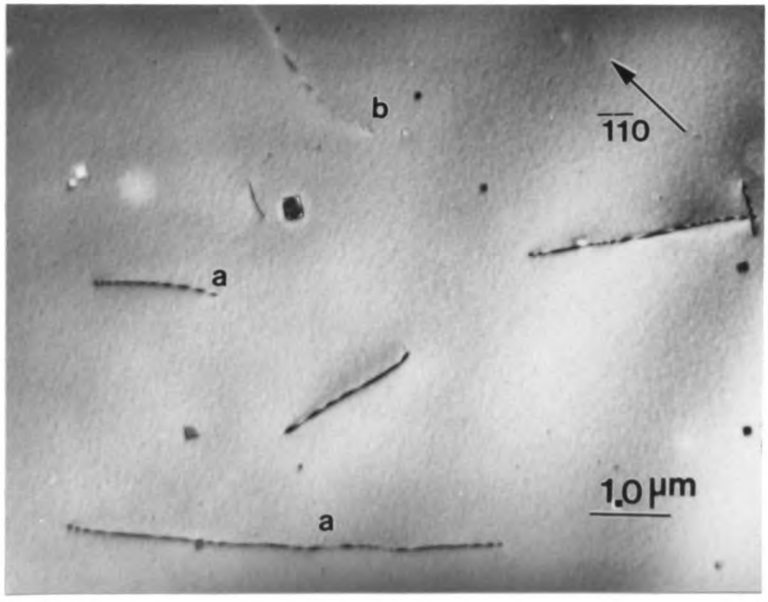

(f)

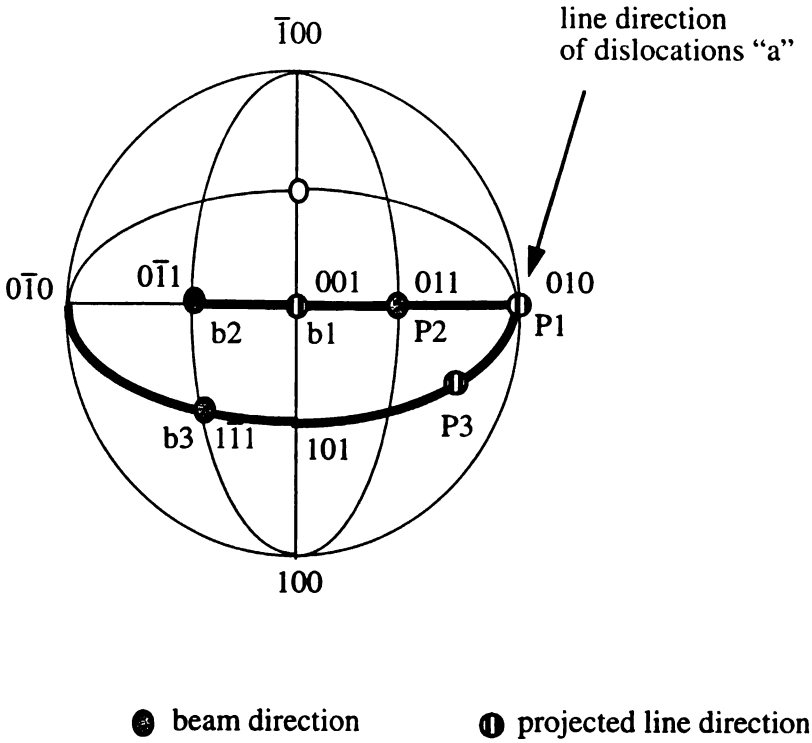

Figurre 35 Dislocation line direction determination by trace analysis for dislocations in fig. 34. Both the beam direction (b_i) and the projected line direction (P_i) are lying on the same great circle. The intersection of two or three great circles give the true line direction of the dislocation.

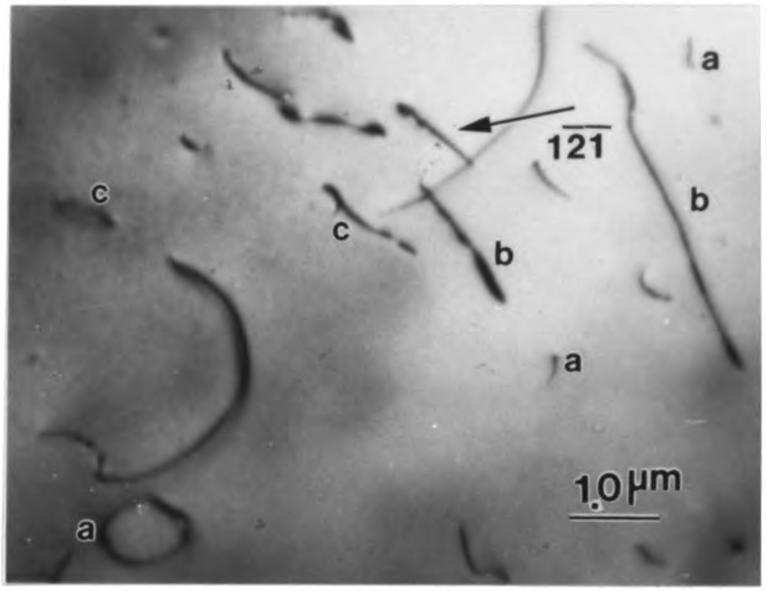

(a)

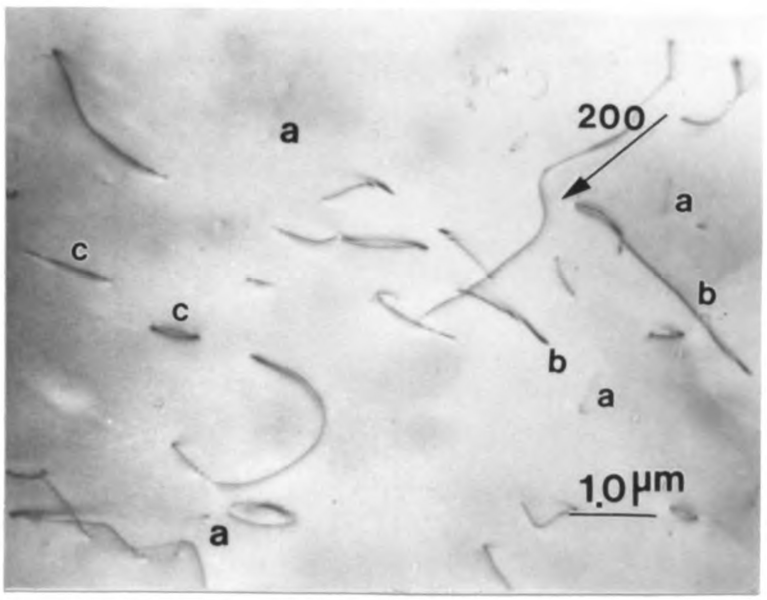

(b)

Figure 36 Dislocation analysis in [123] oriented Co-50Al that was deformed at 1300 K. Three types of dislocations labeled a, b and c were characterized.

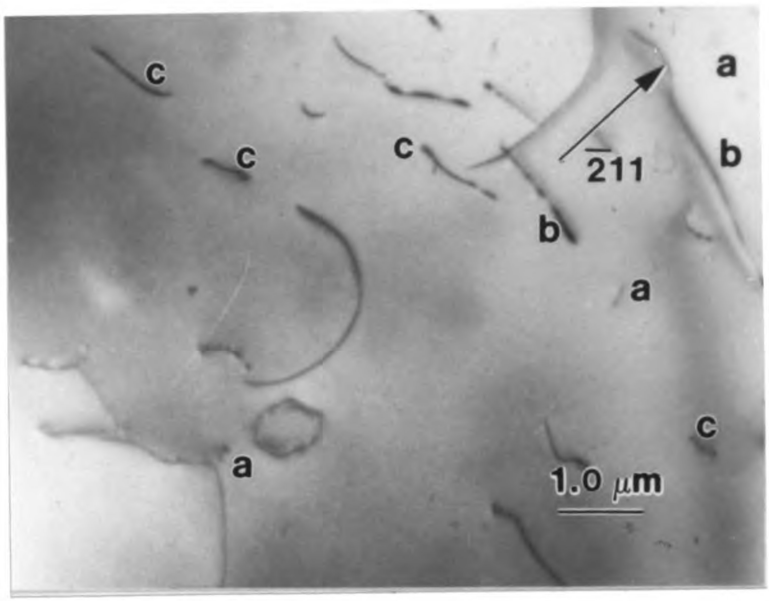

(c)

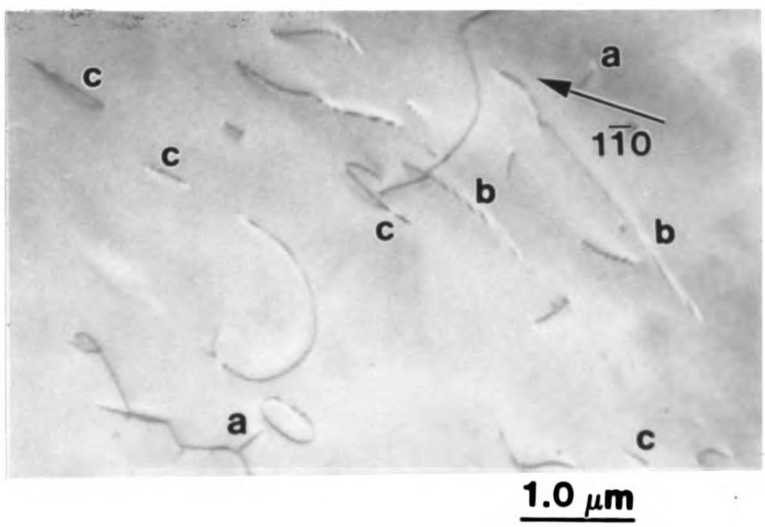

(d)

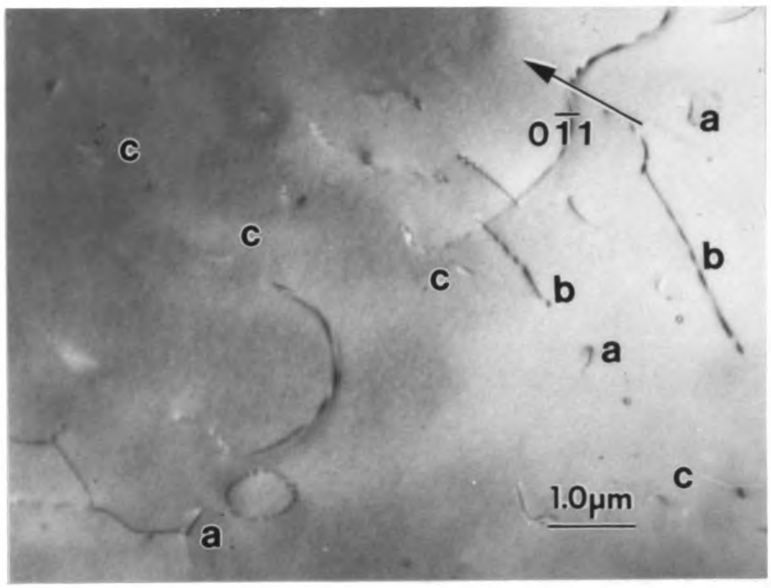

(e)

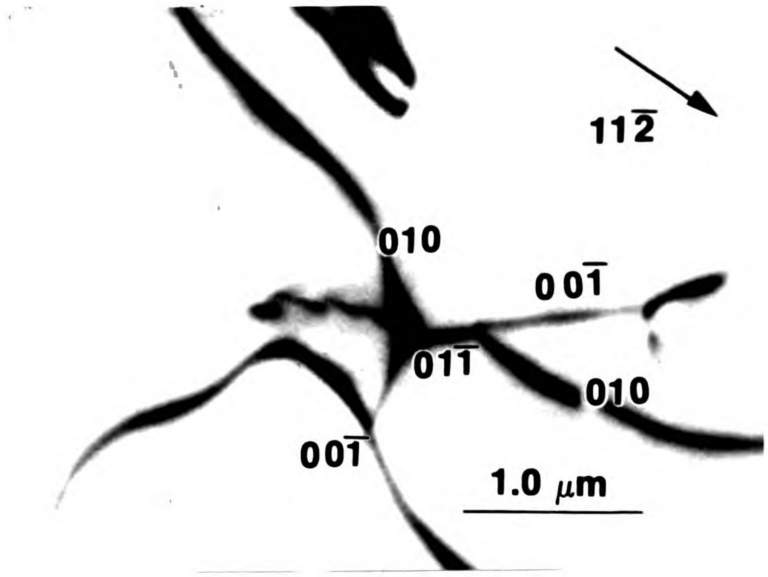

(a)

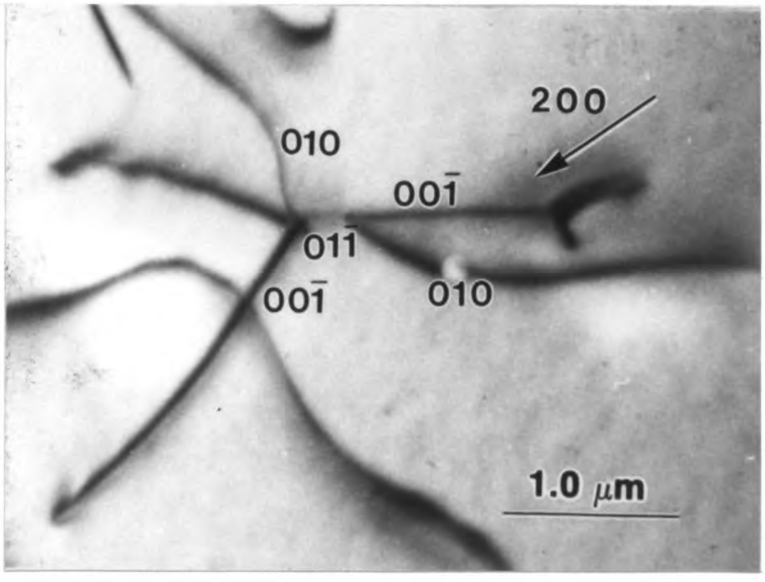

(b)

Figure 37 Dislocation reaction in [123] oriented Co-50Al deformed at 1300 K. Two <100> dislocations form one <110> dislocation.

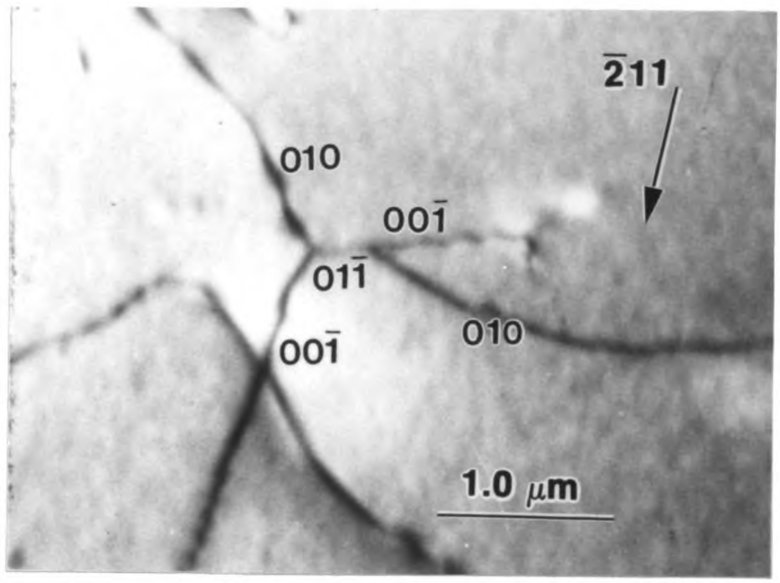

(c)

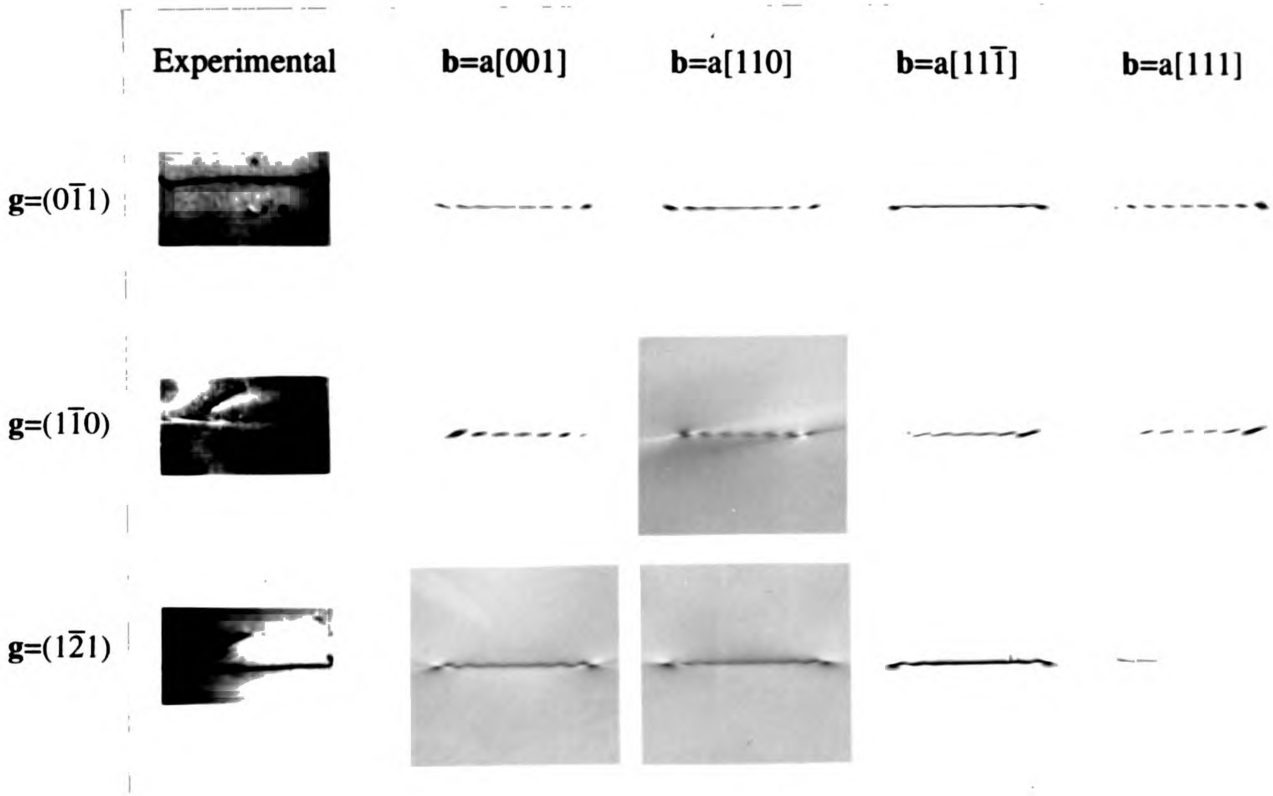

Figure 38 Computer simulation of dislocation labeled "b" in fig. 36. The micrographs were taken at the reflecting conditions **g**=(0$\bar{1}$1), **g**=(1$\bar{1}$0) and **g**=(1$\bar{2}$1). The simulations were performed by varryring the conditions of the **g**-vectors and the Burgers vectors, while the other parameters were kept constant.

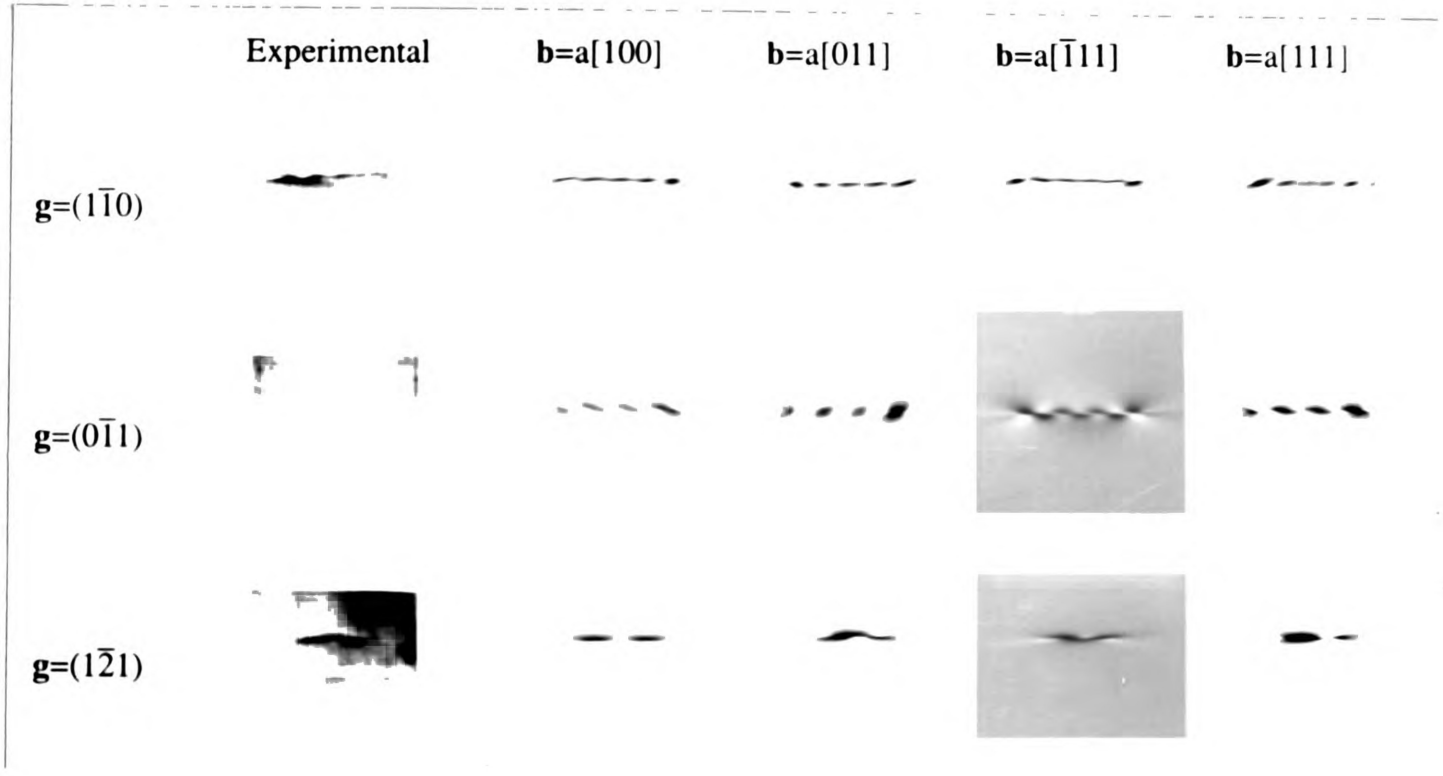

Figure 39 Computer simulation of dislocation labeled "c" in fig. 37. The micrographs were taken at the reflecting conditions **g**=(0$\bar{1}$1), **g**=(1$\bar{1}$0) and **g**=(1$\bar{2}$1). The simulations were performed by varryring the conditions of the **g**-vectors and the Burgers vectors, while the other parameters were kept constant.

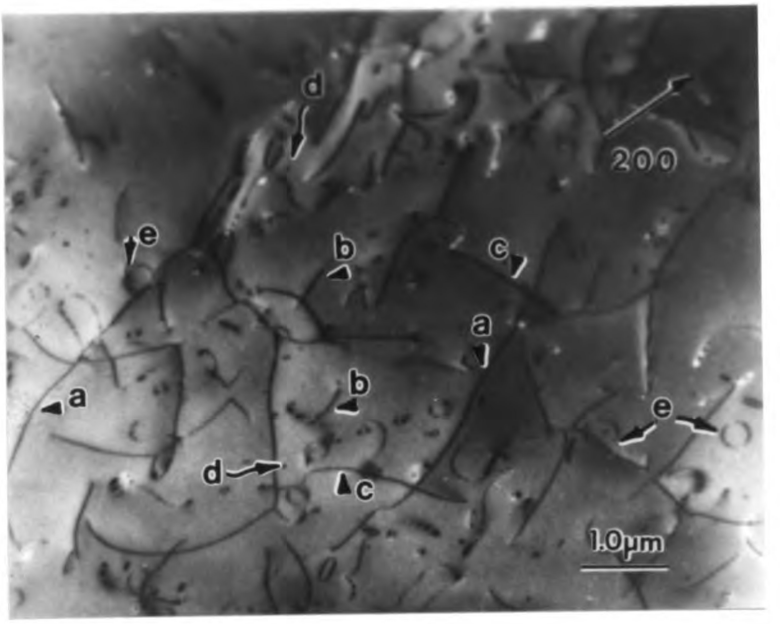

(a)

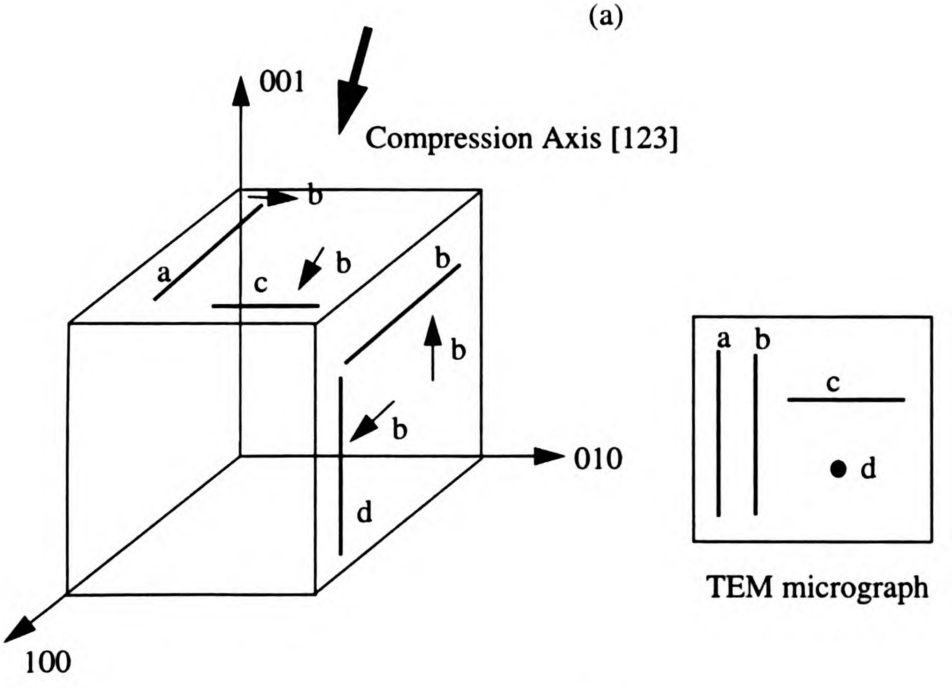

(b)

Figure 40 Dislocations observed in [123] oriented Co-50Al deformed at 1000 K.
(a) Arrangement of dislocations in single crystal compression sample.
(b) Schematic illustration of appearance of dislocation distribution in a (001) foil.

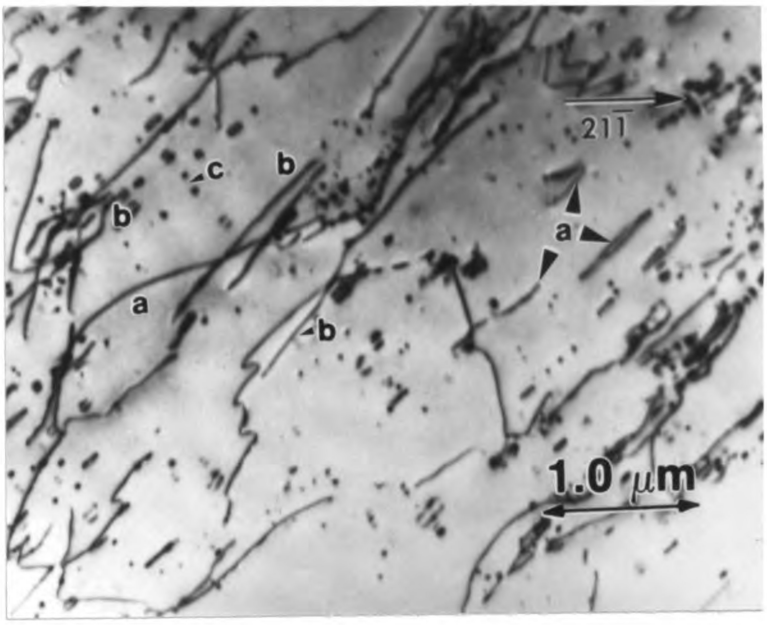

(a)

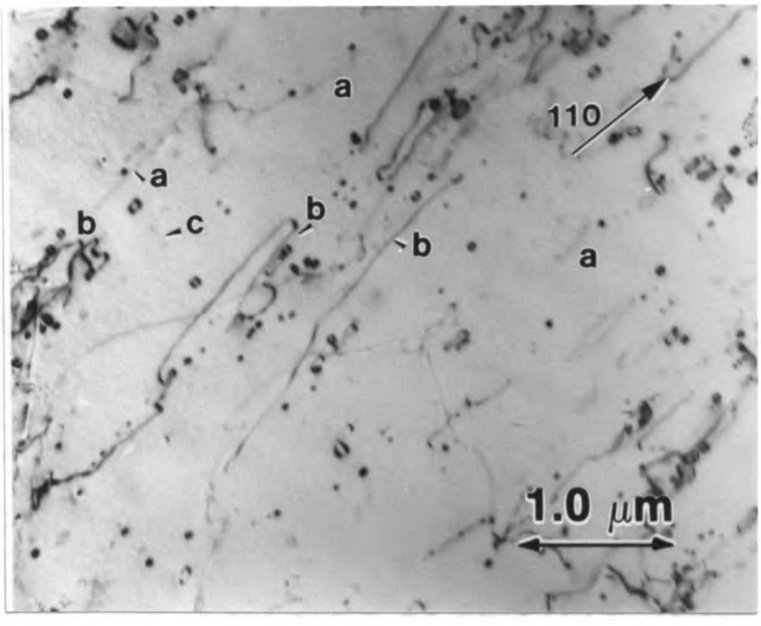

(b)

Figure 41 Dislocation analysis for [011] oriented Co-50Al deformed at 873 K. Inclined dislocations, end-on dislocations and dislocation loops were all observed.

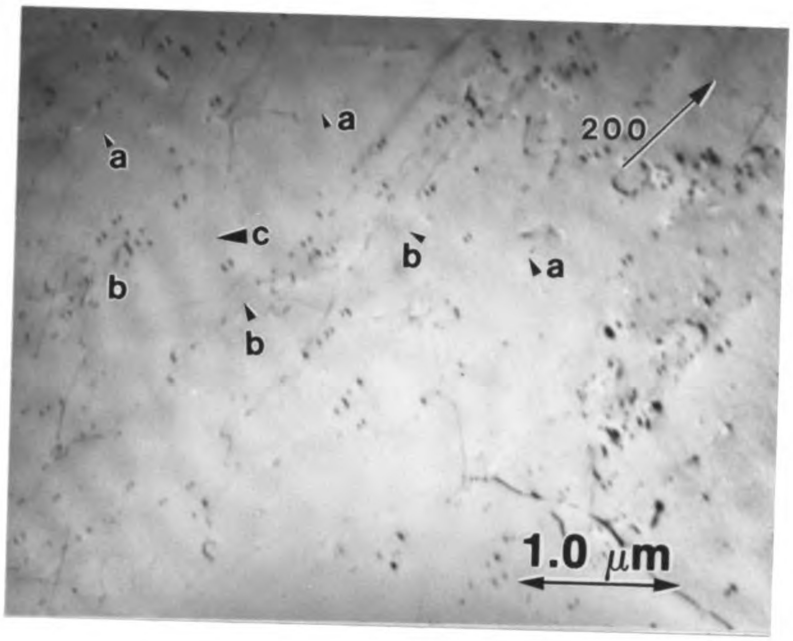

(c)

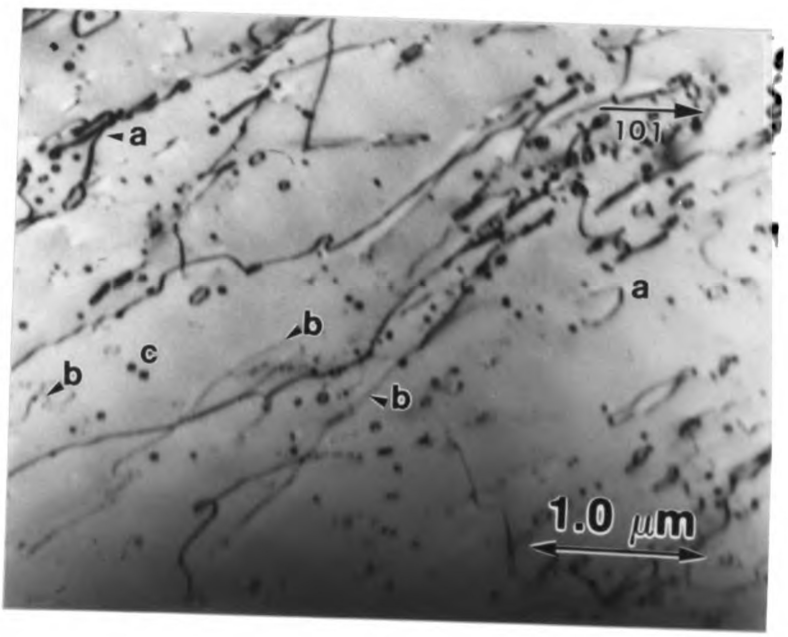

(d)

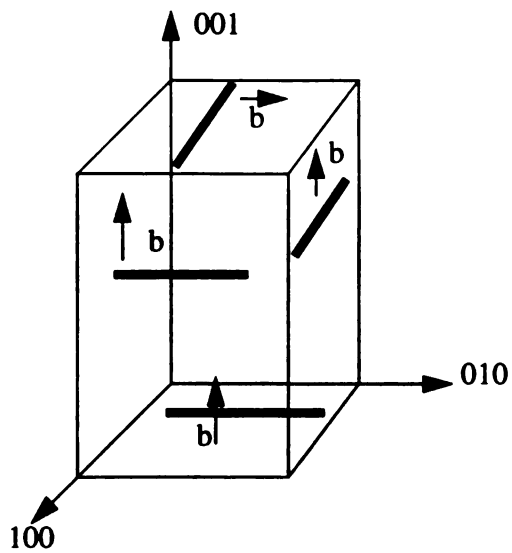

Figure 42 Three dimensional schematic illustration of the distribution of dislocations observed in [011] oriented Co-50Al deformed at 873 K.

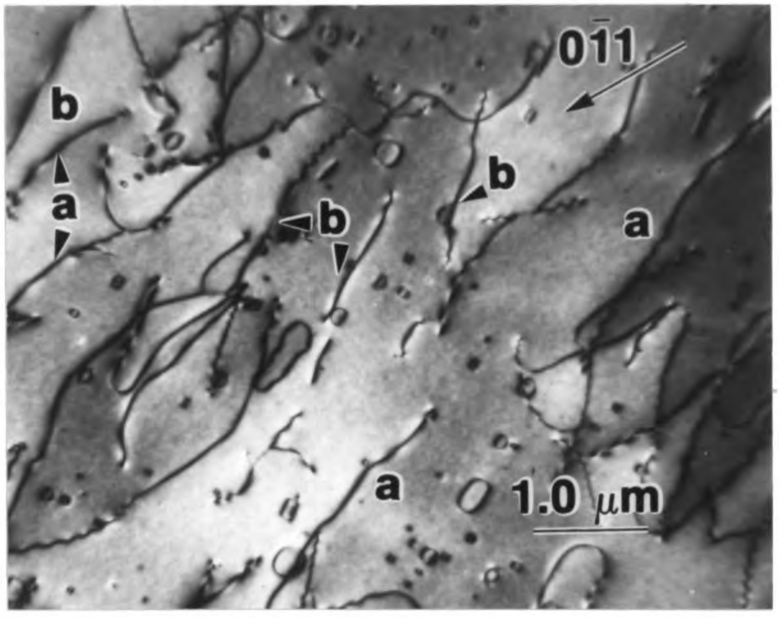

(a)

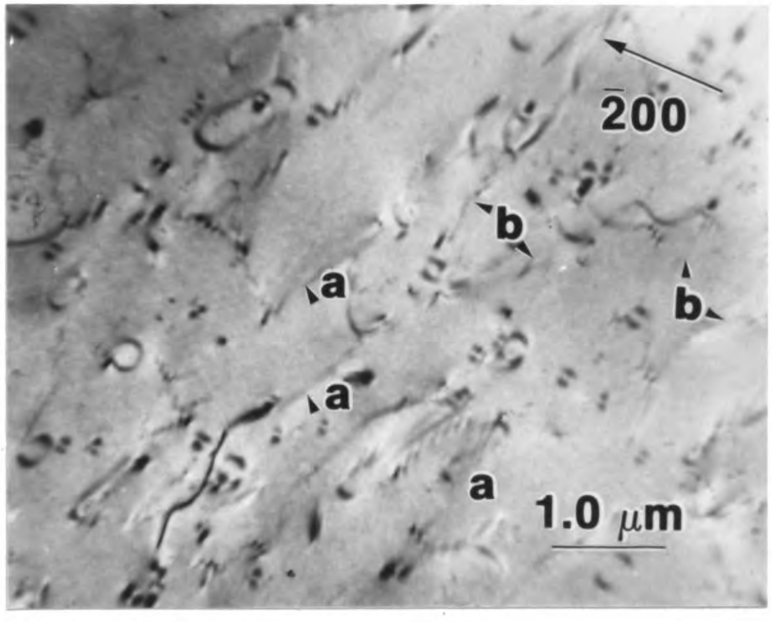

(b)

Figure 43 Dislocation analysis for [011] Co-52Al deformed at 873 K. Inclined dislocations, end-on dislocations and dislocation loops were observed.

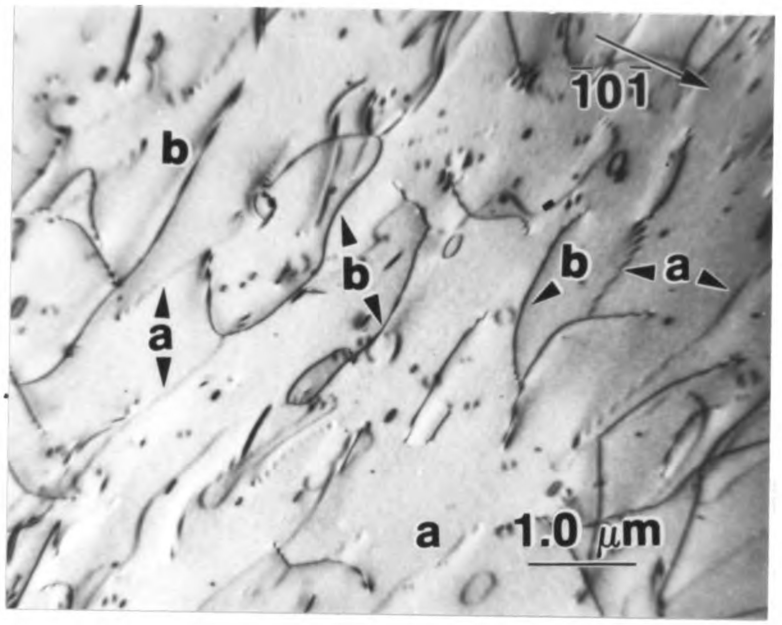

(c)

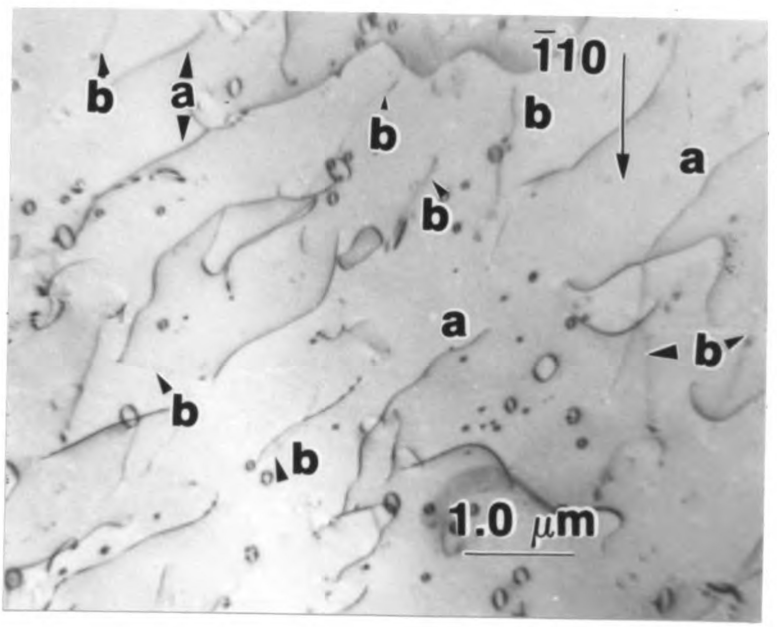

(d)

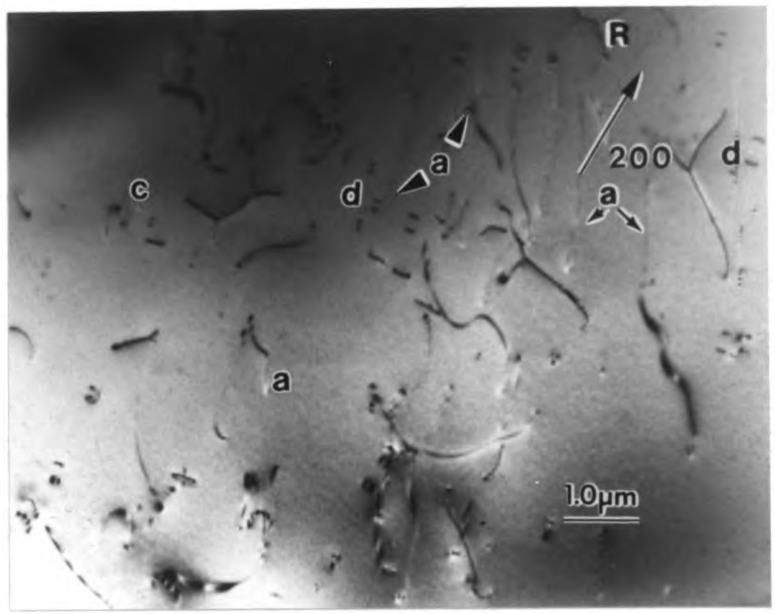

(a)

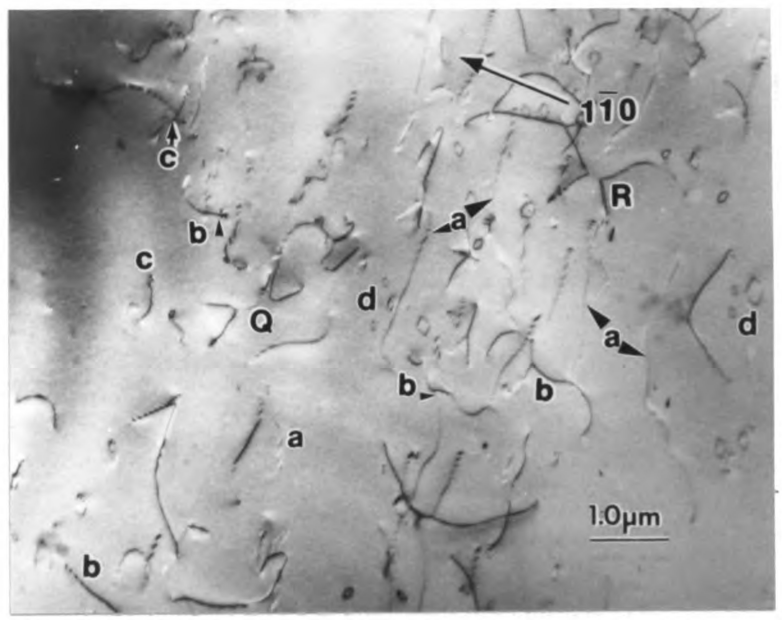

(b)

Figure 44 Analysis of dislocations in [011] Co-50Al deformed at 1300 K. Dislocations labeled "a", "b" and "c" were identified. Dislocation reactions were also observed in the foil.

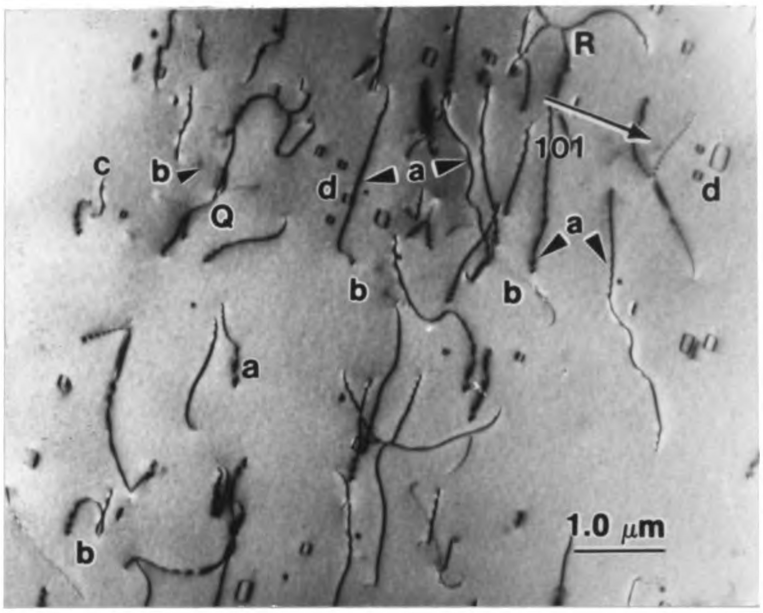

(c)

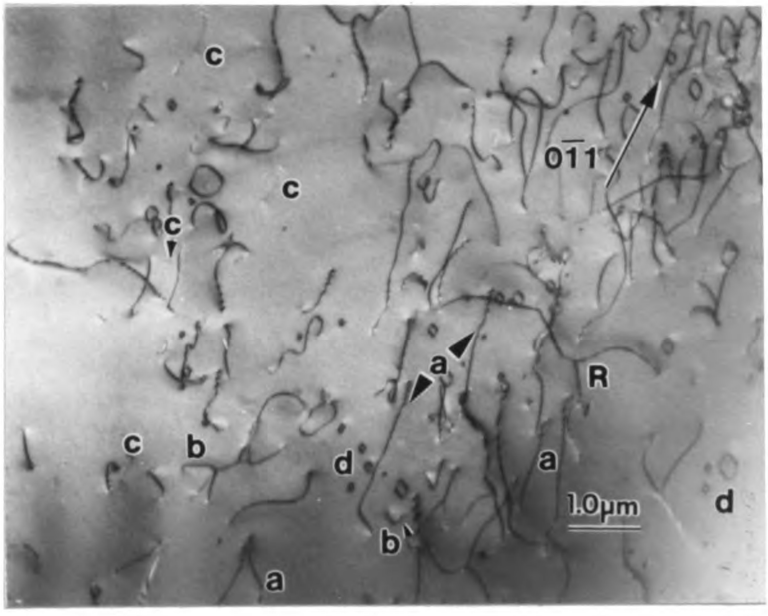

(d)

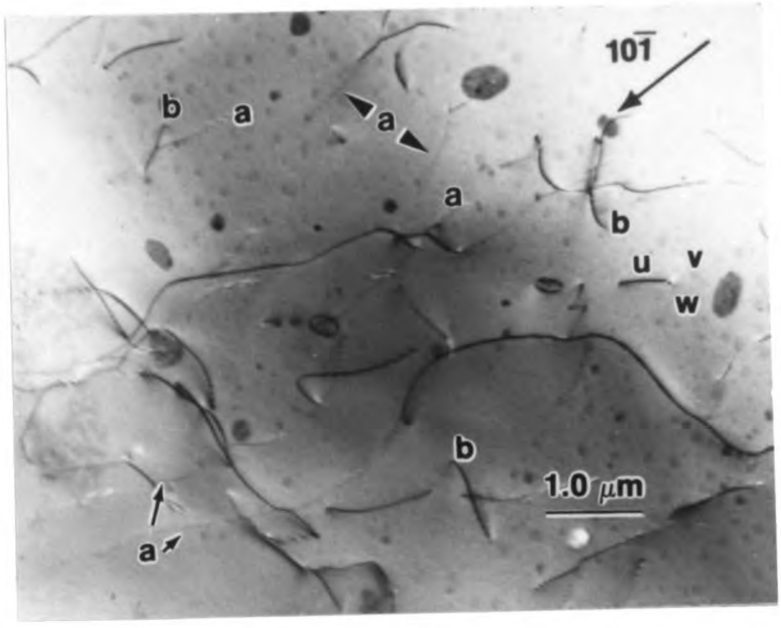

(a)

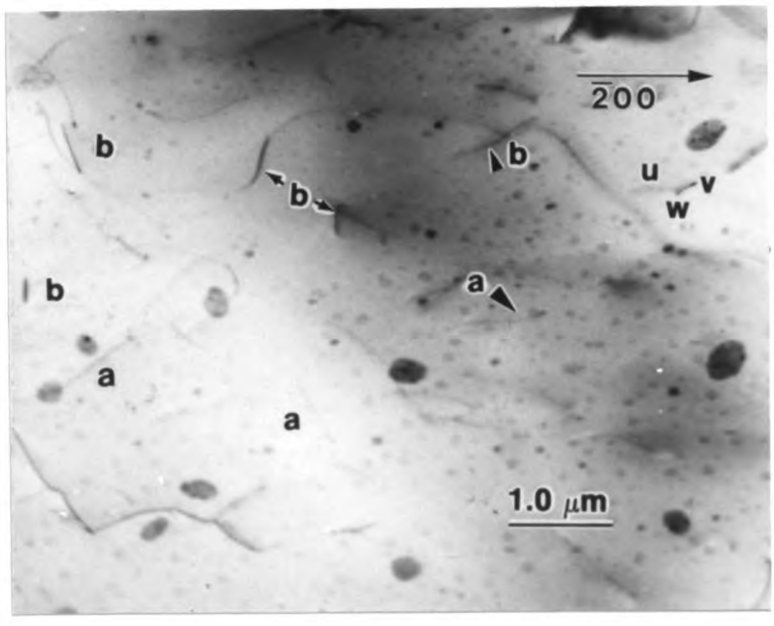

(b)

Figure 45 Dislocation analysis for [011] Co-48Al deformed at 1300 K. Dislocations labeled "a" and "b" were identified.

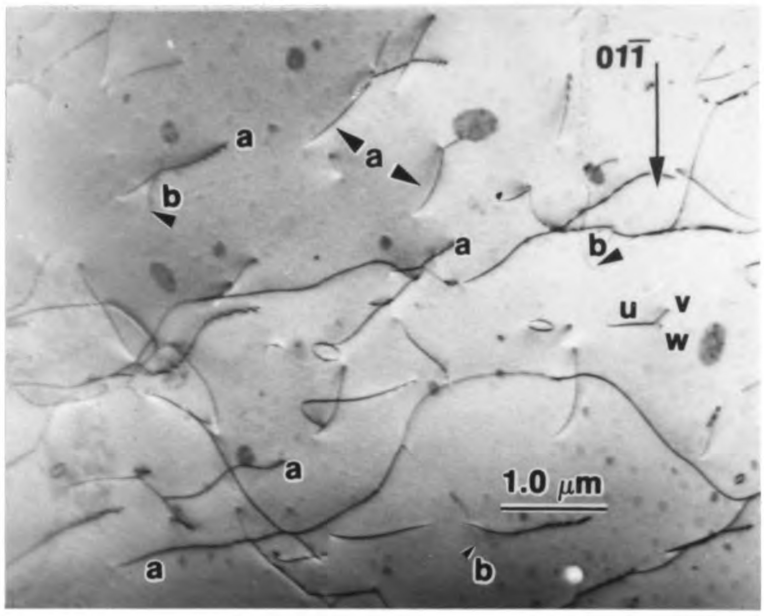

(c)

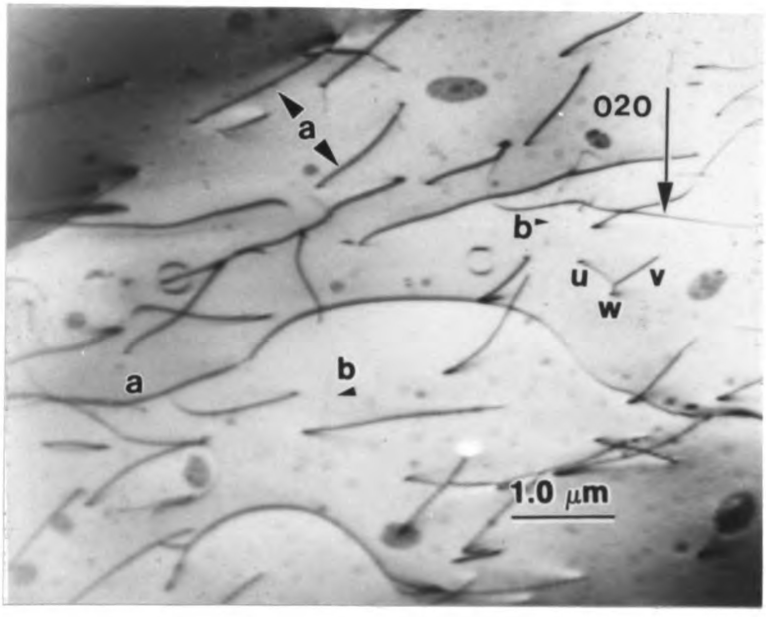

(d)

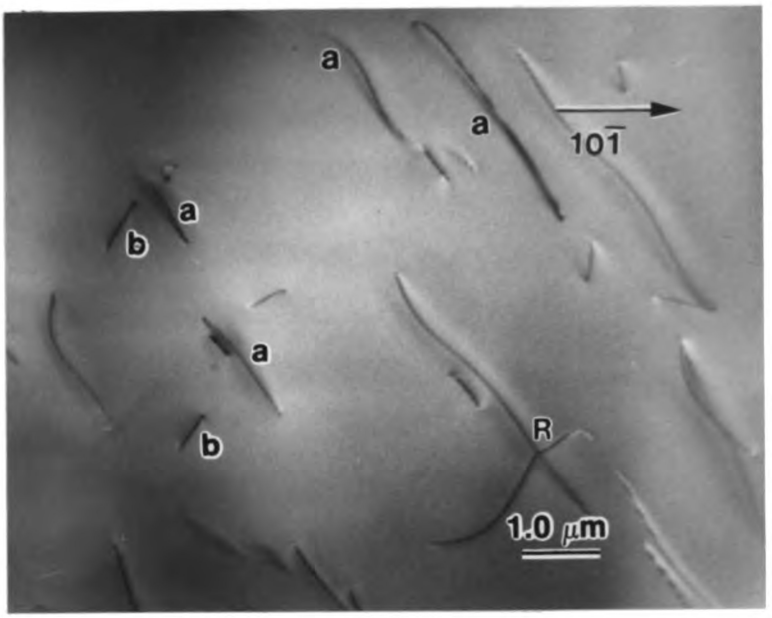

(a)

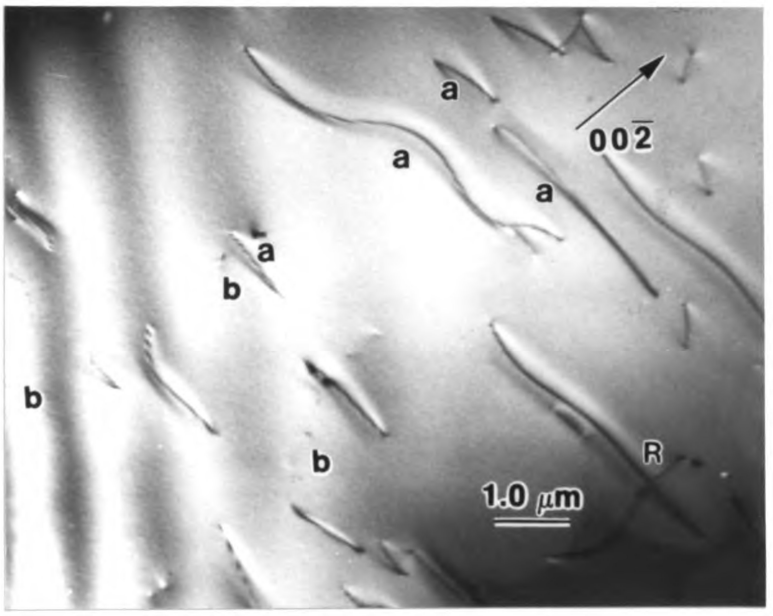

(b)

Figure 46 Dislocation analysis for [011] Co-52Al deformed at 1300 K. Dislocations labeled "a"and "b" were characterized.

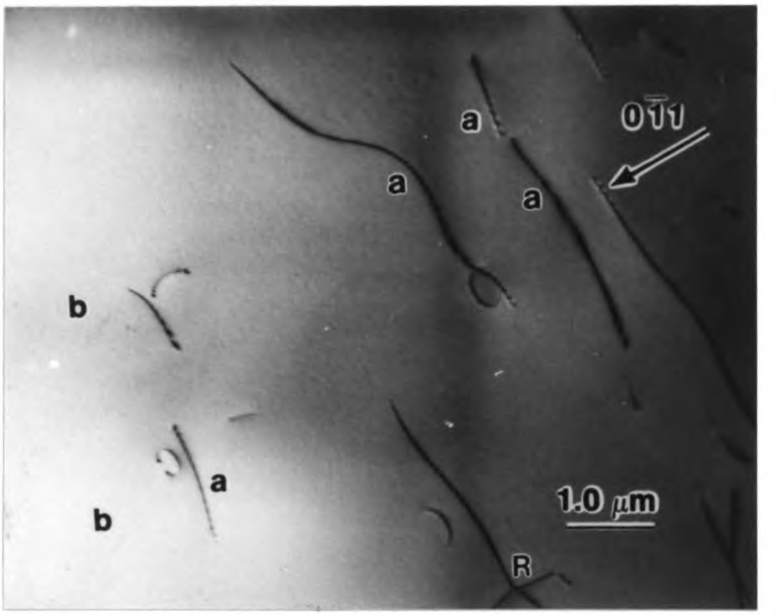

(c)

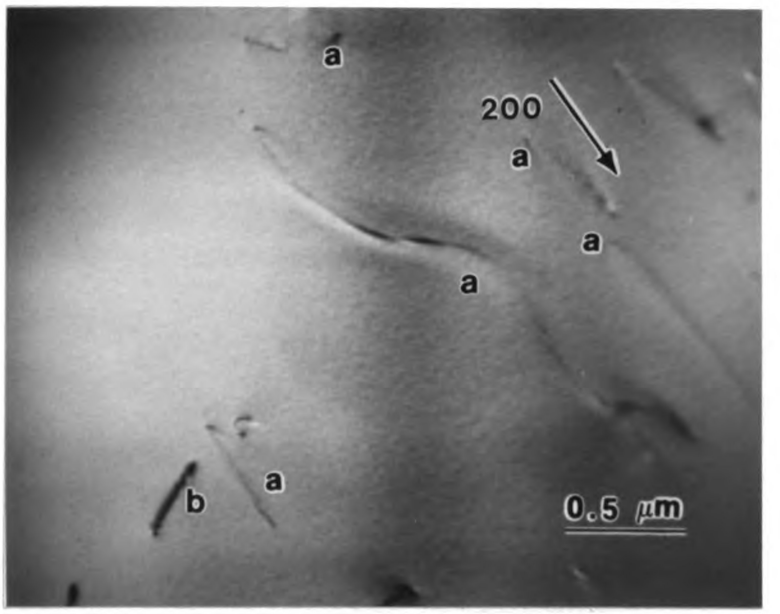

(d)

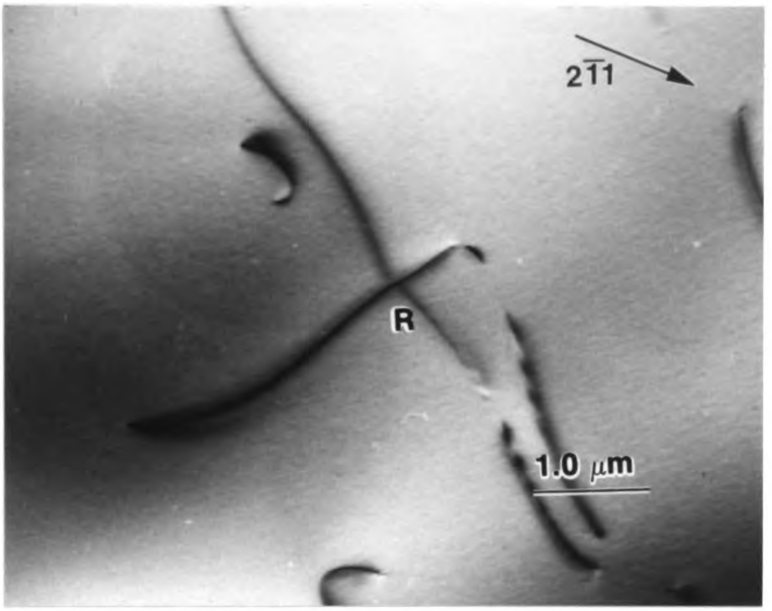

(e)

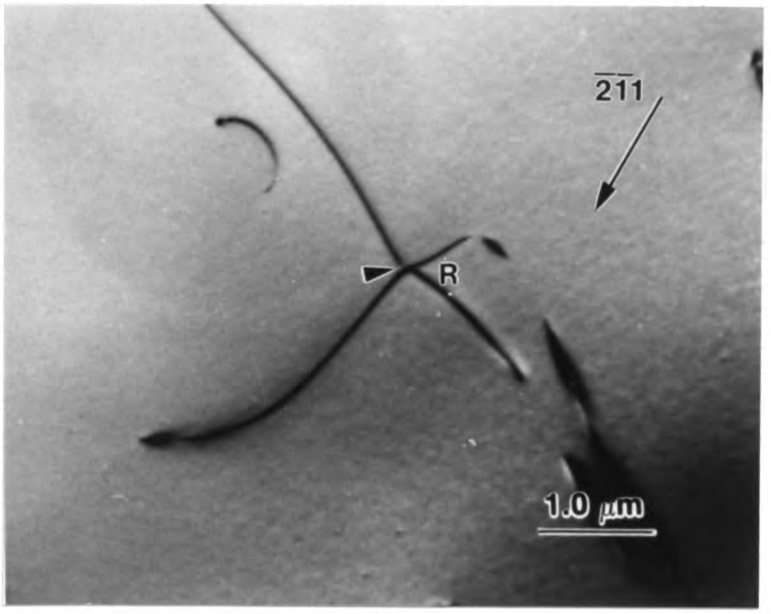

(f)

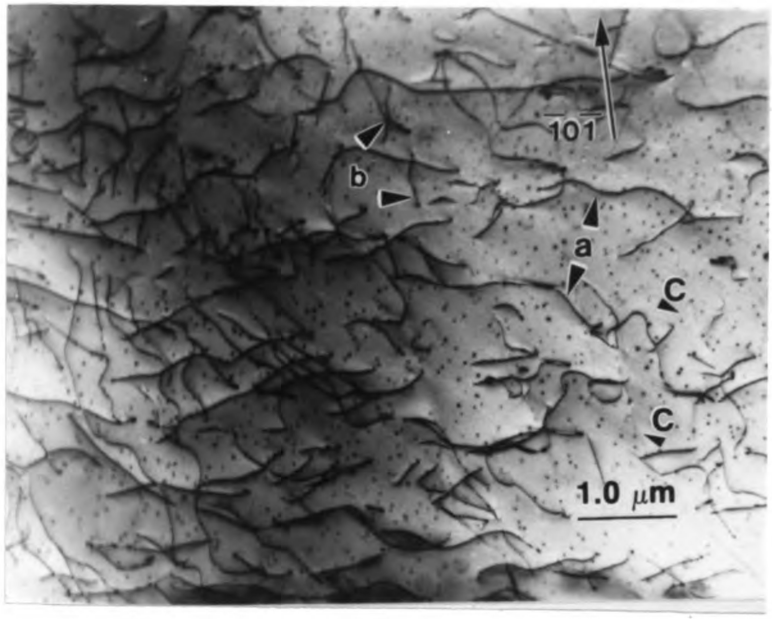

(a)

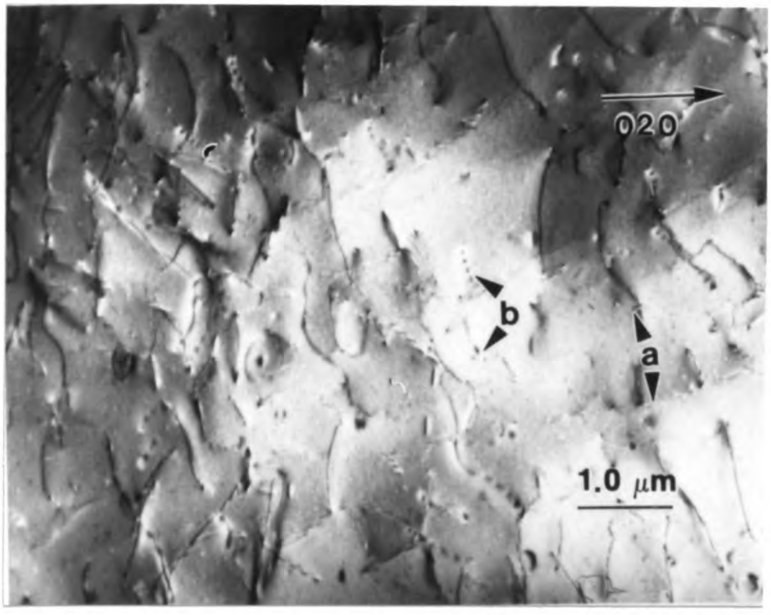

(b)

Figure 47 Dislocation analysis for [001] oriented Co-50Al deformed at 1300 K. <100> dislocations were observed.

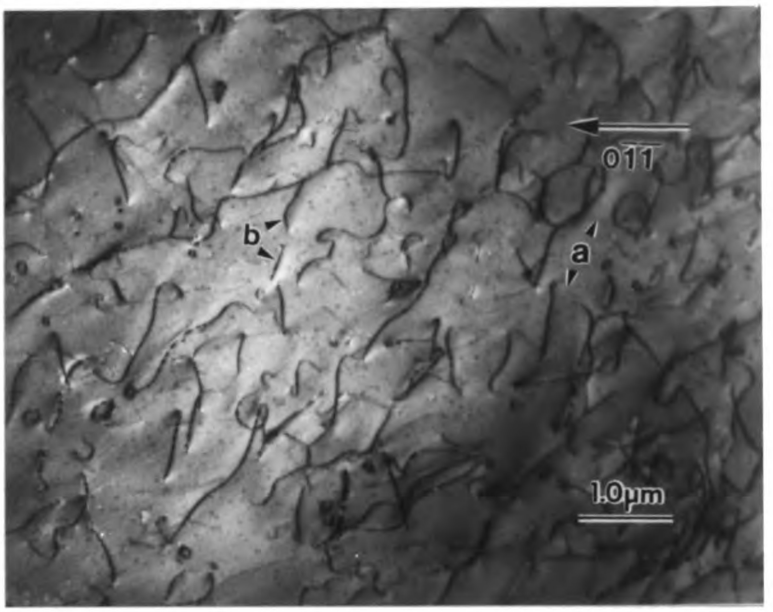

(c)

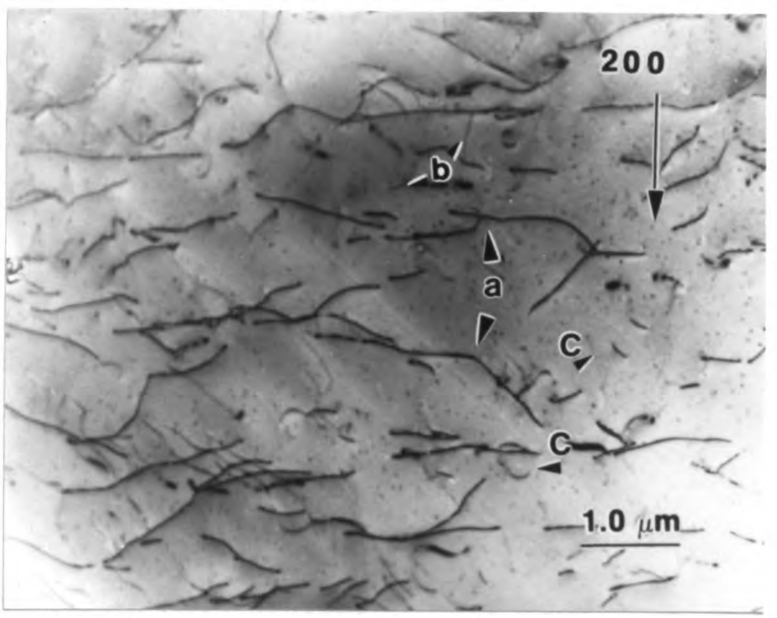

(d)

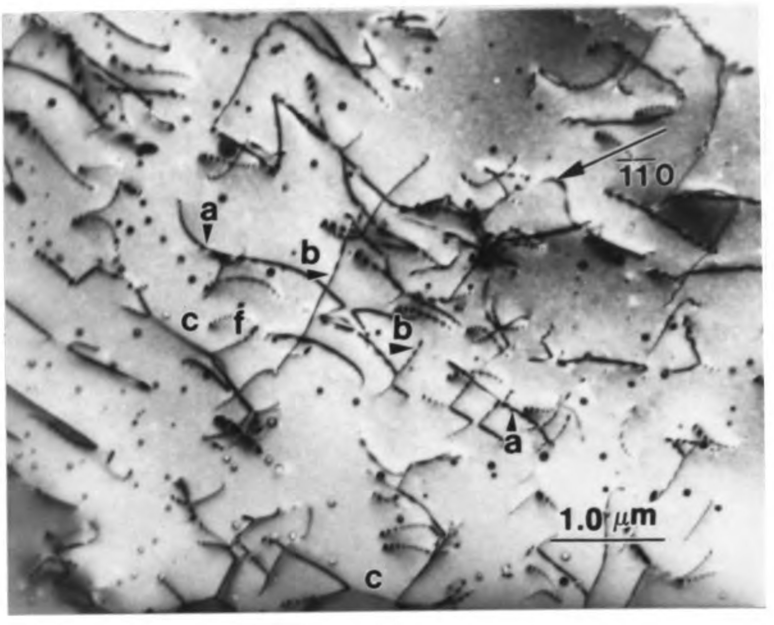

(a)

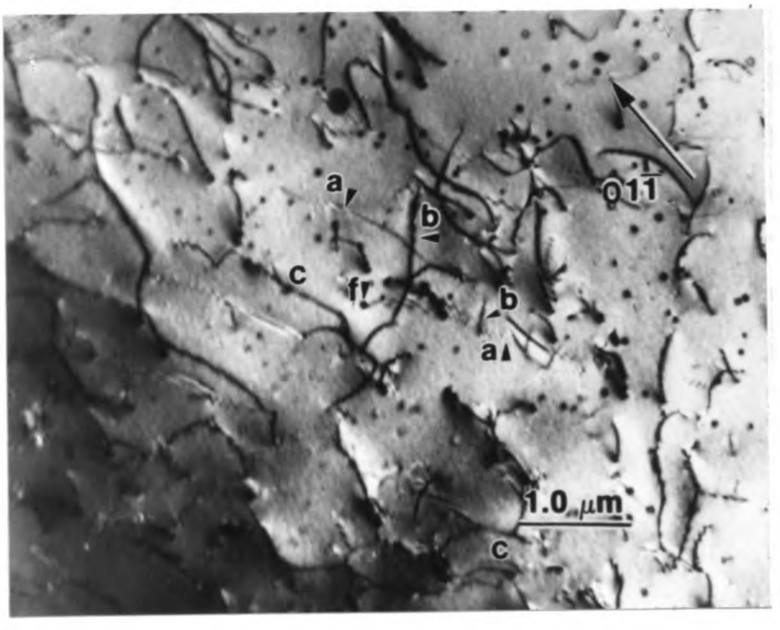

(b)

Figure 48 Analysis of dislocations in [001] oriented Co-50Al deformed at 1300 K. <110> dislocations were found.

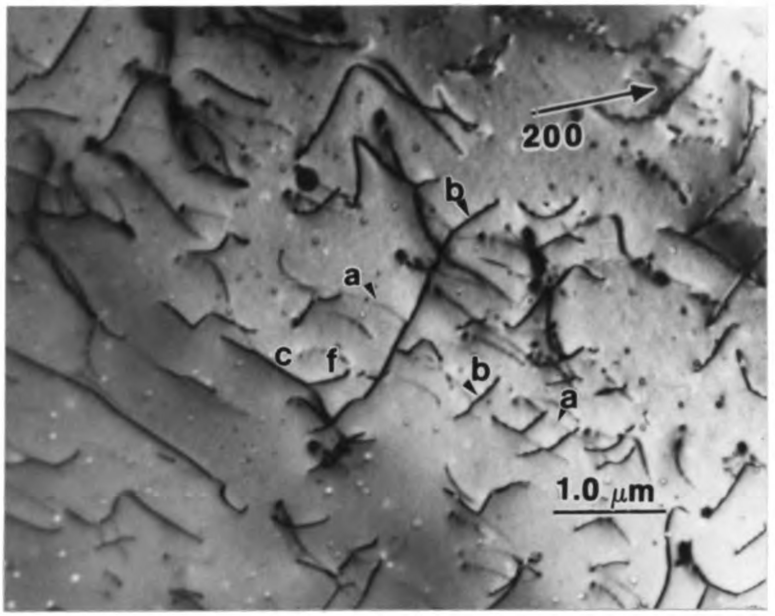

(c)

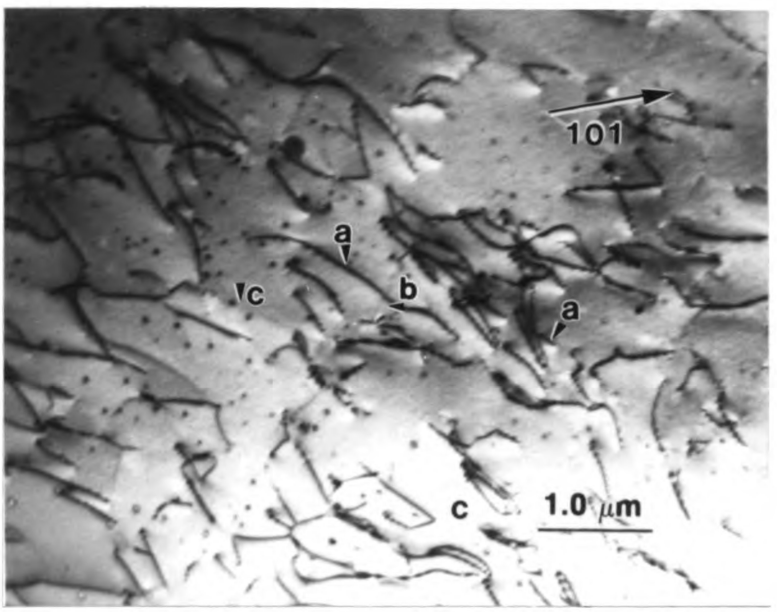

(d)

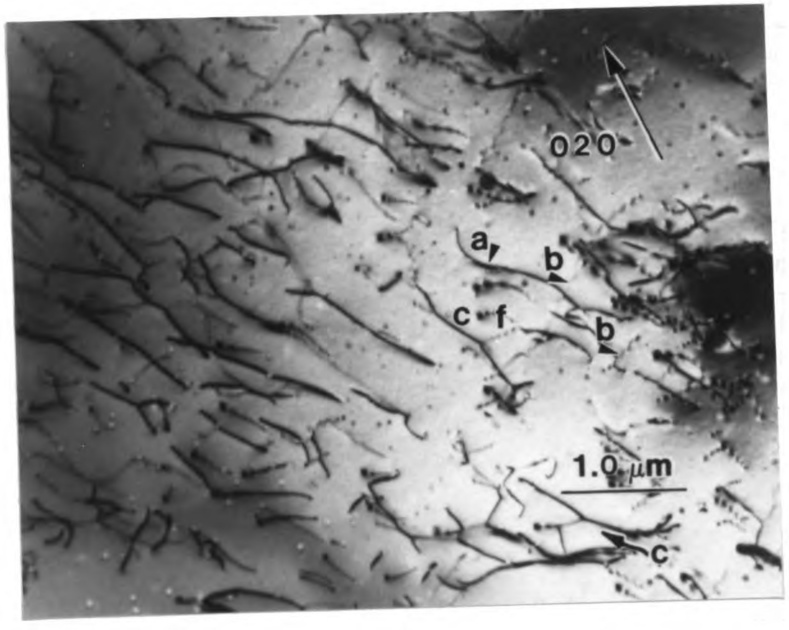

(e)

Table 7 Description of image features in figure 38.

Images	Charateristics
Experimetal image at g=[1$\bar{1}$0]	many segments whose orientations deviate from the dislocaton line direction
simulation for Burgers vector [001]	double image
simulation for Burgers vector [110]	double image
simulation for Burgers vector [11$\bar{1}$]	same features as the experimental image
simulation for Burgers vector [111]	same features as the experimental image
Experimetal image at g=[01$\bar{1}$]	continous dislocation with contrast fluctuation
simulation for Burgers vector [001]	contrast fluctuation is not obvious in the middle of the dislocation
simulation for Burgers vector [110]	same feature as above
simulation for Burgers vector [11$\bar{1}$]	no contrast change
simulation for Burgers vector [111]	same as the experiemental image
Experimetal image at g=[1$\bar{2}$1]	long straight dislocation without contrast change
simulation for Burgers vector [001]	discrete segments at both ends
simulation for Burgers vector [110]	dislocation is wavy at both ends
simulation for Burgers vector [111]	contrast is high at both ends
simulation for Burgers vector [111]	same feature as the experimental image

Table 8 Description of image features in figure 39.

Images	Charateristics
Experimetal image at g=[0$\bar{1}$1]	four segments whose orientations deviate from dislocation line direction.
simulation for Burgers vector [100]	same feature as the experimental image; slightly higher contrast
simulation for Burgers vector [011]	double image segments which are parallel to the line direction of the dislocation
simulation for Burgers vector [$\bar{1}$11]	head ends of the four segments seem to be indented
simulation for Burgers vector [111]	high contrast and double image segments
Experimetal image at g=[1$\bar{1}$0]	long dislocation with a small segment at end
simulation for Burgers vector [100]	same feature as the experimental image
simulation for Burgers vector [011]	same feature as the experimental image
simulation for Burgers vector [$\bar{1}$11]	two segments at both ends
simulation for Burgers vector [111]	doube image
Experimetal image at g=[1$\bar{2}$1]	two descrete segments
simulation for Burgers vector [100]	same feature as the experimental image
simulation for Burgers vector [011]	no segments
simulation for Burgers vector [$\bar{1}$11]	two segments are connected by a faint arc
simulation for Burgers vector [111]	double image; one segment is much larger than the other

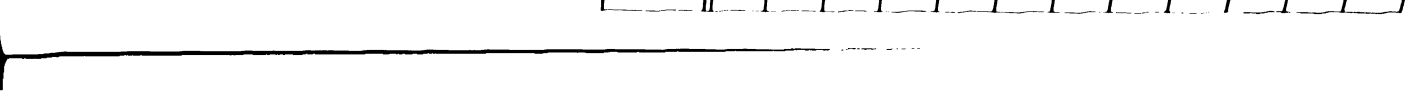

Table 9 Calculation of Dislocation Energies and Mobilities for CoAl [14].

Burgers vector	slip system	type Screw-Edge	Ex10-^{9} (J/m)	Kx10^{11} (N/m^2)	S
a<111>	{110}	S	23.68	0.67	0.706
a<111>	{110}	E	36.36	1.48	0.536
a<111>	{211}	S	23.68	0.96	0.711
a<111>	{211}	E	36.36	1.48	0.727
a<111>	{312}	S	23.68	0.96	0.605
a<111>	{312}	E	36.36	1.48	0.736
a<110>	{110}	S	17.36	1.06	0.533
a<110>	{110}	E	22.11	1.35	0.390
a<010>	{101}	S	11.30	1.38	0.482
a<010>	{101}	E	11.38	1.39	0.478
a<001>	{100}	S	11.30	1.38	0.652
a<001>	{100}	E	11.05	1.35	0.661

E: Dislocation energy S: Dislocation mobility parameter

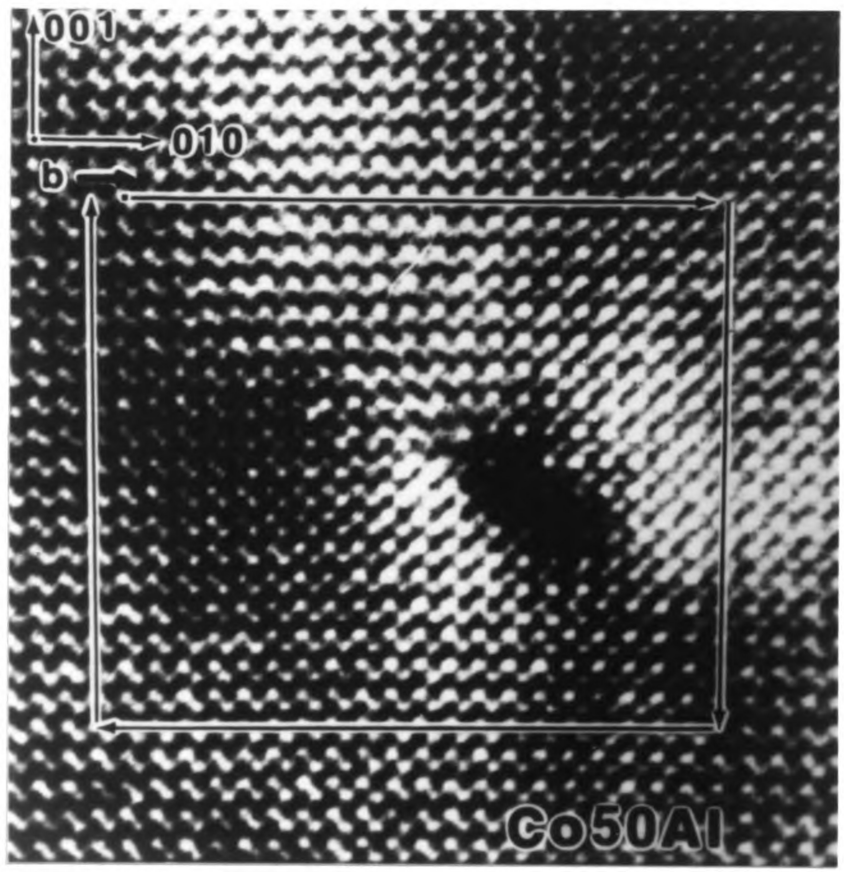

(a)

Figure 49 Core structure of an [010] edge dislocation in Co-50Al deformed at 1300 K:
(a) HREM micrograph and Burgers circuit,
(b) perspective view (front view) along [001] direction,
(c) perspective view (side view) along [010] direction,
(d) perspective view (45° view) along [0$\bar{1}$1] direction,
(e) perspective view (45° view) along [011] direction.

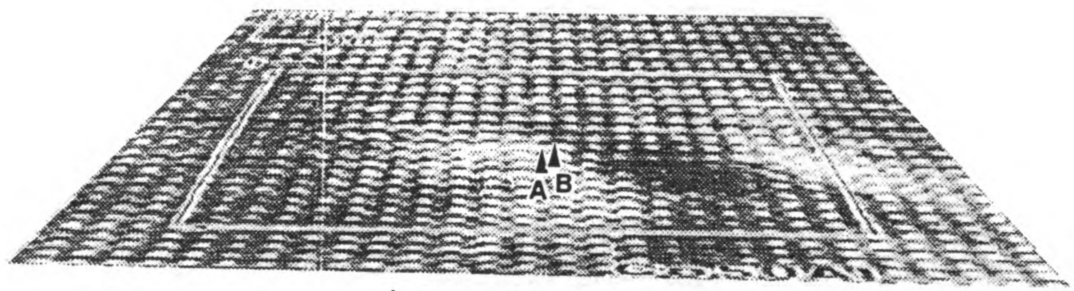

(b)

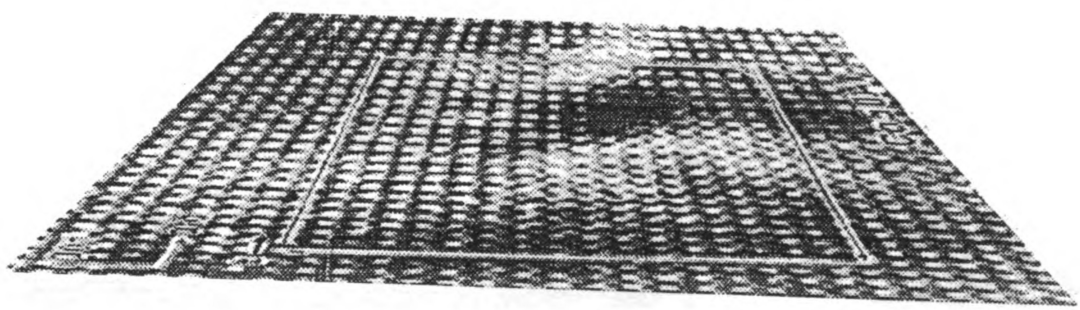

(c)

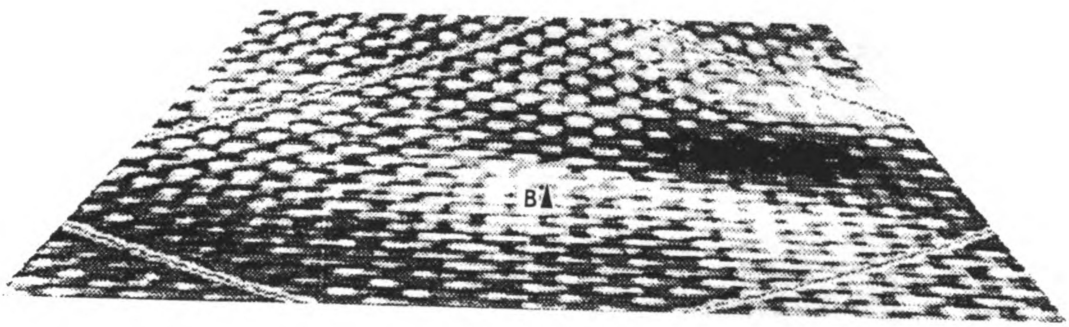

(d)

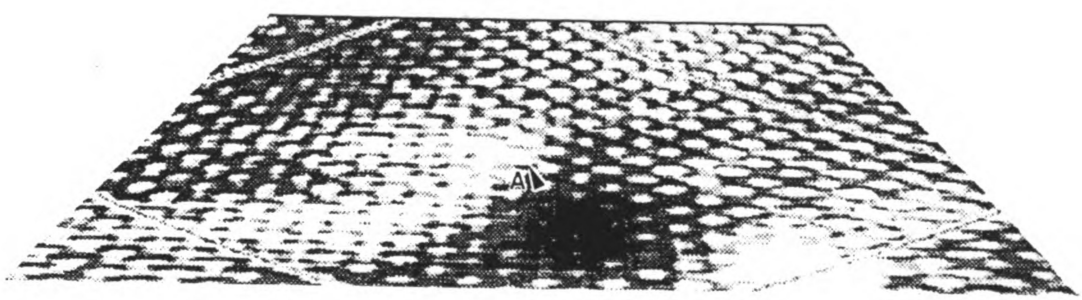

(e)

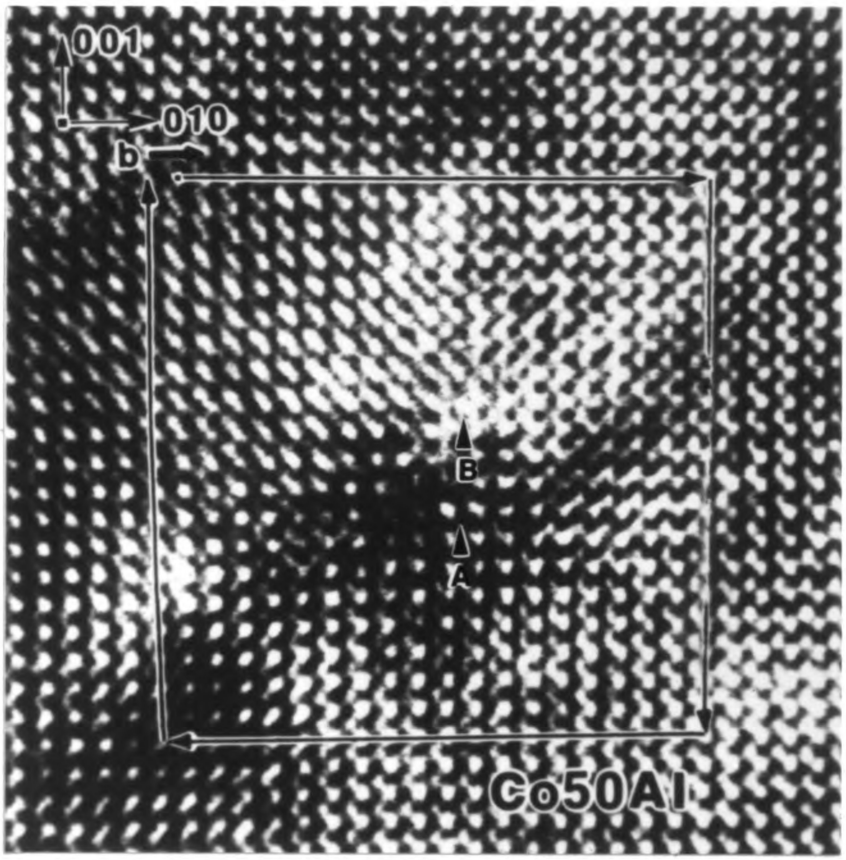

(a)

Figure 50 Core structure of an [010] edge dislocation in Co-50Al deformed at 1300 K:
(a) HREM micrograph and Burgers circuit,
(b) perspective view (front view) along [001] direction,
(c) perspective view (45° view) along [0$\bar{1}$1] direction,
(d) perspective view (45° view) along [011] direction.

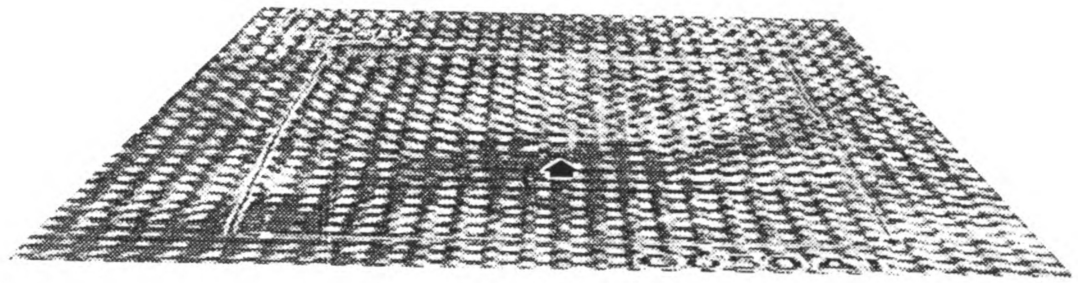

(b)

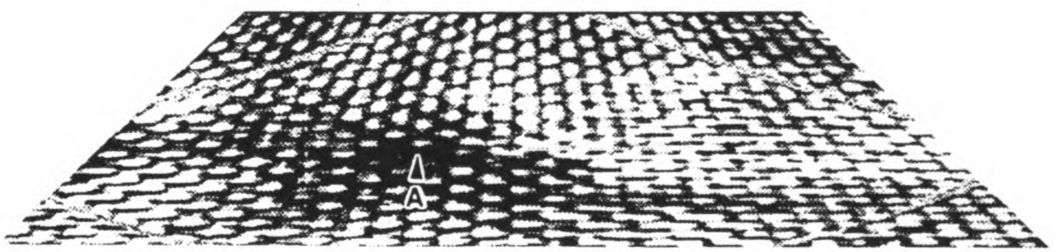

(c)

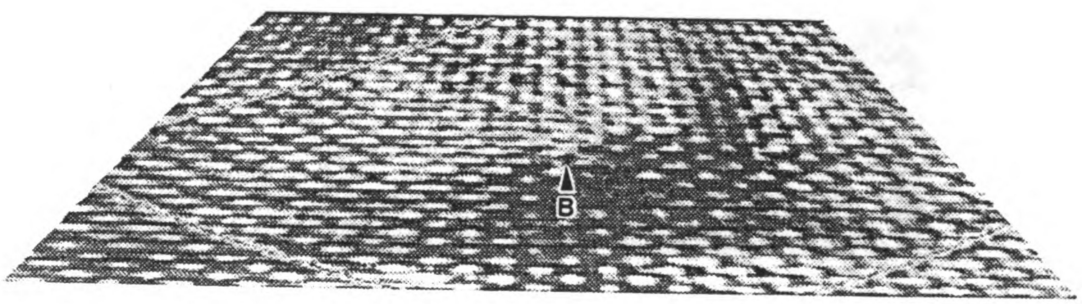

(d)

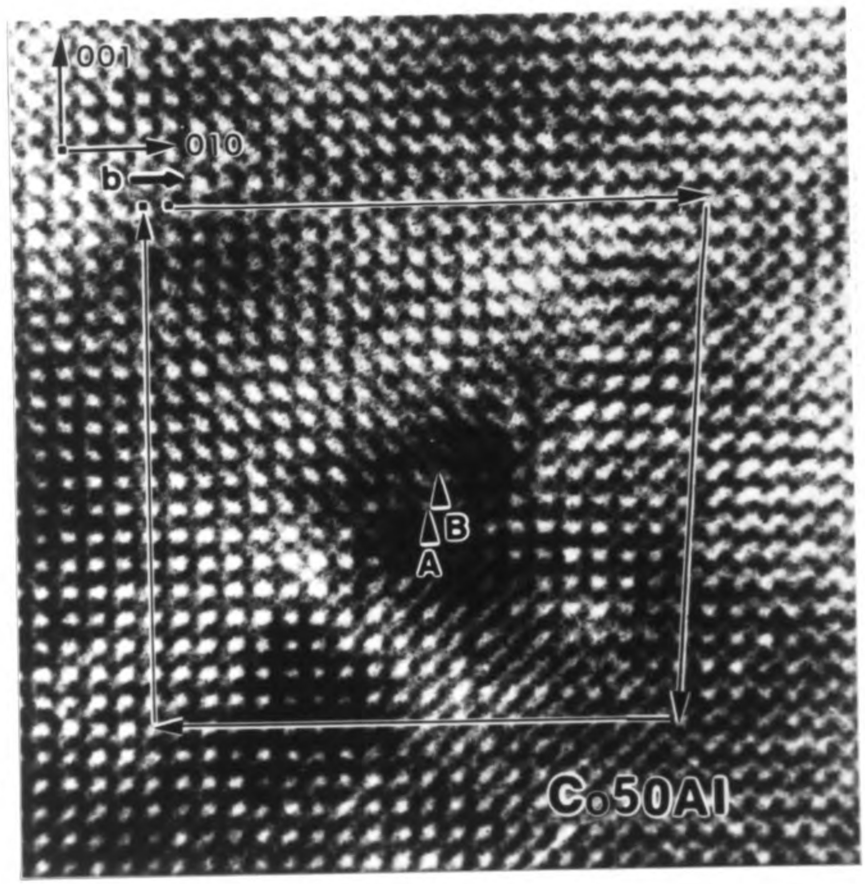

(a)

Figure 51 Core structure of an [010] edge dislocation in Co-50Al deformed at 1300 K:
(a) HREM micrograph and Burgers circuit,
(b) perspective view along [011] direction,
(c) perspective view along [0$\bar{1}$1] direction,
(d) perspective view along [011] direction.

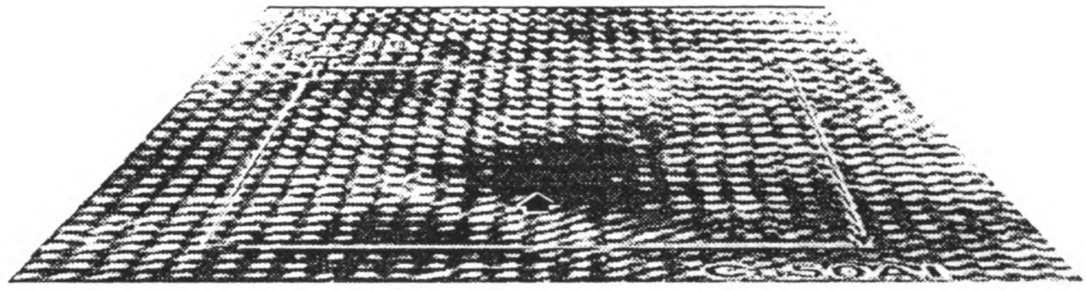

(b)

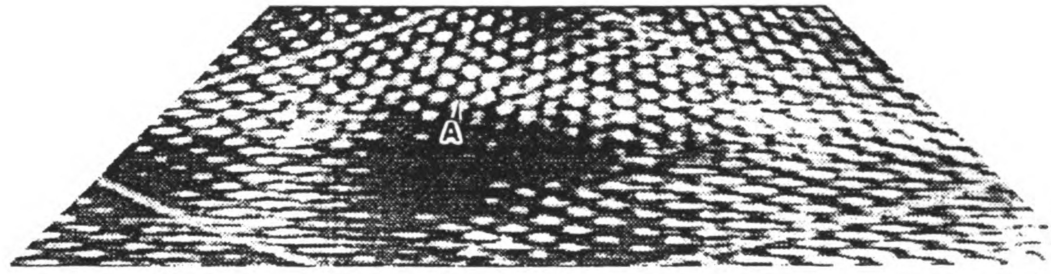

(c)

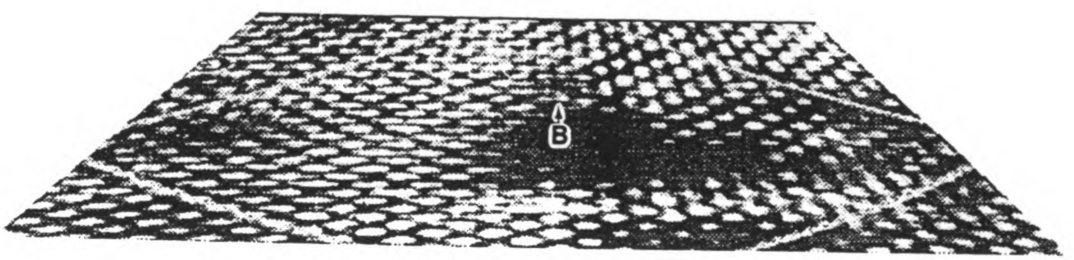

(d)

(a)

Figure 52 Core structure of an [010] edge dislocation in Co-48Al deformed at 1300 K:
(a) HREM micrograph and Burgers circuit,
(b) perspective view (front) along [001] direction,
(c) perspective view (side) along [010] direction,
(d) perspective view along [$0\bar{1}1$] direction,
(e) perspective view along [011]direction,
(f) Burgers circuit on partial dislocations.

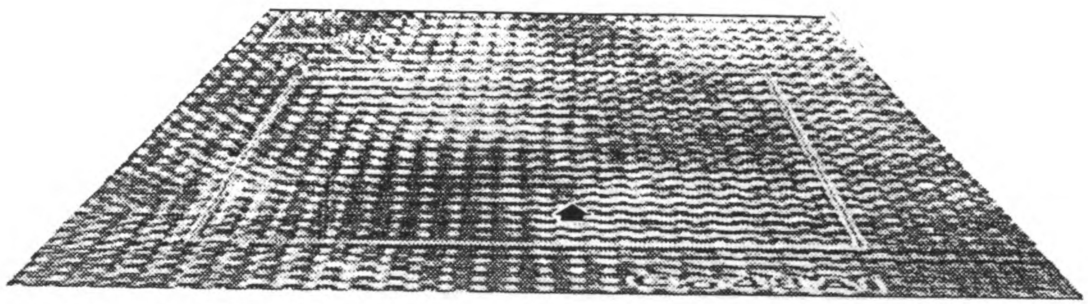

(b)

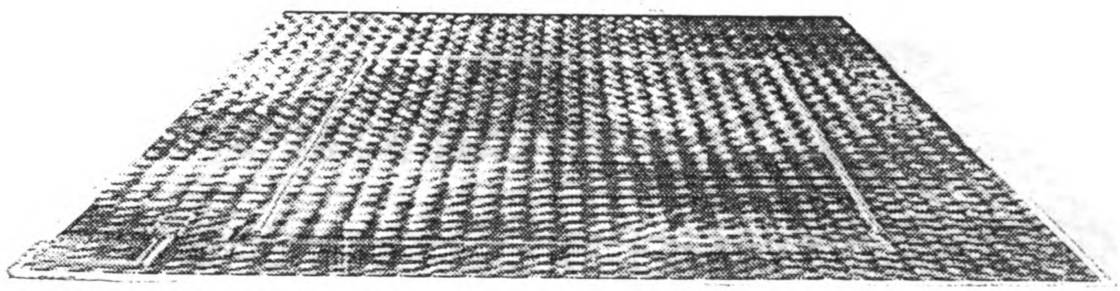

(c)

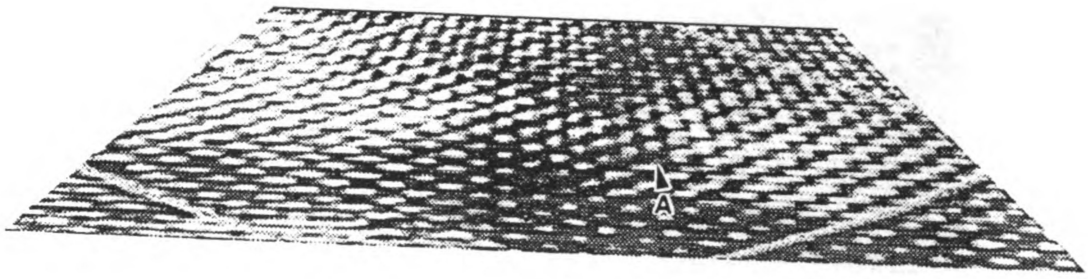

(d)

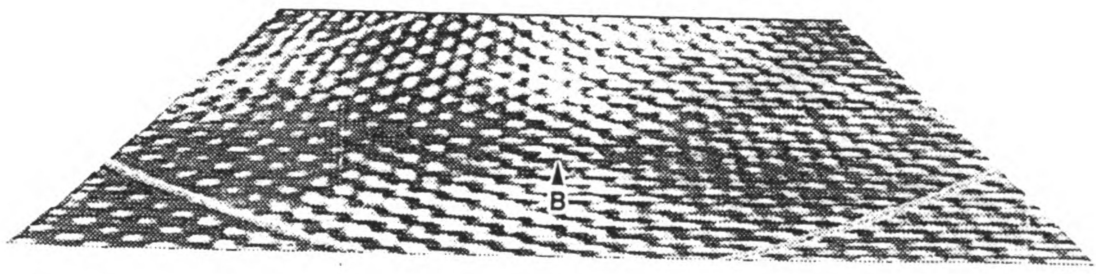

(e)

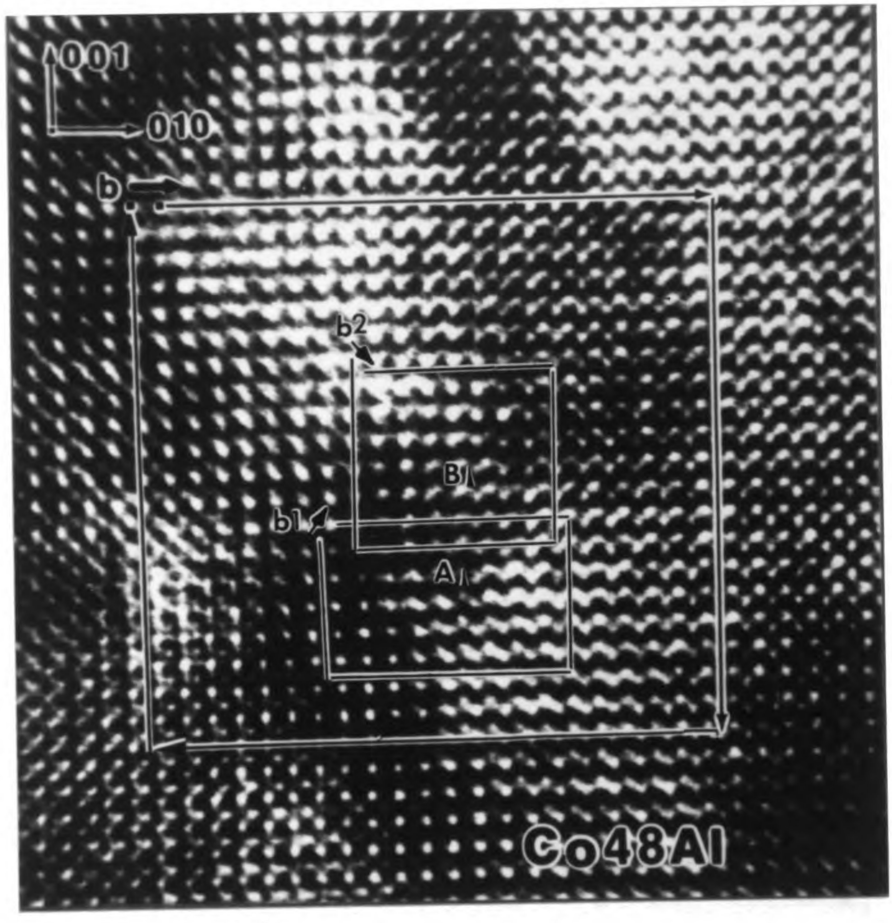

(f)

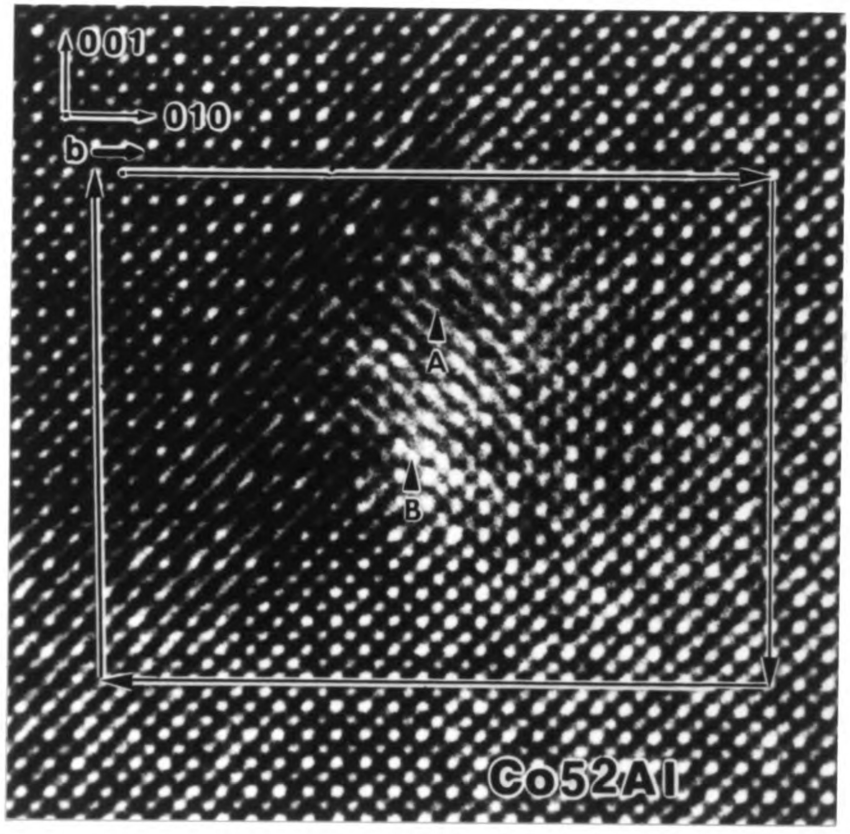

(a)

Figure 53 Core structure of an [010] edge dislocation in Co-52Al deformed at 1300 K.
(a) HREM micrograph and Burgers circuit,
(b) perspective view along [010] direction,
(b) perspective view along [011] direction,
(c) perspective view along [0$\bar{1}$1] direction.

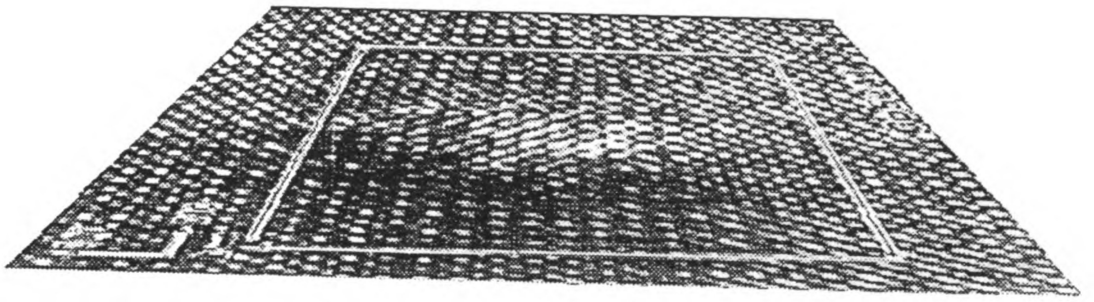

(b)

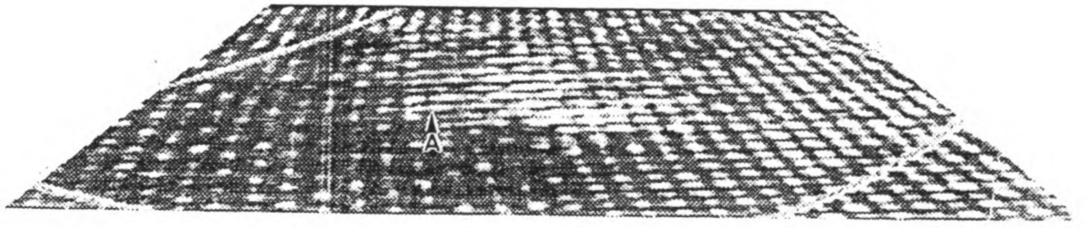

(c)

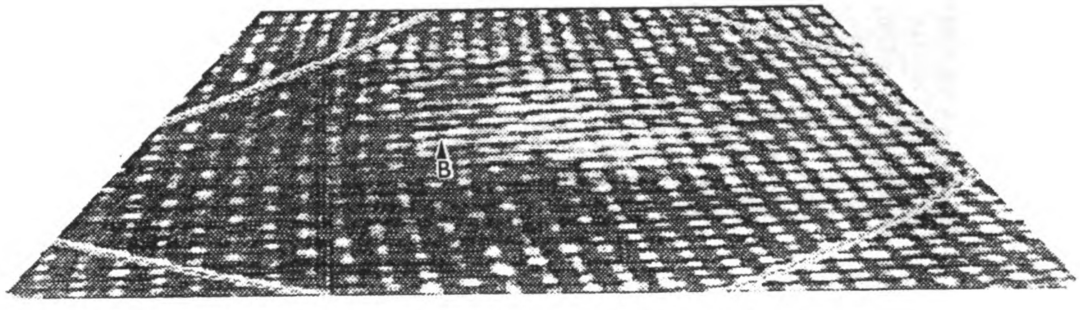

(d)

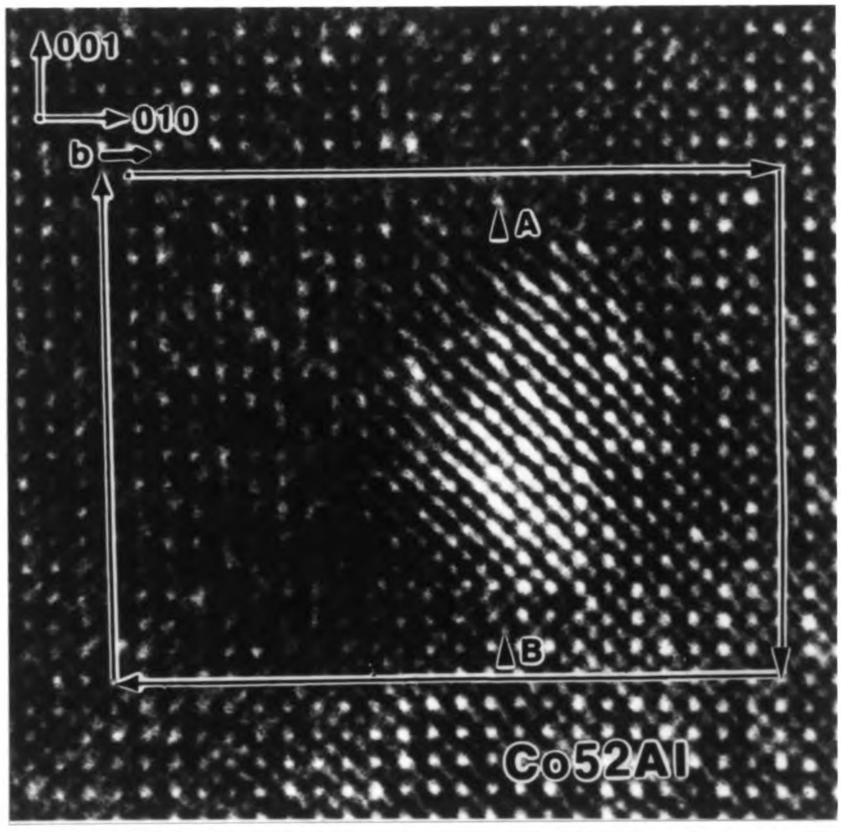

(a)

Figure 54 Core structure of an [010] edge dislocation in Co-52Al deformed at 1300 K:
(a) HREM micrograph and Burgers circuit,
(b) perspective view along [011] direction,
(c) perspective view along [0$\bar{1}$1]direction,
(d) schematic drawing of core structure of [010] edge dislocation in Co-52Al.

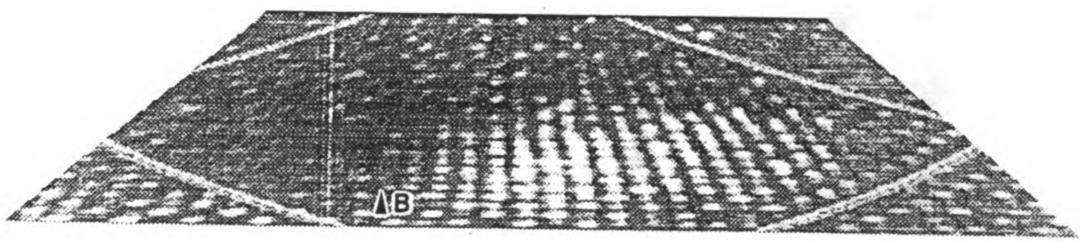

(b)

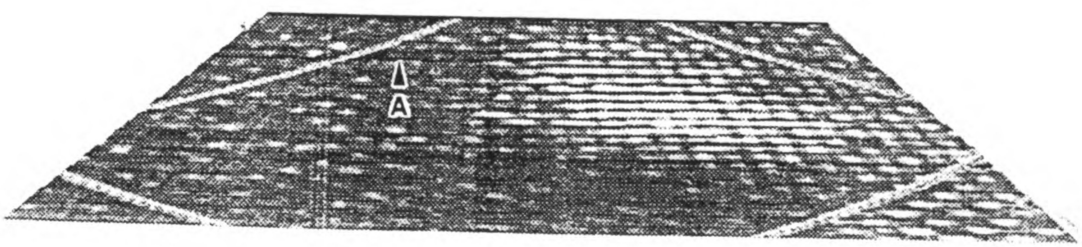

(c)

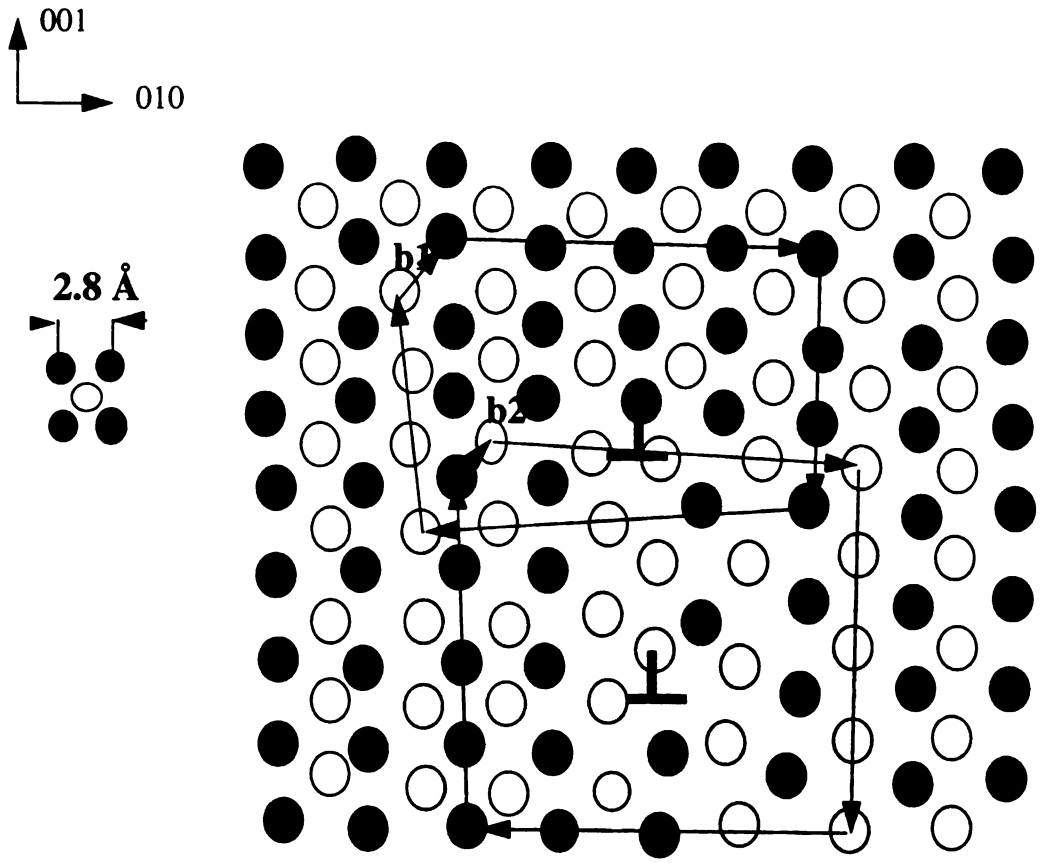

b=[010]
b1=1/2[$\bar{1}$11]
b2=1/2[11$\bar{1}$]

b=b1+APB+b2

(d)

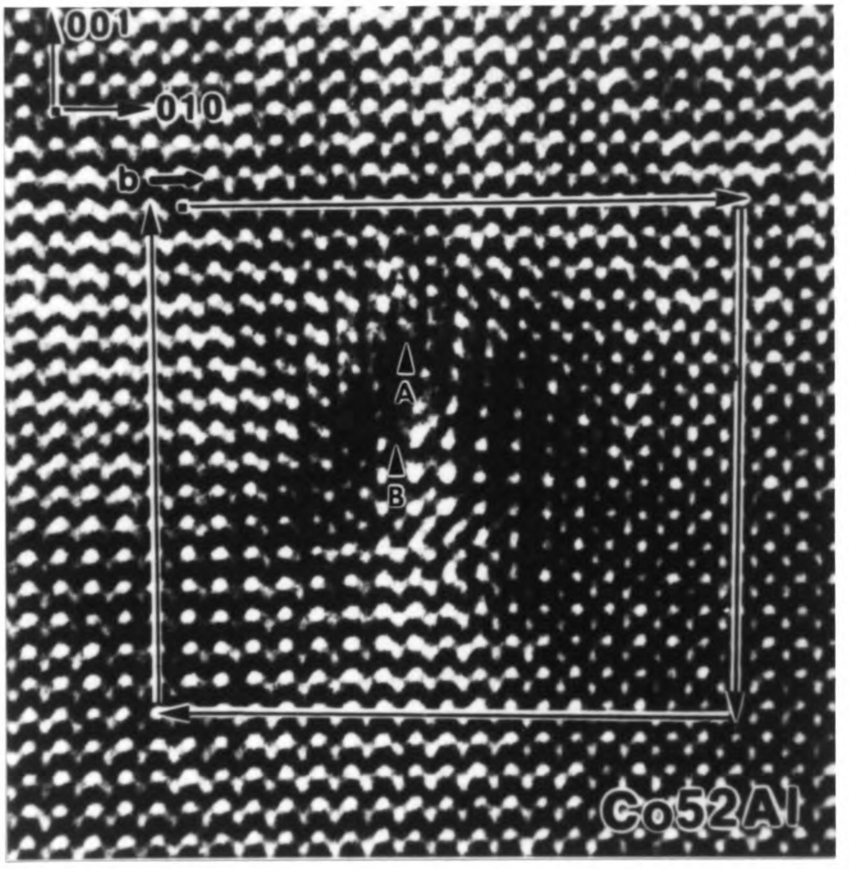

(a)

Figure 55 Another example of a core structure of an [010] edge dislocation in [011] Co-52Al deformed at 1300 K:
(a) HREM micrograph and Burgers circuit,
(b) perspective view (front) along [001] direction,
(c) perspective view (side) along [010] direction,
(d) perspective view along [0$\bar{1}$1] dorection,
(e) perspective view along [011] direction.

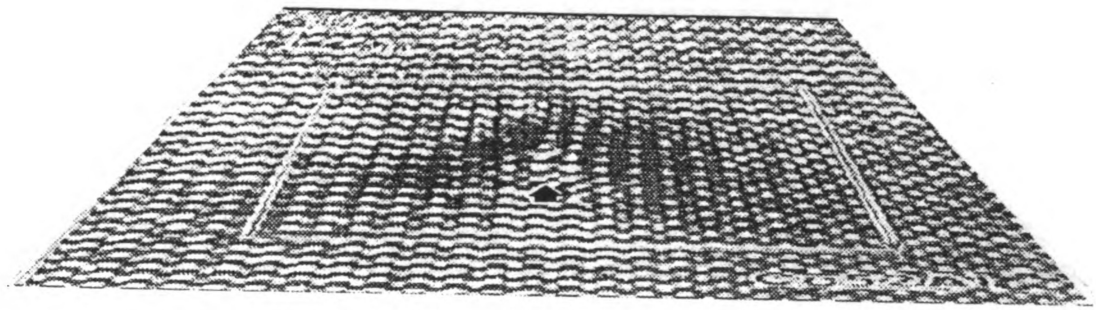

(b)

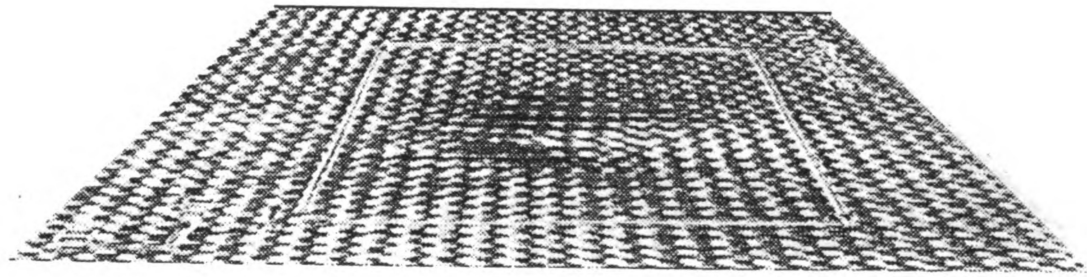

(c)

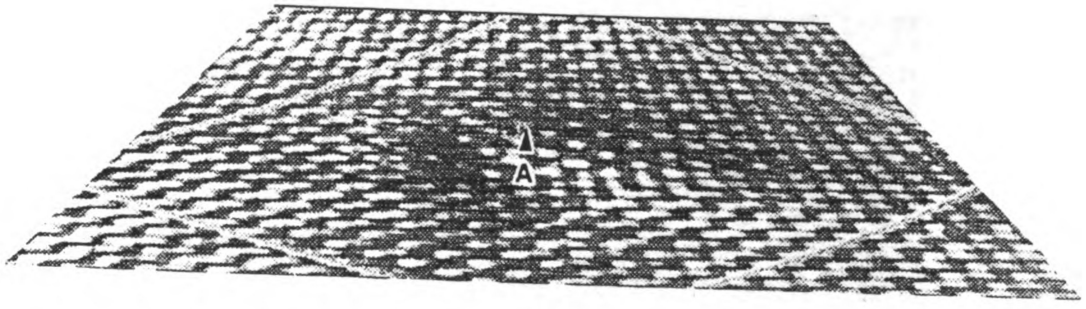

(d)

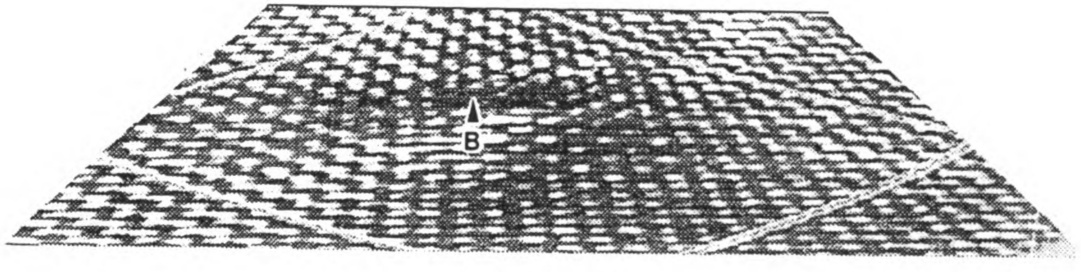

(e)

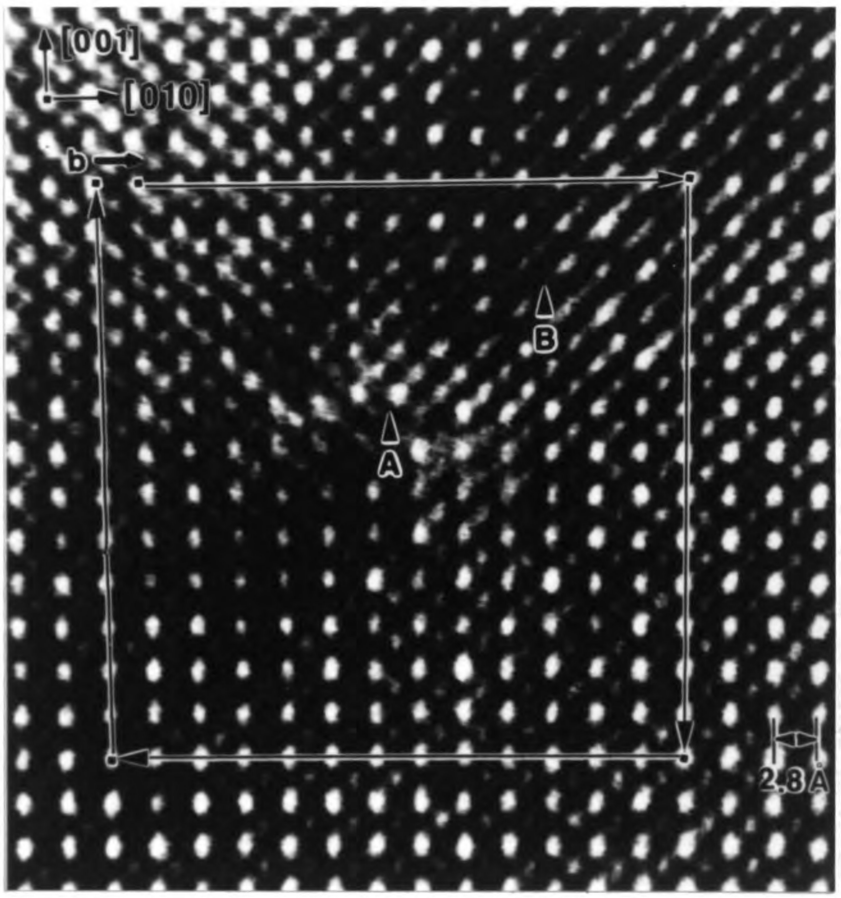

(a)

Figure 56 Another example of a core structure of an [010] edge dislocation in Co-52Al deformed at 1300 K:
(a) HREM micrograph and Burgers circuit,
(b) view along [010] direction.

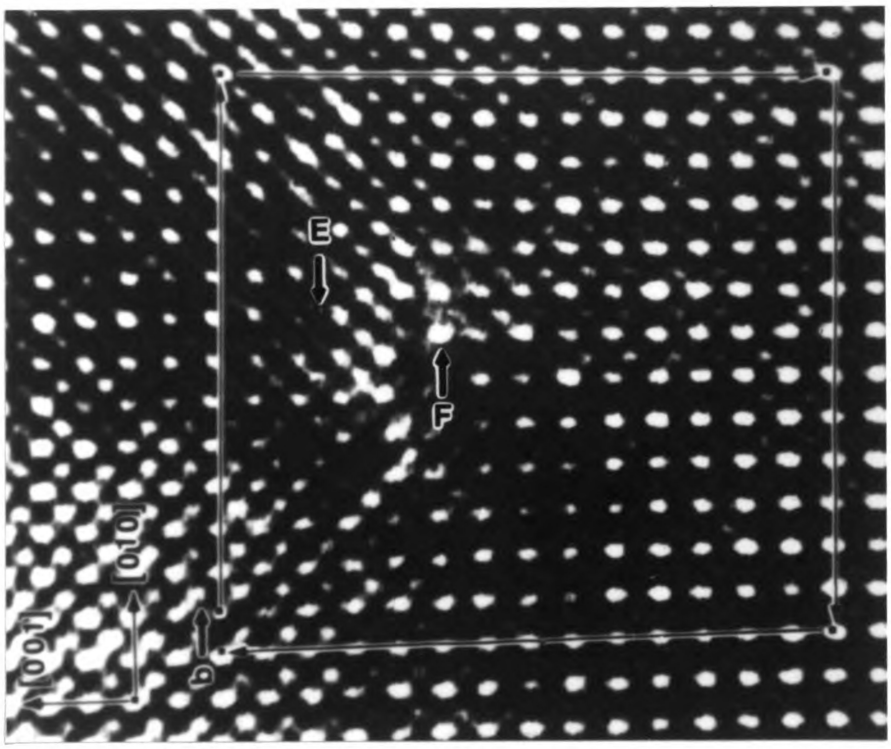

(b)

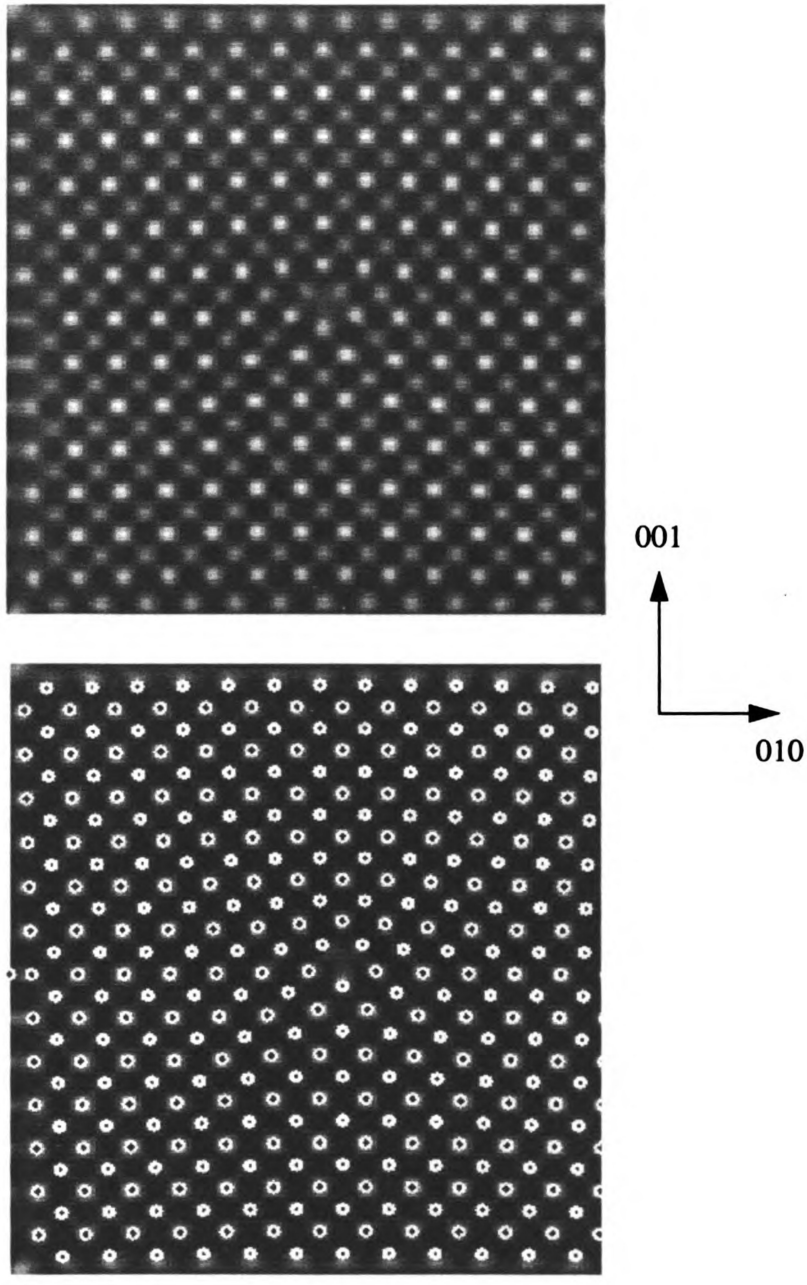

Figure 57 Simulated HREM image of the core structure of a [010] edge dislocation in Co-50Al at the conditions of defocus -70 nm and foil thickness 2.3 nm.

(a) White spots represents atom columns. The core center is characterized by a Al triangle.

(b) Atom positions superimposed onto the HREM image simulation. Large dots represent Co and small dots represent Al.

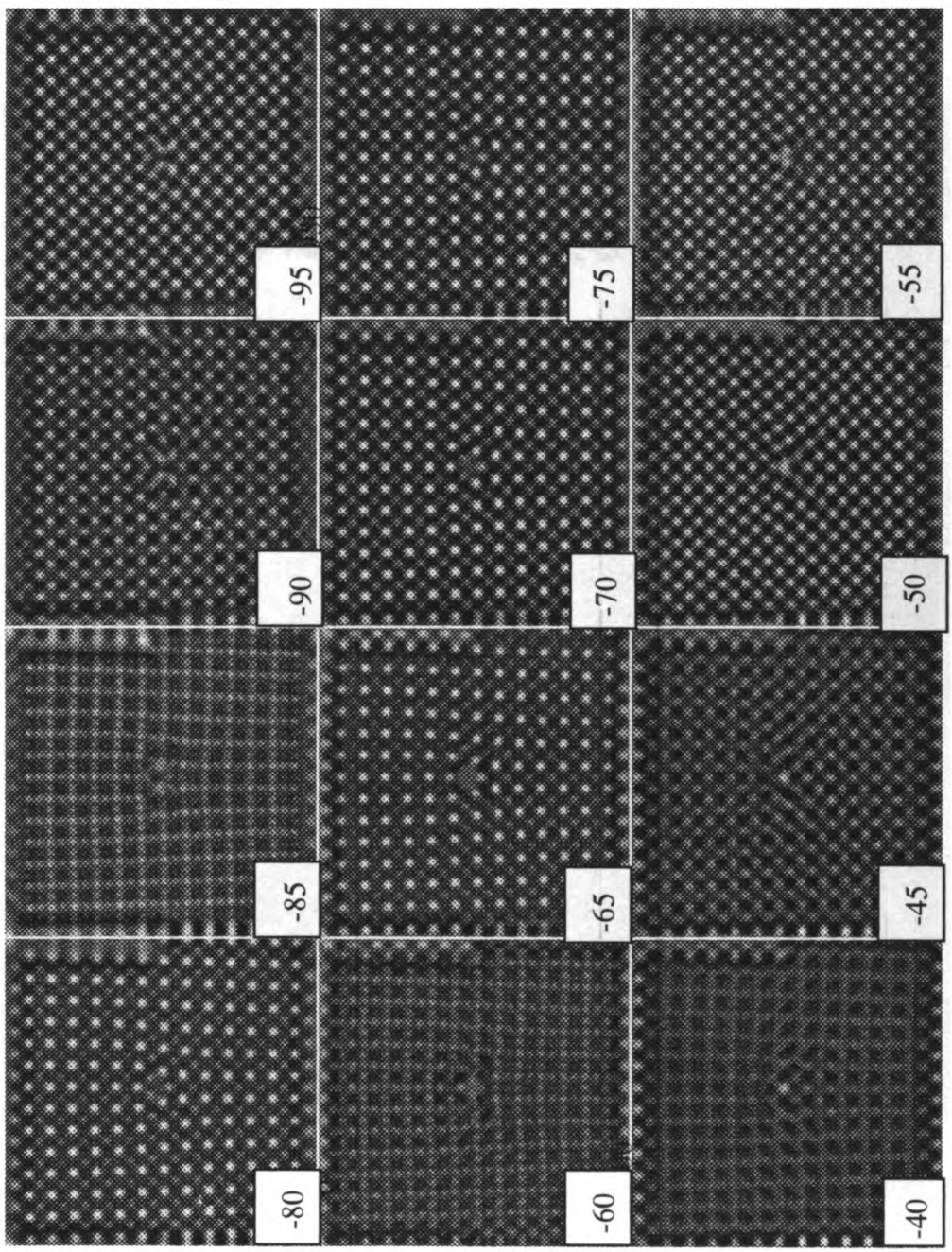

Figure58 A through focal series for core structure simulations of a <100> edge dislocation. Defocus values are marked on the individual images. The foil thickness is 3.4 nm.

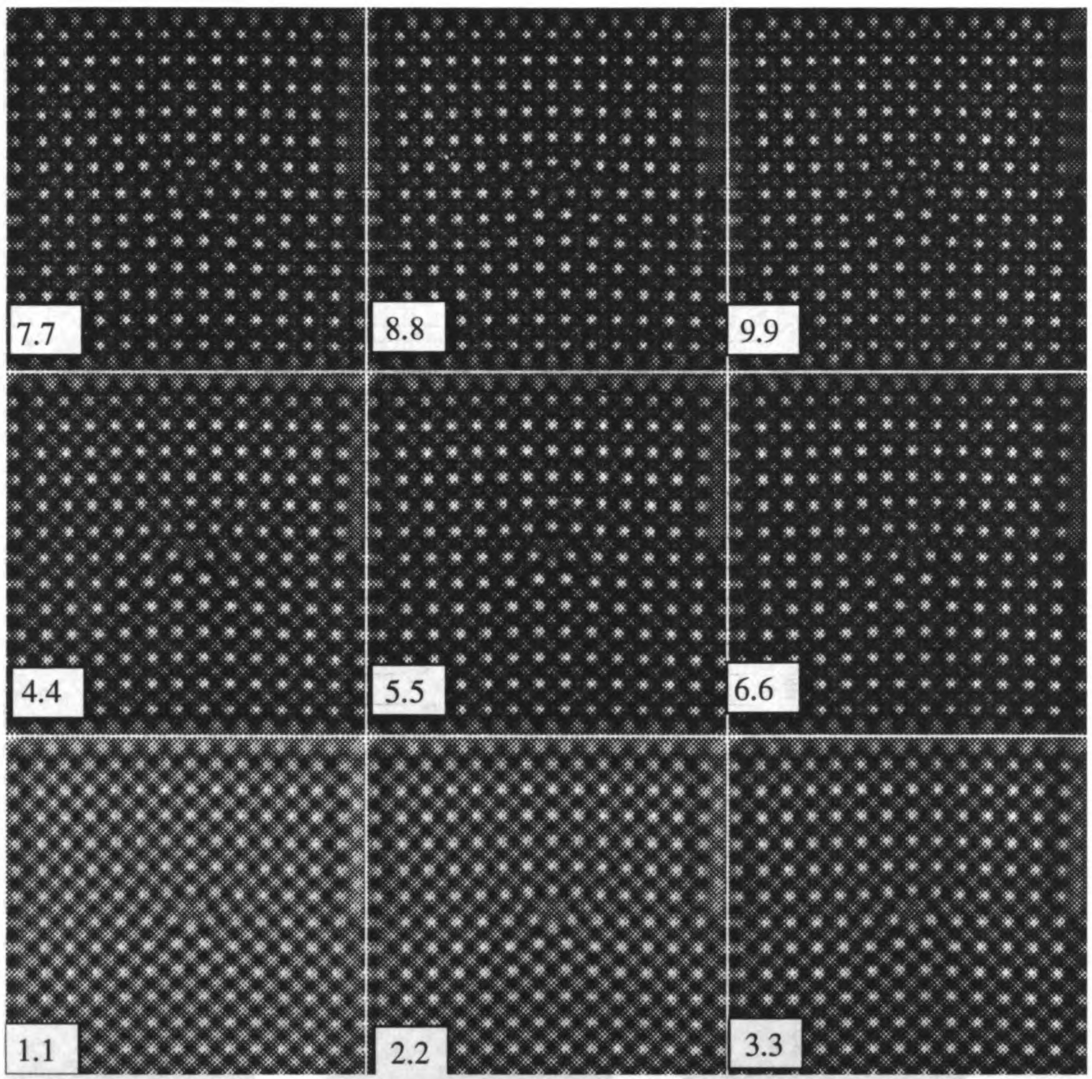

Figure 59 HREM simulation of [010] dislocation. Thickness increases from 1.1 nm to 9.9 nm. The defocus value is -70 nm.

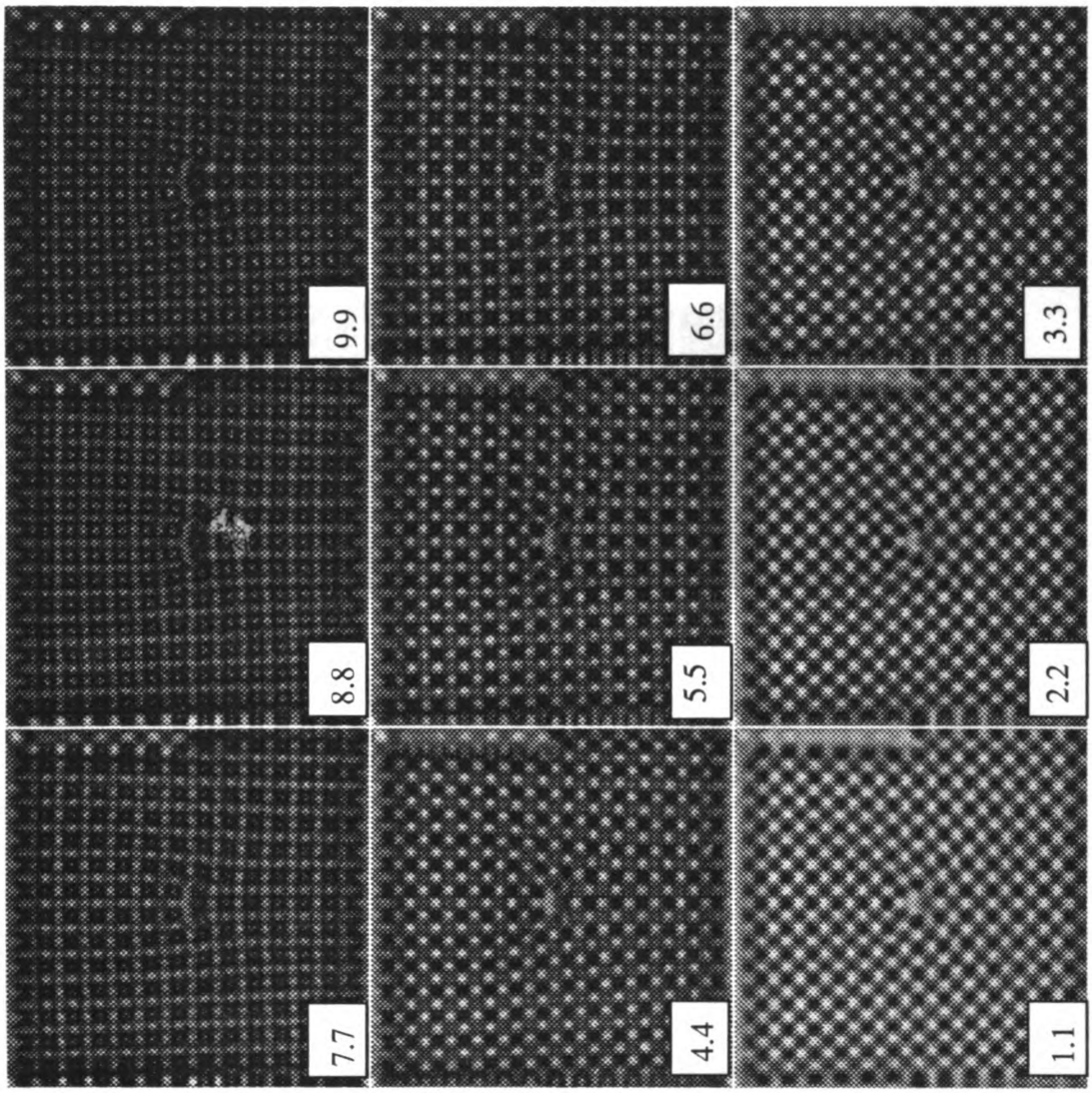

Figure 60 HREM simulations of [010] dislocation. Thickness conditions change the same as figure 59. Defocus value is -60 nm.

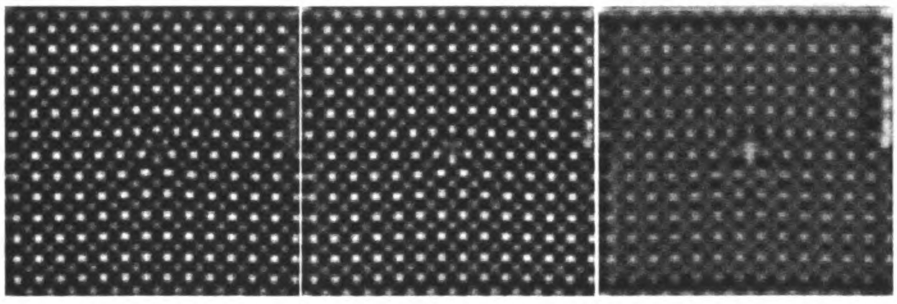

(a) (b) (c)

Figure 61 Effect of temperature on HREM simulations is shown at the conditions of df=-70 nm and thickness of 2.3 nm: (a) 20 K, (b) 93 K, and (c) 293 K.

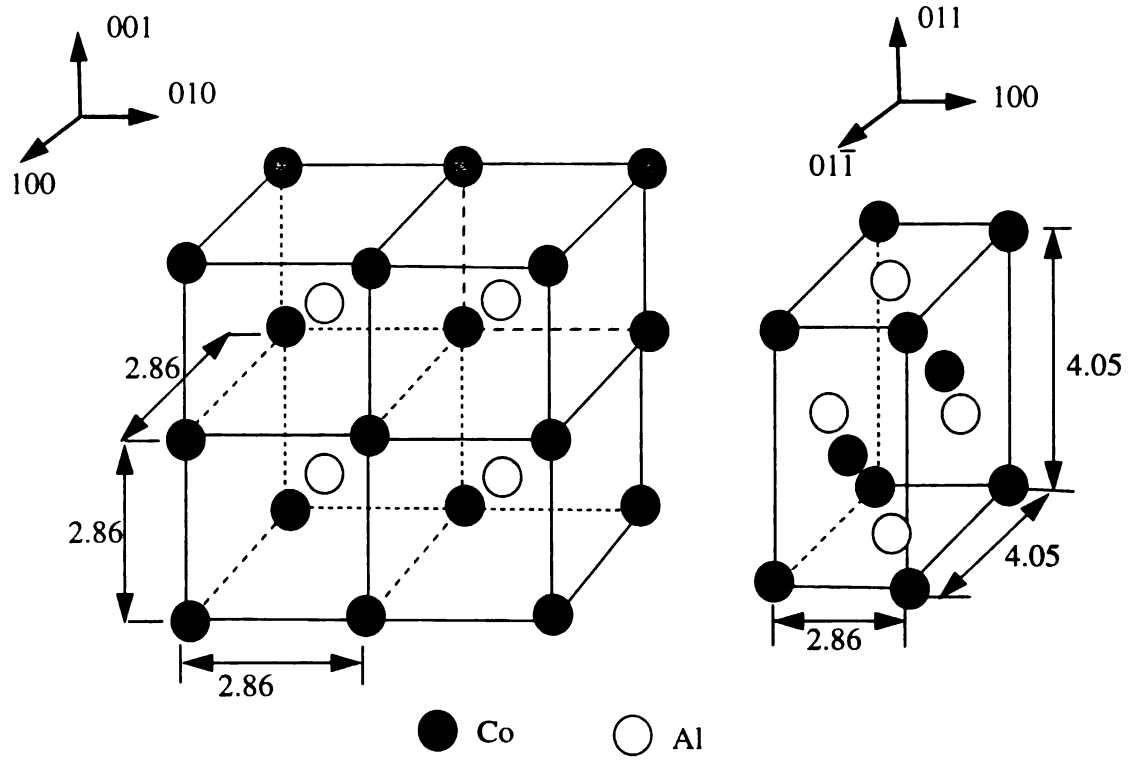

Figure 62 (a) Unit cell configuration used for <100>{001} dislocation image simulations.
(b) Alternate unit cell used for <100>{011} dislocation image simulations.

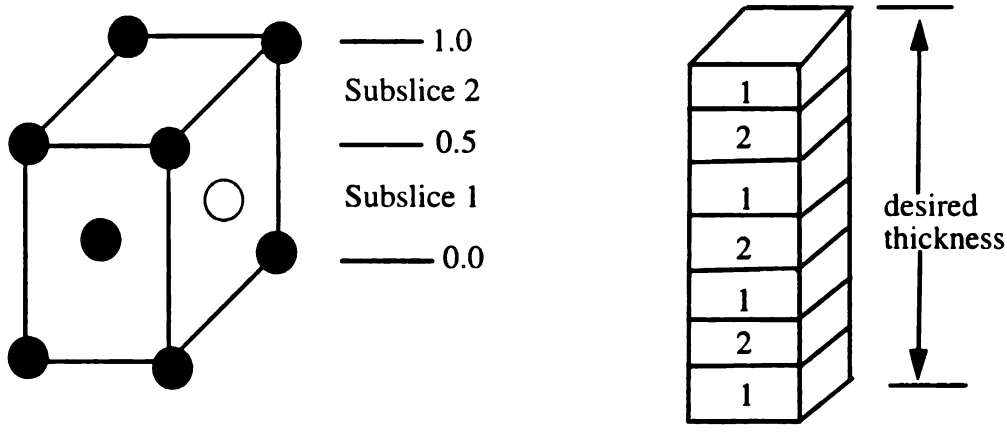

Figure 63 Unit cell sliced used in [100](011) core simulation. The different atom shades indicate which slice the atoms are included.

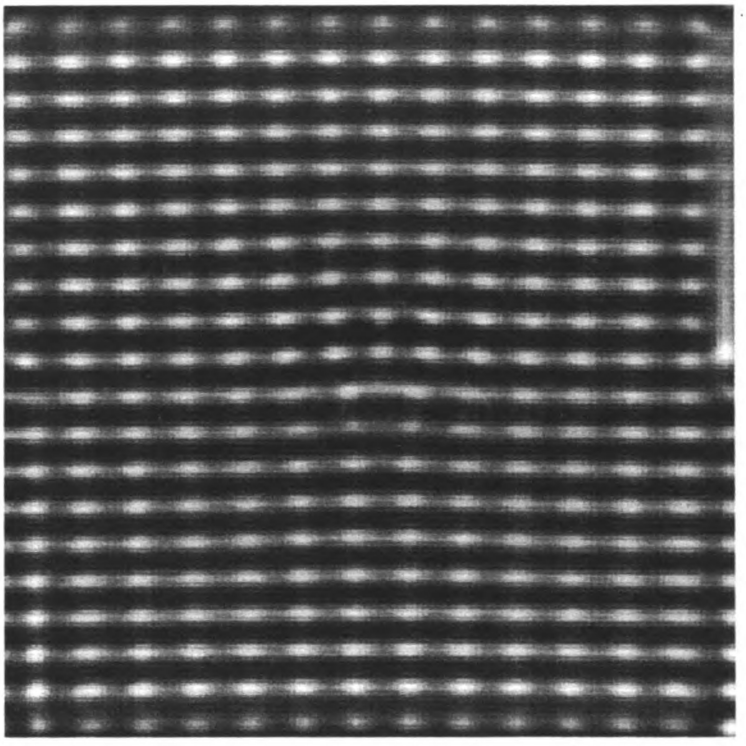

Figure 64 A [100](011) core in Co-50Al simulated at the conditions of df=-70 nm and thickness of 4 nm.

(a)

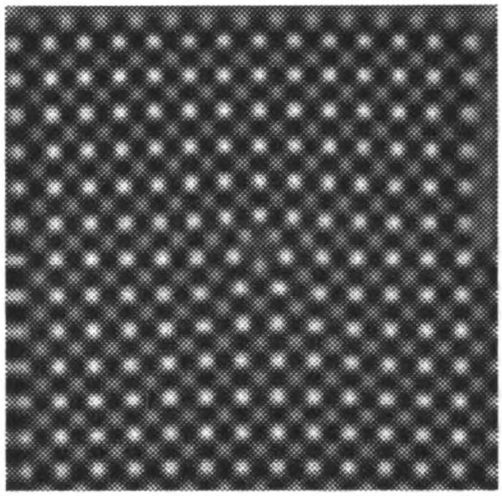

(b)

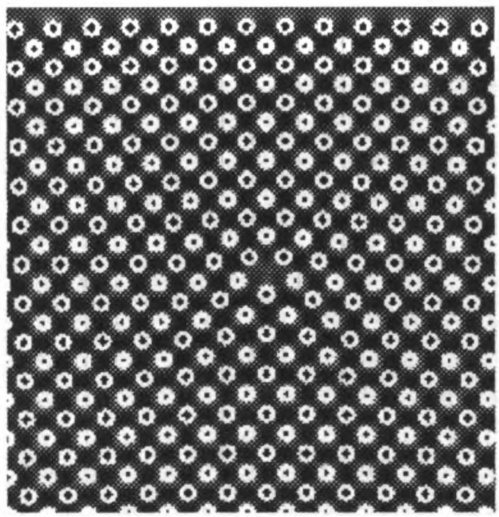

Figure 65 Core structure simulation of an [010](001) dislocation in Ni-50Al simulated at conditions of defocus value -70 nm and thickness 2.3 nm (a) Ni-50Al core, (b) same simulation with superimposed atom positions.

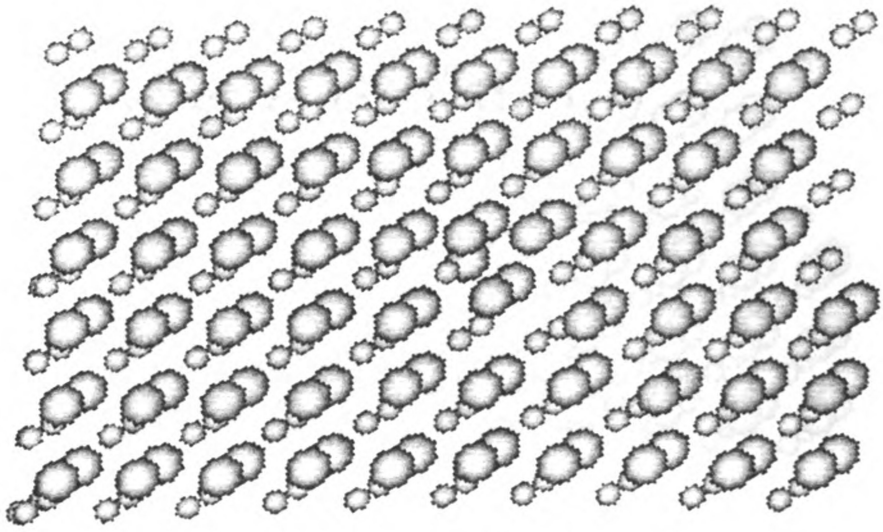

(a)

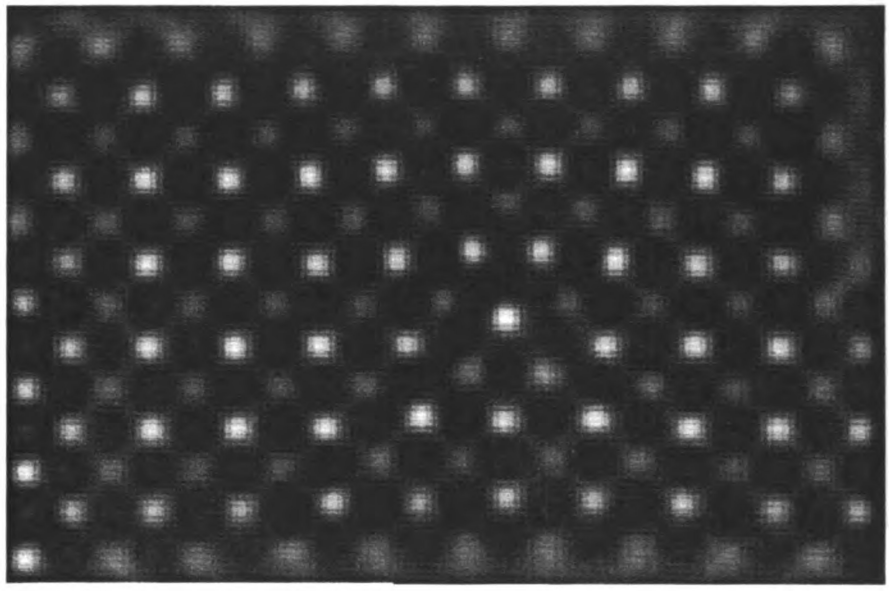

(b)

Figure 66 Effect of off-stoichiometric composition change on the core structure in Ni-50Al. (a) Supercell of [010](001) edge dislocation core in Ni-rich Ni-Al. Large spheres are Ni while small spheres are Al. (b) Simulated HREM image of core structure of [010](001) dislocation in Ni-rich Ni-Al.

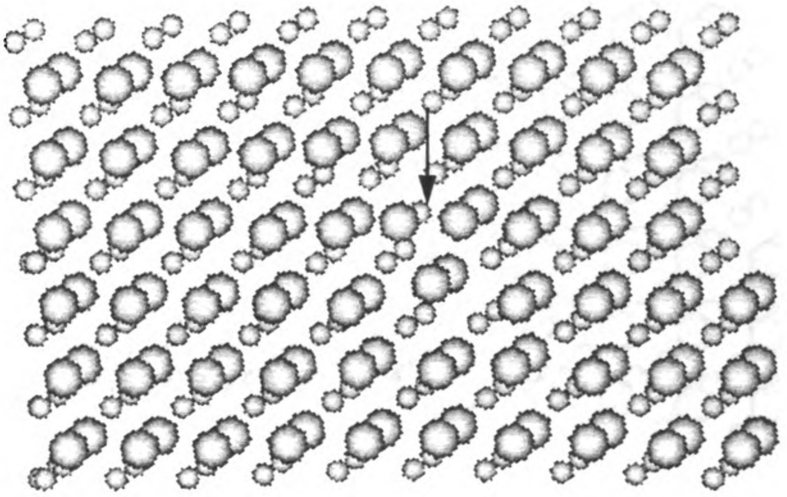

(a)

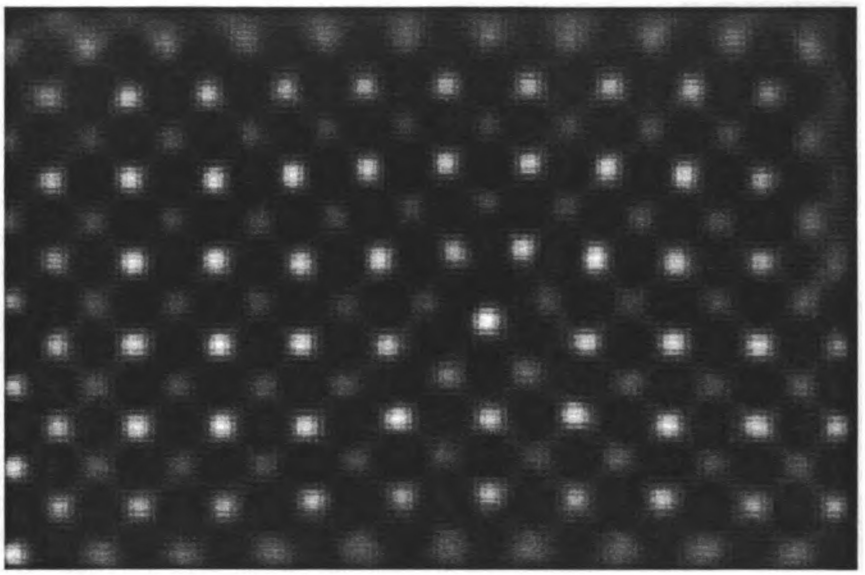

(b)

Figure 67 Effect of stoichiometry deviation (Al rich) on core structure.

(a) Supercell of [010](001) edge dislocation core in Al-rich Ni-Al. Large spheres represent Ni while small spheres are Al. The extra Al atom is indicated by the arrow.

(b) Simulated HREM image of core structure of [010](001) dislocation in Al-rich Ni-Al.

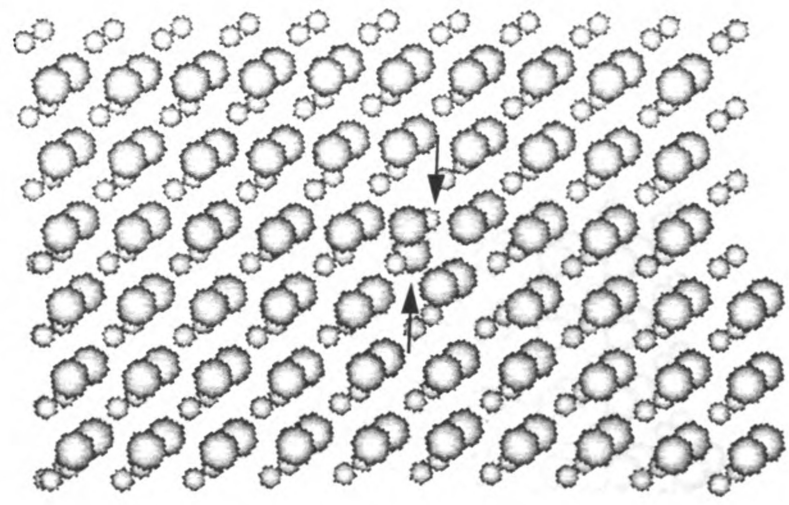

(a)

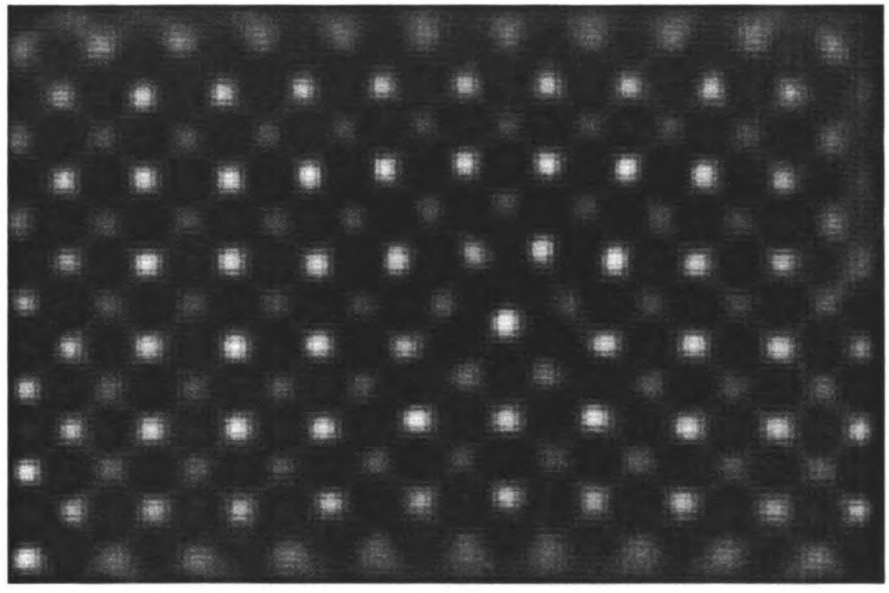

(b)

Figure 68 Anti-site defect in core structure (a Ni atom exchanges position with a Al atom).

(a) Supercell of [010](001) edge dislocation core in Ni-Al. Large spheres represent Ni while small spheres are Al. The anti-sites are indicated by the arrows.

(b) Simulated HREM image of core structure of [010](001) dislocation in Ni-Al.

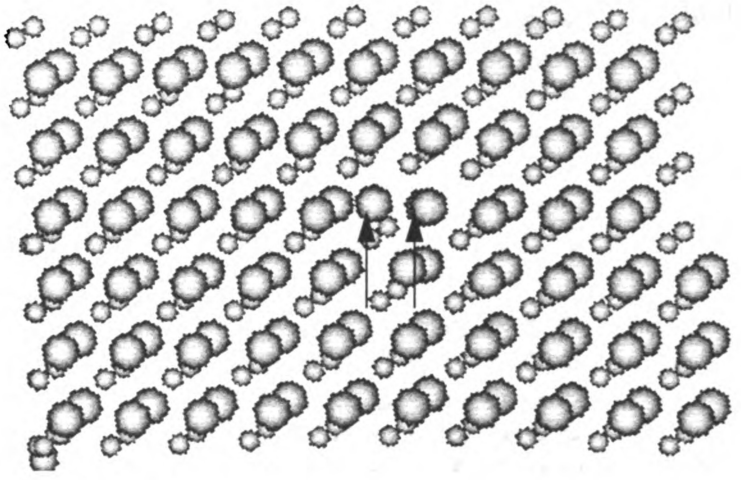

(a)

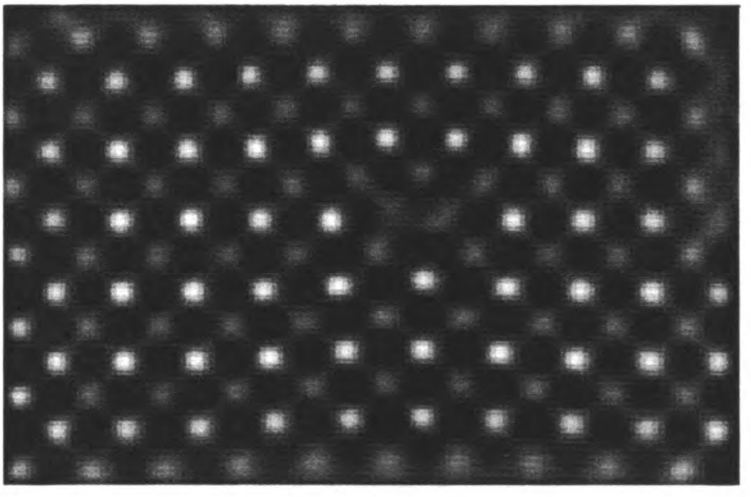

(b)

Figure 69 Effect of right-in-core vacancies in core structure in Ni-Al
(a) Two vacanies exist in dislocation core (indicated by arrows).
(b) HREM image simulated at df=-70 nm and thickness=2.2 nm.

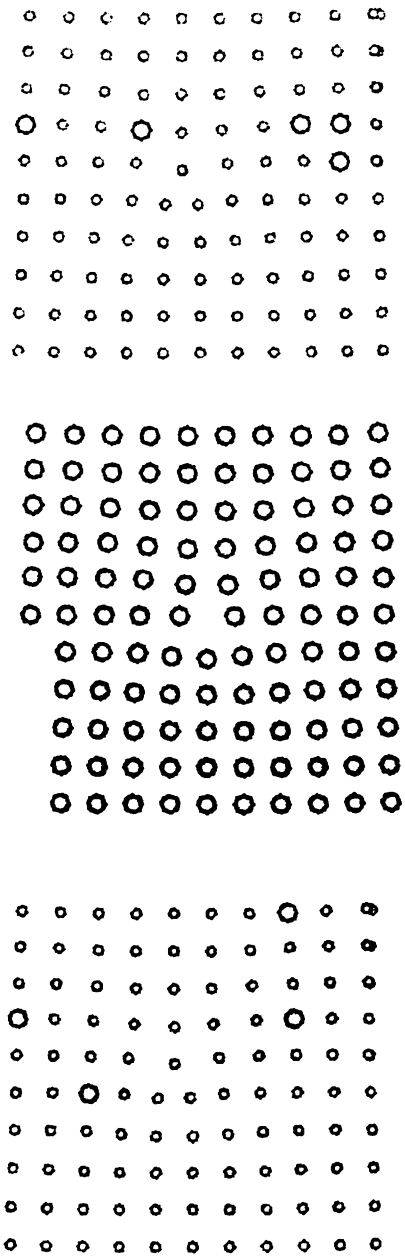

Figure 70 Atom arrangement in Ni48Al model structure. The supercell contains five layers(a) to (e) with Ni substitution. (f) HREM image simulated at df=-70 nm and thickness=2.2 nm.

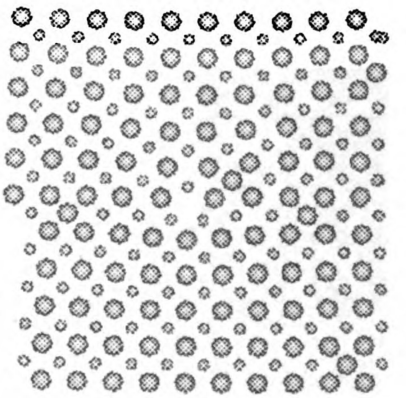

(d) t=0.8

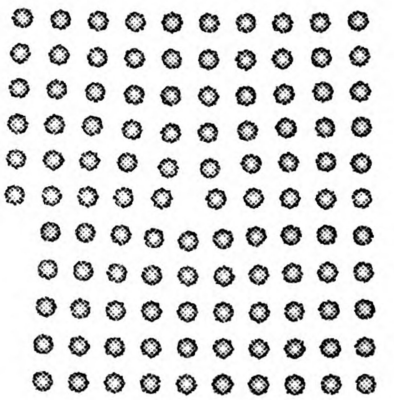

(e) t=1.2

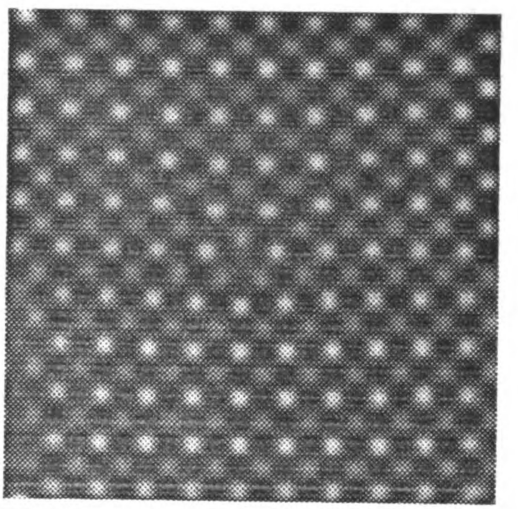

(f)

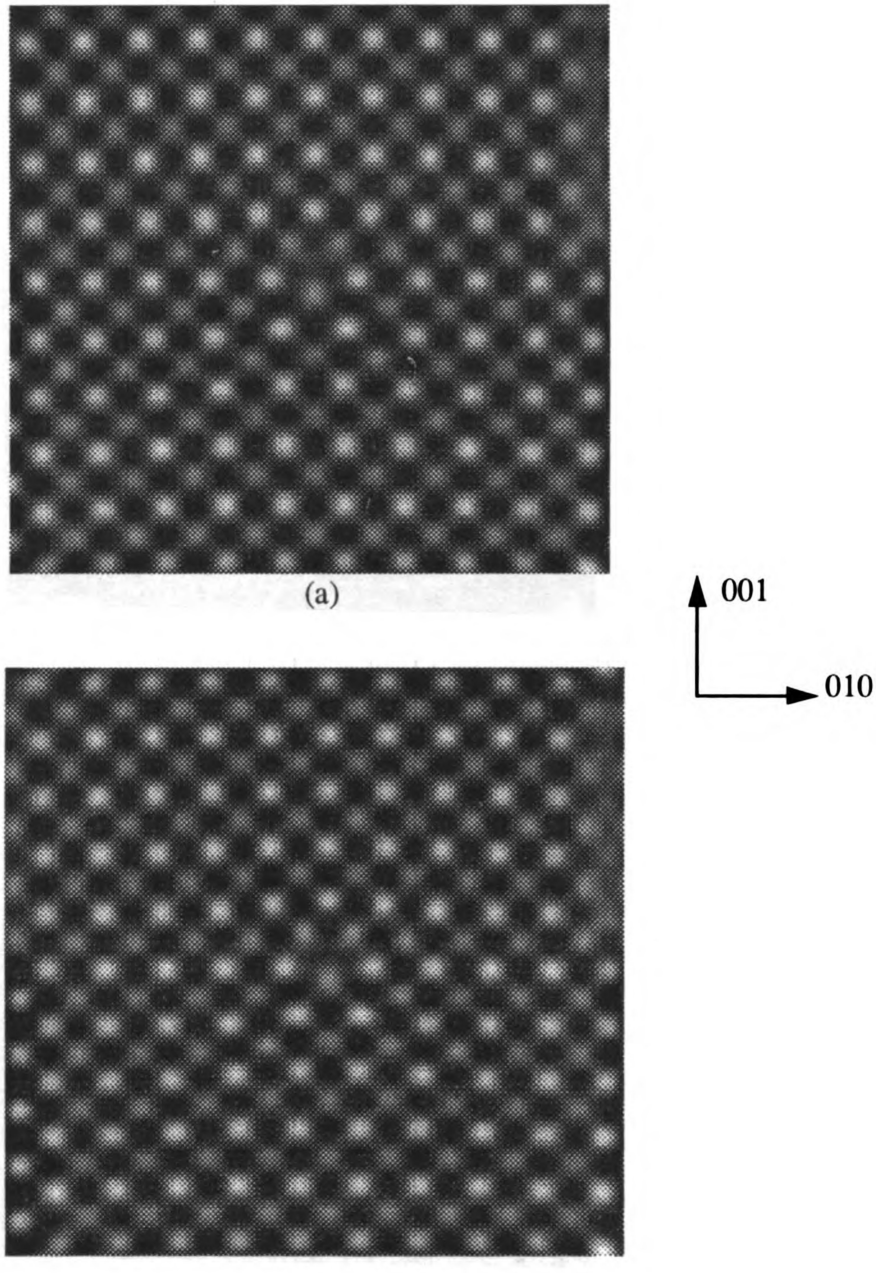

(a)

(b)

Figure 71 Simulated HREM images of core structures with random Ni substitution in Ni-48Al. (a) seed 1 (b) seed 2.

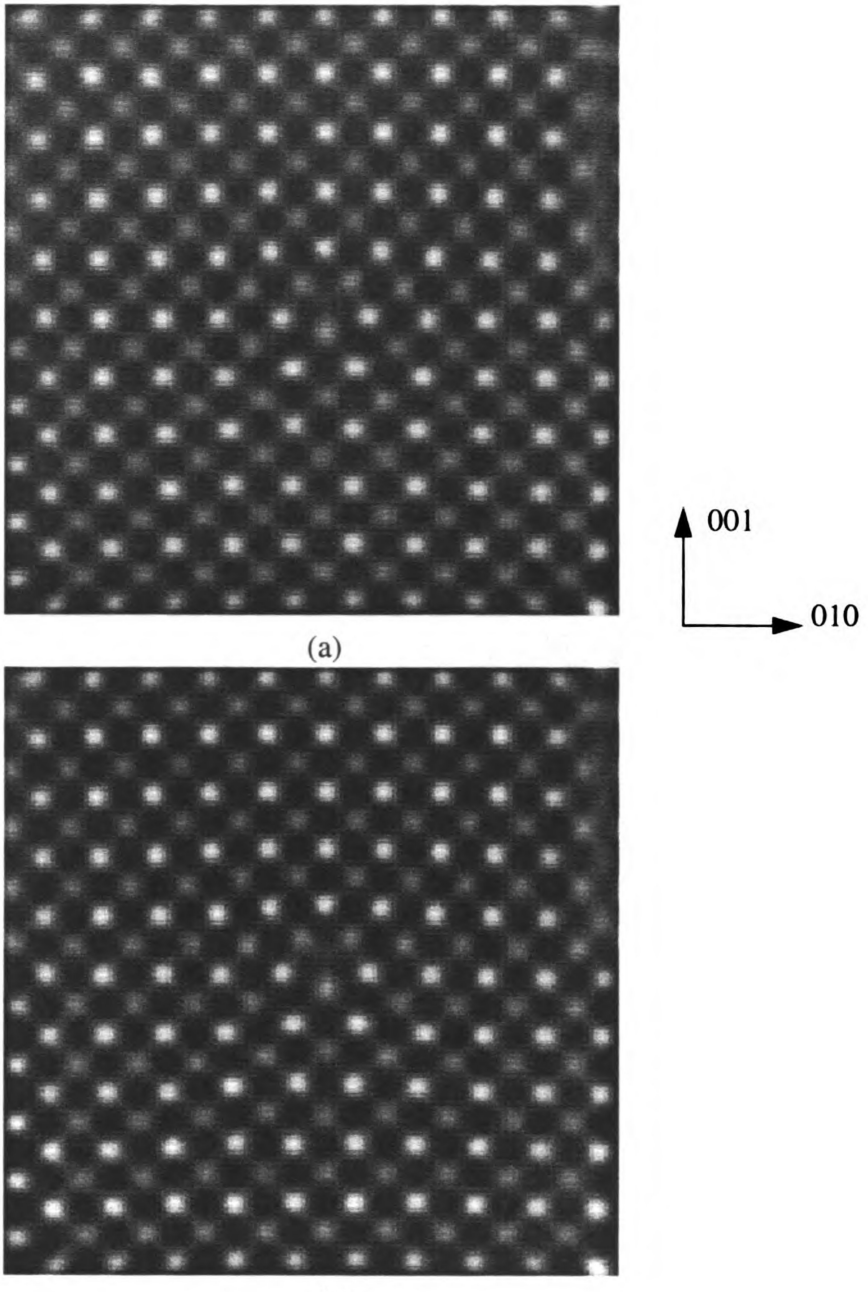

Figure 72 Simulated HREM images of core structures using random Al substitution in Ni-52Al. (a) seed 1, (b) seed 2.

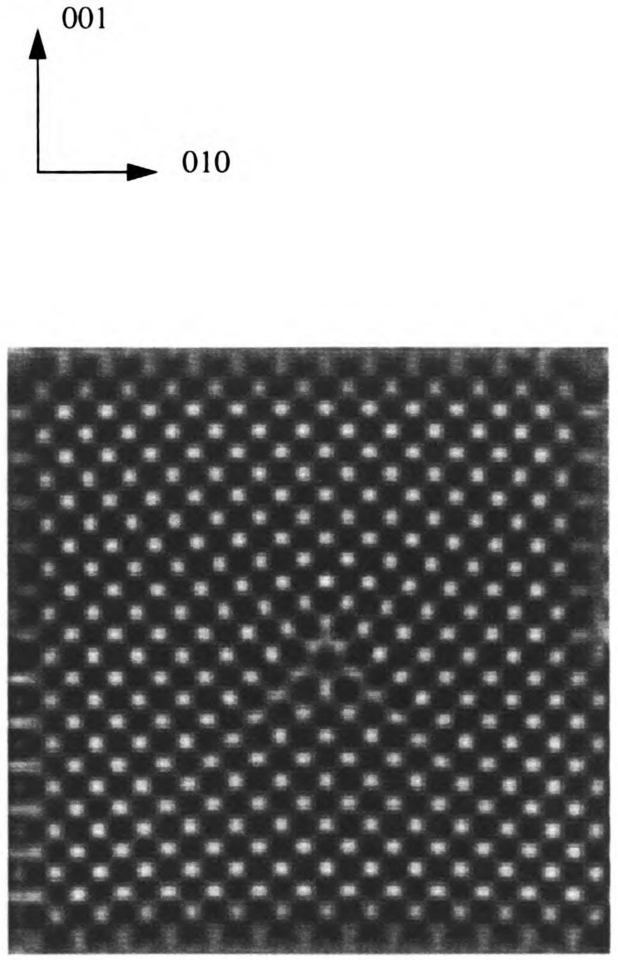

Figure 73 Image simulation of core structure of [010](001) edge dislocation in Ni-50Al with random anti-sites.

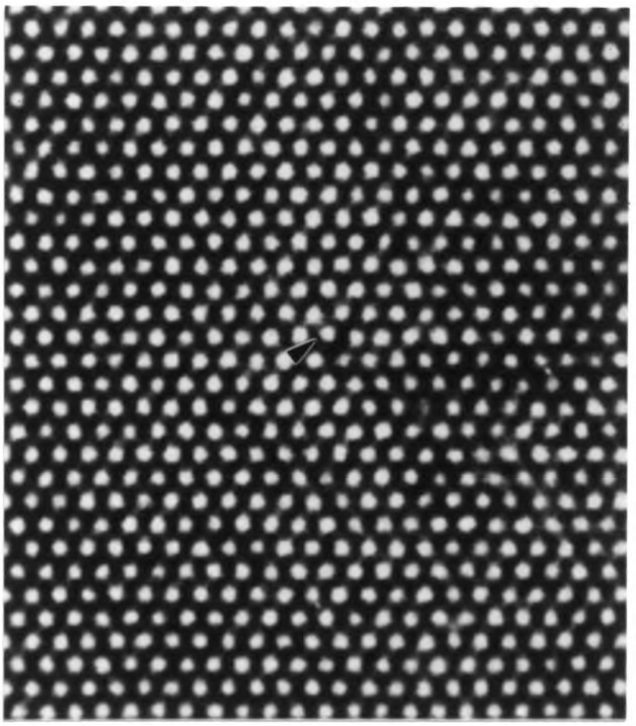

Figure 74 HREM micrograph of a <111> screw dislocation in Ni-50Al.

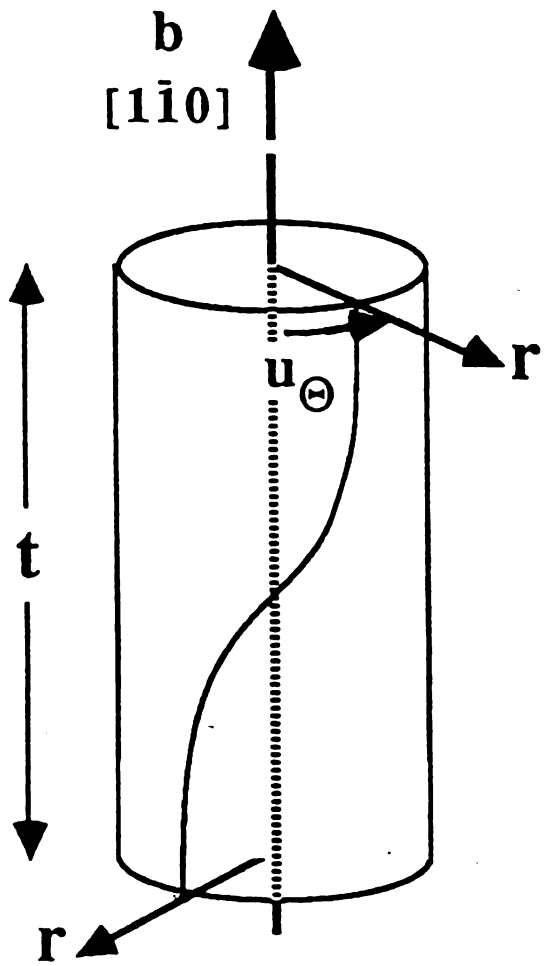

Figure 75 Schematic drawing of a twisted screw dislocation in single crystal.

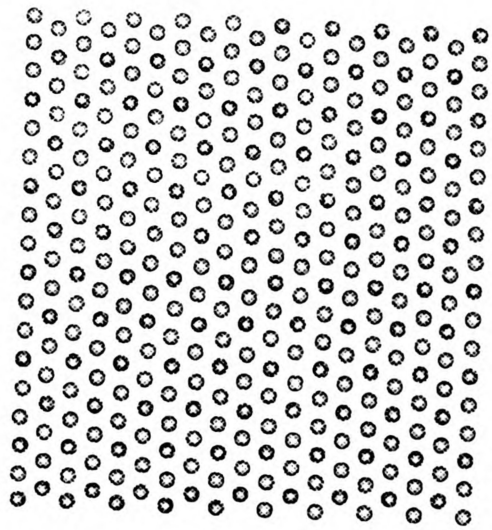

(a)

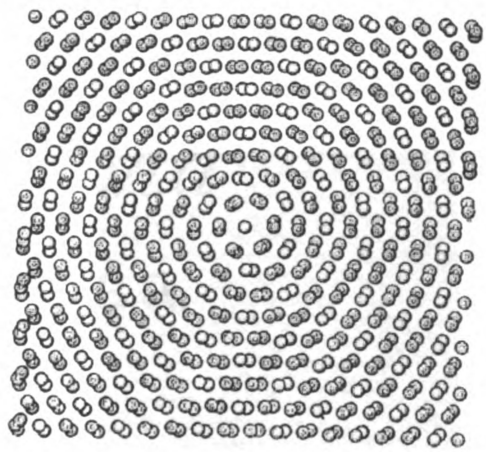

(b)

Figure 76 Atom positions in data file used for core structure simulations of <111> screw dislocation. (a) without Eshelby twist (b) with Eshelby twist.

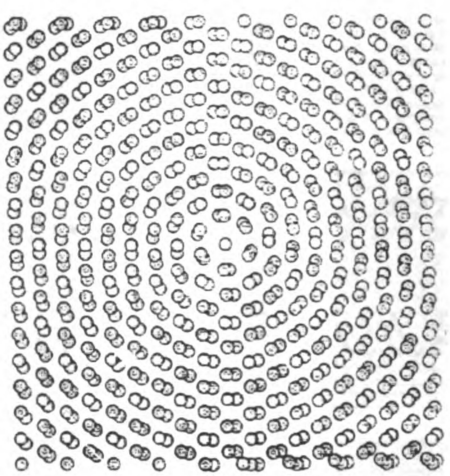

(a)

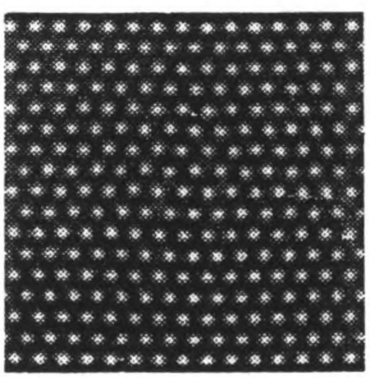

(b)

Fgiure 77 Core structures of <111> screw dislocation in Ni-50Al simulating the Eshelby Twist effect. (a) atom position profile, (b) simulation with twist.

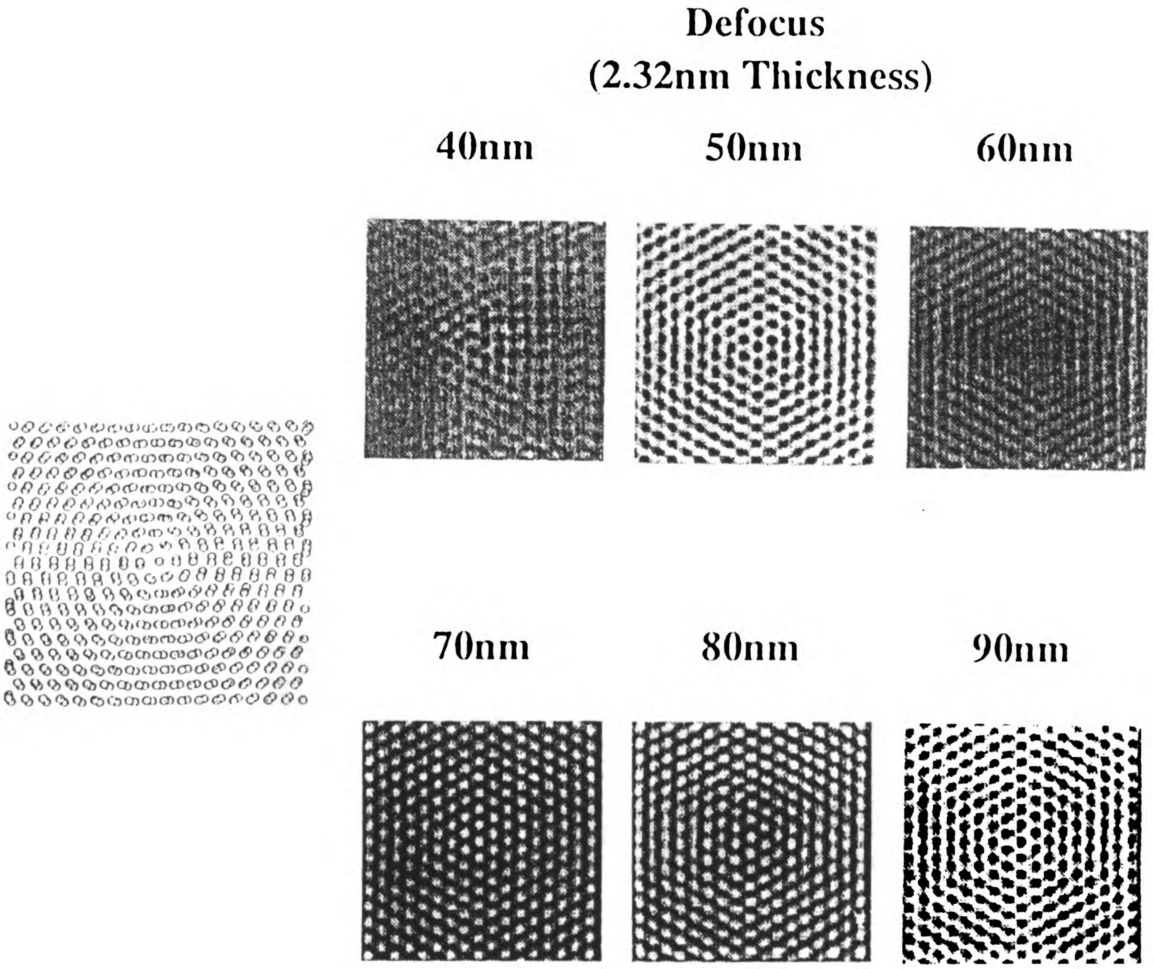

Figure 78 Through focal series of HREM simulations for <111> screw dislocation in Ni-50Al. The foil thickness is 2.32 nm.

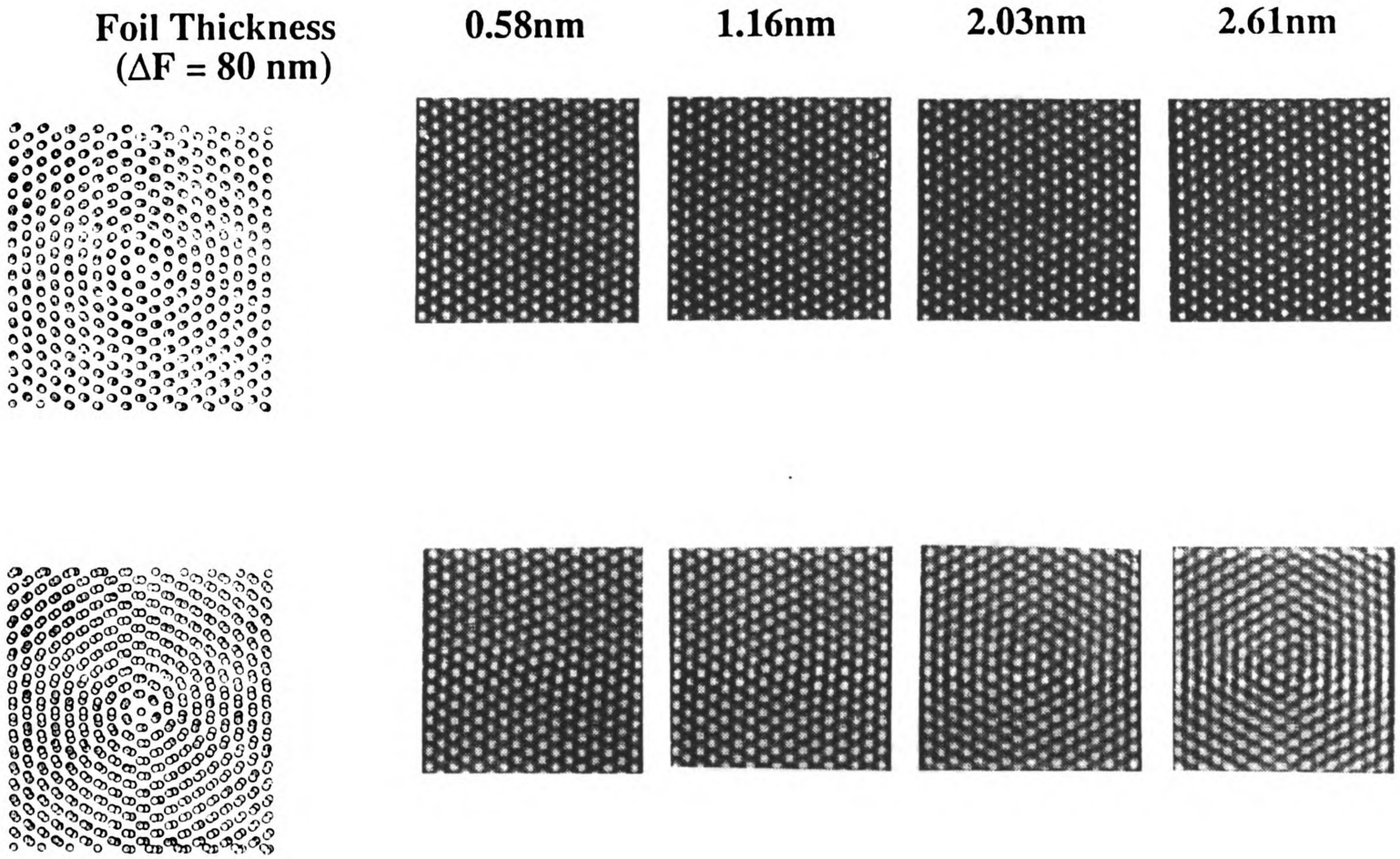

Figure 79 Thickness series of HREM simulations for <111> screw dislocation in Ni-50Al. The defocus value is -80 nm.

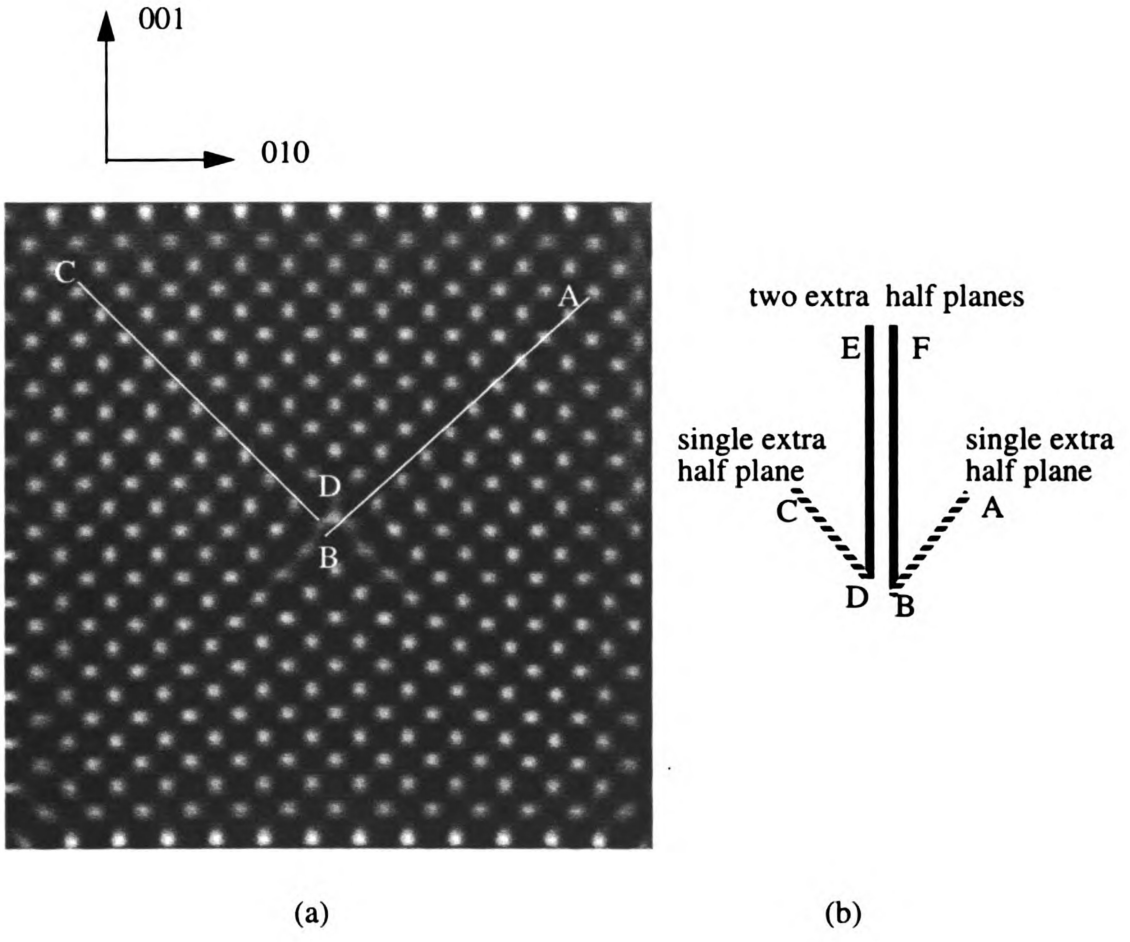

(a) (b)

Figure 80 Core structure of an [010](001) edge dislocation in Fe-50Al. Two extra half planes (ED and FB in (b)) terminate at position D and B in (a). Viewing in the [011] and [0$\bar{1}$1] reveals the single extra half planes.

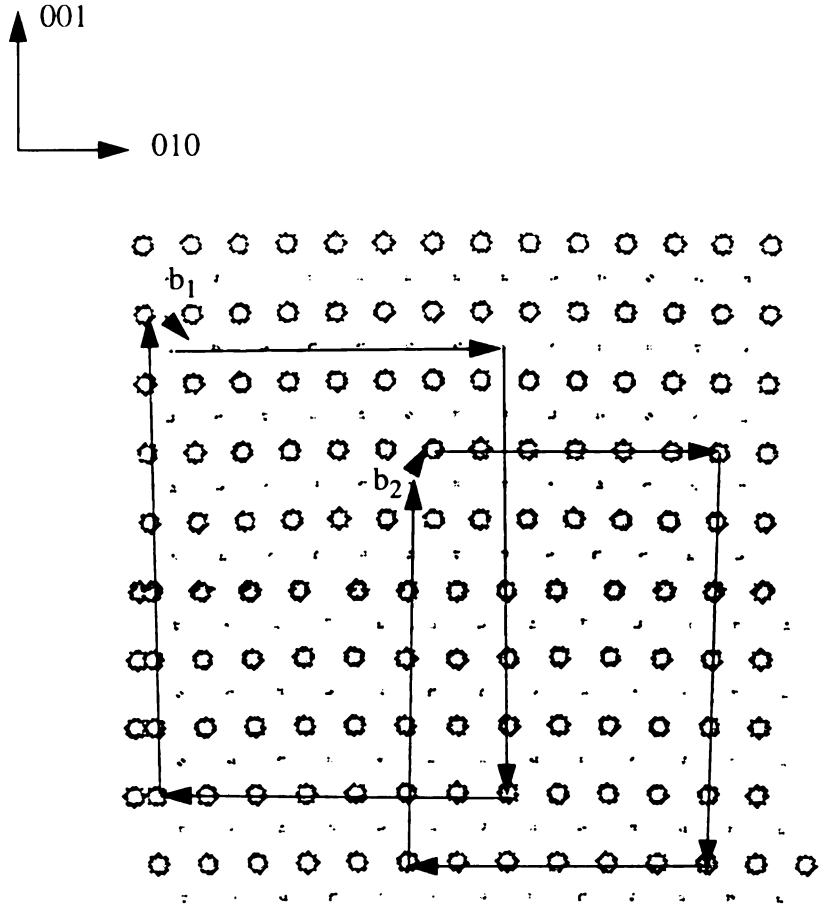

Figure 81 Burgers circuit established on single layer projected images. The Burgers vector of the superpartial dislocation are b1=1/2[$\bar{1}1\bar{1}$] and b2=1/2[111]. The large dots represent Fe and the small dots represent Al.

Table 10 Debye-Waller Factors [111]

Element	D (20 K)	D (93 K)	D (293 K)
Co	0.002	0.045	0.275
Ni	0.001	0.030	0.180
Fe	0.003	0.060	0.350
Al	0.005	0.110	0.640

4. Further Discussion

The differences in the mechanical properties of the B2 aluminides CoAl, NiAl and FeAl are significant. However, the reasons for those difference are still not clear. In this chapter, an attempt will be made to rationalize the differences by making comparative studies of the mechanical testing results, dislocation analysis and core structures obtained by experimental examination.

4.1 Mechanical Properties

4.1.1 Mechanical Properties of Co-Al At Elevated Temperatures

The compressive behavior of the [011] oriented Co-48, -50 and- 52Al are presented in section 3.1. The 0.2 percent off-set yield stresses are obtained from the corresponding stress-strain curves. The slip trace analysis indicates {001} slip planes for all three compositions, while the primary Burgers vector has been determined using TEM contrast analysis to be <100>. The cirtical resolved shear stress (CRSS) which is a measurement of the minimum shear stress need to initiate slip on a certain slip system can then be calculated for <100>{001} slip in these alloys. The CRSS can be calculated using the Schmids law:

$$\tau_{crss} = \frac{P_s}{A}\cos\theta\cos\phi \qquad \text{.....(37)}$$

where;

P_s is the load at yielding

A is the true cross-section area

θ is the angle between the slip direction and the compression axis. and ϕ is the angle between the slip plane normal and the compression axis.

The term $\cos\theta\cos\phi$ is termed as the Schmid factor.The P_y/A values were determined from the 0.2 percent offset yield stress and the angles θ and ϕ were measured using a stereographic projection of the single crystal compression samples. The calculated CRSS values are listed in table 11.

[001] oriented Co-50Al has the much higher yield strength than [011] oriented Co-50Al (fig. 28). The dislocation analysis presented in section 3.4 shows <011>{112} operative slip systems before kinking and <100>{001} operative slip systems after kinking. The Schmid factor is 0.28 for <011>{112} slip system in the [001] orientation. The CRSS has been determined using the Schmid law and is listed in table 11. It is clear that <011>{112} slip system has much higher CRSS value than <100>{001}.

Table 11 indicates that the CRSS of <100>{001} depends on stoichiometry. The 2 at.% off-stoichiometric deviations in composition raise the CRSS values. These differences might be explained by the core structures which occur with changes in stoichiometry. Recalling section 3.3, the [010](001) edge dislocation cores are compact or undissociated in Co-50Al, while the dislocation cores are significantly climb dissociated in Co-48Al and Co-52Al. The complicated core configurations in off-stoichiometric Co-Al make core movement difficult. Since the displacement field in the core region is an elastic strain field, the difference in core structures may be related to some measurable parameters that are indicative of interatomic potentials. Young's modulus is one of those parameters. That is: Young's modulus is believed to reflect the atomic bonding strength. It

means that the difference in Young's modulus should be in agreement with the difference in core structures between Co-Al. The measurement of Young's modulus (296 GPa for Co-Al and 320 GPa for Co-52Al) [31] supports this argument. Therefore the difference in core structures due to stoichiometric deviations may result in the difference in CRSS value among Co-48, -50 and 52Al.

In addtion to potentials, slip plane bending in the core center may affect core movement. Minimum distortion of slip planes in the core center is found in Co-50Al, while the maximum distortion is observed in Co-52Al, which corresponds to the lowest CRSS in Co-50Al and the highest CRSS in Co-52Al.

4.1.2 Mechanical properties of other B2 alloys

Compared to Ni-Al and Fe-Al (see section 2.2), Co-Al has the highest strength and hardness at elevated temperatures (fig. 6). Additionally, the mechanical behavior of Co-Al is more sensitive to stoichiometry deviations than Ni-Al and Fe-Al (fig. 2 and 6). These phenomenon may be explained by characteristics of the dislocation core structures in these alloys.

<100>{001} edge dislocations dominate the plastic deformation process in [011] oriented Co-Al and Ni-Al [46, 114, 115]. This slip system is also observed in [001] oriented Fe-Al [116]. Comparison of core structures of <100>{001} edge dislocations in Co-50Al, Ni-50Al and Fe-50Al (fig. 82) shows that all of the dislocation cores are compact or have minimal dissociation. However, the simulations of Farkas at al. show that the compact <010> cores usually have non-planar spreading. For example, <010>{001} cores in Ni-50Al structures spread on three {110} planes [62,68]. A core with non-planar spread-

ing requires a larger applied stress to slip than a core without non-planar spreading [table 4]. This larger stress is necessary to compress to core into a planar configuration. However, it has not been possible to measure any significant non-planar spreading of a dislocation core from experimental HREM micrographs of dislocations in the stoichiometric alloys.

The effect of composition on the mechanical behavior of the three B2 alloys can be explained by core structures of the <100>{001} edge dislocations. The extra half planes in <100>{001} edge dislocation cores in Co-48Al and Co-52Al are significantly separated (fig. 52-56), whereas such seperation is very limited in Ni-48Al and Fe-40Al (fig. 83). Seperation of extra half planes is also termed as dissociation and it will result in two superpartial 1/2<111> dislocations plus anti-phase boundary in between. These superpartial dislocations can not glide on the {001} slip plane. Hence, movement of a dissociated core needs a high external stress to push the separated extra partials together. The wider the separation, the higher the initiation stress.

4.2 Dislocations in Co-Al, Ni-Al and Fe-Al

4.2.1 Dislocation density in Co-48Al, Co-50Al and Co-52Al

As shown in section 3.3, the majority of the dislocations observed in the deformed Co-Al (except [001] compression samples) are <100>{001} edge dislocations. However, the density of dislocations observed is dependent upon alloy stoichiometry. Even though the dislocation density has not been measured quantitatively due to time limitations, qualitatively the density of dislocations in Co-50Al is the highest among the three compositions. The lack of active dislocations may be one of the main reasons for lack of the

plasticity in the off-stoichiometric Co-Al. On the other hand, the core structures of the dislocations may to a large degree determine the dislocation activiation under the conditions of stress, temperature and orientation. The <010> dislocations in Co-50Al have compact cores, while the <010> dislocations in Co-48Al and Co-52Al have dissociated cores. Furthermore, the dislocation cores in Co-52Al are more complicated than those in Co-48Al. If core dissociation plays a more important role in dislocation initiation than core spreading, the difference in dislocation density due to stoichiometry may be explained by core dissociation. Dislocation cores in Co-50Al display minimal dissociation and the corresponding dislocation density is the highest; dislocation cores in Co-52Al have complicated dissociations (climb dissociation and mixed dissociation), and the corresponding dislocation density is the lowest.

4.2.2 Dislocation density in Ni-Al and Fe-Al

Typical dislocation structures in Co-50Al, Ni-50Al and Fe-50Al deformed at 673-873 K are shown in figure 41 and else where [116,117]. <010>{001} edge dislocations dominate the deformation process in Co-Al and Fe-Al. In addtion to <010>{001} dislocations, <010>{101} edge dislocations are also observed in Ni-50Al [127]. The dislocation density is lower in Co-Al than in either Ni-Al or Fe-Al when these images are compared. Furthermore, this difference is more dramatic when off-stoichiometric Co-Al, Ni-Al and Fe-Al are compared.

The core structures of the <010>{001} edge dislocations may influence these differences in dislocation densities. In stoichiometric Co-50Al, Ni-50Al and Fe-50Al, the core structures of the <010>{001} edge dislocations are similar experimentally and theo-

retically. However, the simulations show that in Ni-50Al, the compact core of <100>{001} edge dislocation spreads in three {011} planes. If this argument is true, the non-planar spreading of the dislocation core may determine dislocation activation under the testing conditions. Increases in applied stress and temperature will overcome the barrier of non-planar spreading of dislocation cores.

In non-stoichiometric Co-Al, Ni-Al and Fe-Al, dislocation dissociation may play a key role in slip initiation. The dislocation densities observed in the compression specimens are a result of dislocation generation versus motion (fig. 42) [116,117]. If dislocation generation is difficult and dislocation movement is easy, the corresponding dislocation density should be low; if dislocation generation is easy and dislocation movement is difficult, the corresponding dislocation density is high. The core structure should affect both generation and motion of dislocations. Recalling the slip trace density on the compression specimens, Co-50Al has the highest slip line density, while Co-52Al has the lowest slip line density. It is reasonable to say that dislocation core structure influences the dislocation initiation more significantly than the dislocation movement. The larger the dissociation, the lower the activated dislocation density. Co-52Al has a more complicated dislocation dissociation, and its dislocation density is the lowest.

4.3 Core structures

Comparison of the core structures of various B2 aluminides will be performed in this section. The local lattice distortion, spreading and dissociation of the cores will be emphasized.

4.3.1 Core structures in stoichiometric B2 alloys

Compactness is the common feature of <100>{001} cores in Co50Al and Ni-50Al (fig. 82). However, simulations indicate there exists non-planar spreading on {110} planes which is not readily observed by HREM. This non-spreading nature of a compact core is explained in detail as follows:

A necessary condition for dissociation of a dislocation core into partial dislocations is the existence of a stable planar fault which corresponds to the local minima of the γ surface. In B2 Ni-Al, there are no stable planar faults except for an APB on {110} and {112} [62,65]. This is why there is no dissociation of the core into partial dislocations except 1/2<111> superpartials in Ni-Al. However, the γ energy increase on γ surfaces may not be uniform in all the directions. In some directions, the energy increases at slower rate than other directions. Therefore the core tends to spread along these directions. These directions are also termed corridor directions [115]. Figure 84a is the (110) γ surface on which [110] is the corridor direction. Figure 84b shows the (100) γ surface and the planar fault is completely symmetric. This means that no corridor direction can be defined in this region. Figure 84c shows the (111) γ surface and three 1/2<112> vectors are corridor directions. Figure 85 compares the energy curves along the preferred directions along each plane, indicating <100>{001} slip requires more initiation stress than the other slips. From previous analysis on B2 NiAl, [010] edge dislocations with line direction [100] and slip plane (001) dominate deformation process. However, a [010] displacement vector can not spread on its slip plane because the energies for planar faults on this plane are high. Therefore, the displacement field is most likely to spread on the (011) and $(0\bar{1}1)$ planes along the corridor directions $[01\bar{1}]$ and $[0\bar{1}1]$. In contrast, a <100>{011} core can spread

on its own slip plane and therefore is planar. According to model calculations, the activation stress of a non-planar core is ten times as high as that of a planar core [68]. According to this point of view, <010>{101} edge dislocations should have a CRSS lower than <010>{001} edge dislocations. However, no <010>{101} edge dislocations were found in [011] oriented Co-Al and Ni-Al except [011] Ni-50Al. There are two possibilities for lack of <010>{101} slip: (1) the Schmid factor for this system (0.35) is not large enough to activiate <010>{101} edge dislocations; (2) <010>{101} edge dislocations are activiated and sweep out of the crystal due to high mobility, leaving <100>{001} edge dislocations in the crystals. For the second possibility, <010>{001} slip would be a slower process than <010>{101} slip, and then would become a dominating factor in plastic deformation. However, recalling the slip traces observed on the compression specimens, only {001} slip planes are involved in plastic deformation. Therefore, it is reasonable to regard <100>{001} as the primary slip systems in Co-Al. Additionally, the dislocation interaction between <100> dislocations, which forms <110> and <111> dislocations, also reduces the mobility of <100> dislocations.

4.3.2. Core structures in off-stoichiometric B2 alloys

Characteristic of the core structures of <010> edge dislocations in B2 Co-48Al, Co-48Al, Ni-48Al and Fe-40Al is their dissociation. Climb dissociation and mixed dissociation exist in off-stoichiometric Co-Al (fig. 83a), while the corresponding dissociation in nickel rich Ni-Al and iron rich aluminides Fe-Al is minor. Figure 83b is an example of <100> core with edge character in Ni-48Al. The extra Ni half plane is separated from the extra Al half plane at the distance of two atom spacings in the [010] direction. Therefore,

this is a case of slight glide dissociation. Shown in figure 83c is the core structure of <100> edge dislocation in Fe-40Al. The extra Ni half plane and the extra Al plane are adjacent to each other, indicative of the compact nature. Recalling the core structures of <100> edge dislocations in Co-48Al and Co-52Al, the climb dissociation width is over four interatomic spaces. Hence, the differences in core dissociation between Co-Al, Ni-Al and Fe-Al can be characterized by two issues. One is the dissociation type. Ni-48Al has glide dissociation, while Co-48Al and Co-52Al have climb/mixed dissociations. To compress a glide dissociated core only requires glide motion of atoms, whereas to compress a climb dissociated core requires the climb motion of atoms. The latter process is more difficult than the former process. The second issue is the extent of dislocation dissociation. The extra half planes are only separated at one or two lattice spacings in Ni-48Al and are not separated in Fe-40Al, while this separation is more significant in Co-48Al and Co-52Al. These two factors make motion of the Co-Al core difficult to initiate. Therefore, core structures play a very important role in mechanical behavior of B2 aluminides Co-Al, Ni-Al and Fe-Al.

Stoichiometric deviations do not necessarily directly change the local chemical composition in the core region. Therefore, the core dissociation may not be directly related to core chemistry. However, off-stoichiometric composition creates numerous structural vacancies in these materials. Vacancies are very active at high temperature. Generation, segregation, migration and interaction of the structural and thermal vacancies may have significant influences on core structure and dislocation mobility.

4.3.3. Simulations of core structures

The simulated images agree well with the compact core structures. However, the simulations do not depict the minor differences in core structures between Co-Al, Ni-Al and Fe-Al. By carefully examining the simulated core structures of these alloys, one will find that each core configuration is exactly the same as the others because the potentials used for simulations are all similar for CoAl, NiAl and FeAl. The simulations also do not describe the climb dissociation of a dislocation core. Although vacancies and anti-site defects were set in the different locations of the core area during simulation, the simulated images do not changed visually. This can be attributed to the fact that the models do not utilize the composition dependent potentials, vacancy and interaction characteristics.

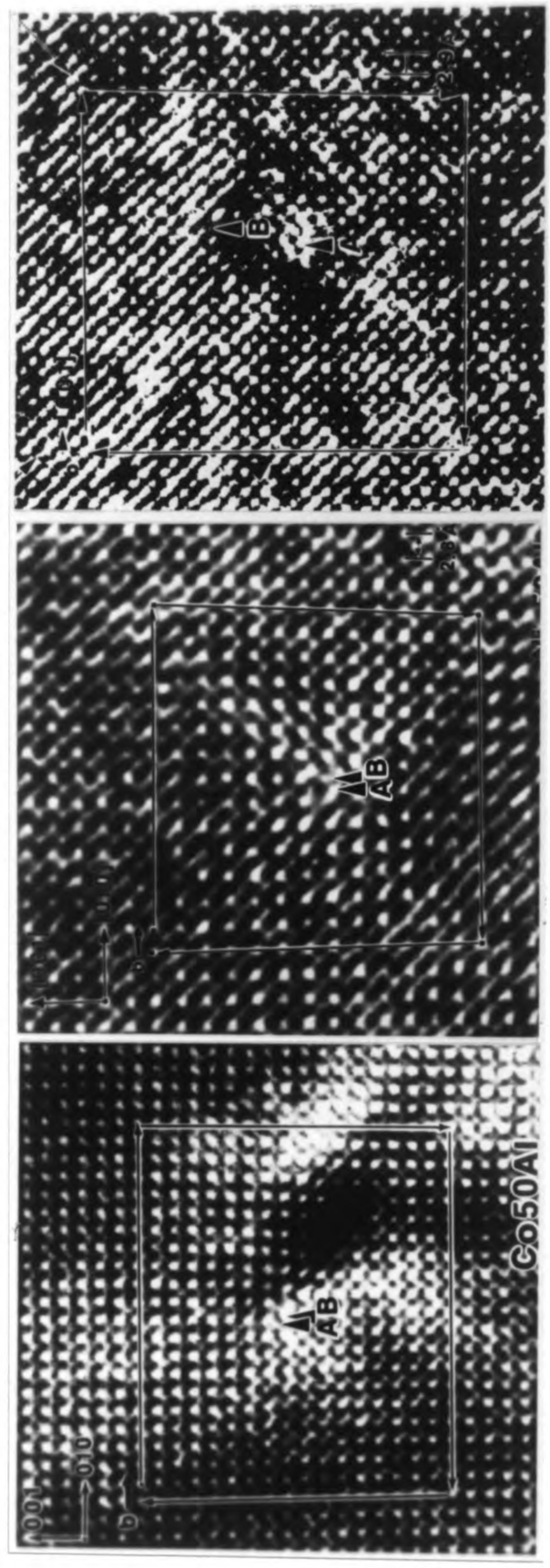

Figure 82 Comparison of core structures among the stoichiometric Co-50Al, Ni-50Al and Fe-50Al (from left to right).

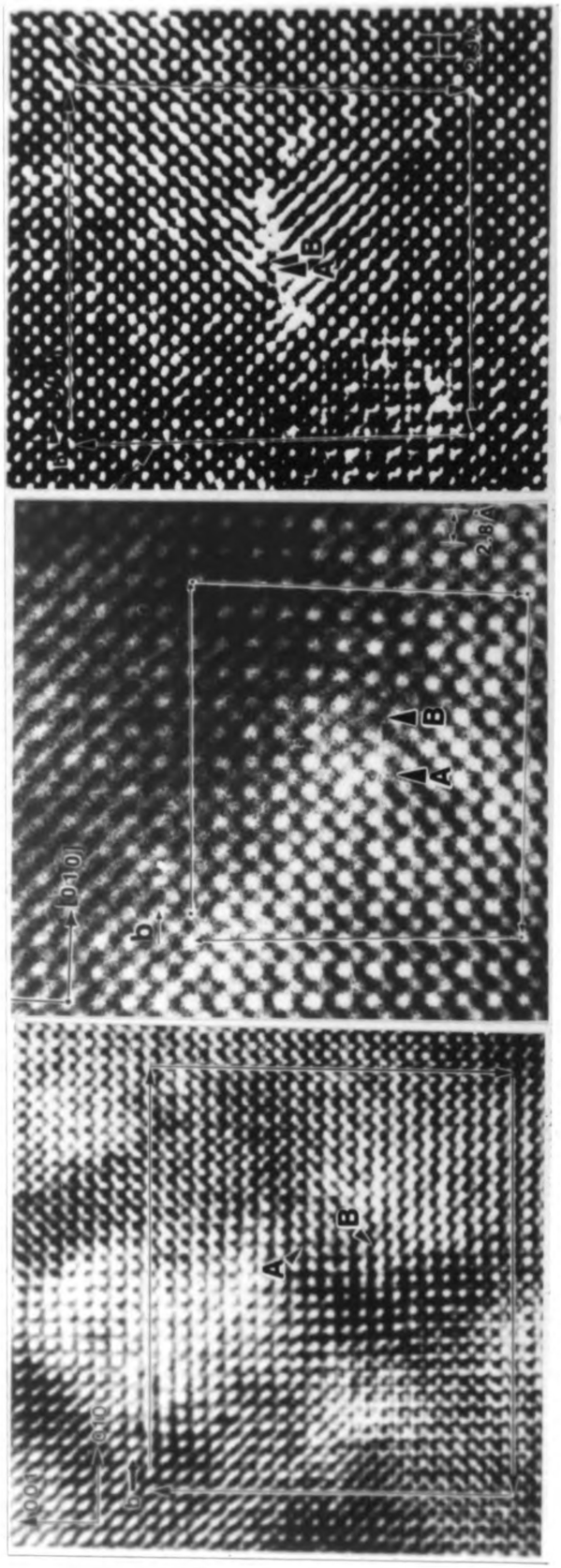

Figure 83 Comparison of core structures among the off-stoichiometric Co-48Al, Ni-48Al and Fe-40Al (from left to right).

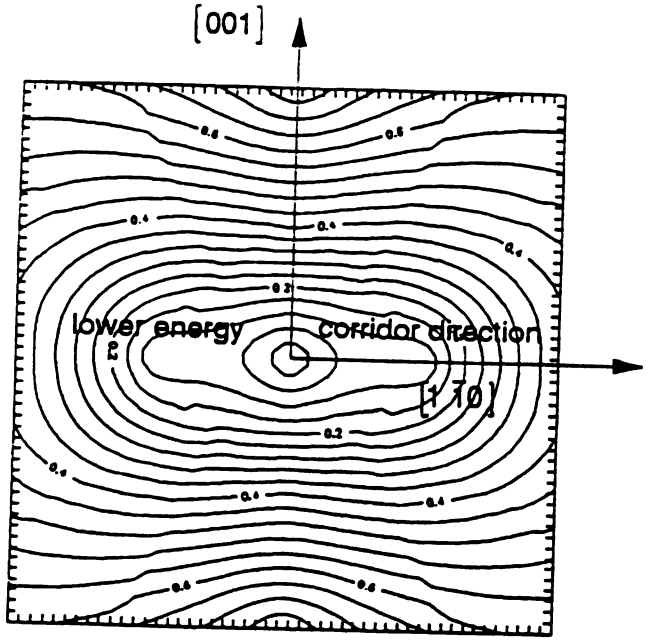

(a)

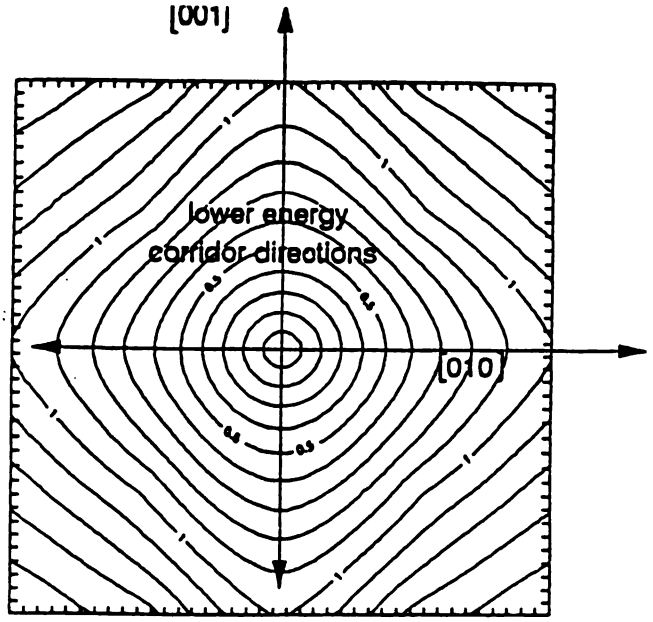

(b)

Figure 84 Comparison of the γ surfaces for <100>{011}, <100>{001} and <111>{112} slip systems

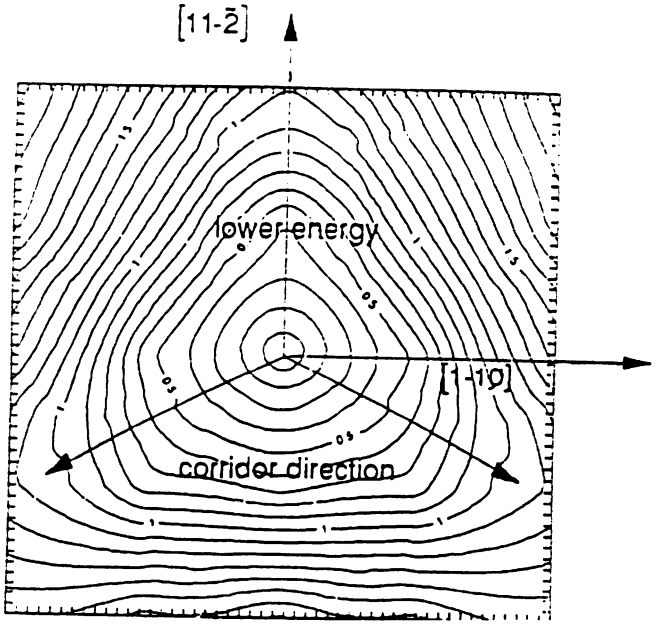

(c)

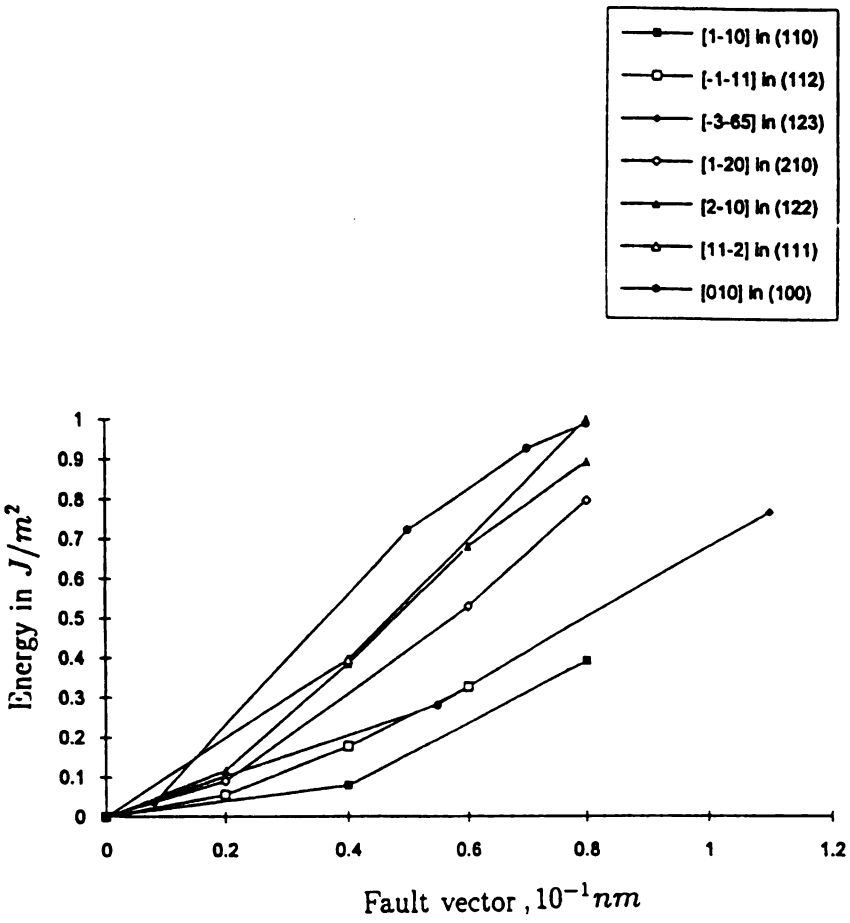

Figure 85 Comparison of the energy curves along the prefered directions in various slip systems [115].

Table 11 CRSS of [011] Co-Al and [001] Co-50Al

Slip system	Schmidt factor	$S_{0.1}$ (Mpa)	CRSS (Mpa)
<010>{001} in [011] Co-50Al	0.50	50	25
<010>(001} in [011] Co-48Al	0.50	60	30
<010>{001} in [011] Co-52Al	0.50	70	35
<011>{112} in [001] Co-50Al	0.28	240	69

5. Conclusions

Oriented B2 Co-Al alloys were mechanically tested at high temperatures and the corresponding slip planes were determined by slip trace analysis. The deformation-introduced dislocations and the dislocations in their as-grown state were analyzed using the **g•b=0** method. Core structures of <100>{001} edge dislocations were carefully examined using HREM. Image simulations were performed to interpret experimental results. A comparative study of the mechanical behavior, dislocation density and their core structures were conducted. Based on all the experimental results and analysis, conclusions are made as follows:

5.1 Mechanical properties

At room temperature, Co-Al is much more brittle than Ni-Al. At high temperatures, Co-48 and Co-52Al are significantly stronger than Co-50Al. In the [001] "hard" orientation, Co50Al exhibits much higher deformation resistance and displays the kinking phenomenon.

5.2 Dislocations and slip systems

<100>{001} cubic slip systems were observed in all the orientations, compositions and testing temperatures, indicating that the <100>{001} slip systems are easiest to be activated. <110> dislocations and <111> dislocations were also found in [123] oriented Co-50Al and [011] oriented Co-50Al and Co-48Al deformed at 1300 K. However, these dislocations were not activated at the lower temperature of 1100 K. In the [001] orientation, both <110> and <100> dislocations were seen in Co50Al deformed at 1300 K. <110> slip has much higher CRSS than <100> slip and therefore greatly lifts the compressive strength of the [001] oriented Co-50Al in the initial stage of deformation. After kinking,

the local orientation is shifted to non-<100> direction, the <100> slip is then predominant in deformation. Therefore the <100> edge dislocations are the most important dislocations in high temperature deformation of B2 aluminide Co-Al.

5.3 Core structures of <010> edge dislocations

Core structures of <100> edge dislocations in Co-50Al are characterized by compactness with non-planar spreading and/or slight dissociation. Dislocation core structures in Co-48Al display climb dissociation. Dislocation core structures in Co-52Al exhibit both climb and mixed dissociation.

5.4 Computer simulations

Computer simulations based on Farkas' core model match the experimental observations of core structures in Co50Al. The simulated core structures are always compact when the vacancy and anti-site defects are considered. Simulations of core structures in off-stoichiometric B2 alloys are not in good agreement with experimental images. The main reasons may be that the role of vacancies in core structures is not clear.

5.5 Mechanical behavior and core structures

Mechanical properties of B2 Co-Al, Ni-Al and Fe-Al are related to the <100>{001} edge dislocation core structures in these aluminides. In stoichiometric alloys, non-planar spreading of the <100>{001} edge dislocation cores plays the key role in dislocation slip initiation. Co-50Al cores may have more non-planar spreading than Ni-50Al and Fe-50Al. This may be responsible for the higher strength of Co-50Al than Ni-50Al and Fe-50Al. In off-stoichiometric aluminides, core dissociation may strongly influence the CRSS of <100>{001} edge dislocations. Co-48Al and Co-52Al have climb/mixed dissociated core structures, while Ni-48Al and Fe-40Al have glide dissociated

cores. Dissociation type and dissociation degree makes off-stoichiometric Co-Al stronger and more brittle than off-stoichiometric Ni-Al and Fe-Al.

References

[1]. C.T. Liu and K.S. Kumar, JOM, May, (1993), p. 38.

[2]. R. Darolia, JOM, Mar. (1993), p. 44.

[3]. E.P. George and C.T. Liu, J. Mater. Res., 5, (1990), p. 754.

[4]. D.F. Lahrman, R. Field and R. Doralia, Scr. Metall. Mater., Vol. 28, (1993), p. 709.

[5]. M.A. Crimp and K. Vedula, Mater. Sci. Eng., 78, (1986), p. 193.

[6]. T. Cheng, Scr. Metall. Mater., Vol.27, (1992), p. 771.

[7]. K. Ishida, R. Kinuma, N. Ueno and T. Wishizawa, Metall. Trans. A, Vol.22A, Feb, (1991), p. 441.

[8]. R. Darolia, D. Lahrman and R. Field, Scr. Metall. Mater., Vol.26, (1992), p. 1007.

[9]. R. Darolia, JOM, 43(3), (1991), p. 44.

[10]. C.T. Liu, and M. Takeyama, Scr. Metall. Mater., 24, (1990), p. 1583.

[11]. C.T. Liu, E.H. lee and C.G. Mckamey, Scr. Metall. Mater., Vol.23, (1989), p. 875.

[12]. R.W. Margevicius and J.J. Lewandowiski, Scr. Metall. Mater., Vol. 25, (1991), p. 2017.

[13]. J.H. Westbrook, J. Chem. Soc., Vol.103, (1956), p. 54.

[14]. M.A. Crimp, Ph.D. Dissertatioin, Case Western Researved Univ., (1988).

[15]. G. J. Drelles, M.S. Theses, Mich. Tech. Univ., (1985).

[16]. R.J. Wasilewski, S.R. Butler and J.E. Hanlon, Trans. TMS-AIME, Vol.239, Sept.

(1967), p. 1357.

[17]. R.L. Fleischer and R.J. Zabala, Metall. Trans. A, Vol. 21, (1990), p. 2709.

[18]. K.H. Hahn and K. Vedula, Scr. Matell. Mater., 23, (1989), p. 7.

[19]. J.D. Destefani, Advanced Mater. Proc., 2, (1989), p. 37.

[20]. R.R. Vandervoort, Trans of ASM, Vol.59, (1966), p. 1307.

[21]. R.L. Fleischer, J. Mater. Res., Vol.18, No.1, Jan. (1993), p. 59.

[22]. R.D. Noebe, R.R. Bowman, C.L. Cullers and S.V. Raj, "High Temperature Ordered Intermetallic Alloys IV", MRS symp. proc., Pittsburgh, PA(1990), p589.

[23]. R.T. Pascoe and C.W.A. Newey, Met. Sci. J., Vol.5, (1971). p. 50.

[24]. A. Ball and R.E. Smallman, Acta Metall., Vol.14, (1966), p. 1350.

[25]. L.A. Hocking, P.R. Strutt and R.A. Dodd, J. Inst. Met., 99, (1971), p. 98.

[26]. D.L. Yaney and W.D. Nix, J. Mater. Sci., 23, (1988), p. 3088.

[27]. J.D. Whittenberger, Mater. Sci. Eng., 73, (1985), p. 87.

[28]. J.D. Whittenberger, J. Mater. Sci., 22, (1987), p. 394.

[29]. F.C. Nix and F.E. Jaumot, Phys. Rev., 83, (1951), p. 1275.

[30]. C.F. Hancock and B.R. McDonnell, Phy. Stat. Sol., (a), 4, (1971), p. 143.

[31]. M.R. Harmouche and A. Wolfenden, Mater. Sci. Eng., 84, (1986), p. 35.

[32]. D.B. Miracle, Acta Metall. Mater., Vol. 41, No. 3, (1993), p. 649.

[33]. K.M. Chang, R. Doralia and H.A. Lipsitt, "High Temperature Ordered Intermetallic Alloys IV", MRS, symp. proc., Pittsburgh. PA, (1990), p. 597.

[34]. T. Takasugi, S. Watanabe and S. Hanada, Mater. Sci. Eng., Vol.A149, (1992), p.183.

[35]. D.L. Yaney, A.R. Pelton and W.D. Nix, J. Mater. Sci., Vol.21, (1986), p. 2083.

[36]. M. Yamaguchi and Y. Umakoshi, Progress Materials Science, Vol. 34 , (1990), p. 1.

[37]. A. Ball and R.E. Smallman, Acta Metall., Vol.14, (1966), p. 1517.

[38]. W.R. Kanne Jr., P.R. Strutt and R.A. Dodd, Trans. TMS-AIME, Vol.245, June (1969), p. 1259.

[39]. I. Baker and E.M. Schulson, Met. Trans. A, Vol.15A, June, (1984), p. 1129.

[40]. N.J. Zaluzer and H.L. Fraser, Scr. Metall., 8(1974)p1049.

[41]. A. Lasalmonie, J. Mater. Sci., 17, (1982), p. 2419.

[42]. H.L. Fraser, R.E. Smallman and M.H. Loretto, Phil. Mag., 28, (1973), p. 651.

[43]. R. Darolia, D.F. Lahrman, R.D. Field and A.J. Freeman, "High Temperature Ordered Intermetallic Alloys III", MRS symp. proc., Pittsburgh, PA, (1988), p. 113.

[44]. R.T. Pascoe and C.W.A. Newey, Physica Status Solidi, 29, (1968), p. 357.

[45]. H.L. Fraser, R.E. Smallman and M.H. Loretto, Phil. Mag., 28, (1973), p. 667.

[46]. Y. Zhang, S.C. Tonn and M.A. Crimp, "High Temperature Ordered Intermetallic Alloys VI" MRS symp. proc., Pittiburgh, PA, (1992), p. 397.

[47]. P.R. Munroe and I. Baker, Scr. Metall. Mater., Vol.23, (1989), p. 495..

[48]. P. Nagpal and I. Baker, J. Mater. Sci. Letter, 11, (1972), p. 1209.

[49]. J.T. Kim, Ph.D. dissertation, Univ. Mich., (1991).

[50]. M.H. Loretto and K.J. Wasilewski, Phil. Mag., 21(1971), p. 1311.

[51]. Y. Umakoshi and M. Yamaguchi, Phil. Mag., A, Vol.44, (1980), p. 711.

[52]. M.G. Mendiratta, H.M. Kim and H.A. Lipsitt, Metall. Trans., Vol. 15A, Feb. (1984), p. 395.

[53]. P.R. Munroe and I. Baker, J. Mater. Sci., 24, (1989), p. 4246.

[54]. G.I. Taylor and C.F. Elam, Proc. R. Soc. (Lond.), A112, (1926), p. 337.

[55]. G.I. Taylor , Proc. R. Soc. (Lond.), A118, (1928), p. 1.

[56]. V. Vitek, R.C. Perrin and D.K. Bowan, Phil. Mag., 21, (1970), p. 1049.

[57]. J.F. Frenkel and T. Konterava, Phy. Z. Sowj. Un. 13, (1938), p. 1.

[58]. R.E. Peierls, Proc. Phys. Soc., 52, (1940), p. 23.

[59]. F.R.N. Nabarro, Proc. Phys. Soc., 59, (1947), p. 256.

[60]. M.S. Duesbery, V. Vitek and D.K. Bowan, Proc. R. Soc. (Lond.), A332, (1973), p.85.

[61]. V. Vitek, Crystal Lattice Defects, Vol.5, (1974), p. 1.

[62]. R. Pasianot, D. Farkas and E.J. Savino, J. Phys. III, 1, (1991), p. 997.

[63]. M.S. Duesbery, "Dislocations in solids", ed. F.R.N. Nabarro, North Holland Amsterdam. Vol.8, (1989), p. 67.

[64]. V. Paider, D.P. Pope and V. Vitek, Acta Metall., 32, (1984), p. 435.

[65]. M. Khantha, V. Vitek and D. P. Pope, "High Temperature Ordered Intermetallic Alloys IV", MRS sysm. proc., (1992), p. 229.

[66]. M. Yamaguchi and Y. Umakoshi, Phys. Stat. Sol., (a) , 31, (1975), p. 101.

[67]. K. Benhaddane and P. Beauchamp, Phys. Stat. Sol. (a), 98, (1986), p. 195.

[68]. T.A. Parthasarathy, S.I. Rao and D.M. Dimiduk, Phil. Mag. A, Vol.67, No.3, (1993)p643.

[69]. V. Vitek, Progress in Materials Scienc, Vol.36, (1992), p. 1.

[70]. V. Vitek and M. Yamaguchi, "Interatomic and Crystal Potentials", ed J.K. Lee, Conf. Proc. AIME,(1981), p. 223.

[71]. V. Vitek, Proc. Roy. Soc. London, A352, (1976), p. 109.

[72]. R. Chang and L. J. Graham, Phys. Stat. Sol. Vol.189, (1966), p. 18.

[73]. S. Takemchi, Phil. Mag., 39,(1979), p. 661.

[74]. J. Th. M. De Hosson, Interatomic potentials and Crystal Defects, ed. J.K. Lee, (1981), p. 3.

[75]. R.A. Johnson, Phys. Rev., 134, (1964), p. 1329.

[76]. R.A. Johnson, Phys. Rev., 145, (1966), p. 423.

[77]. C.C. Matthai, P.J. Grout and N.H. March, Phys. Lett. 68A, (1978), p. 351.

[78]. C.C. Matthai, P.J. Grout and N.H. March, Int. Quantum Chem., 12s, (1978), p. 443.

[79]. J. Th. M. De Hosson, D.M. Eastering, C.C. Matthai and N.H. Maech, to be pub lished.

[80]. P.M. Mose, Phys. Rev., 134, (1929), p. 57.

[81]. W.A. Harrison, "Pseudopotentials in the Theory of Metals", Benjamin (Reading), 1966, p. 6.

[82]. K.I. Masuda and A. Sato, Phyl. Mag., 371, (1978), p. 531.

[83]. A. Sato and K.I. Masuda, Sol. Sta. Commun., 29, (1979), p. 545.

[84]. A.R. Willians, J. Kuer and C.D. Gelatt, Phy. Rev, B19(1979)6094.

[85]. M.S. Daw, "Atomic Simulation of Materials", ed. V. Vitek, and D.J. Srolovitz, Plenum Press, N.Y., (1989), p. 181.

[86]. M.A. Crimp, Phil. Mag. Lett., No.2, Vol.60, (1989), p45.

[87]. K.J. Hemker, B. Viguier and M.J. Mills, Mater. Sci. Eng., A164, (1993), p. 39.

[88]. M.J. Mills and D.B. Miracle, Acta Metall., Vol.41, (1993), p. 85.

[89]. M.J. Mills, M.S. Daw, S.M. Foils and D.B. Miracles, "High Temperature Ordered Intermetallic Alloys IV", MRS symp. proc., (1992), p. 257.

[90]. Center D'Information Du Cobalt, Cobalt Monography, Brussels, (1960), p. 172.

[91]. R.W. Hertzburg, "Deformation and Fracture Mechanics of Engineering Materials"

ed J. Wile. & Sons, Inc., (1976), p45.

[92]. J.E. Hack, J.M. Brzeski and R. Darolia, Scr. Metall. Mater., Vol.27, No.10, (1992), p. 1259.

[93]. S. Takeuchi, "Interatomic Potentials and Crystalline Defects", ed. J.K. Lee, Conf. Proc., (1980), p. 210.

[94] M.A. Crimp and P.M. Hazzledine, "High Temperature Ordered Intermetallic Alloys III", MRS symp. proc., (1988), p. 131.

[95] P.M. Hazzledine and Y.Q. Sun, "High Temperature Ordered Intermetallic Alloys IV", MRS symp. proc., (1990), p. 209.

[96] J.M. Howe and S.J. Rozeveld, Microscopy Res. and Tech. 23, (1992), p. 230.

[97] A.K. Head, P. Humble, L.M. Clarebrough, A.J. Morton and C.T. Forwood, "Defect in crystalline solids", Vol.7, ed. S. Amelinckx, North-Holland Pub., Co. (1973).

[98]. P. Stadelmann, Mannual of the EMS software package, (1991).

[99]. R.T. Pascoe and C.W.A. Newey, Metal Sci. J. Vol. 5, (1971), p. 50.

[100]. J.D. Whittenberger, R.D. Noebe, C.L. Cullers, K.S. Kumar and S.K. Mannan, Metall. Trans. A., Vol. 22A, July, (1991), p. 1595.

[101]. R.T. Pascoe and C.W.A. Newey, Metal. Sci., Vol. 2, (1968), p138.

[102]. C.R. Feng and K. Sadananda, Sciptas Metall. Mater., Vol.24, (1990), p. 2107.

[103]. P.R. Munroe and I. Baker, Acta Metall. Mater., Vol.5, (1971), p. 1311.

[104]. D.I. Potter, Mater. Sci. Eng., 5, (1960/70), p. 201.

[105]. Y.Q. Sun, R. Darolia, P.M. Hazzledine and G. Taylor, " "High Temperature Ordered Intermetallic Alloys VI", MRS symp. proc., (1994), p. 261.

[106]. D.B. Miracle, Acta Metall., Vol. 39, (1991), p. 1457.

[107]. M. Dollar, S. Dymek, S.J. Hwang and P. Nash, Script Metall. Vol.26, (1992), p. 23.

[108]. J. Bevk, R.A. Dodd and P.R. Strutt, Met. Trans., 4, (1973), p159.

[109]. J.C. Barry, "Computer Simulation of Electron Microscopy Diffraction and Images", ed. W. Krakow and M. O'keefe, TMS, (1989), p. 57.

[110]. M.J. Mills, "Computer Simulation of Electron Microscopy Diffraction and Images", ed. W. Krakow and M. O'keefe, TMS, (1989), p. 239.

[111]. "International Tables for X-ray Crystallography", Vol.3, ed. C.H. Macgillavry and G.D, Rieck, the Kynoch Press, (1962), p. 204.

[112]. P.A. Stadelmann, Ultramicroscopy, 21(1987), p. 131.

[113]. Y.Q. Sun and G. Taylor, Proc. 3rd Japan, Int'l SAMPE Symp. on Intermetallic Compounds for High Temperature Structural Application", eds. M. Yamaguchi and H. Fokutom, Chibam, Japan, (1993), p. 1230.

[114]. R.D. Field, D.F. Lahrman and R. Darolia, Acta Metall., 41, (1993), p. 649.

[115]. D. Farkas and C. Vailhe, J. Mater. Res., Vol. 8, N0. 12, Dec. (1993), p. 3050.

[115] M.A. Crimp and Y. Zhang, "High Temp. Intermetallic VI", Boston, J Horton et al. eds. MRS Proc., Vol. 364, (1995), p. 53.

[116] M.A. Crimp, S.C. Tonn and Y. Zhang, Mater. Sci. Eng., A170, (1993), p. 95.

[117] D. Scharrott, M.S. Thesis, Michigan State University, (1994).

[118]. H. Xiao and I. Baker, Acta Metall. Mater., Vol. 42, No.5, (1994), p. 1535.

[119]. J.P. Neumann, Y.A. Chang and C.M. Lee, Acta Metallurgica, Vol. 24, (1976), p. 593.

[120]. D. Hull and D.J. Bacon, "Introduction to Dislocations", 3rd edition, Perga Mon Press, (1992), p. 215.

[121]. Y.Q. Sun, Private communication.

[122]. D. Farkas and K. Ternes, Private communication.

[123]. J.D. Eshelby and A.N. Stroh, Phil. Mag., 42, (1951), p. 81.

[124]. W.J. Tunstall, P.B. Hirsch and J. Steeds, Phil. Mag., 9, (1964), p. 99.

[125]. Y. Umakoshi and M. Yamaguchi, Phil. Mag. A, 44, (1981), p. 711.

[126]. D. Scharrott and M.A. Crimp, Mater. Sci. Eng.,(A), Vol.15 , (1995), p. 83.

[127]. S.C. Tonn, M.S. Thesis, Michigan State University, (1993).

[128]. N. Rusovic and E.T. Heuing, Phys. Stat. Sol. A, 57, (1980), p. 529.

[129]. T. Godecke and W. Koster, Z. Metallkule, 77, (1986), p. 408.

[130]. F.N. Rhines and J.B. Newkirk, Trnas., ASM, 45, (1953), p. 1029.

[131]. Kubaschewski and Ortrud, Iron-Binary Phase Diagrams, Germany, Springer Verlag Berlin/Heidelberg., (1982).

Appendices

Appendix 1 The parameters used in computer image simulation (Head's program)

Elastic constants: C11=2.705 C12=1.073 C44=1.397

Anomalus absorption coeffient : ANO=0.07

LU is direction of dislocation line

LBM is electron beam direction

LFN is foil normal

W is deviation from Bragg condition

Thick is foil thickness

12. Parameters used for simulation of dislocation "b"

Dislocation "b"	g=(0$\bar{1}$1)	g=(1$\bar{1}$0)	g=(1$\bar{2}$1)
b=[001]	LU=[4 23 3] LBM=[1 $\bar{1}$ 19] LFN=[26 9 25] W=0.82 Thick=3.75	LU=[$\bar{4}$ 23 3] LBM=[2 2 57] LFN=[26 9 25] W=0.82 Thick=3.67	LU=[$\bar{4}$ 23 3] LFN=[26 9 25] LBM=[5 6 7] W=0.15 Thick=7.07
b=[110]	LU=[4 23 3] LBM=[1 $\bar{1}$ 19] LFN=[26 9 25] W=0.82 Thick=3.75	LU=[$\bar{4}$ 23 3] LBM=[2 2 57] LFN=[26 9 25] W=0.82 Thick=3.67	LU=[$\bar{4}$ 23 3] LFN=[26 9 25] LBM=[5 6 7] W=0.15 Thick=7.07
b=[11$\bar{1}$]	LU=[4 23 3] LBM=[1 $\bar{1}$ 19] LFN=[26 9 25] W=0.82 Thick=3.75	LU=[$\bar{4}$ 23 3] LBM=[2 2 57] LFN=[26 9 25] W=0.82 Thick=3.67	LU=[$\bar{4}$ 23 3] LFN=[26 9 25] LBM=[5 6 7] W=0.15 Thick=7.07

Table 13 Parameters used for simulation of dislocation "c"

Dislocation "c"	$\mathbf{g}=(1\bar{1}0)$	$\mathbf{g}=(0\bar{1}1)$	$\mathbf{g}=(1\bar{2}1)$
b=[100]	LU=[$\bar{1}$ 19 1] LBM=[2 2 57] LFN=[26 9 25] W=0.62 Thick=3.0	LU=[$\bar{1}$ 19 1 LBM=[5 4 4] LFN=[26 9 25] W=0.82 Thick=6.07	LU=[$\bar{1}$ 19 1] LBM=[5 7 6] LFN=[26 9 25] W=0.390 Thick=1.05
b=[110]	LU=[$\bar{1}$ 19 1] LBM=[2 2 57] LFN=[26 9 25] W=0.62 Thick=3.0	LU=[$\bar{1}$ 19 1 LBM=[5 4 4] LFN=[26 9 25] W=0.82 Thick=6.07	LU=[$\bar{1}$ 19 1] LBM=[5 7 6] LFN=[26 9 25] W=0.390 Thick=1.05
b=[111]	LU=[$\bar{1}$ 19 1] LBM=[5 4 4] LFN=[26 9 25] W=0.62 Thick=3.0	LU=[$\bar{1}$ 19 1 LBM=[5 4 4] LFN=[26 9 25] W=0.82 Thick=6.07	LU=[$\bar{1}$ 19 1] LBM=[5 7 6] LFN=[26 9 25] W=0.390 Thick=1.05

Appendix 2 Conversion program

```
c    Program Convert
     implicit real*8 (a-h,o-z)
     character*2 al,ni
     open (unit=10,file='Ni50Al',status='old')
     open (unit=11,file='msm001cel',status='new')
     open (unit=12,file='msm001.atom',status='new')
     al='Al'
     ni='Ni'
     fe='Fe'
     co='Co'
     nzal=13
     nzni=28
     nzco=27
     nzfe=26
     dwal=0.005
     dwni=0.001
     dwfe=0.003
     dwco=0.002
     one=1.
     izero=0
     ir=0.1
     ik=10
     write(6,*) 'type in lattice parameter'
     read(5,*) xlat
     write(6,*) 'type in primitive crystal vector along dislocation '
     write(6,*) 'line; put a decimal point in each number and separate'
     write(6,*) 'them by a comma or a space'
     read(5,*) x,y,z
     az=sqrt(x*x+y*y+z*z) * xlat
     write(6,*) 'type in the minimum and maximum values in the'
     write(6,*) 'x-direction; put in a decimal point in the'
     write(6,*) 'numbers and separate them with a comma or space'
     read(5,*) xmin,xmax
write(6,*) 'numbers and separate them with a comma or space'
     read(5,*) ymin,ymax
     write(6,*) 'so that I know where the file ends type in the'
     write(6,*) 'first three numbers of the last line of data'
     write(6,*) 'put a decimal point in each number and separate'
     write(6,*) 'them by a comma or a space'
     read(5,*) xl,yl,zl
     write(6,*) 'type in the stream number you have assigned the'
     write(6,*) 'data file to'
```

```
      read(5,*) nin
      write(6,*) 'type in the stream number for the output'
      read(5,*) nout
      write(6,*) 'thankyou'
      ax=xmax-xmin
      ay=ymax-ymin
      zmax=az/2.
      zmin=-az/2.
      xninety=90.
      write(nout,30)
30    format(10h;supercell)
      write(nout,20) ik,ax/10,ay/10,az/10,xninety,xninety,xninety
20     format(1x,i2,1x,6f8.4)
      read(nin,*)
      natoms=0
      kount=0
10    read(nin,*) x,y,z,xa,ya,za,kat
      if(x.eq.xl.and.y.eq.yl.and.z.eq.zl) then
       write(6,*) 'dunnit'
       write(6,*) 'number of atoms in output file=',natoms
       write(6,*) 'cell sides=',ax,ay,az
      write(12,1000)natoms
1000  format(1x,i3)
       stop
      endif
if(x.lt.xmin) goto 10
      if(x.gt.xmax) goto 10
      if(y.lt.ymin) goto 10
      if(y.gt.ymax) goto 10
      natoms=natoms+1
c     x=x+xa
c     y=y+ya
c     z=z+za
      x=x - xmin
      y=y - ymin
      x=(x+xa)/ax
      y=(y+ya)/ay
      if(z.lt.0.) z=z+az
      if(z.gt.az) z=z-az
     z=z/az
      if(kat.eq.1) then
       write(nout,100) x,y,z,one,dwal,ir,izero,izero
      endif
      goto 10
100   format(1x,2hAl,1x,8f8.4)
      end
```

Appendix 3 Autorun in C-shell

```
#!/bin/csh
# Purpose: Automate repetitious execution of ems-ms1 program with
#       slightly varying input files.
# File Requirments: subconstant files must end last line of text with a
#               return.  new0xx files should begin with a new001 file
#               previously created by ms1 run manually.

if ($#argv < 4) then
  echo ' '
  echo -n 'Usage: autorun ems_program iterations data_file_constant'
  echo ' input_file_constant'
  echo -n '   ie: autorun    ms1        10         subconstant'
  echo '       new [showtmps]'
  echo ' '
  exit(1)
endif

set showtmps = false

if ($#argv == 5) then
  if ($5 == 'showtmps') set showtmps = true
endif

@ i = 1
while ($i < $2)
@ constcnt = 0
foreach file ($3*)$1 < $inputfile > tmpout$$.$i
  if ($showtmps == 'false') /bin/rm -f $inputfile
  @ i++
endif
end
end
exit 0
@ constcnt++
if ($i <= $2 && ($i != 1 || $constcnt != 1)) then
  set inputfile = tmpinp$$.$constcnt
  cat $file > $inputfile
  if ($i < 10) then
echo $4'00'$i >> $inputfile
  else
echo $4'0'$i >> $inputfile
  endif
```